Universidade do Minho
Escola de Ciências

Tiago Dias do Vale

Search for heavy fermions with LHC data

Search for heavy fermions with LHC data

Tiago Dias do Vale

julho de 2021

Universidade do Minho
Escola de Ciências

Tiago Dias do Vale

Search for heavy fermions with LHC data

Doctoral Thesis in Physics

Work supervised by
Professor Doutor Nuno Filipe da Silva
Fernandes de Castro

Julho de 2021

DECLARAÇÃO

Nome: Tiago Dias do Vale

E-mail: tiago.vale@cern.ch

Telefone: +351964946489

Número de Cartão de Cidadão: 14020611 6 ZX8

Título da Tese: Search for heavy fermions with LHC data

Orientador: Professor Doutor Nuno Filipe da Silva Fernandes de Castro

Ano de Conclusão: 2021

Designação do Doutoramento: Doutoramento em Física

Universidade do Minho, 30 de Julho de 2021

Assinatura:

DECLARAÇÃO DE INTEGRIDADE

Declaro ter atuado com integridade na elaboração do presente trabalho académico e confirmo que não recorri à prática de plágio nem a qualquer forma de utilização indevida ou falsificação de informações ou resultados em nenhuma das etapas conducente à sua elaboração.

Mais declaro que conheço e que respeitei o Código de Conduta Ética da Universidade do Minho.

Universidade do Minho, 30 de Julho de 2021

_____

(Tiago Dias do Vale)

Acknowledgements

My journey through this PhD has been exciting and it would not have been possible without a lot of people tha deserve my thanks.

My advisor, Nuno Castro, has been an incredible help, source of advice and inspiration, constantly guiding me through all aspects of doing work in physics.

A very special thanks goes to Patricia Conde Muiño for the constant support, especially with my technical work, which would have been impossible to do without her. I would also like to thank everyone at LIP for making this lab a great place to work. In particular everyone here in Braga with whom I shared all these moments. Henrique Carvalho for the great company and all the help; Guilherme Guedes for the help that was always provided in hilarious form and Maria Ramos for teaching me so patiently. To Rute Pedro and Miguel Romão I want to thank for their knowledge and support during our phenomenological work.

My colleagues from the Heavy Quarks and Tops subgroups deserve my gratitude for the help and supervision of the analyses development. I would like to thank Johannes Erdmann and Tim Andeen for their tremendous support; Nikiforos Nikiforou for the analysis work and for helping me being an analysis contact; Elena Freundlich with whom I worked closely since my Masters; Avik Roy and Mesut Unal for being great colleagues.

To all my friend here in Braga I thank you for all the great moments. A special thanks to all my jiujitsu friends that made my nights after work even more work. In particular a big thank you to Berto Lima for creating such a large and beautiful family.

To Ana Peixoto I thank you for being the most incredible friend I could ever ask for. I would never have made this far without you.

Lastly, I would like to thank my loving family, especially my parents.

Abstract

This thesis presents two searches for vector like top (VLT) and vector like bottom (VLB) using data collected by the ATLAS experiment during the second run of the Large Hadron Collider operations, at a center of mass energy of $\sqrt{s}$ = 13 TeV. These analyses target vector like quarks (VLQ) decaying to a Z boson and a third generation quark, in events with the Z boson decaying to electrons or muons. Since it is known from previous searches that, if VLQs exist in nature, they should have high masses, a selection based on multiplicity and transverse momentum of the final state objects was implemented.

The first analysis presented uses a partial run-2 dataset, corresponding to data collected between 2015 and 2016, amounting to an integrated luminosity 36.1 fb^{-1} of data. It features searches for pair and single production of vector like quarks. As no deviation from the Standard Model expectation was found, upper mass limits were derived. VLT (VLB) masses below 1.03 (1.01) TeV for the singlet hypothesis and 1.21 (1.13) TeV for the doublet hypothesis are excluded. The results, when assuming branching ratio exclusively to Z, are 1.34 and 1.22 TeV for the VLT and VLB, respectively.

A second iteration of the analysis using the complete run-2 dataset, amounting to 139 fb^{-1}, is the main focus of the present thesis. It focuses exclusively on pair production of VLT and VLB, and features a new search strategy, which includes a signal region categorization based on multiplicities of tags of a deep neural network trained to classify jets as originated from top quarks, W or Z bosons, Higgs bosons or background jets. In this search no deviations from the Standard Model expectation were found so upper mass limits were derived. Masses below 1.27 and 1.20 TeV are excluded for singlet VLT and VLB, respectively. These values, for the doublet hypothesis, are 1.46 and 1.32 TeV for VLT and VLB, respectively. In the scenario where all VLQ decay exclusively to Z bosons, the excluded masses are 1.42 and 1.60 TeV for VLB and VLT, respectively. These results represent a significant improvement from the previous iteration of the analysis and are currently the most stringent limits obtained in Zt/b final states.

Resumo

Esta tese apresenta duas pesquisas de quarks vectoriais top (VLT) e bottom (VLB) com dados colectados pela experiência ATLAS durante a segunda ronda de operações do Large Hadron Collider, com uma energia de centro de massa de 13 TeV. Estas análises procuram quarks vectoriais (VLQ) em decaimentos para um bosão Z e um quark de terceira geração, em eventos em que o bosão Z decai para electrões ou muões. Como é sabido de pesquisas passadas que, se os VLQs existerem, eles devem ter alta massa, uma seleção com base na multiplicadade e momento transverso das partículas de estado final foi implementada.

A primeira análise apresentada usa um conjunto de dados parcial da segunda ronda, correspondendo aos dados colectados entre 2015 e 2016, numa luminosidade integrada total de 36 fb^{-1}. Contém pesquisas de produção em pares e simples de quarks vectoriais. Dado que nenhum desvio em relação à expectativa do Modelo Padrão foi encontrada, limites de massa foram obtidos. Massas de VLT (VLB) abaixo de 1.03 (1.01) TeV para o singleto e 1.21 (1.13) TeV para a hipótese de dubleto foram excluídas. Os resultados, quando uma probablidade de decamentos exclusiva para o bosão Z é assumida, são 1.34 e 1.22 TeV para o VLT e VLB, respectivamente.

A segunda iteração da análise, usando o conjunto completo da segunda ronda, num total de 139 fb^{-1}, é o foco principal desta tese. Foca-se exclusivamente na produção por pares de VLT e VLB, e tem uma nova estratégia de pesquisa, que inclui uma categorização da região de sinal baseada na multiplicidade de tags de uma rede neuronal treinada para classificar jactos como originados de quarks top, bosões W ou Z, bosões Higgs ou jactos de fundo. Nesta pesquisa nenhum desvio em relação à expectativa do Modelo Padrão foi encontrada, portanto limites de massa foram obtidos. Massas inferiores a 1.27 e 1.20 TeV são excluídas para singletos de VLT e VLB, respectivamente. Estes valores, para a hipótese de dubleto, são 1.46 e 1.32 TeV, respectivamente. No cenário em que os VLQ decaem exclusivamente para bosões Z, as massas excluídas são 1.42 e 1.60 TeV, respectivamente. Estes resultados representam uma melhoria significativa em relação à iteração anterior da análise e são os melhores limites até à data em estados finais de Zt/b.

Contents

List of Figures

List of Tables

Introduction

The Standard Model of Particle physics (SM) describes all known particles and their interactions. Since the discovery of the Higgs boson in 2012, the Standard Model became a more complete picture as the presence of a particle responsible for the mechanism that breaks electroweak symmetry and generates bosons and fermions mass was found. However, despite the many achievements of the SM, it does still leave some important unanswered questions. It does not have a quantum field description of gravity; it does not have a candidate for dark matter or dark energy; it does not offer an explanation for the experimental evidence for the existence of neutrino masses; it does not describe how the asymmetry between matter and antimatter originated and it does not have a solution for the hierarchy problem. Attempts at answering these questions lead to many new physics models, most of which predict the existence of new particles. Finding these particles would significantly aid in the understanding of the particle physics puzzle. Because of that both ATLAS and CMS experiments developed an extensive search programme that covers many new particles, motivated by many classes of new physics models. These are experiments of the Large Hadron Collider at the European Organization for Nuclear Research (CERN), a 27 km particle accelerator located near Geneva, Switzerland. Using superconducting magnets it circulates proton bunches up to high energies, and collides them at the interaction points corresponding to the four experiments: Alice and LHCb besides the aforementioned ATLAS and CMS.

One interesting set of particles that are a feature of interest in many models that try to solve the open questions of the Standard Model are vector like quarks (VLQ). These are spin 1/2 colored fermions that have the same the same electroweak (EW) quantum numbers for the left- and right-handed components. An interesting consequence of this is that they do not need a Yukawa coupling to the Higgs boson to generate their mass, and so they avoid many experimental constraints that make the existence of a fourth

chiral quark family disfavored. They can have different mechanisms of production, produce tree-level flavor-changing neutral currents and other interesting phenomenological features that will be explored within this thesis.

Searches for VLQ have been performed during the first run of the Large Hadron Collider by both the ATLAS and CMS experiments, setting upper limits on their masses. However, with the increase of center of mass energy and luminosity, new approaches to search for VLQ become possible. This thesis presents searches for VLQ performed during the second run of ATLAS data taking at $\sqrt{s}$ = 13 TeV. It focuses on analyses that target decays of VLQ to a leptonically decaying Z boson and a third generation quark. The first iteration of the analysis uses a partial dataset collected during 2015 and 2016, amounting to an integrated luminosity of 36.1 fb^{-1}. It searches for vector like top (VLT) and vector like bottom (VLB) in events with at least two opposite-sign, same flavor leptons whose invariant mass is within a 10 GeV window of the Z boson mass. It requires at least 1 b-tagged jet, which is expected from the decay of the VLQ, and particles with large amounts of transverse momentum (p_T). This analysis covers VLQ produced in pairs and singly, each with dedicated dilepton and a trilepton channels. All channels have signal regions together with control regions, in which the signal contribution is low, used to constraint uncertainties of the main backgrounds and aid the fit in correcting mismodelling. This analysis was performed in collaboration with the TU Dortmund group in Germany, the University of Arizona group in the USA, the Kyoto University group in Japan and the University of Texas at Austin group in the USA. The author of this analysis was the main analyzer of the dilepton channel with 0 or 1 large radius jets, targeting pair production of VLQs.

The second iteration of this analysis, of which the author of this thesis is the analysis contact for the ATLAS Collaboration, uses the full run 2 dataset, which amounts to 139 fb^{-1}. It focuses on pair production of VLB and VLT, in the same leptonic Z boson topology, split into a dilepton and a trilepton channel. It requires at least 1 b-tagged jet, 2 opposite-sign, same flavor leptons within the Z boson mass window, used to reconstruct a Z boson candidate, which is required to have large transverse momentum. The main improvement from this iteration is the inclusion of a deep neural network tagger that outputs the probability of jets being originated from top quarks, W or Z bosons, H bosons or background jets. The multiplicity of jets tagged as each of these classes is used to build a categorization of the signal regions, assisted by control regions. The significant increase in luminosity allows for this exploration of the different decay topologies that VLQ pair production can provide, with high p_T objects, resulting in a fit with many regions with different background compositions and signal to background ratios. This analysis was done in collaboration with the TU Dortmund group in Germany and the University of Texas in the USA. The author of this thesis was the main analyzer of the trilepton channel and responsible for the combined fit and limit setting. Both analyses try to either discover VLQs or set stringent upper limits on their masses.

The thesis starts with a description of the Standard Model, given in chapter 2. It describes, using gauge theory, quantum electrodynamics, quantum chromodynamics and the electroweak theory, corresponding to the interactions described by the SM. It follows a description of the Higgs mechanism and how it generates

bosons and fermions masses. Following a description of the SM shortcomings, a brief description of Composite Higgs models is given. This is one of the classes of models that predicts the existence of vector like quarks and it is used as an example throughout the thesis. The chapter ends with a description of VLQs and their phenomenology.

In chapter 3, the experimental setup is described. Starting by the LHC, and following with the ATLAS detector, a description of each component that makes the experiment work is given. The ATLAS detector is described by its main components, the inner detector, the calorimeters and the muon spectrometer; the trigger system and the Worldwide LHC Computing grid. Besides the central detector, a description of the ATLAS Forward Proton (AFP) is given. This subdetector, located at around two hundred meters from the ATLAS central detector, complements the central system by measuring the trajectory of protons that remain from the collisions at the interaction point. The chapter ends with a description of the development of a trigger chain designed to target central exclusive production of jets. This work was performed as the qualification task, which is required by ATLAS to all the new members of the Collaboration.

The chapter that follows, chapter 4, details the searches for vector-like quarks with a partial run-2 dataset amouting to 36.1 fb^{-1} of ATLAS data It gives an overview of the results obtained by the ATLAS and CMS experiments using data collected during 2015 and 2016. To it follows a description of the ATLAS combination that was performed at the time of the analysis publication, to which the author of this thesis was the analysis liaison. It combined all pair production analysis performed by the ATLAS Collaboration, which allowed to significantly improve the results obtained by the individual analyses.

The last chapter of the thesis, chapter 5, describes searches with the full run 2 dataset. The first section describes the data used in the analysis and the Monte Carlo simulations, used as prediction for signals being searched and the expected backgrounds. The definitions of the different objects used in the analysis are given in the next section. It describes the kinematic requirements made for each type of object, how they are identified and reconstructed. The next section describes the event selection. This is done by motivating the requirements of the analysis, and showing how they affect the final distributions, the expected yields, the modelling of basic variables and the signal efficiency. To that follows a detailed description of all the systematic uncertainties included in the analysis. Next, a description of the statistical framework that will be used to fit the systematic uncertainties and either set for a discovery of VLQs or stringent mass limits is given. The results that are obtained following the statistical procedure are shown in the next section. A description of the fit is done, in order to understand its behavior, followed by a description of the test for discovery and the setting of mass limits and interpretation of these results. The chapter ends with a brief discussion of the limitations of the analysis and what could guide the next round of VLQ searches.

Theoretical introduction

2.1 The Standard Model of Particle Physics

2.1.1 Symmetry

Symmetry is a cornerstone concept in physics and it is a core part of the formulation of the Standard Model of Particle Physics. It can be defined as a set of transformations under which the physical system at study stays invariant. Besides its beauty, the concept of symmetry becomes truly powerful after the remarkable discovery by Emmy Noether, known as the Noether's theorem [1]. It shows that every differentiable symmetry of a given action has a corresponding conserved quantity. A notable application of this theorem shows how energy conservation is a consequence of time translation symmetry.

One of the symmetries that serves as the foundation of the SM is gauge symmetry. A simple example of gauge symmetry can be shown for a massive scalar field ψ with mass m. This Lagrangian [1] can be defined as:

$$\mathcal{L} = \partial^\mu \psi^\dagger \partial_\mu \psi - m^2 \psi^\dagger \psi \tag{2.1}$$

This Lagrangian will remain invariant under transformations such as:

$$\psi(x) \longrightarrow \psi(x)e^{i\alpha} \quad , \quad \psi(x) \longrightarrow \psi(x)e^{-i\alpha} \tag{2.2}$$

These are rotations of α in the complex plane and are defined by the $U(1)$ group, the one-dimensional group of unitary transformations. Therefore it is said that the Lagrangian has a global $U(1)$ symmetry. Let it be noted, however, that the same Lagrangian will not remain invariant if the α angle has a dependence

---

[1]Technically it is a Lagrangian density but from now on referred to as Lagrangian for simplicity.

on x, i.e. under *local* $U(1)$ transformations. This can be seen as the derivative term will produce an extra factor from the exponential argument differentiation. In order to force the Lagrangian to have local symmetry we can redefine the derivative so that this extra factor is cancelled. This concept is known as covariant derivative and for this particular Lagrangian we can define it as:

$$D_\mu = \partial_\mu + iqA_\mu(x) \tag{2.3}$$

where $A_\mu(x)$ is a new vector field that transforms as $A_\mu \rightarrow A_\mu - \frac{1}{q}\partial_\mu\alpha(x)$ and q is the coupling strength between the scalar and vector fields. The A_μ field is introduced to restore local gauge symmetry and is therefore called a *gauge field*. The number of necessary gauge fields, following the aforementioned procedure, is defined by the number of generators of the symmetry group. In this simple example the gauge symmetry is $U(1)$ which only has one generator. This procedure can be generalized to any gauge symmetry by defining the partial derivative as:

$$D_\mu = \partial_\mu - \frac{1}{2}igT_aA_\mu^a \tag{2.4}$$

$T_a(a \in \{1, .., N\})$ are the generators of the symmetry group. The A_μ^a field is transformed as:

$$A_\mu^a \longrightarrow A_\mu^a + \frac{1}{g}\partial_\mu\alpha^a(x^\mu) + f_{abc}A_\mu^b\alpha^c(x^\mu) \tag{2.5}$$

where f_{abc} are the structure constants of the group, which are given by the commutation relations of the generators: $[T_a, T_b] = if_{abc}T_c$. This procedure will be used to describe all the electromagnetic, weak and strong interactions as gauge theories.

2.1.2 Quantum electrodynamics

A fermion with mass m can be described by the Dirac lagrangian,

$$\mathcal{L} = \bar{\psi}(i\gamma^\mu\partial_\mu - m)\psi \tag{2.6}$$

with γ being the Dirac matrices that generate the Clifford algebra defined by $\{\gamma^\mu, \gamma^\nu\} = 2g^{\mu\nu}$, with $g^{\mu\nu}$ being the Minkowsky metric with the $(+ - --)$ signature. This Lagrangian has a global U(1) symmetry, but we need it to be invariant under local transformations. Fortunately we can follow the procedure we described before. As the Lagrangian has a U(1) symmetry we have the same covariant derivative as in the example we followed, given by eq. (2.3). In this case A_μ is the gauge field of Quantum electrodynamics (QED), that we know as the photon. The charge in this covariant derivative is the electron charge, that we will from now on define as e. Also following from the example we know that the photon field transforms as

$$A_\mu = A_\mu - \frac{1}{e}\partial_\mu\alpha(x) \tag{2.7}$$

The lagrangian for a free vector field is

$$\mathcal{L} = -\frac{1}{4}F^{\mu\nu}F_{\mu\nu} \tag{2.8}$$

with $F^{\mu\nu} = \partial^\mu A^\nu - \partial^\nu A^\mu$. This corresponds to the kinetic term of the photon. This is explicitly omitting a mass term $\frac{1}{2}m^2 A_\mu A^\mu$ as it would break our gauge symmetry and we know that the photon is experimentally consistent with being a massless particle [2]. With this we can assemble the lagrangian for QED, using eqs. (2.6) and (2.8)

$$\mathcal{L}_{QED} = \bar{\psi}(i\gamma^\mu D_\mu - m)\psi - \frac{1}{4}F^{\mu\nu}F_{\mu\nu} \tag{2.9}$$

If we expand eq. (2.9) we obtain the following

$$\mathcal{L}_{QED} = \bar{\psi}(i\gamma^\mu \partial_\mu - m)\psi - e\bar{\psi}\gamma^\mu A_\mu \psi - \frac{1}{4}F^{\mu\nu}F_{\mu\nu} \tag{2.10}$$

This describes the kinetic energy and fermion mass, the kinetic energy of the photon and the interaction between the two fields.

2.1.3 Quantum chromodynamics

Quantum chromodynamics (QCD) is the theory that describes the strong force. The gauge group to which the theory Lagrangian is invariant is SU(3). This group has 8 generators, corresponding to 8 gluon fields. The QCD Lagrangian can be written as:

$$\mathcal{L}_{QCD} = \bar{q}(i\gamma^\mu \partial_\mu - m)q - g_s(\bar{q}\gamma^\mu \frac{\lambda_a}{2}q)G_\mu^a - \frac{1}{4}G_{\mu\nu}^a G_a^{\mu\nu} \tag{2.11}$$

where q are the quark fields and m its masses, g_s is the strong coupling constant, λ_a are the Gell-Mann matrices, responsible for generating the SU(3) symmetry. G_μ^a are the gluon fields that transform under SU(3) as $G_\mu^a \rightarrow G_\mu^a - \frac{1}{g_s}\partial_\mu \alpha_a - f_{abc}\alpha_b G_\mu^c$, where f_{abc} is the group structure constant. You may notice this is a term that was not present in the Quantum electrodynamics field transformation. This is because the group is non-abelian, and it implies that gluon fields interact not only with quarks but also with themselves. $G_{\mu\nu}^a$ is the kinetic term of the gluon fields. Again, due to the self-interaction, this means the inclusion of an extra term: $G_{\mu\nu}^a = \partial_\mu G_\nu^a - \partial_\nu G_\mu^a + g_s f_{abc}G_\mu^b G_\nu^c$. The sum over c corresponds to the 6 quark flavors. An interesting feature of QCD is that its coupling is smaller for shorter quark distances. In the case of sufficiently short distances (or, equivalently, large enough exchanges of momentum), quarks become asymptotically free. Therefore QCD is only perturbative at high energies [3, 4]. On the other end of the spectrum, as quark distances become larger so does their coupling, leading to quark confinement. This property of QCD disallows the existence of isolated quarks and gluons, meaning they must form bound states of colorless hadrons. Another interesting consequence of this is that if one tries to extract a quark from a hadron, as their distance increases so does the energy that needs to be supplied to increase their distance. At some point it becomes energetically favorable for a new quark and anti-quark pair to be

created and they form new bound states. Because all quarks are always bound to form colorless states, when quarks are produced in our experiments there is the associated production of its counterparts, in a process called hadronization.

2.1.4 Electroweak theory

Weak interactions are governed by a SU(2)$_L$ theory. The subscript indicates that only left-handed chiral states have weak interactions. Therefore fermions are grouped into SU(2)$_L$ doublets (with $T = \frac{1}{2}$ and $T_3 = \pm\frac{1}{2}$) if they are left-handed and singlets (with $T = 0$ and $T_3 = 0$) if they are right-handed. Weak interactions can be unified with electromagnetic interactions into a single theory called the electroweak (EW) theory. Its group is SU(2)$_L$×U(1)$_Y$, with Y being the weak hypercharge, that is related to the electric charge and the third weak isospin component T_3 by $Q = T_3 + \frac{Y}{2}$. The 3 SU(2)$_L$ generators result in 3 gauge bosons $W_\mu^{1,2,3}$ while the B_μ field is associated with the U(1)$_Y$ group. The covariant derivative of the electroweak interactions can be written as:

$$D_\mu = \partial_\mu + ig_W T_i W_\mu^i + ig_Y Y B_\mu^i \qquad (2.12)$$

with g_W and g_Y being the weak and electromagnetic coupling constants. By expanding the covariant derivative we can write the EW Lagrangian as:

$$\mathcal{L}_{EW} = -\frac{g_Y}{2}(\bar{\psi}\gamma^\mu\psi)B_\mu - g_W(\bar{\psi}_L\gamma^\mu T_i\psi_L)W_\mu^i - \frac{1}{4}F_{\mu\nu}^i F_i^{\mu\nu} \qquad (2.13)$$

With $F_{\mu\nu}^i$ being the kinetic term of the gauge bosons, given by $F_{\mu\nu}^i = \partial_\mu W_\nu^i - \partial_\nu W_\mu^i + g_W \epsilon_{ijk} W_\mu^j W_\nu^k + \partial_\mu B_\nu^i - \partial_\nu B_\mu^i$.

It should be clarified that the B_μ boson does not directly correspond to the photon field. From the EW Lagrangian it can be seen that the B_μ interacts with the two components of the isospin doublets, which include the neutrino fields, whereas the photon does not couple to neutrinos as they electrically neutral particles. After the EW symmetry break, that will discussed later, the photon and the Z boson fields arise from a mixing of the B_μ and W_μ^3 fields, given by:

$$\begin{pmatrix} A_\mu \\ Z_\mu \end{pmatrix} = \begin{pmatrix} \cos\theta_W & \sin\theta_W \\ -\sin\theta_W & \cos\theta_W \end{pmatrix} \begin{pmatrix} B_\mu \\ W_\mu^3 \end{pmatrix} \qquad (2.14)$$

where θ_W is the Weinberg angle. The $W^\pm$ bosons are a linear combination of W^1 and W^2 given by $W^\pm = \frac{1}{\sqrt{2}}(W^1 \mp iW^2)$. There is also a correspondence of the electric charge and the coupling constants given by $g_W \sin\theta_W = g_Y \cos\theta_W = e$.

2.1.5 Higgs mechanism

With the introduction of the B_μ and W_μ^3 fields we complete our description of the fundamental interactions (again, gravity not withstanding). It was mentioned in the description of QED that the mass term for the
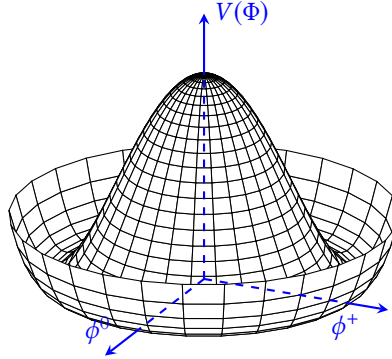
Figure 2.1: Shape of the Higgs potential in two dimensions, as a function of the field components.

photon field is not included as we know it to be massless. However, no mention to the masses of the EW gauge bosons was made, and it can be seen that their introduction would not preserve gauge symmetry. Does this imply that the $W^{\pm}$ and Z bosons are massless? We have experimental knowledge that this must not be the case, so there seems to be a problem with the given descriptions. This problem of keeping gauge invariance while introducing masses to the gauge bosons was solved by Higgs, Brout, Englert, Guralnik, Hagen and Kibble in 1964 [5–7] and will be referred to in this text as the Higgs mechanism.

The description of this mechanism starts with the introduction of a complex scalar SU(2) doublet Φ that couples to the gauge fields:

$$\Phi = \begin{pmatrix} \phi^+ \\ \phi^0 \end{pmatrix}, \tag{2.15}$$

and a scalar potential given by:

$$V(\Phi) = \mu^2 |\Phi^\dagger \Phi| + \lambda (|\Phi^\dagger \Phi|)^2, \tag{2.16}$$

with $\lambda > 0$. The shape of this potential, for $\mu^2 < 0$, can be seen in fig. 2.1.

For the case where $\mu^2 > 0$ there is a trivial minimum for $\phi^+ = \phi^0 = 0$. When $\mu^2 < 0$, the minimum changes and is not at 0 and the scalar field develops a vacuum expectation value (VEV), v.

From the shape of the potential we can see that the direction of the minimum is not relevant, as any choice of alignment still leaves the physics invariant, and so we can choose a convenient point:

$$\Phi \equiv \frac{1}{\sqrt{2}} \begin{pmatrix} 0 \\ v \end{pmatrix}. \tag{2.17}$$

The scalar has $Y = 1$, as we know it to be a SU(2) doublet, and the choice made in eq. (2.17) sets $T_3 = -1$, so we get that $Q = \frac{-1+1}{2} = 0$. This means that we spontaneously broke the SU(2)$_L \times$U(1)$_Y$ symmetry by choosing a specific realisation of the Φ field, but electromagnetism remains unbroken, i.e. our spontaneous symmetry break is:

$$SU(2)_L \times U(1)_Y \rightarrow U(1)_{EM} \tag{2.18}$$

The Lagrangian for the scalar is:

$$\mathcal{L}_S = (D^\mu \Psi)^\dagger (D_\mu \Psi) - V(\Psi) \tag{2.19}$$

with

$$D_\mu = \partial_\mu + i g_W T W_\mu + i g_Y B_\mu Y \tag{2.20}$$

In order to investigate the physical consequences of the symmetry break we perturb the Higgs field around its minimum:

$$\Psi = \frac{1}{\sqrt{2}} \begin{pmatrix} 0 \\ v + h \end{pmatrix} \tag{2.21}$$

By plugging this into eq. (2.19) we get a contribution to the gauge boson masses that comes from the scalar kinetic term:

$$M^2 \approx \frac{1}{2}(0, v)(g_W T W_\mu + g_Y B_\mu)^2 \begin{pmatrix} 0 \\ v \end{pmatrix} \tag{2.22}$$

By making use of the field definitions set in function of the Weinberg angle at eq. (2.14) we arrive at the gauge boson masses:

$$m_W = \frac{1}{2} g_W v = 81 \text{ GeV}, \tag{2.23}$$

$$m_Z = \frac{1}{2}\sqrt{(g_W^2 + g_Y^2)} v = \frac{m_W}{\cos \theta_W} = 91 \text{ GeV} \tag{2.24}$$

and

$$m_\gamma = 0 \tag{2.25}$$

The scalar mass is set by $m_H = \sqrt{-2\mu^2} = \sqrt{2\lambda v^2} = 125$ GeV. All that is left to determine are the fermion masses, which we can do in a similar procedure. We start by writing the fermion fields in terms of their left- and right-handed components:

$$\psi_{L,R} = \frac{1}{2}(1 \mp \gamma_5)\psi \tag{2.26}$$

with $\gamma_5 = i\gamma_0\gamma_1\gamma_2\gamma_3$. We can write a SU(2)$_L$ doublet as:

$$L_L = \begin{pmatrix} v_L \\ e_L \end{pmatrix} \tag{2.27}$$

Despite the experimental knowledge that neutrinos have mass [8], its mass formulation requires a Beyond the Standard Model (BSM) construction. Therefore the SM is constructed with no right-handed neutrino. So, with this definition of left-handed fermions and knowing that right-handed fermions do not interact with W bosons we can write their coupling to the gauge fields as

$$\mathcal{L}_{lepton} = i\bar{e}_R\gamma^\mu(\partial_\mu + g_Y Y_e B_\mu)e_R + i\bar{L}_L\gamma^\mu(\partial_\mu + g_W T W_\mu + i g_Y Y_L B_\mu)L_L \tag{2.28}$$

We know that a fermion mass term of the form $\mathcal{L}_{mass} = -m\bar{\psi}\psi$ would not be gauge invariant, because of their chirality, i.e. as the left-handed component is a SU(2)$_L$ doublet and the right-handed component is a singlet the result would not be a scalar quantity. However we can write a Higgs doublet coupling to the fermions of the form

$$y_f[\bar{\psi}_L\Phi\psi_R + \bar{\psi}_R\bar{\Phi}\psi_L], \tag{2.29}$$

with y_f being the Yukawa coupling constant. Given that the scalar field is a SU(2) doublet these terms are SU(2)$_L$ singlets, and consequently gauge invariant. When we expand this term with the scalar formulation when perturbed around its minimum, given by eq. (2.21), we get mass terms with the form

$$m_f = y_f\frac{v}{\sqrt{2}} \tag{2.30}$$

In a similar fashion to what was discussed in the EW section, the fermion mass eigenstates are mixtures of their electroweak eigenstates. This mixing, in the case of quarks, is determined by the Cabibbo-Kobayashi-Maskawa (CKM) matrix.

2.1.6 Shortcomings

The SM has had enormous experimental success for decades, describing most of the interactions we see. It is capable of describing with very high accuracy a large range of physics phenomena at a very large range of energies. This is notably summarized in fig. 2.2. It has, however, some shortcomings, of which a few were already mentioned:

- No quantum field theory description of gravity;

- No explanation for neutrino masses that have experimental evidence of being nonzero [10];

- No dark matter [11–13] candidate;

- No dark energy candidate, or any other explanation for the observed accelerated expansion of the Universe [14];

- No explanation for the matter and antimatter asymmetry, that would require CP violating effects beyond what the is seen in EW interactions [15].

- The Higgs mass has one-loop contributions that are quadratically sensitive to high scales, with $\delta m_H^2 \approx -\frac{y_t^2}{8\pi^2}\Lambda^2$, with y_t being the Yukawa coupling to the top quark and Λ the cutoff scale. This is not a problem per se, unless one assumes that the aforementioned problems require BSM physics at a higher scale. In that case these contributions lead to a necessity of fine-tuning that may be considered unnatural [16]. This problem is know as the naturalness problem, or the hierarchy problem.
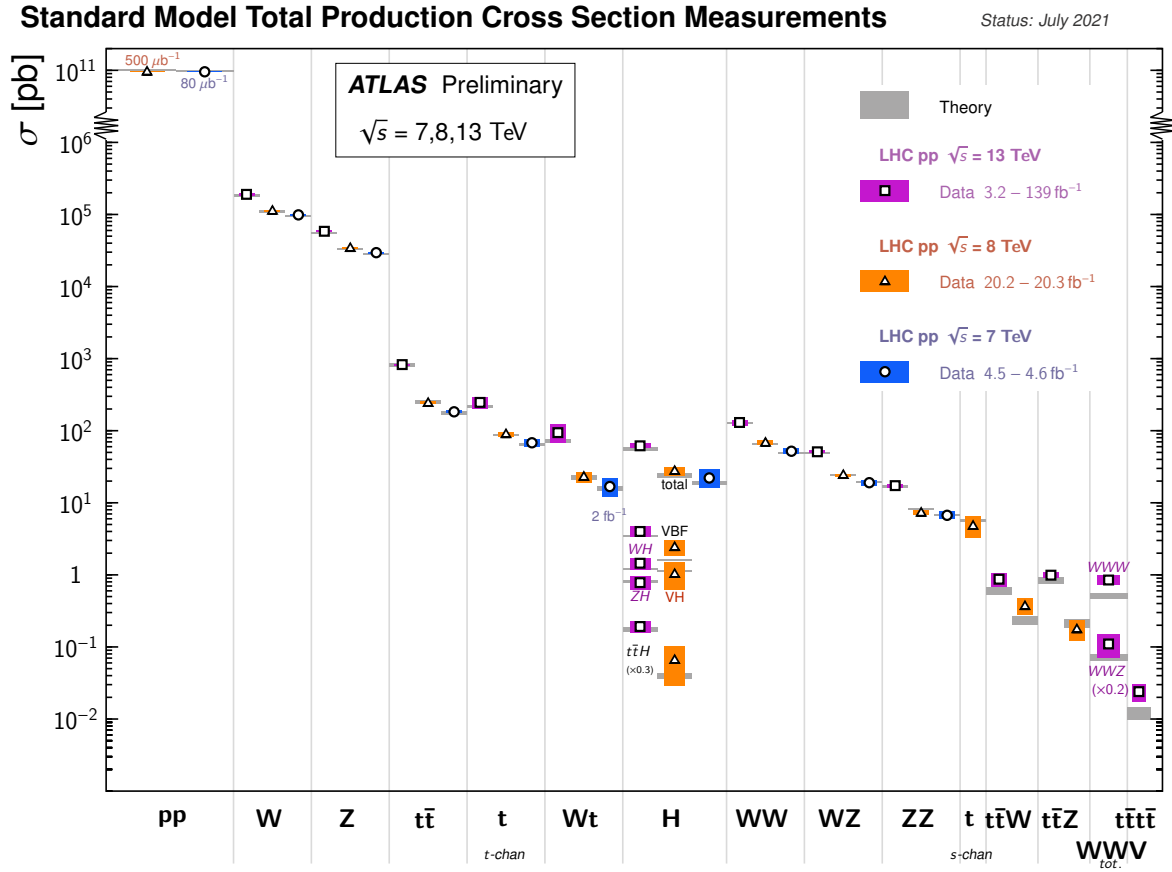
Figure 2.2: Summary of several cross section measurements compared to the corresponding theoretical expectations. [9]

There are many proposed ways of solving the hierarchy problem, of which a few of the most popular are:

- Supersymmetry (SUSY): as was shown in the description of the hierarchy problem there is a direct dependency on the Yukawa coupling to the quarks (of which only the top quark was explicitly written as it the largest by a large difference). SUSY [17–22] proposes that for each of the SM fermion/boson that is included in the Higgs mass correction there is a boson/fermion partner. The supersymmetrical particle would enter the loop with the opposite sign of its partner and therefore protect the Higgs mass from its quadratic sensitivity to the high scales. SUSY is a very popular proposal, it has many different classes of models and is heavily searched for at the LHC experiments.

- Large extra dimensions: this class of models [23, 24] solves the hierarchy problem by setting gravity to become strongly interacting and thus shortening the distance between the weak scale and the cutoff scale. They come with predicted observables at colliders, like quantum black holes, that are searched for at LHC experiments.

- Composite Higgs models [25, 26]: a proposed solution to the hierarchy problem that is particularly

relevant to this thesis and so it will be discussed in more detail in the following section.

2.2 Composite Higgs models

In Composite Higgs Models (CHM) the SM Higgs boson is a Goldstone boson of a new strong sector. This strong sector binds the Higgs as a composite particle, and thus eliminates any concerns regarding quadratic quantum corrections to its mass. The Higgs is dynamically generated with a light mass, in an analogous manner to pions in QCD. CHM usually start with a large global symmetry group G, that spontaneously breaks to a subgroup H. The minimal choice for a $G \rightarrow H$ break that contains the EW SU(2)$_L \times$U(1)$_Y$, leaves at least 4 Goldstone bosons to parametrize the Higgs boson and preserves custodial symmetry is SO(5)$\times$U(1)$_X$ $\rightarrow$ SO(4)$\times$U(1)$_X$. U(1)$_X$ is included in order to preserve hypercharge in the unbroken group. By including mixing of SM fermions to fermions of this new strong sector, that appear as resonances of the new strong sector, in a mechanism called partial compositeness, we can parametrize their mixing via an angle ϵ as

$$|observed\ particle\rangle \sim |elementary\rangle + \epsilon\,|composite\rangle \qquad (2.31)$$

which can be seen as a degree of compositeness. Top partners are naturally predicted to be vector-like, i.e. to have the same left- and right-hand SU(2)$_L$ quantum numbers. Due to the linear mixing of the top partners with SM quarks, top partners must have SU(3)$_C$ quantum numbers. This leads to the natural prediction that there is a color mediator in the composite sector, a spin-1 color octet called heavy gluon. This heavy gluon is predicted to have a high mass, at around 3 TeV, due to constraints in EW precision data [27]. This means that top partner production can come via decays of the heavy gluon as well as production via SM gluon fusion. This will raise questions in the interpretations of top partner searches and will be a topic of discussion in this thesis.

CHM can be extended beyond the minimal choice of groups in order to achieve different features. One hypothesis is, given here as an example, to have a SO(6)$\rightarrow$SO(5) break. In the minimal case we got 4 Goldstone bosons from the broken generators, that were used to parametrize the Higgs boson. In this example we would retain 5 broken generators and the extra Goldstone boson can be interpreted as a dark matter candidate.

2.3 Vector-like quarks phenomenology

Vector-like quarks are colored spin $\frac{1}{2}$ fermions that have the same left- and right-handed SU(2)$_L$ quantum numbers. This means that a bare mass term of the form $\bar{Q}_L M^0 Q_R + hermitian\ conjugate$ is gauge invariant, avoiding constraints coming from the Higgs sector. VLQs are predicted to mix with SM quarks and bosons. This mixing sets some constrains on the possible quantum numbers that preserve gauge

Electric charge	T	B	$\begin{pmatrix} T \\ B \end{pmatrix}$	$\begin{pmatrix} X \\ T \end{pmatrix}$	$\begin{pmatrix} B \\ Y \end{pmatrix}$	$\begin{pmatrix} X \\ T \\ B \end{pmatrix}$	$\begin{pmatrix} T \\ B \\ Y \end{pmatrix}$
Isospin	0	0	1/2	1/2	1/2	1	1
Hypercharge	2/3	-1/3	1/6	7/6	-5/6	2/3	-1/3

Table 2.1: VLQ multiplets allowed by the mix with SM quarks through Yukawa couplings.

invariance. Therefore VLQs can have isospin of 0, $\frac{1}{2}$ and 1. They can also have SM-like electric charges of $\frac{2}{3}|e|$ (T) and $-\frac{1}{3}|e|$ (B) or exotic charges of $\frac{5}{3}|e|$ (X) and $-\frac{4}{3}|e|$ (Y). This information is summarized in table 2.1.

As is commonly done in BSM models that predict VLQs, it will be assumed that they mix only with the third generation of SM quarks. The branching ratio (BR) of each decay is set by the SU(2)$_L$ multiplet hypothesis, as can be seen in fig. 2.3. By setting this mixing a mechanism analogous to what is done in the SM with the CKM matrix [28, 29], i.e. a matrix to obtain the mixing between mass and weak eigenstates after the EWSB:

$$\begin{pmatrix} t_{L,R} \\ T_{L,R} \end{pmatrix} = \mathcal{U}^u_{L,R} \begin{pmatrix} t^0_{L,R} \\ T^0_{L,R} \end{pmatrix} = \begin{pmatrix} \cos\theta^u_{L,R} & -\sin\theta^u_{L,R}e^{i\phi_u} \\ \sin\theta^u_{L,R}e^{i\phi_u} & \cos\theta^u_{L,R} \end{pmatrix} \begin{pmatrix} t^0_{L,R} \\ T^0_{L,R} \end{pmatrix} \quad (2.32)$$

where $\mathcal{U}$ are the mixing matrices that diagonalize the mass matrix, as $\mathcal{U}^q_L M^q (\mathcal{U}^q_R)^\dagger = M^q_{diag}$, $\theta_{L,R}$ are the mixing angles for the left- and right-handed components, respectively, and ϕ_u is a phase. Fields in their weak eigenstate basis are denoted by a 0 superscript. The mixing procedure shown above is specific to the up sector, but the down sector is obtained with same procedure.
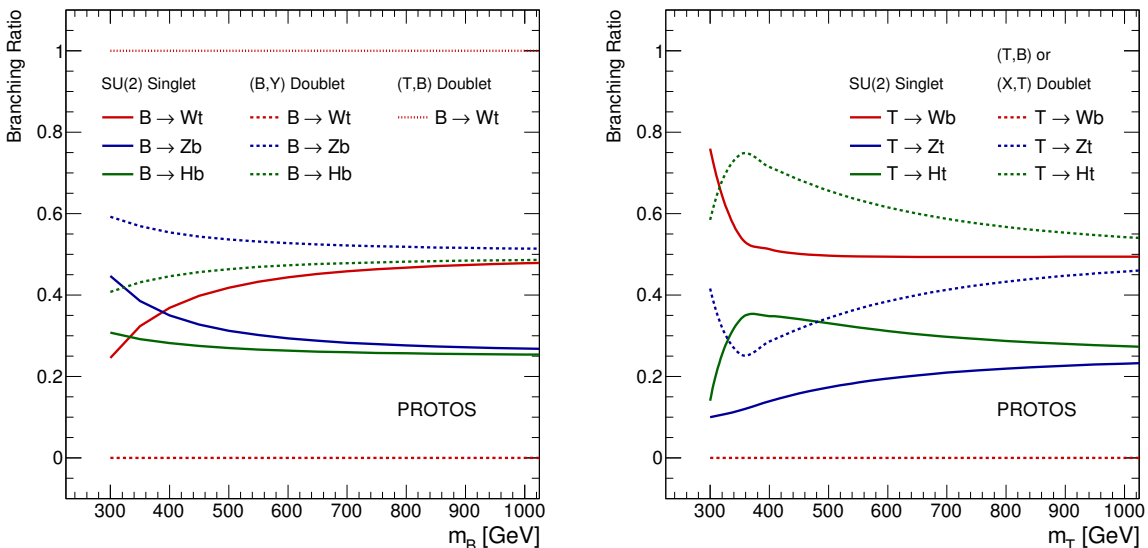
Figure 2.3: Branching ratios for the three different decays channels of the vector-like B and T [30].

13

VLQ production can be done in two ways: gluon fusion producing a pair of VLQs, or via an EW vertex with a single VLQ and a SM quark. Pair-production is fairly model independent as gluon fusion is a well modeled process and VLQs are expected to couple to gluons the same way SM quarks do. Single-production cross-section, however, depends on the coupling of the VLQ to SM bosons. This introduces some model dependency and makes the interpretation of experimental results trickier than in the pair-production case. Pair-production is the dominant mechanism until high VLQ masses are considered, in which case single-production cross-sections start to dominate, mostly due to phase-space restrictions as only one massive quark is being produced. This can be seen in fig. 2.4.
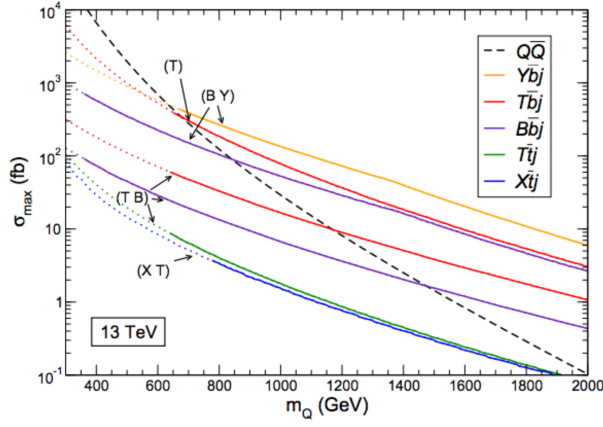
Figure 2.4: Leading order cross-sections for pair and single production of the different vector-like quarks [31].
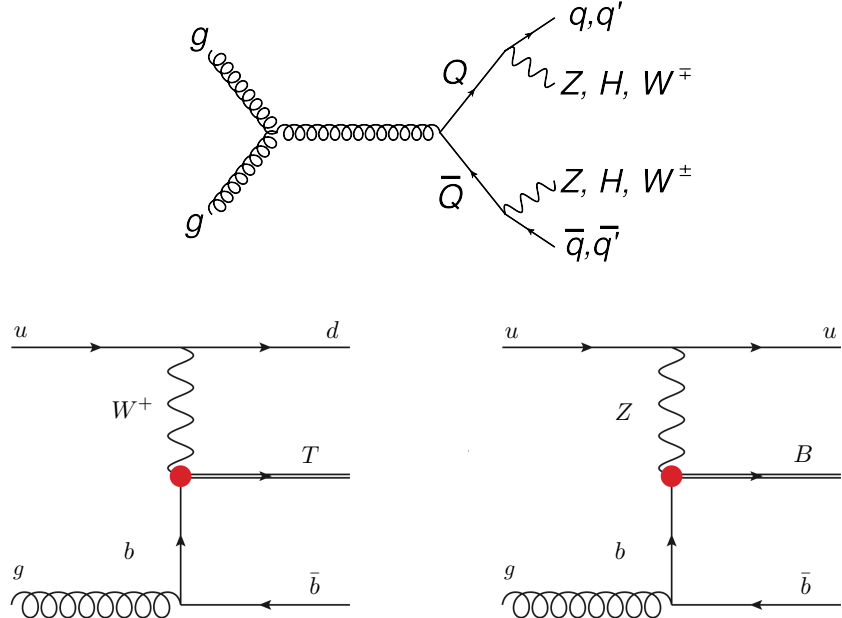
Figure 2.5: Examples of pair and single production Feynman diagrams. [30].

An overview of current experimental constraints on VLQ production will be given in section 4.1.

3

Experimental setup

3.1 CERN

CERN (acronym for Conseil européen pour la recherche nucléaire) is a particle physics laboratory located near Geneva, Switzerland. It was idealized at the end of the second world war and founded in 1954. Its personnel counts with about 18,000 people from over 110 nationalities [32]. It is the host of many projects and experiments, with the prime example being the LHC.

3.2 The Large Hadron Collider

The LHC [34] is a 27 km circular particle accelerator, located underground at an average depth of about 100m. It consists of a chain of superconducting magnets that operate at 1.9K and produce a field of around 8.4 T at a current of 11,700 A, that allow for the acceleration and collision of protons (most of the machine time) and heavy ions (a few weeks at the end of the year). Protons in the LHC reach a center of mass energy of 13 TeV, and collide head-on at specific interaction points along the ring, that are shown in fig. 3.1. These interacting points correspond to the 4 LHC experiments: ATLAS [35] and CMS [36], two multi-purpose experiments that try to cover a wide range of physics interests; LHCb [37] that is focused on B hadron decays and ALICE [38], dedicated to the study of heavy ion collisions.

The choice for colliding protons instead of electrons is mostly due to the higher mass of the former, and the minimization of energy loss due to radiative energy, that are inversely proportional to the forth power of the mass. The drawback from this choice is that protons are composite particles, and their total momentum is divided among its constituents in proportions that are not always the same. This means that even though protons are accelerated to a $\sqrt{s} = 13$ TeV, the scattering momentum only takes the momentum of each

CERN's Accelerator Complex
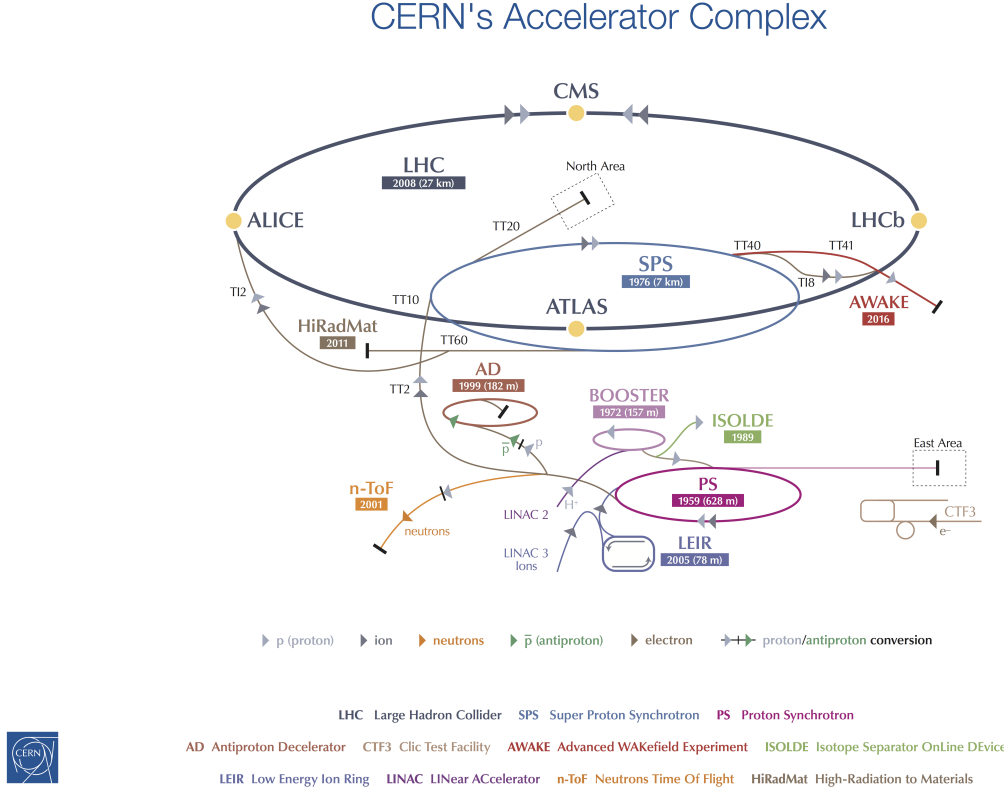
Figure 3.1: LHC accelerator complex [33].

parton. This fraction is unknown for each event and can only be quantified cumulatively in distribution functions, called Parton Distribution Functions (PDF). An additional issue with the use of protons is that they have to be accelerated in bunches, in order to have a significant probability of interaction. Proton beams contain about 2800 bunches of about 10^{11} protons, spaced by 25ns. So for each bunch crossing there will be multiple collisions, and when an interesting event containing a hard scattering is recorded, it occurred simultaneously with other interactions not directly related to the interesting process. The number of interactions per bunch crossing is called pileup. This effect can create a challenge in order to determine the interaction vertex corresponding to the interesting collision and adds an experimental uncertainty.

For a process with a given cross-section, the rate of events is given by:

$$\frac{dN_{event}}{dt} = \mathcal{L}\sigma_{event} \tag{3.1}$$

with $\mathcal{L}$ being the instantaneous luminosity, that is set by the beam parameters as:

$$\mathcal{L} = \frac{N_b^2 n_b f_{rev} \gamma r}{4\pi\epsilon_n \beta^*} [cm^{-2}s^{-1}] \tag{3.2}$$

where N_b is the number of particles per bunch, n_b is the number of bunches per beam, f_{rev} is the frequency given by the number of circulations of each bunch per second, γ is the relativistic gamma factor,

ϵ_n is the normalized transverse beam emittance and β^* is the focusing function at the interaction point that is given by the size of the bunch cross-section at the interaction point.
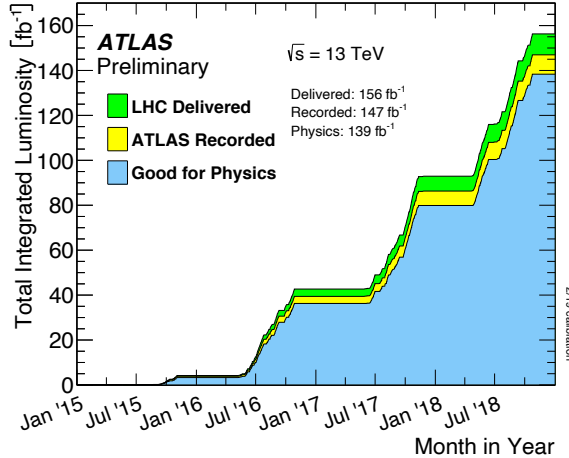
Figure 3.2: Luminosity delivered to the ATLAS detector (in green), recorded by ATLAS (in yellow) and that is certified as good quality data (in blue), taken between 2015 and 2018 [39].

The total number of collisions in a given period of time is given by the integrated luminosity $L = \int \mathcal{L} dt$. Figure 3.2 shows the integrated luminosity delivered to the ATLAS detector.

3.3   The ATLAS Experiment
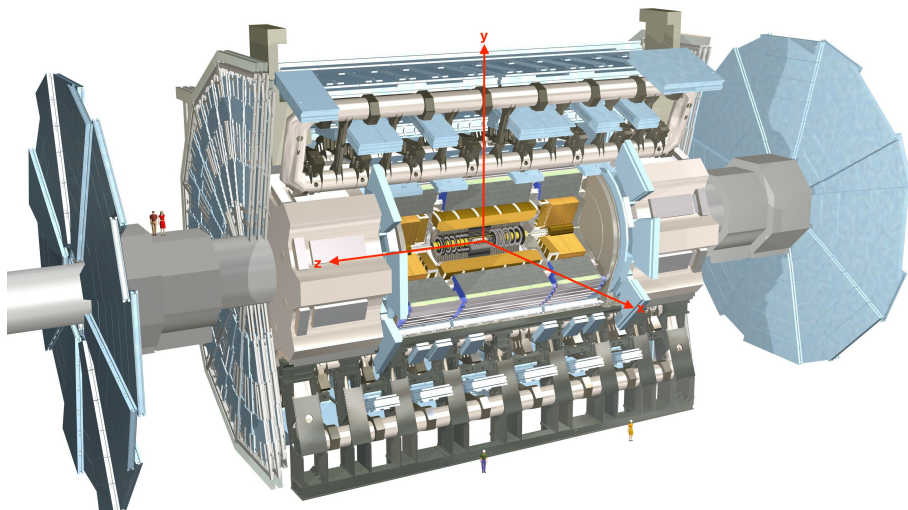
Figure 3.3: Computer generated image of the ATLAS detector, with a superimposed coordinate system [35].

Along with CMS, ATLAS (A Toroidal LHC ApparatuS) [35] is one of the two general purpose detectors of the LHC. It has a cylindrical geometry that centers around the beam pipe. The detector is 45m long, 25m high and weights at about 7000 tons.

ATLAS uses a right-handed coordinate system as is shown in fig. 3.3, with the z axis going along the beam pipe and the x axis point towards the center of the LHC ring. The $x - y$ plane defines the transverse plane and all transverse quantities (i.e. p_T, E_T, E_T^{miss}) are defined along it. The azimuthal angle ϕ is measured around the z axis, while the polar angle θ is measured around the beam direction. A pseudorapidity η, defined as $-\ln[\tan(\frac{\theta}{2})]$, is used along with ϕ, as distances in pseudorapity are Lorentz invariant. The angular separation between two particles is defined by the quantity $\Delta R = \sqrt{\Delta \eta^2 + \Delta \phi^2}$.

3.3.1   Inner detector
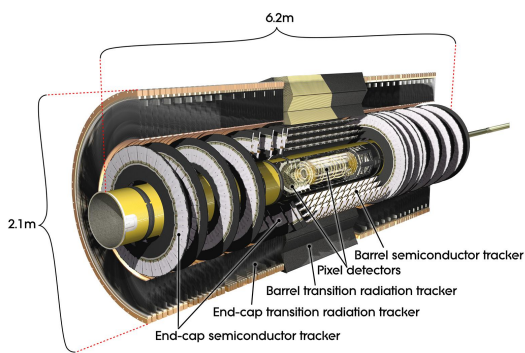
Figure 3.4: Schematic view of the inner detector, showing all its components [35].

The innermost part of the ATLAS detector is the inner detector (ID)[40–42]. It is composed by 4 parts: the Insertable B-layer (IBL) [43], the silicon pixel detector [44, 45], the semiconductor tracker (SCT) [46–48] and the transition radiation tracker (TRT) [49–53]. These work in combination with a 2T magnetic field produced by a superconducting solenoid to measure the tracks of charged particles as well as to reconstruct primary and secondary vertices within a pseudorapity region of $|\eta| < 2.5$. Due to the proximity to the interaction point its design requires high resistance to radiation damage. As LHC events are high in number of tracks the ID needs to have high granularity to allow for the necessary precision in the measurement of track parameters and vertex reconstruction.

The innermost layer of the Pixel Detector (PD) is the IBL. Inserted in 2014, it provides better vertexing resolution and primary vertex position measurement, particularly due to the increase in pileup that was expected at the time of the insertion. The pixel detector has 4 cylindrical layers of pixel sensors in the barrel region and 3 discs that are perpendicular to the beam pipe in the two end-cap regions. The pixel sensors provide a resolution of 10 μm in the $R - \phi$ plane and 115 μm along the z axis, with about 92 million readout channels.

Surrounding the pixel detector is the SCT, consisting of 4 layers of silicon microstrip sensors in the barrel region and 18 disks in the two end-cap regions. It has a spatial resolution of 16 μm in the transverse plane and 580 μm along the beam axis.

The outer part of the ID is the TRT, made of 4 mm diameter straw drift tubes up to 144 cm long. These are operated with a gas mixture of 70% Xe, 27% CO_2 and 3% O_2. At the center of each straw is a gold-coated wire with 31 μm in diameter, serving as an anode kept at ground potential. The cathodes are the walls of each straw, kept at a negative potential of -1.5 kV. As charged particles traverse a straw they ionize the gas mixture, causing electrons and positive ions to drift apart in the electric field, thus producing a signal that is proportional to the energy deposited by the particle. A single track typically goes trough about 30 straws, yielding a spatial hit resolution of 130 μm in a plane perpendicular to the wire.

The four components of the ID, used in measurements in combination, provide a experimental resolution of p_T of $\frac{\sigma_{p_T}}{p_T} = \frac{0.05\%}{\text{GeV}} p_T \oplus 1\%$ [35].

3.3.2 Calorimeter system
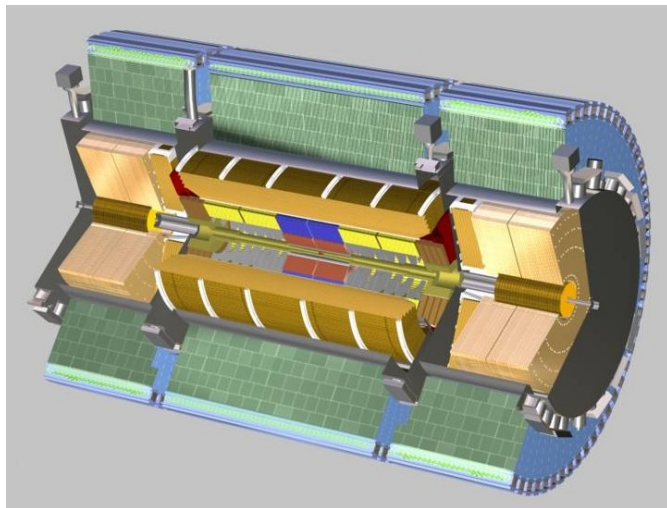
Figure 3.5: Schematic view of the calorimeter systems, showing all its components [54].

As particles exit the ID they meet the ATLAS calorimeters. These cover a range up to $|\eta| < 4.9$, composed by towers that segment the system in η and ϕ. The calorimeter system is divided in order to measure the energy from electromagnetic and hadronic showers. For that two systems are used: the Liquid Argon (LAr) [55] and hadronic calorimeters. They consist of alternating layers of dense absorber materials to induce particle showers and active materials to measure the deposited energy.

In the LAr calorimeter electrons lose energy by bremsstrahlung and photons lose energy by electron pair production. Given the amount of matter that is traversed by these interactions (called radiation length X_0), one can measure the initial energy of the incoming particle. In the case of the photon, X_0 is equivalent to 7/9 of its mean free path, and for the electron it represents $1/e$ of its energy loss. In order to contain the majority of the particle shower it is important that the calorimeter has the appropriate depth. For that LAr has the length of 22 X_0 in the barrel and 24 X_0 in the end-caps. The absorber plates and electrodes are arranged in an accordion-like shape thus ensuring coverage in the ϕ range, with a granularity of

$\Delta\eta \times \Delta\phi = 0.003 \times 0.025$. This fine segmentation is very important for the detection of single photons in $\pi^0 \to \gamma\gamma$. The target energy resolution of the LAr calorimeter is, in GeV, $\frac{\sigma_E}{E} = \frac{10\%}{\sqrt{E}} \oplus \frac{17\%}{E} \oplus 0.7\%$ [35].

High energy hadronic interactions produce showers of secondary particles that are very different from those found in electromagnetic showers, so there is the need for a different design in order to measure them. In the hadronic calorimeters, that surround the electromagnetic calorimeters, the energy of hadronic showers is measured within $|\eta| < 3.2$. They are composed of three parts: the Tile hadronic calorimeter (TileCal) [56], the Liquid-Argon hadronic end-cap calorimeter (HEC) and the Liquid-Argon forward calorimeter (FCal). The TileCal is made of plastic polystyrene scintillating tiles that act as the active medium with steel, acting as the absorber. It has a total thickness of 9.7 X_0 in the barrel and 10 X_0 in the end-caps. The scintillating material and the steel are oriented radially into 3 read-out layers in order to measure the longitudinal profile of the hadronic showers. The polystyrene is connected to photomultiplier tubes (PMTs) that convert the light produced in the scintillators into an amplified electric signal. The TileCal contains about 4672 readout cells read into both sides by two PMTs, making a total of 9852 PMTs. The granularity of the TileCal is $\Delta\eta \times \Delta\phi = 0.1 \times 0.1$. The HEC has two wheels per end-cap situated behind the electromagnetic end-cap calorimeter, covering the range of $1.5 < |\eta| < 3.2$. Its design is equivalent to the LAr but it has copper plates instead of lead. Finally the FCal provides calorimetry for both electromagnetic and hadronic showers at the range of $3.1 < |\eta| < 4.9$ with a thickness of about 10 X_0. It uses copper as the absorber in the first layer and tungsten in the second and third layers.

The measured energy resolution, in GeV, of a single isolated charged pion measured in combination by the LAr and tile calorimeters is $\frac{\sigma_E}{E} = \frac{55\%}{\sqrt{E}} \oplus 2.3\% \oplus \frac{3.2}{E}$ [35].

3.3.3 Muon spectrometer
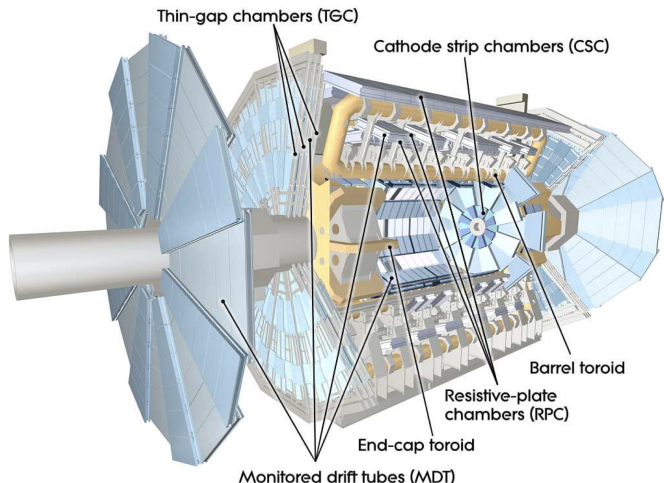
Figure 3.6: Schematic view of the muon spectrometer in a cut-away view, showing all its components [35].

As all the aforementioned parts of the detector interact with the particles produced in the interaction

point, only muons and neutrinos should not be absorbed by this point. Therefore the muon spectrometer [57] is the outermost part of the ATLAS detector. With this detector a high precision measurement of the muons momentum down to 3 GeV can be achieved, using a toroidal magnetic field of up to 1 T to deflect their tracks. The range of the muon spectrometer goes up to $|\eta| < 2.7$ in the momentum measurement and $|\eta| < 2.4$ in the muon based triggers, with a small gap for $|\eta| < 0.1$ for service cables. The spectrometer is composed of a central barrel and two end-caps. The tracks in the muon spectrometer are measured by two different systems: the Monitored Drift Tubes (MDTs) [58] in the barrel and the Cathode Strip Chambers (CSCs) [59] in the forward regions. The MDTs measure track coordinates within $|\eta| < 2.7$. The CSCs are multiwire proportional chambers with cathodes that are segmented into strips, used within $2.0 < |\eta| < 2.7$. The Thin Gap Chambers (TGC) [60] is used in the trigger system, covering a range of $|\eta| < 1.05$, while the Resistive Plate Chambers (RPC) cover the region of $1.05 < |\eta| < 2.4$. Where the trigger chambers lose in spatial resolution they make up in faster signals that are required for the first level muon trigger.

3.3.4   Trigger system

As it was mentioned previously, the LHC, during the Run 2 data taking, provides a bunch crossing every 25 ns, meaning a rate of 40 MHz. Due to limited storage space, less than 2000 events per second can be saved so a realistic rate that can be processed and recorded is of about 1 kHz. The role of the trigger system [61] is to perform a run-time event selection based on the event features, filtering the interesting ones while keeping an affordable rate. The current ATLAS trigger system is composed of two trigger levels: a hardware-based level (L1) that uses measurements from the calorimeters and muon systems; and a software-based high-level trigger (HLT) that allows for a finer selection. The first level of the trigger system reduces the initial 40 MHz rate to about 100 kHz. A further reduction to the desired 1 kHz is made by the HLT. The L1 trigger searches for potentially interesting features such as high transverse momentum objects, large $E_\mathrm{T}^\mathrm{miss}$ and large total energy. From there a Region of Interest (ROI) is defined, that will be used by the HLT to refine the L1 selection. Having a software based trigger levels allows for a more specialized selection of events. To that end a trigger menu is built in order to manage the bandwidth and storage of each type of trigger that will be essential to the many physics signatures that are of interest to the collaboration. The menu is usually built around the topological information of the event, so that a signature can be focused on it, i.e. having signatures dedicated to electrons, muons, jets, $E_\mathrm{T}^\mathrm{miss}$ and so on. In some cases, in order to stay within the rate constraints some triggers need to be prescaled, i.e. only a fraction of the selected events can be recorded. Prescale factors can be adjusted during data taking and some triggers may even be disabled for technical reasons.

3.3.5 Worldwide LHC Computing grid

As was just discussed, the trigger system does an excellent job at reducing the event rates to be recorded from 40 MHz to 1 kHz. Still, as the average file size has about 1.6 MB [62], the task of processing and recording the events of the four main experiments is daunting and so the Worldwide LHC Computing Grid (WLCG) was created. It is designed to deal with around 15 Petabyte of data per year, i.e. to preserve it and its redundancy, and make it readily available to the approximately 5000 scientists around the world. The WLCG is a distributed computing grid composed of 160 different computing centers, divided into three tiers:

- A Tier-0 is located at CERN, connected to another Tier-0 located at Budapest with a 100 Gbit/s data link. It is at this tier that the first data reconstruction is performed and copied to tier 1 center for further processing.

- Tier-1 centers store and process data and simulation. There are 14 active Tier-1 centers around the globe.

- There are 149 active Tier-2 centers that make end-user analysis and simulation possible.

- Even though they are not managed by the WLCH, local computer clusters at universities and institutes are often referred to as Tier-3.

3.3.6 ATLAS Forward Proton

Working as a complement to the ATLAS detector is the ATLAS Forward Proton (AFP) detector [63], aiming to measure protons that result from the central interactions and stay intact, but that through energy loss are deflected and travel through the beam pipe. This allows for the study of diffractive processes where the proton remains intact, such as central exclusive production, soft diffractions processes (that can be single or double diffraction and that are only distinguishable with proton tagging), Pomeron interactions, or even anomalous quartic gauge boson couplings [64].

In order to be able to detect these far travelling protons, stations at both sides of the ATLAS detectors are placed, located at 205 and 217 m from the interaction point, as can be seen in fig. 3.7. These stations consist of Roman Pots (RP), that allow the detectors to be horizontally inserted and removed from the beam pipe without breaking the vacuum. Each station contains four Silicon Trackers (SiT) that allow for a precise measurement of the proton trajectory as a track. The chosen chip for readout was FE-14, designed for the inner detector. They cover an area of approximately 16×20 mm^2 with pixels of 50×250 μm^2, placed with a 14 degree angle. The resolution of each plane, i.e. each SiT, is about 6 μm in the x direction and 30 μm in the y direction. The typical acceptance is $0.02 < \xi < 0.12$, with ξ the proton energy loss, given by $\xi = 1 - \dfrac{E_{proton}}{E_{beam}}$. The stations located farther from the interaction point (named far stations),

also contain Time of Flight (ToF) detectors, timing detectors capable of measuring the time of arrival of each proton. This is very important in conditions of high pileup, where the ToF can provide background rejection by calculating the difference in arrival time of each proton, resulting in the position of the vertex that originated these protons, that can be checked against the primary vertex position. ToF can also provide a trigger signal to the central system. The resolution of these detectors is expected to be between 20 and 30 ps.
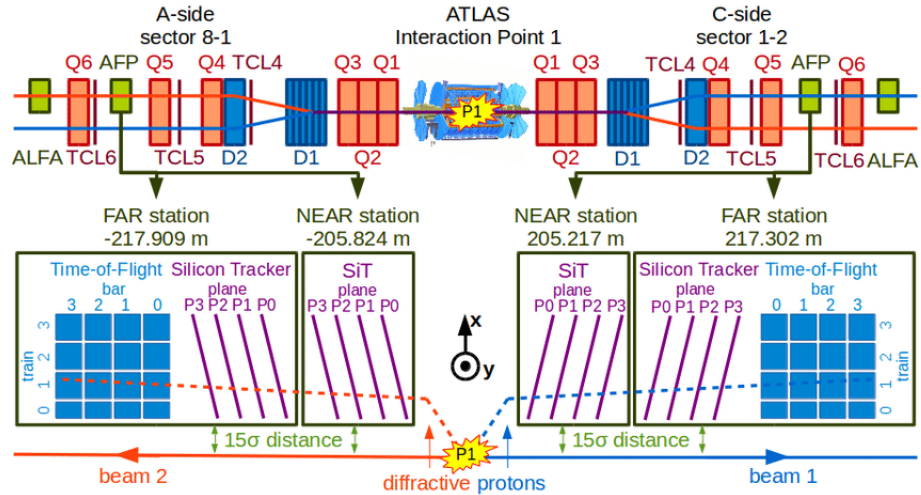
Figure 3.7: Schematic view of the ATLAS Forward Proton detectors [65].

3.3.7 Exclusive jet trigger

From the listed physics processes of interest, central exclusive production is one of the most promising, particularly with jets. These are processes where both protons remain intact, but are deflected by the energy lost in radiating jets. Figure 3.8 shows a schematic diagram of the process. Its detection could help study the gluon distributions in protons, given the purely gluonic nature of the process, and even set constraints on the exclusive Higgs production [66].
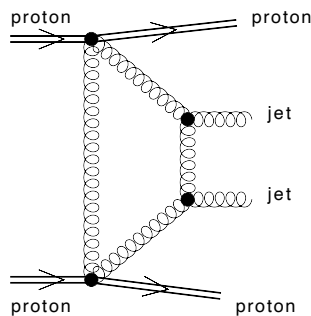
Figure 3.8: Schematic Feynman diagram of central exclusive jet production [66].

There is, however, a big challenge in detecting these events. As can be seen in fig. 3.9, the geometric acceptance of the AFP detector is dependent on the proton p_T and its energy loss The latter will dictate of the proton deflection is within in the detector acceptance, taking into account the beam properties and the detector geometry and position. As the proton's energy loss will be corresponding exactly to the
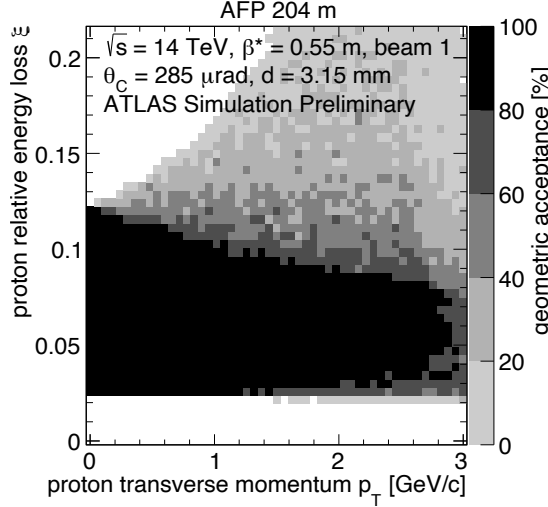
Figure 3.9: Geometric acceptance of the AFP detector as a function of the proton energy loss and its p_T [66].

energy of the radiated jets, the kinematic range of the jets that will result in a proton tag at AFP is at minimum 140 GeV [66]. The problem with this is that the trigger rates at this p_T are very high, requiring large prescales, and, as it can be seen in fig. 3.10, the cross section of these processes falls steeply with the jet p_T. The chosen solution to still be able to record these events was to have a dedicated trigger. The
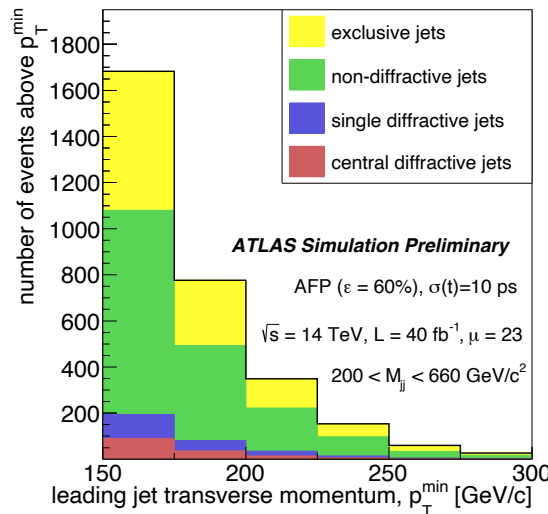
Figure 3.10: Exclusive jet production cross section as a function of the leading jet p_T [66].

plan is to measure the kinematics of the jets using the central detector, and tag the protons at AFP, making

a decision on their compatibility, i.e. verify if the measured energy position is compatible with the energy of the jet pair measured in the central system.

In exclusive jet events, the energy of the dijet system is given by:

$$E_{jj} = e^{\pm y_{jj}} \frac{m_{jj}}{\sqrt{s}} \qquad (3.3)$$

where y_{jj} and m_{jj} are the rapidity and mass of the dijet system [67]. Knowing that the energy lost by each proton corresponds to the energy of each jet, it can be derived from eq. (3.3) as

$$E_p = \frac{\sqrt{s}}{2}(1 - E_{jj}) \qquad (3.4)$$

given that the initial proton energy is half of the center of mass energy. The sign of each jet rapidity will then be used to derive the energy of each proton. Knowing the proton energy and the optics of the LHC beam, one can parameterize its trajectory along the beam pipe and predict its position at AFP. This quantity, then, can be used to compare against the actual proton position measured at AFP and assess the compatibility of the dijet system with the proton tags.

There is, however, the complications given by pileup. In normal detector conditions, where the pileup is high, many tracks are expected to be measured by the AFP detectors. Therefore, this can represent a large background of AFP tracks that match the dijet kinematics, despite not being originated in a exclusive jet event. This issue can be mitigated with the use of ToF. By measuring not only the proton positions but also their time of arrival at AFP, one can use their time difference to predict the z position of the primary vertex and compare it to the one obtained by the tracking algorithms used in the central detector. This further requirement is expected to suppress a large number of combinatorics background events.
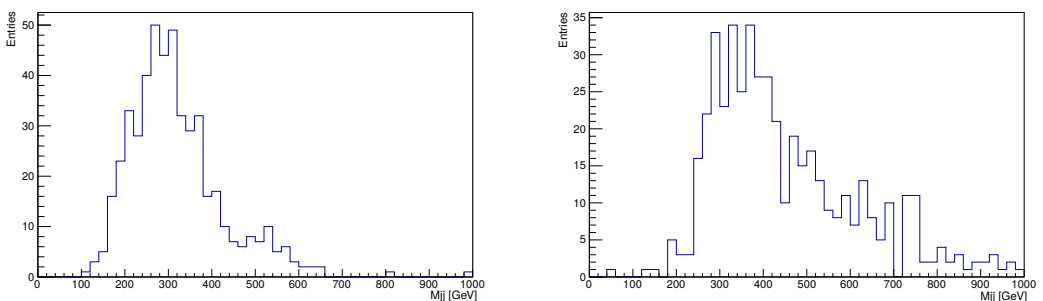
Figure 3.11: Dijet system invariant mass before any algorithm cuts are applied. To the left is the exclusive jet simulation and a non-diffractive jet sample is shown as background, on the right.

Figure 3.11 shows the invariant mass of the dijet system, on a sample of 498 central exclusive jet events on the left, and a non-diffractive jet sample on the right. Both processes were generated with the nominal run 2 pileup conditions.

The rapidity distribution is shown on fig. 3.12, and it can seen that the distribution is wider for the background case. As the name indicates, central exclusive jet production results in very central jets.
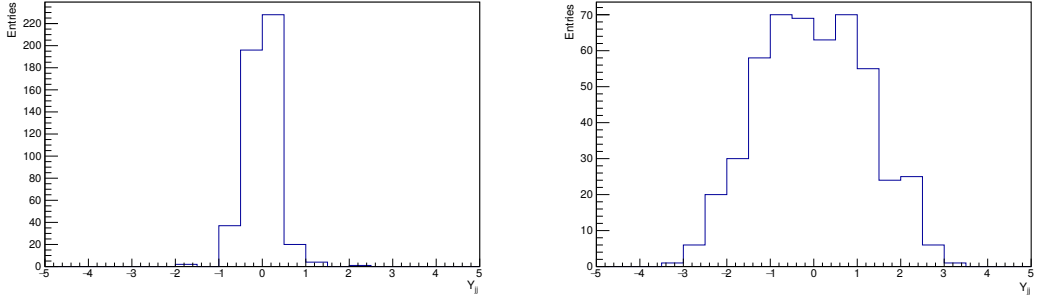
Figure 3.12: Dijet system rapidity before any algorithm cuts are applied. To the left is the exclusive jet simulation and a non-diffractive jet sample is shown as background, on the right.
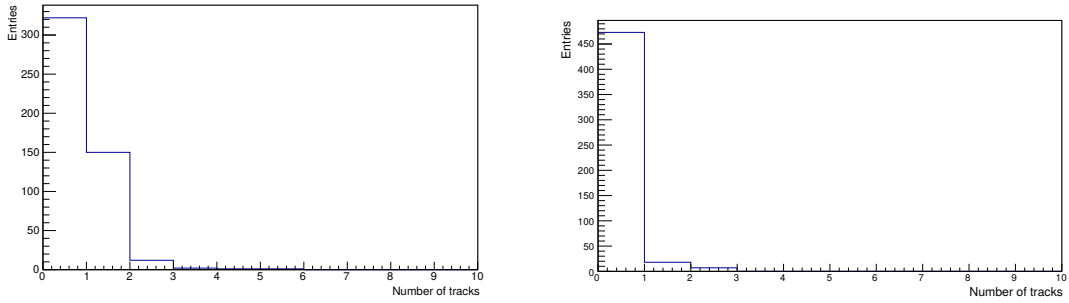
Figure 3.13: Track multiplicity on the A side station before any algorithm cuts are applied. To the left is the exclusive jet simulation and a non-diffractive jet sample is shown as background, on the right.
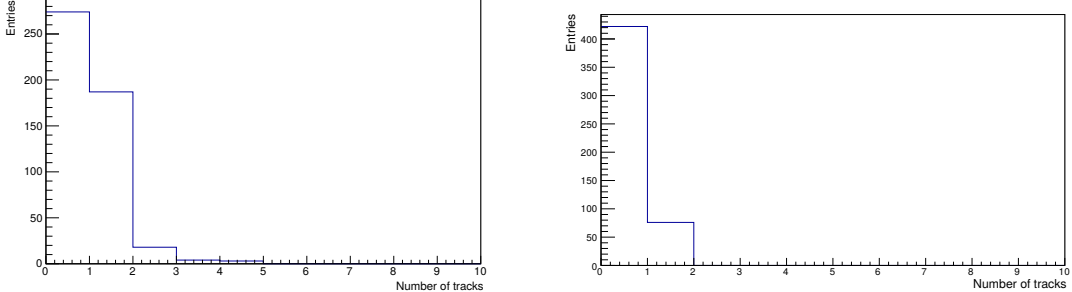
Figure 3.14: Track multiplicity on the C side station before any algorithm cuts are applied. To the left is the exclusive jet simulation and a non-diffractive jet sample is shown as background, on the right.

Figures 3.13 and 3.14 show the multiplicity of tracks on the A and C side stations (as indicated in fig. 3.7). The signal distributions show a larger expectation of track multiplicity.

Assembling this trigger strategy some of the required information was already available due to existing ATLAS trigger algorithms. Namely, the jets information is reconstructed by some jet trigger algorithms, and some b-tagging trigger algorithms reconstruct the primary vertex position. This can be used by the trigger chain we want to assemble, and complement it with the missing information about the AFP measurements. At the end, the trigger scheme will follow the aforementioned steps and is schematized in fig. 3.15.

L1_J75 & AFP_L1xxx

TrigJetRec

HLTJetHypo

Tools:

AFP_RawDataProviderTool

HLT::FexAlgo — Trig_AFPSiTrkReco — Calls → AFP_Raw2DigiTool

AFP_SIDLocRecoTool

HLT::Hypo — TrigAFPJetAllTE ← AFP_ProtonTransportTool

HLT::FexAlgo — EFBtagFexSplit_EFID

HLT::Hypo — TrigAFPToFHypo ← AFP_ToFRecoTool
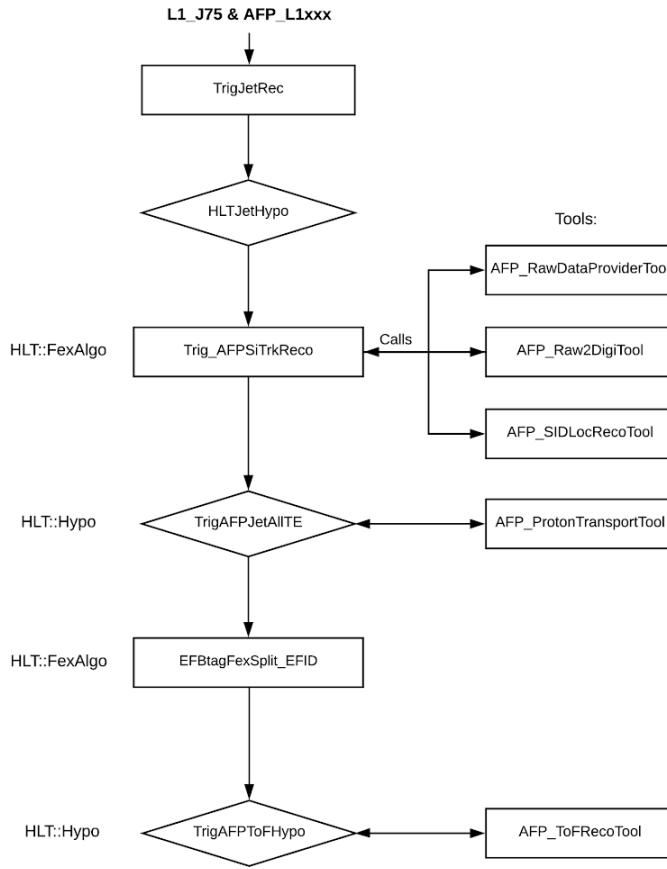
Figure 3.15: Exclusive jet production trigger scheme.

Going from the top of the scheme, the level 1 trigger that starts the trigger chain should be an AND operation of a single jet trigger that requires a $p_T > 75$ GeV and any AFP trigger that will collect the necessary AFP information. `TrigJetRec` is the reconstruction algorithm[1] that will collect the jet information from the calorimeters and pass it to the HLTJetHypo. This, as the name may serve as indication, is an hypothesis algorithm, i.e. an algorithm that makes decisions. In this case it will just select the jet information and apply the p_T requirement. For the purpose of this trigger chain the procedure being applied by the jet algorithms is not important, as it was the same as offline, and they are included in the chain as a means to obtain jet information from the central detector. The first AFP algorithm to be ran is `Trig_AFPSiTrkReco`. This algorithm will use the raw AFP data obtained by the level 1 algorithm and call the necessary tools to convert the raw data into proton tracks. To that end, it first calls `AFP_RawDataProviderTool`, that is followed by `AFP_Raw2DigiTool`, the tool that takes the raw data and does the digitization, achieving Silicon hits. These Silicon hits will be reconstructed as tracks by the `AFP_SIDLocRecoTool`. At the end of this process the `Trig_AFPSiTrkReco` will be able to pass reconstructed AFP tracks to the next algorithm: `TrigAFPJetAllTE`. This is the first AFP hypothesis algorithm, and it combines the jet information with the AFP information to make a decision. It calls the `AFP_ProtonTransportTool` tool that takes the proton

---

[1]In this scheme all reconstruction algorithms are shown in rectangles, as opposed to the diamonds, reserved to decision algorithms.

energy measurements, given by eq. (3.4), and outputs a prediction of the proton positions at AFP. With the predicted position and the measured position of the AFP tracks it makes a decision. For events with at least two jets, so that the proton energy calculation can be performed, and at least two AFP tracks, corresponding to at least two proton measurements, it compares the distance between the proton measured and predicted positions, as a set of two cuts:

$$\sqrt{(x_{pred} - x_{meas})^2 + (y_{pred} - y_{meas}^2)} < 2.0\text{mm}$$
$$|x_{pred} - x_{meas}| < 2.5\text{mm}; |y_{pred} - y_{meas}| < 2.0\text{mm}$$

(3.5)

with x_{pred} and y_{pred} being the predicted x and y positions while x_{meas} and y_{meas} are the measured x and y positions. The cut values were obtained by comparing simulation of exclusive jet events with non-diffractive events as background and will be tweaked with data collected by this trigger chain. For events with more than two jets, the two most energetic jets will be selected. If an event has more than two AFP tracks, the two closest to the predicted proton position will be used.
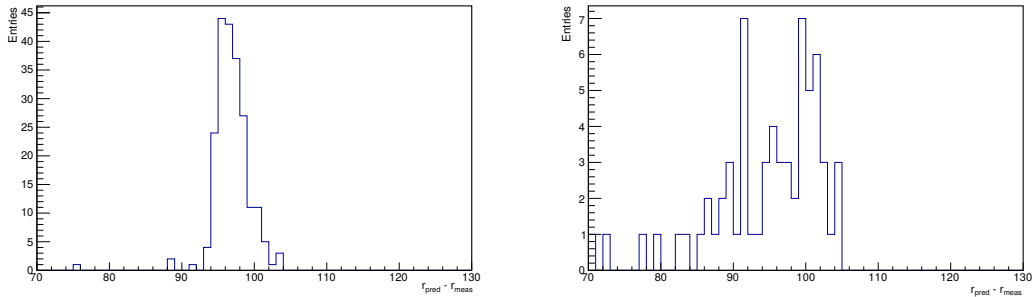
Figure 3.16: Radial position difference between prediction and measurement on the C side station before any algorithm cuts are applied. To the left is the exclusive jet simulation and a non-diffractive jet sample is shown as background, on the right.

Figure 3.16 shows the radial difference in the predicted position and the position of the AFP track on the C side station. It can be seen that while a peak is defined for the signal case, the background distribution is wider.

The next stage in the trigger chain is related to the ToF measurements and the comparison with the primary vertex position. The EFBtagFexPlit_EFID algorithm, developed for b-tagging triggers, calculates the primary vertex position, that will be passed on to the final hypothesis algorithm: TrigAFPToFHypo. This algorithm calls the AFP_ToFRecoTool, that transforms raw data from ToF into time information and then uses it to make a prediction of the z position to be compared with the obtained measurement.

The development of the trigger chain was done in a staged approach that allowed for implementing and debugging each step separately. In addition, it facilitates the commissioning and validation of the trigger chains, allowing to switch on and off the complete chain or just the jets and track selection. The first chain implemented focused on the kinematic matching between the dijet system and the AFP silicon

tracks, ending with the `TrigAFPJetAllTE` algorithm. It went through the necessary steps to be included into ATLAS software and the trigger menu. The validation plots indicated that when it ran in over real data it showed no trigger rates. This is an obvious indication of some issue with the code, possibly a problem with the thresholds selected, differences between offline and online code, or some other unforeseen problem. It is now under study by the AFP group, looking towards an integration into the third LHC run. The second stage of the implementation consisted in a full central exclusive chain, including also the primary vertex reconstruction using the tracks associated to the dijet system and the ToF information in AFP. The implementation of the calculation of the primary vertex position is done, needing only the measured position from the ToF information. Given that data taking in 2018 was performed without ToF, the implementation of the second part of the chain decreased in priority. The lack of a ToF detector in 2018 data taking was due to an unexpected high radiation damage during the 2017 data taking, leading to the removal of the detector at the end of the year. A satisfactory resolution for this problem was not found, resulting in the detector not being installed again in 2018. The focus of the group moved towards the understanding and solution of the problem. The chain is currently under development by the LIP group in close collaboration with the AFP team. In the same way as with the first stage, the ToF reconstruction will use available tools from the offline reconstruction incorporated into the trigger framework using AthenaMT, the ATLAS software framework that is being rebuilt into a multithread software.

Searches for vector-like quarks with partial run-2 dataset

VLQs are an important feature of many BSM theories, so naturally they are a major focus of the BSM search strategies at ATLAS and CMS. Given the many possible decays that VLQs can have, it would not be practical to dedicate searches to specific decay modes. So the strategy employed by the ATLAS collaboration is to target phase space regions and be general. Given that VLQs can decay to H, W, and Z, as was shown in section 2.3, searches look to target the a specific SM boson decay instead. So typically they look for a final state of the form of $H/W/Zq$ + X, with q being a third generation quark. This way searches can cover most of the phase space by individually covering a particular corner of the BR plane and at the end they can all be combined and thus have the best of both worlds: optimized sensitivity from each analysis and the complete statistical power from the combination.
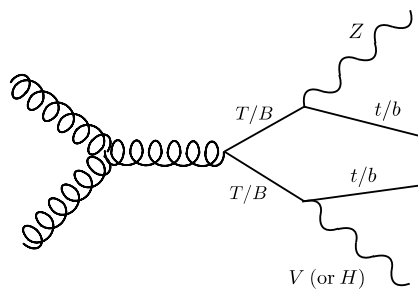

Figure 4.1: Search for the pair-production of vector-like T or B and at least one Z boson [68].

The analysis presented in this thesis targets pair production of VLQ with SM-like electric charges (T

and B) decaying to a third generation quark with the presence of a leptonically decaying Z boson. So the targeted final state is Zt/b + X, where X can be any of the other possible decay modes, i.e. Wq, Zq or Hq, as is shown in fig. 4.1.

4.1 Current results

4.1.1 $Zt/b + X$ final state

The analysis presented in this text follows previous searches using a partial run-2 dataset amounting to 36.1 fb^{-1}. Most notably it is the successor of an analysis targeting the same final state [68]. It was performed by a largely overlapping set of analyzers, including the author of this thesis, whose master thesis [69] presents this search without data in the signal regions. This is because this analysis (and mostly all searches, including the one described in the current thesis), follows the ATLAS blinding procedure. It consists of a series of steps intended to prevent analyzers to bias themselves with possible data fluctuations in sensitive bins. So the analysis strategy is developed without ever consulting data in signal enriched regions (in control regions, after being verified that do not present a large signal contamination, data can be looked at). The analysis team, in consultation with its ATLAS sub-group, should reach a final analysis setup that, if approved by the sub-group can be unblinded, i.e. can have its signal regions populated with data events. It should be noted that decisions on the sensitivity of the analysis take only expected limits into account. In the case of the analysis presented in this thesis there was even an intermediate step where data was only shown in signal regions bins with signal over background ratio below 5%, to assess the stability of the fit and the control of the main backgrounds, before the full unblinding. The remainder of the analysis development, from the unblinding step until its publication represented the first step of the PhD work done by the author of this thesis [68].

The 36.1 fb^{-1} analysis search for pair and single production of VLQ, in the same leptonic Z channel. The pair production channels search for VLT and VLB, while the single production channels focus exclusively on VLT production. There are 3 pair production channels: two 2ℓ channels split by multiplicity of large radius jets[1] and a 3ℓ channel. The 2ℓ channel with 0 or 1 large radius jet was labeled as PP 2ℓ 0-1J while the other channel with two leptons, that required at least 2 large radius jets was labeled PP $2\ell \geq$2J. The two single production channels were split by lepton multiplicity: a channel with 2 leptons and a channel with at least 3 leptons. The main features of the analysis pre-selection were the multiplicity of b-tagged jets, given the assumption of VLQ decays only to third generation quarks and p_T of the reconstructed Z boson candidate, as a large boost from the high VLQ masses is expected. The single production channels had an additional requirement of at least 1 forward jet, a typical feature of VLQ single production signals, as the spectator quark from the t-channel production is expected to have large $|\eta|$, which also allows to suppress

---

[1]More details about jets and their reconstruction will be shown in section 5.2.

some background. Both PP 2ℓ channels feature $t\bar{t}$ and Z+jets control regions, their main backgrounds, that can be seen in figs. 4.2 and 4.3. The $t\bar{t}$ CRs are defined by inverting the cut on the mass of the leptons that reconstruct the Z boson candidate, trying to reject events with a Z boson candidate with mass compatible with a Z boson. Both 2ℓ channels signal regions apply a cut on the scalar sum of jets p_T, which is inverted in order to define their Z+jets CRs. This variable is used as the PP 2ℓ 0-1J discriminant variable, while the invariant mass of the Z boson candidate and the leading b-tagged jet is the PP 2ℓ $\geq$2J discriminant variable. Both can be seen in fig. 4.4. The PP 2ℓ 0-1J has two signal regions, splitting by events with 0 and 1 large radius jets, as it was found to improve the channel's sensitivity. The PP 3ℓ channel has a Dibosons CR by requiring exactly 0 b-tagged jets, and a $t\bar{t}$ $+X$ CR by inverting the cut on the p_T of the reconstructed Z boson candidate. The discriminant variables in these control regions can be seen in figs. 4.2 and 4.3. As opposed to the 2ℓ channels, that require at least 2 b-tagged jets, the 3ℓ channel (with the exception of the Dibosons CR) requires at least 1 b-tagged jet, as it was found to improve the channel's sensitivity. The discriminant variable for this channel is the scalar sum of jets and leptons, as the additional leptons should be useful for signal discrimination, and it can be seen in fig. 4.4.

The SP 2ℓ has two control regions, defined by their b-tag multiplicity: a 0 and a $\geq 1b$-tag regions, that can be seen in fig. 4.5. This allows a control of the main background, Z+jets, in the phase space with no heavy flavor jets, and in a phase space closer to the SR, that requires at least 1 b-tagged jet. Given that the decay products of the VLT often have large p_T, it is common that they are all contained within the same large radius jet. To that end this channel applies top tagging to the selected large radius jets. This is a method of determining if a jet is likely a decay of a top quark, by taking into account its mass and the n-subjettiness [70], which is a quantification of the degree to which a jet can be regarded as composed of n subjets. In this case by doing the ratio of the 3-subjettiness with the 2-subjettiness, given that top quarks almost exclusively decay to Wb, will provide a unique signature. Given that the main background of this channel is Z+jets, it is unlikely that it fulfills this requirements, so a significant suppression of the main background is expected. The discriminant variable of this channel is the invariant mass of the Z boson candidate and the leading large radius jet that is tagged as a top quark, thus reconstructing the VLT resonance, as can be seen in fig. 4.6, for a choice of coupling of the VLT to the EW boson in the production diagram of 0.5. The last selection requirement is that the scalar sum of jets p_T plus the E_T^{miss} is lower than the aforementioned invariant mass, in order to suppress pair production contamination. The SP 3ℓ channel SR has a requirement that only events in which the highest p_T lepton has a p_T of at least 200 GeV are selected. Pair production contamination is reduced by requiring the scalar sum of jets p_T multiplied by the number of jets to be below 6 TeV. A Dibosons region is built by selecting events with no b-tagged jets, while a $t\bar{t}$ $+X$ CR is built by inverting the p_T of the Z boson candidate requirement and vetoing forward jets. The discriminant variables for these control regions can be seen in fig. 4.5. The scalar sum of jets and leptons p_T is used as the discriminant variable and can be seen in fig. 4.6.

As no deviation from the SM expectation was found, upper limits on the VLQ mass were derived at
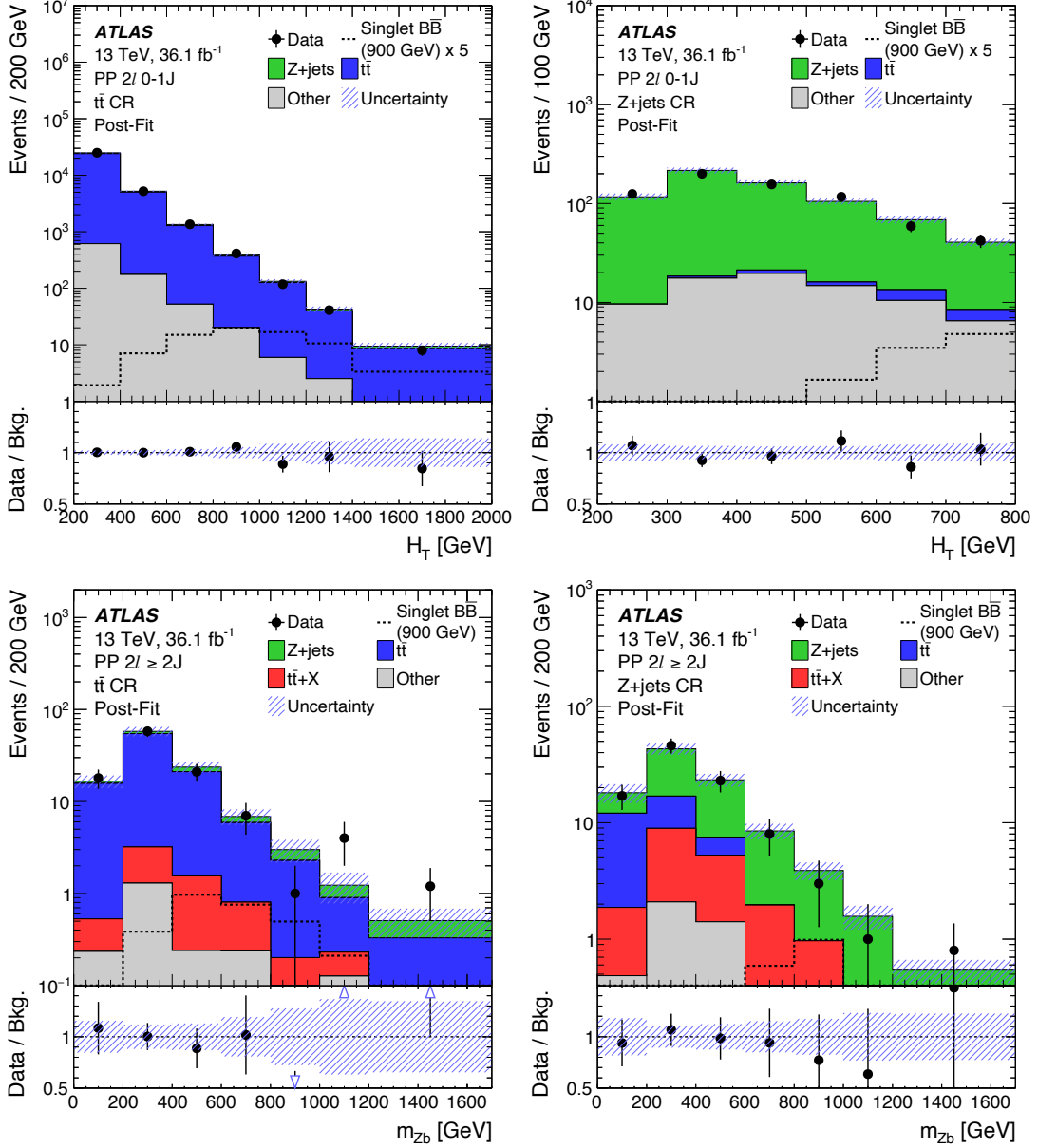
Figure 4.2: Discriminant variables of the pair production 2ℓ control regions after a background only fit. Expected signal distribution is overlaid, for a benchmark model of a singlet VLB with 900 GeV mass, multiplied by a factor of 5 for visibility purposes, except for the PP 2ℓ $\geq$2J channel.
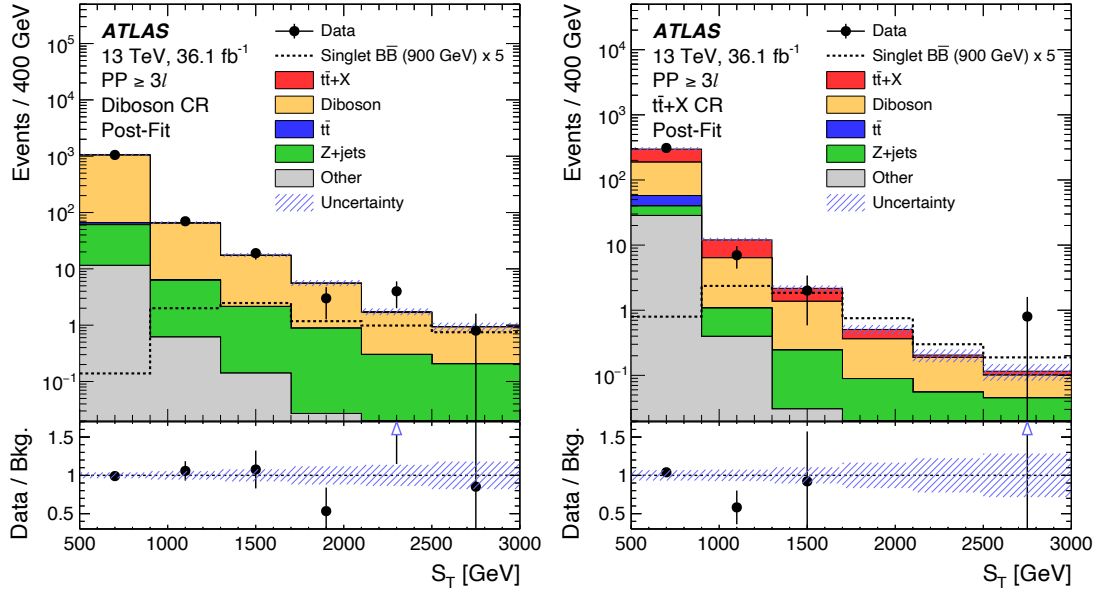
Figure 4.3: Discriminant variables of the pair production 3ℓ control regions after a background only fit. Expected signal distribution is overlaid, for a benchmark model of a singlet VLB with 900 GeV mass, multiplied by a factor of 5 for visibility purposes.

95% CL. More details about the statistical procedures of limit setting will be given in section 5.5. For pair-produced VLQ, masses below the TeV range were excluded, with singlet VLT (VLB) masses excluded up to 1.03 (1.01) TeV, and doublet VLT (VLB) masses excluded up to 1.21 (1.14) TeV. In the case of BR(Z) = 1, VLT (VLB) masses were excluded up to 1.34 (1.22) TeV. Limits as a function of VLQ mass can be seen in fig. 4.7. More details about the differences in sensitivity with regard to VLQ isospin and charge will be given in section 5.6. Limits across all branching ratio possibilities are shown in fig. 4.8. It shows that the sensitivity is mostly located for high Z boson BR, as expected. Given the dependency of single production cross section with the VLQ coupling to EW bosons, the interpretation of results is trickier. Only single production via the coupling of T to the W boson, as is shown in fig. 2.5, is considered, as its cross section is about one order of magnitude higher than the diagram with the Z boson for the same coupling value [71]. For a set coupling of k_T = 0.5, corresponding to c_W = 0.45 in the parameterization that will be shown for the coupling scan, expected and observed limits as a function of VLQ can be seen in fig. 4.9. Figure 4.10 shows expected and observed limits on the VLT mass as a function of its coupling to the W and Z bosons. As the analysis is not sensitive to VLQ chirality, the couplings are shown as a sum in quadrature of the left- and right-handed couplings. It can be seen that for large couplings masses below 1.6 TeV can be excluded.
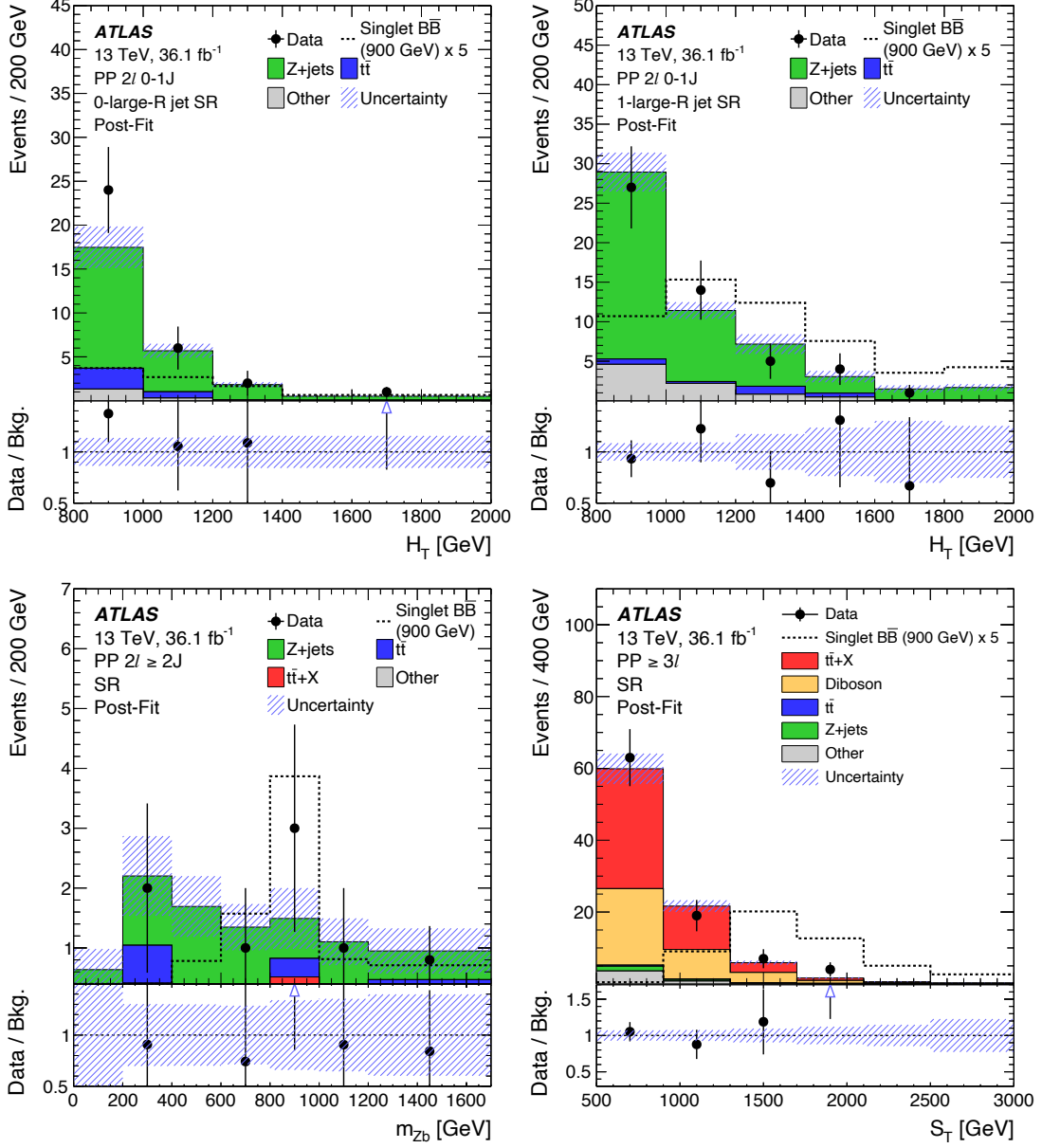
Figure 4.4: Discriminant variables of the pair production channels after a background only fit. Expected signal distribution is overlaid, for a benchmark model of a singlet VLB with 900 GeV mass, multiplied by a factor of 5 for visibility purposes, except for the PP $2\ell \geq 2$J channel.
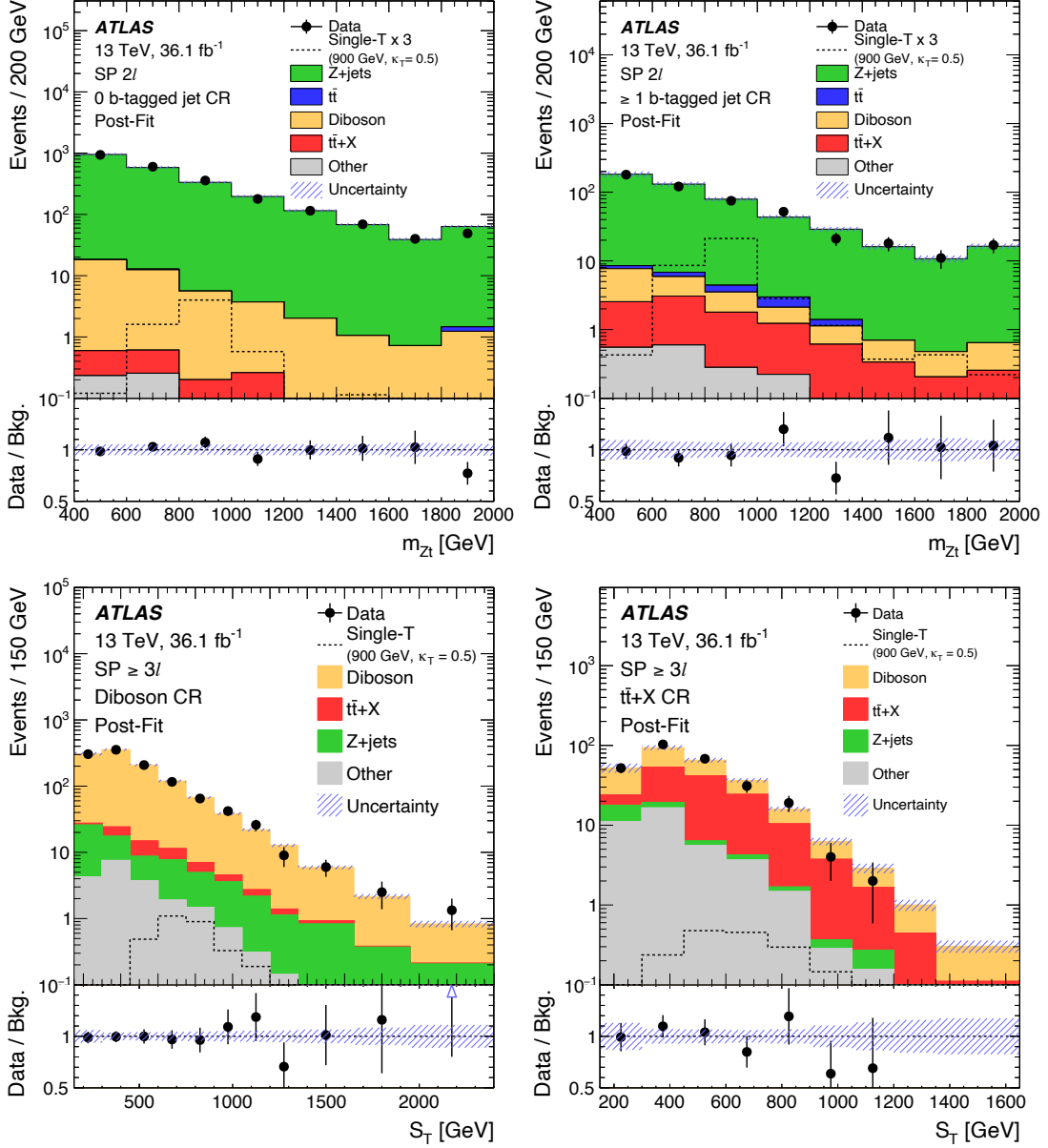
Figure 4.5: Discriminant variables of the single production control regions after a background only fit. Expected signal distribution is overlaid, for a benchmark model of a singlet VLT with 900 GeV mass and $k_T = 0.5$, multiplied by a factor of 3 for visibility purposes in the SP 2ℓ channel.
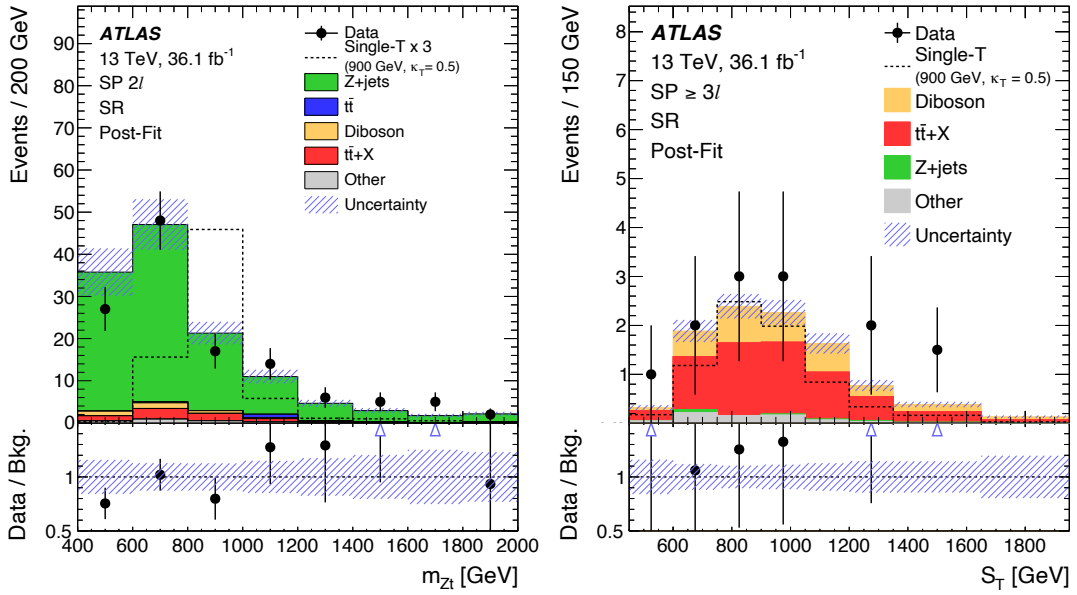
Figure 4.6: Discriminant variables of the single production channels after a background only fit. Expected signal distribution is overlaid, for a benchmark model of a singlet VLT with 900 GeV mass and $k_T = 0.5$, multiplied by a factor of 3 for visibility purposes in the SP 2ℓ channel.

4.1.1.1 Other results of VLQ to Z

Besides the search shown above, other results were obtained for VLQ decaying through a Z boson. Namely, the CMS Collaboration has a search for pair production of VLT and VLB decaying through a leptonically decaying Z boson [72] at $\sqrt{s} = 13$ TeV, with 35.9 fb^{-1} of data. A similar strategy is applied, i.e. selecting events with high p_T jets and Z boson candidate, as was the scalar sum of jets and leptons p_T. Top tagging is applied to large radius jets, in a similar fashion to what was described for the SP 2ℓ channel. Small radius jets are also tagged as W, Z, H or top quark jets. Afterwards, for VLT events, categories are built based on the multiplicity of jets tagged as b, V (i.e. W or Z), H or top. b-tagged jet multiplicity can be 1 or ≥ 2, the number of V, H or top tagged jets can be 0 or ≥ 1, so 16 catergories can be built. However, regions with similar $S/\sqrt{B}$ are grouped together, so at the end 9 categories are left. For the VLB search, 5 categories are built, based on the same multiplicities. The discriminant variable used is the scalar sum of jets and leptons. After no deviation from the SM expectation was found, upper mass limits were derived. For the scenario where BR(Z) = 1, masses below 1.28 (1.13) TeV were excluded for VLT (VLB). These results are compatible with those found in the aforementioned ATLAS analysis (1.34 and 1.22 TeV for VLT and VLB, respectively).

VLQ decays through a Z boson were also searched in single production by both the ATLAS and CMS Collaborations. An ATLAS search with 36.1 fb^{-1} of run-2 data searched for T decays to tZ where the Z boson decays invisibly [73], a final state usually referred to as monotop. This final state is characterized by a top quark and large missing transverse momentum, which is useful to search not only for VLT single
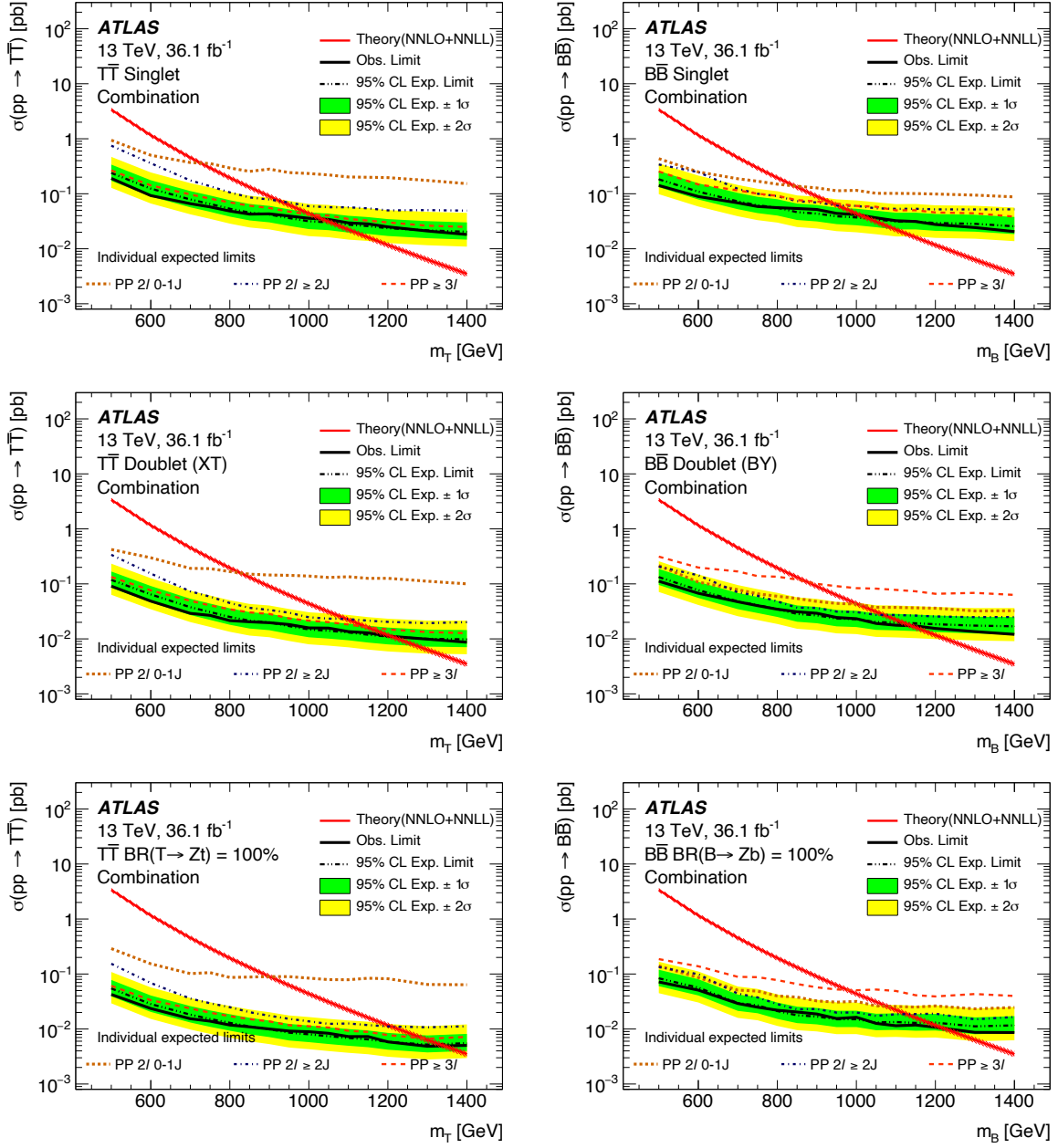
Figure 4.7: Expected and observed combined limits at 95% CL on the production cross-section for $T\bar{T}$ $B\bar{B}$ for the singlet and doublet benchmarks and for the case where BR(Z) = 1. The individual channel lines represent their expected limits.

production but also for dark matter candidates that could produce the same final state. Because ZTt prodution is suppressed, as was the case in the ATLAS search with a leptonically decaying Z boson, only WTb production is considered. A forward jet is required by this search, as well as exactly 0 leptons, $E_T^{miss} >$ 200 GeV and at least 1 large-R jet tagged as a top quark. The signal region is built by taking advantage of the asymmetry between E_T^{miss} and the p_T of the top tagged jet that is expected to be smaller for events with jets mis-reconstructed as E_T^{miss} in multijet production backgrounds. Background supression is also
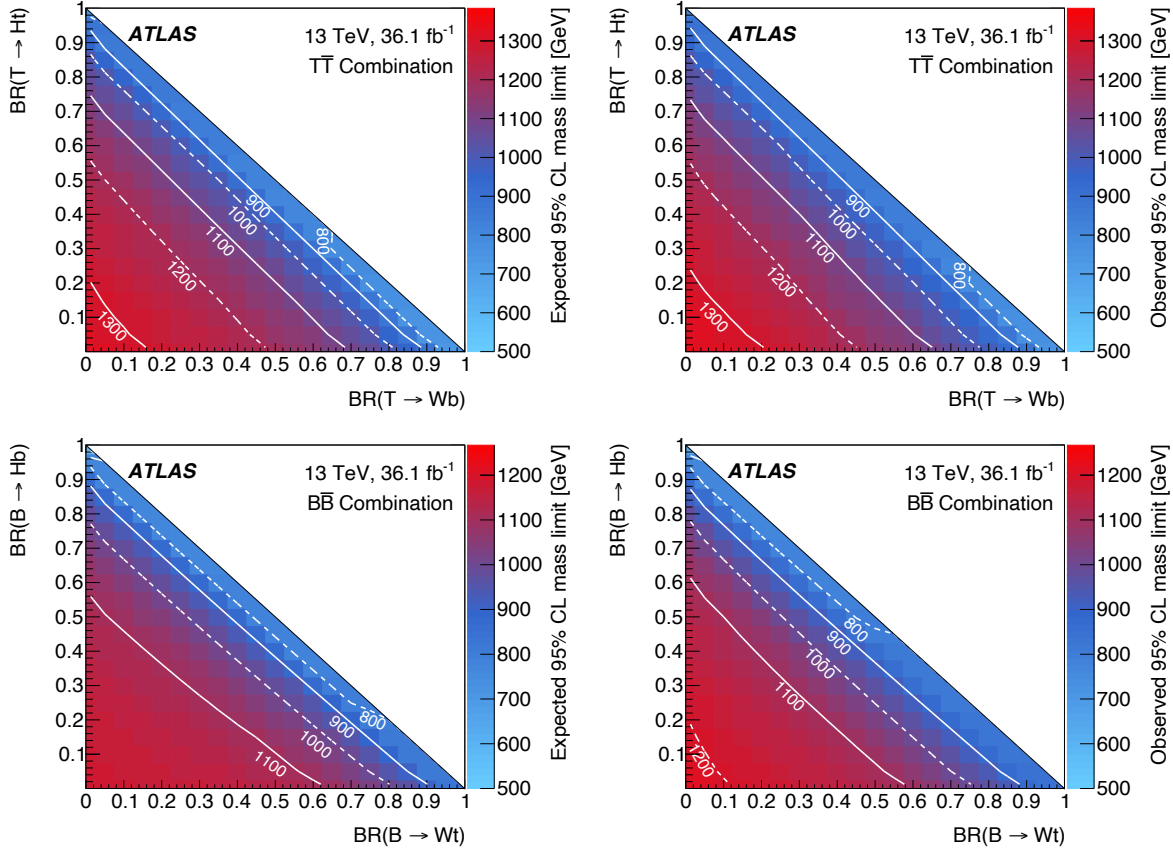
Figure 4.8: Expected and observed lower mass limits for the different BR possibilities. The white lines represent the contours of given VLQ masses.
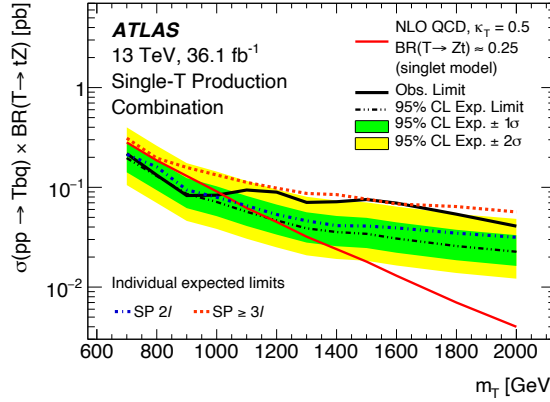
Figure 4.9: Expected and observed limits on the VLT mass as a function of the VLQ mass for a coupling $k_T = 0.5$. The grey are represents the region that is not excluded for any mass value tested.

achieved by requiring that the distance in the azimuthal angle ϕ of the top tagged jet and E_T^{miss} is larger than $\pi/2$, as these are expected to be mostly back-to-back in signal events. Upper mass limits as a function of the couplings to the EW bosons were derived, which were found to be compatible with those derived by the other ATLAS search for singly produced T, mentioned at the top of this section. Namely, for couplings
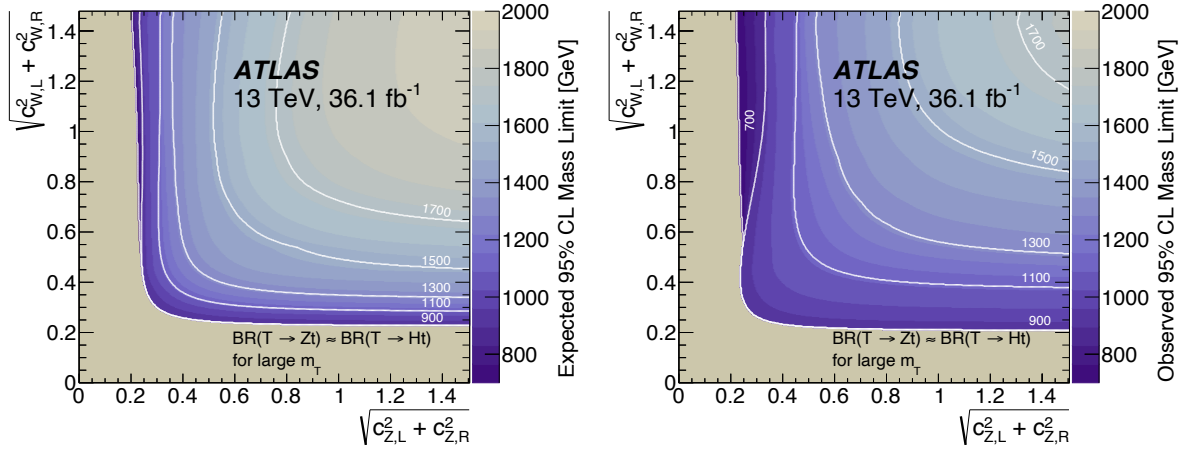
Figure 4.10: Expected and observed limits on the VLT mass as a function of its coupling to the W and Z bosons. The grey are represents the region that is not excluded for any mass value tested.

of T to W boson above 0.7 masses below 1.4 TeV were excluded at 95% CL.

CMS also has a couple of searches for single production of vector like quarks in Z boson final states. It started with an analysis performed with 2.3 fb^{-1} of run 2 data [74], which was upgraded with the partial dataset amounting to 35.9 fb^{-1} [75]. It searches for single production of VLT decaying to a leptonic Z boson and a third generation quark. The major improvement of the successor analysis, besides the increase in luminosity, came from the implementation of a categorization based on the presence of forward jets and the analysis of the mass spectrum a reconstructed T contained within a single large radius jet. The later part leads to 3 categories: a fully merged top quark that should result in a top tagged large radius jet; a partially merged top quark where jets are tagged as W and b; and a resolved top quark with 3 small radius jets. These categories, associated with the multiplicity of forward jets (being 0 or ≥ 1) leads to ten categories. Further requirements include a leading lepton with $p_T > 120$ GeV and at least one b-tagged jet. For a coupling with the W boson of 0.5 masses were excluded in the range of 0.7 to 1.2 TeV.

Both ATLAS and CMS Collaborations performed single production searches in other final states with W and H bosons [76–80]. There have also been some efforts to construct a generalized interpretation of single-production results, focusing on the possibility for a model independent recasting of the results [81].

There are also interesting results constraining VLQ production from indirect results. Most notably there is a search [82] that looks at LHC measurements and examines their sensitivity to VLQ production using the Contour framework [83]. With it signal is injected into these results and indirect constraints are obtained, that can be fairly competitive with direct searches.

4.1.2   ATLAS combination of searches for pair production of VLQ

Results from the CMS collaboration set stringent limits on VLQ pair-production, with the highest exclusion coming from the all-hadronic analysis [84], in which masses up to 1.37 TeV are excluded for the $T \rightarrow tH$

decay. These were obtained by using a neural network that identifies jets as being a likely decay of 6 different topologies: top quark, W, Z and H bosons, b quark and a light $u/d/s/c$ quark or gluon. With these multiplicities 126 independent signal regions were built, with the scalar sum of jets p_T being used as the discriminant variable. These results, along with the ATLAS pair production combination [85], represent the highest mass limits published yet. The author of this thesis was the analysis liaison for this combination, with the responsibility of producing the combined fit with the correct naming conventions necessary for such a large scale combination; doing the necessary checks to avoid overlaps with other analyses[2], along with other checks and tests.

The ATLAS combination took contributions from 7 pair production searches performed with 36.1 fb^{-1} of run 2 data. The advantage of doing a combination at a sub group scale is that it takes the best of both worlds: performant analyses carefully developed under the subgroup supervision and the statistical power of all these statistically independent events. These analyses were developed independently, each targeting its own phase space region to which they are optimized. At the end the combination takes the sensitivity that each analysis provides to a different region of the phase space, covering as much of it as possible. Looking at each analysis from the point of view of which BR corner it mostly covers, and starting from the Z corner:

- $Z(\ell\ell)t/b + X$: The analysis presented at the top of this section, largely contributing to the Z corner in leptonic events.

- $Z(\nu\nu)t + X$ [86]: A search for VLT pair production with at least one the branches decaying as $T \to Zt + X$, in events where the Z boson decays into a pair of neutrinos and exactly one charge lepton is produced, wether by the top quark decay or from the other branch of the T pair decay. This results in a final state with multiple jets, high E_T^{miss} and one charge lepton, motivating a cut on $E_T^{\text{miss}} > 300$ GeV; a cut on lepton multiplicity, which by requiring exactly one lepton should suppress dileptonic $t\bar{t}$. Similarly to the monotop search, which also deals with a final state of a top quark and large E_T^{miss}, a selection based on the azimuthal angle ϕ and jets is applied. The distance in this angle between E_T^{miss} and the two leading jets ordered by p_T must be higher than 0.4, in an attempt to reject E_T^{miss} from mismeasured jets. At least one b-tagged jet is required, given the presence of a top quark. The main backgrounds in this search are single lepton $t\bar{t}$ and $W +$ jets. In order to suppress contribution from the former, cuts on reconstructed transverse masses of the W boson and a generalized mass of two or more particles are applied. Control regions for these two main backgrounds are built by modifying the requirements on the transverse W mass that are made in the single bin signal region.

- $H(bb)t + X$ [87]: Search for pair production of VLT with at least one decay as $T \to Ht$, with $H \to \bar{b}b$. The final state is characterized by an isolated lepton, large E_T^{miss} and high jet multiplicity.

---

[2] More details about this will be given later in this section.

The search is split into a 0 lepton channel, in which E_T^{miss} >200 GeV is required, and a 1 lepton channel in which the E_T^{miss} requirement is relaxed to 20 GeV. In the 0 lepton channel, the 4 most energetic jets are required to have a $\Delta\phi > 0.4$ with E_T^{miss}, to suppress multijet background. Although the main target of the search is $T \rightarrow H \rightarrow \bar{b}b$, the channel with no leptons is also sensitive to high p_T Z bosons decaying invisibly, or W boson decays to an undetected lepton. The signal region is categorized based on jet multiplicity, b-tagged jet multiplicity, and H and top-tagged jet multiplicity, resulting in 22 regions for the 0 lepton channel and 12 for the 1 lepton channel. The main background is $t\bar{t}$ + jets. The scalar sum of jets and leptons and missing transverse momentum is used as the discriminant variable.

- Fully hadronic [88]: Search for pair production of VLQ decaying into a fully hadronic final state with low E_T^{miss}. In this final state, a large sensitivity for $B \rightarrow Hb$ decays is available. The hadronic objects used by the analysis are small radius jets, some of which are reclustered as large radius jets. These reclusted jets are inputs to a deep neural network that tags them into four categories: V bosons, H bosons, top quarks or background jets. These tags are used to categorize the signal region by their multiplicity, after the $E_T^{\text{miss}} < 200$ GeV and 2 b-tagged jet requirements. The discriminant variable is the signal probability given a matrix element method using each signal region. The main background, multijets, is derived by a data driven method.

- Trilepton/same-sign dilepton [77]: Search for events with two same sign lepton, or three leptons and a b-tagged jet, which, after some kinematic requirements should allow for only a few known backgrounds, namely $t\bar{t} + V/H$ and dibosons. This analysis has its sensitivity mostly focused on $T \rightarrow Z/Ht$ and $B \rightarrow Wt$. Eight signal regions are defined based on the multiplicity of leptons and b-tagged jets, all in single-bin histograms, after cuts on the scalar sum of jets p_T and E_T^{miss} are applied. Data driven techniques are used to estimate backgrounds coming from prompt leptons that results from the decay of heavy-flavor hadrons.

- $W(\ell\nu)b + X$ [89]: Search for $TT \rightarrow WbWb$ events, with one leptonically and one hadronically decaying W boson. The final state consists of a high-p_T charged lepton and E_T^{miss} from the leptonic W decay, a high p_T large radius jet from the hadronic W decay, and b-tagged jets. The main background is $t\bar{t}$. The analysis strategy consists on the reconstruction of the T candidates in both the leptonic and hadronic channels, using large and small radius jets, E_T^{miss} and leptons. This is done by pairing each W boson candidate with a b-tagged jet. In events with more than 2 b-tagged jets, the two most energetic will be used. The choice of each pair is done by minimizing the absolute value difference of the two reconstructed masses. In events with only one b-tagged jet, the other mass is reconstructed with the small radius jet that minimizes the same mass difference. Signal region events are required to have ΔR (lep,ν) < 0.7, for the two objects from the leptonically decaying W candidate. The scalar sum of jets and leptons p_T must also be higher than 1.8 TeV. The main

backgrounds are $t\bar{t}$, W + jets and single-top. In order to suppress some $t\bar{t}$ and single-top events, the difference between the 2 reconstructed T masses must be lower than 300 GeV. There is a $t\bar{t}$ control region that is achived by changing the requirements on the scalar sum of jets and leptons p_T. The mass of the leptonic T is used as the discriminant variable.

- $W(\ell\nu)t + X$ [90]: A search very similar to the $W(\ell\nu)b+_X$ search, modified to target $B \rightarrow Wt$ events. Two signal regions are built, based on the multiplicity of large radius jets: one with at least 3 large radius jets that uses the mass of the hadronic decay of B for discrimination, and another, inclusive, that uses a Boosted Decision Tree.

These analyses were ensured to be orthogonal by removing some overlapping events. Namely, the $W(\ell\nu)b + X$ and $Z(\nu\nu)t + X$ analyses did not contribute for events with more than 6 small radius jets and 3 b-tagged jets as they overlapped with the $H(bb)t + X$ selection. The $Z(\nu\nu)t + X$ analysis added a cut on the scalar sum of jets and leptons p_T in a control region in order to remove overlaps with a $W(\ell\nu)b + X$ signal region. The trilepton/same-sign dilepton team removed events with more than 3 leptons or events with 2 leptons inside the Z boson mass window of 10 GeV in order to not overlap with the $Z(\ell\ell)t/b + X$ signal region. The overlap of events was evaluated to be less than 1% between any two signal regions and less than 3% between any two control and signal regions, all with negligible impact on the results. A consistent definition of physics objects across all analyses was also verified.

Modelling uncertainties are uncorrelated across analyses in the fitting procedure. The fit behavior in the combination is shown to be consistent with the fits from individual analyses. As no significant excess from the SM expectation was observed in data, upper mass limits where derived. Masses below 1.31 TeV are excluded for singlet T, and 1.37 TeV for the doublet scenario. For B, masses below 1.22 and 1.14 TeV are excluded for the singlet and doublet hypothesis.

The combination presents a significant improvement from the individual analyses. As can be seen in fig. 4.11, in which the individual analyses lines are shown, the results are consistently better for the combination. Using the singlet T case as an example, limits are improved by a factor of 1.7 TeV, representing an improvement of 110 GeV in the mass limit.

Another interesting observation is the complementarity between analyses. In fig. 4.12 the exclusion achieved by each analysis is shown, in binary, i.e. the BR area that can be excluded is painted for each analysis, for each mass point tested. It shows that the different analyses cover most of the BR plane, in a complementary way. As VLQ masses get higher, analyses loss sensitivity but it can be seen that the regions closer to the corners still have some sensitivity. For reference, the analysis of which the author of this thesis was a part ($Z(\ell\ell)t/b + X$) is represented by the purple area. As expected it mostly covers the Z corner, but as masses get higher it is crucial in providing sensitivity to this phase space region.
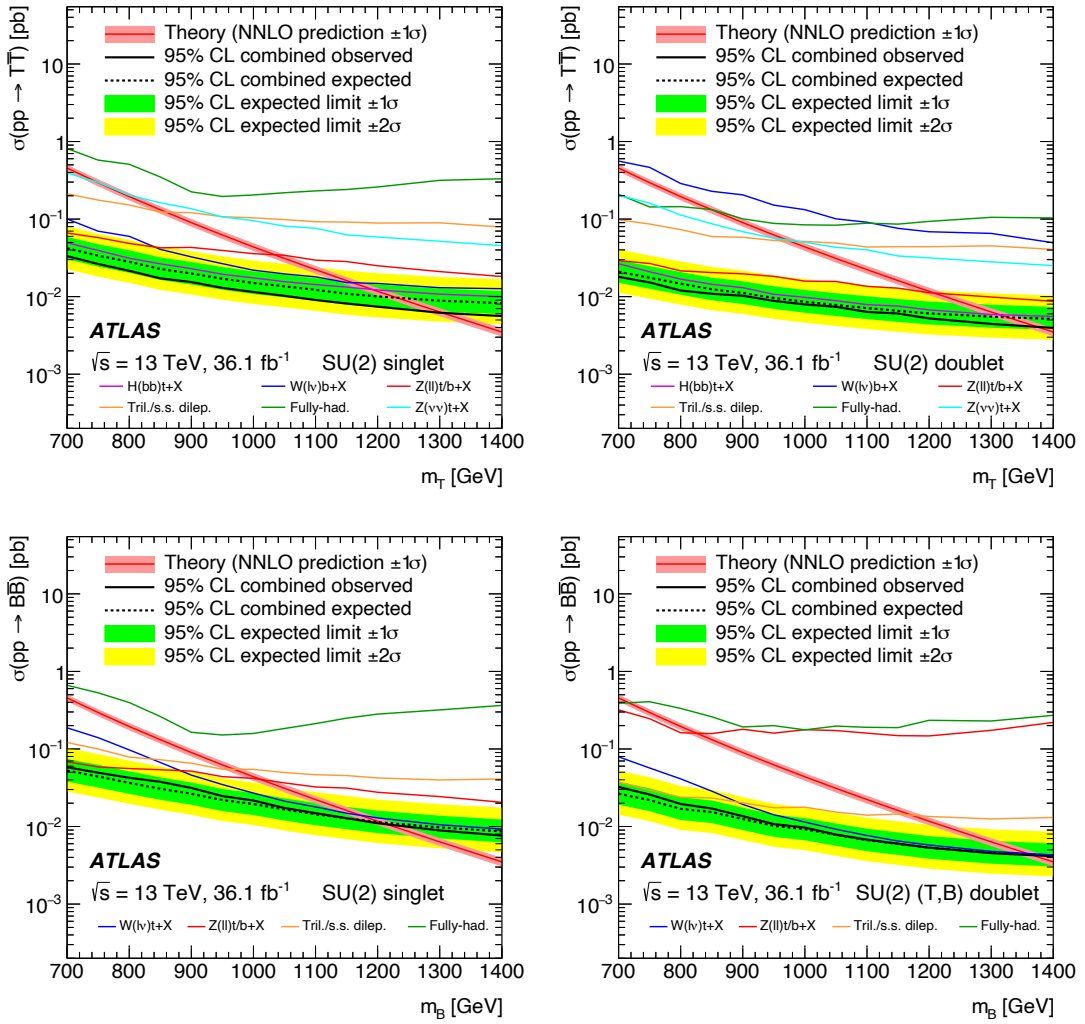
Figure 4.11: Expected and observed lower mass limits for VLT and VLB, singlet and doublet. The individual lines represent the observed limits for each analysis.
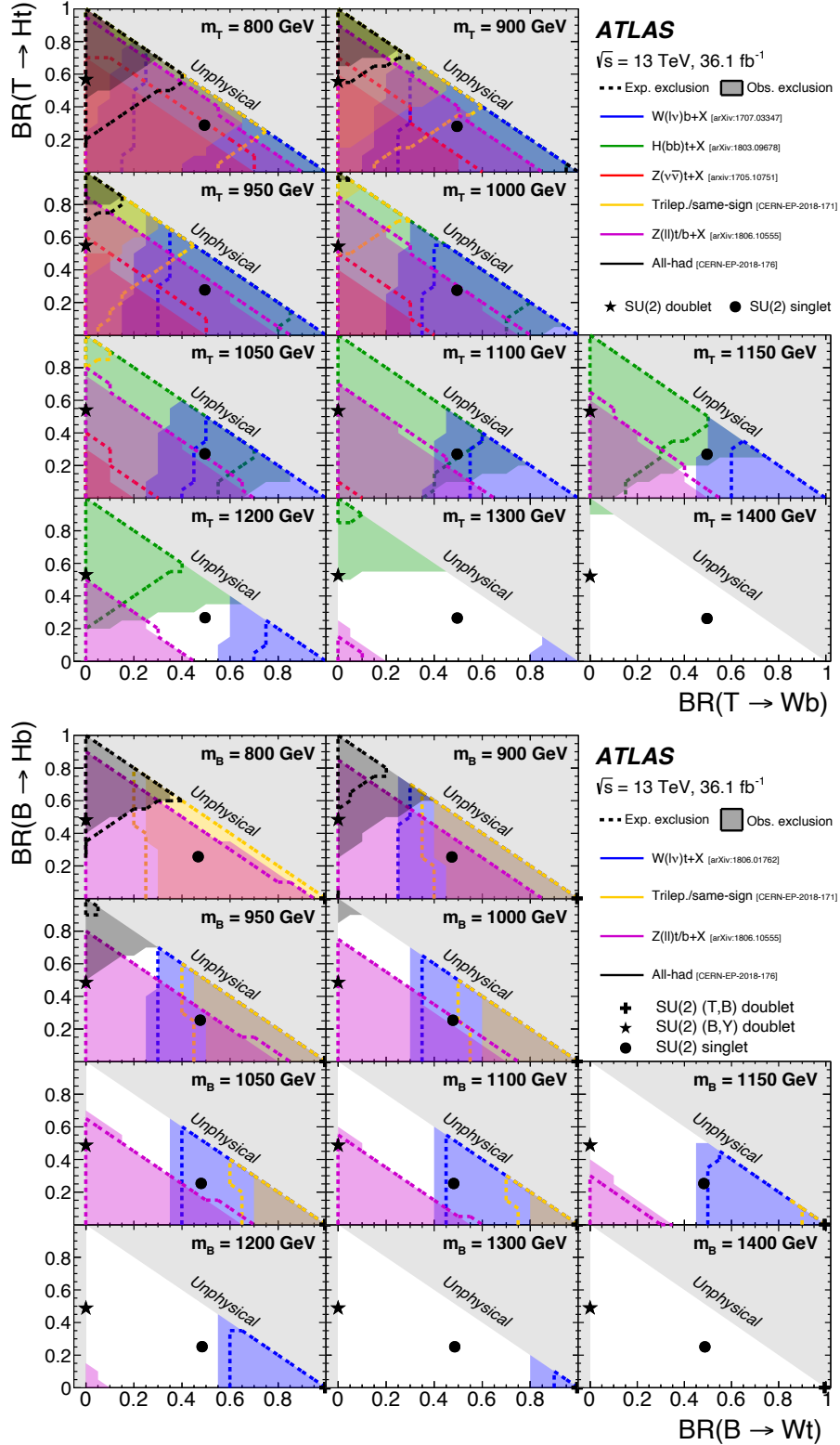
Figure 4.12: Observed (filled area) and expected limits (dashed lines) for T as a function of the BR for each analysis.

Search for VLQs in the $Zt/b + X$ channel with full run-2 dataset

Following the analyses with a partial run-2 dataset, taking advantage of the data further collected in the remainder of the second run of LHC operations, a new analysis was performed. It focuses on the same final state, a leptonically decaying Z boson and a third generation quark, but it exclusively targets pair production of VLT and VLB. While it is an update of the analysis with the partial dataset it features a new strategy and much improved results that will be discussed in the present chapter.

5.1   Data and Monte Carlo samples

The analysis uses data collected by the ATLAS experiment during the run 2 at $\sqrt{s} = 13$ TeV, amounting to an integrated luminosity of 139 fb^{-1}. In order to make a realistic comparison of the simulated samples with the collected data a detailed simulation of the ATLAS detector has to be performed. This is achieved using Geant4 [91] to replicate the detector effects and applying the same reconstruction algorithms as those used for data.

The simulation of the Z boson production associated with jets (henceforth referred to as Z + jets) was done using Sherpa 2.2.1 [92–95]. It includes events that were generated with up to two partons at next-to-leading order (NLO), up to four partons at leading-order (LO) and using the next-to-next-to-leading-order (NNLO) [96] cross-section for normalization. The collection of processes with a pair of bosons (i.e. WW, WZ and ZZ, and from this point referred to as dibosons and VV for short) was simulated using Sherpa 2.2.2, with the NNPDF3.0 [97] NNLO PDF set. For diboson processes the samples include events up to one parton at NLO, three partons at LO and NLO cross-section for normalization. The simulation of events

with multiple jets can be a difficult task, so algorithms were developed attempting to match the theoretical prediction with the experimental precision. Some are dedicated to the matrix element (ME) calculation and some deal with the simulation of parton showers at particle level. At the end these two need to be merged. This can, however, lead to complications as double counting needs to be avoided, especially in the cases where the ME was calculated at higher order. For the Z + jets and VV samples the parton shower simulation was done using Sherpa and was merged to the matrix element according to the ME+PS@NLO prescription [98].

The $t\bar{t}$ production was simulated with Powheg-Box v2 [99, 100] using the NNPDF3.0 NNLO PDF set. Pythia 8.230 was used for parton shower and hadronization simulations, with the A14 tune [101]. NNLO cross-section calculation was used for normalization, including next-to-next-to-leading logarithmic (NNLL) resummation calculated with TOP++ [102–108].

The production of $t\bar{t}$ associated with a vector boson (i.e. Z or W, from now on referred to as $t\bar{t} + X$) was generated with MadGraph5_aMC@NLO 2.3.3, with Pythia 8.210 for hadronization and using the NNPDF2.3LO PDF set with the A14 tune.

Single-top processes were simulated with Powheg-Box v1 or v2. The PDF set is NNPDF3.0 NLO, interfaced with Pythia 8.234 with the A14 tune. NLO cross-sections are used for normalization, with the additional NNLL soft gluon terms.

The signal samples were simulated with Protos [109], using Pythia [110] 8.186 with the A14 tune, and the NNPDF2.3LO PDF set. VLQ masses from 800 GeV up to 2 TeV where generated assuming the singlet scenario. These were produced assuming a BR of 1/3 to all 3 decays, for practical reasons, allowing them to be reweighted at event level, suiting the different BR scenarios that will be explored. This relies on the assumption that there are no relevant kinematic changes from the singlet to the doublet scenario, which was tested during the analysis development and a relevant study can be seen in appendix D. In it the discriminant variables used in the analysis are shown for singlets and doublets, and their ratios below, and it can be seen that the agreement is fair and mostly flat. For a VLT with 1.2 TeV, the expected limits on the signal strength using a doublet sample or the reweighting procedure just described change by about 2%. Signal cross-sections were calculated using TOP++ at NNLO+NNLL, using as the PDF set MSTW 2008 [111–113] at NNLO. These details are summarized in table 5.1.

5.2   Object definitions

This analysis uses electrons, muons[1] and jets in order to perform an event selection and construct the discriminant variables that will be used in the fit.

---

[1]In the context of this analysis, electrons and muons will be collectively referred to as leptons, intentionally excluding the unused taus, and abbreviated as ℓ.

Sample	Generator	Parton Shower	PDF set	Tune
Z + jets	Sherpa 2.2.1	Sherpa	NNPDF3.0	Sherpa default
Dibosons	Sherpa 2.2.2	Sherpa	NNPDF3.0	Sherpa default
$t\bar{t}$	PowhegBox	Pythia8	NNPDF3.0	A14
$t\bar{t} + X$	MadGraph5_aMC@NLO	Pythia8	NNPDF2.3LO	A14
Single-top	PowhegBox	Pythia8	NNPDF3.0	A14
VLQ	Protos	Pythia8	NNPDF2.3LO	A14

Table 5.1: Parameters used to generate the Monte Carlo samples for the analysis.

5.2.1 Electrons

Electron reconstruction is done from the clusters formed in the electromagnetic calorimeter, using tracks measured in the inner detector to match the clusters. The matching tries to avoid electron candidates coming from background processes such as hadrons, photon conversion or heavy flavor hadron decays. For that a multivariate analysis technique is used in a likelihood-based method that will serve as the electron identification, with different criteria levels: *Loose, Medium* and *Tight*, in increasing order of background rejection [114]. Electrons in this analysis must fulfill the *tight likelihood* criteria. They must also have at least $p_T > 28$ GeV and $|\eta| < 2.47$ but be outside the transition region between the EM barrel and its end-cap $(1.37 < |\eta| < 1.52)$. In order to suppress fake electrons from pileup jets, they are required to pass impact parameter cuts that try to ensure that the electron is associated with the primary vertex of the event.

5.2.2 Muons

Muons are reconstructed from tracks measured in the muon spectrometer and the inner detector, combined with a requirement of fulfilling the *medium* identification criteria [115]. They must have $p_T > 28$ GeV and $|\eta| < 2.5$. The tracks used must also be sufficiently isolated from other tracks. To ensure that is the case, the scalar sum of all tracks within a ΔR cone is calculated (excluding the track from the muon in consideration). The ratio of this sum over the p_T of the muon must be under 0.15 for the muon to be selected. The cone ΔR is considered to be the smaller value between 0.3 and 10 GeV/p_T^l, with p_T^l being the candidate muon p_T. Lastly, muons must also satisfy requirements that ensure they are associated with the primary vertex.

5.2.3 Jets

Colored particles cannot exist as free states, due to confinement[2], so there is always the production of additional colored particles in the process of hadronization. As a consequence there is no unique detector signature that we can use to individually characterize colored particles in our detector, so we have to

---

[2]As discussed in section 2.1.3.

reconstruct the collimated spray of hadrons into a singular object we call jets. There is not a unique way of defining a jet, multiple algorithms can be used, most of them based on clustering energy deposits in the calorimeters into a singular object, through different clustering criteria. The algorithm used in this analysis is the anti-k_t [116] clustering algorithm. It takes as input the energy clusters deposited in the calorimeters and clusters them sequentially by picking those with the smallest distance. This distance, which is the definition that characterizes the algorithm, is given by:

$$d_{ij} = \min{(k_{T,i}^{2p}, k_{T,j}^{2p})} \frac{\Delta R_{ij}^2}{R^2} \tag{5.1}$$

with $\Delta R_{ij}^2 = (y_i - y_j)^2 + (\phi_i - \phi_j)^2$, $k_{T,i}$ is the p_T of the ith constituent and R is the parameter that defines the radius of the reconstructed jet. p is the parameter that governs the the relative importance of geometry and geometrical scales in the reconstruction. $p = 1$ defines the k_t algorithm, $p = 0$ is the Cambridge/Aachen algorithm and $p = -1$ is the anti-k_t algorithm that is used in this analysis. This choice of p makes the algorithm tend to cluster the hardset constituents together. The procedure then is to choose the constituent that has the smallest d_{ij}, and recombine them into a single constituent. This process is repeated until no constituent is found within a distance given by $d_{iB} = \frac{1}{k_{T,i}^2}$. At that point the jet is considered complete and the process repeats with the new set of constituents not present in the reconstructed jet, until no constituents are left. The radius parameter R will define the size of the clustered jets. This analysis uses $R = 0.4$, called small-R jets. The effects of the choice of the parameter p in the clustering can be seen in fig. 5.1

It is common to also use jets with $R = 1.0$, called large-R jets, to cluster multiple hadrons that are contained inside the same radius due to some boost coming from the high mass of the decaying mother particle. However in this analysis there will be the use of reclustered jets instead. They are obtained using the anti-k_t algorithm with $R = 1.0$ but using already reclustered small-R jets as input. This is because they will be used in a multivariate algorithm and since the small$-R$ jets are already calibrated there is no need to calibrate the reclustered jets. More details about the multivariate algorithm will be given in section 5.3.

Jet calibration is done obtaining an energy scale coming from measurements with data and simulation in combination [117]. Jets must have $p_T > 25$ GeV and $|\eta| < 2.5$. In order to reduce contamination from pileup jets a two dimensional likelihood discriminant is used for jets with $|\eta| < 2.4$ and $p_T < 60$ GeV. This is called jet-vertex-tagger (JVT) [118] and the score must be higher than 0.59.

5.2.4 b-tagged jets

The ability to characterize jets that were initiated by the hadronization of a b-quark can be very important. In our analysis we target decays to third generation quarks, and top quarks decay to a W boson and a b nearly 100% of the times, so the presence of a b quark is to always be expected in signal events. Sophisticated multivariate algorithms can be developed to use the properties of b hadrons in order to discriminate against
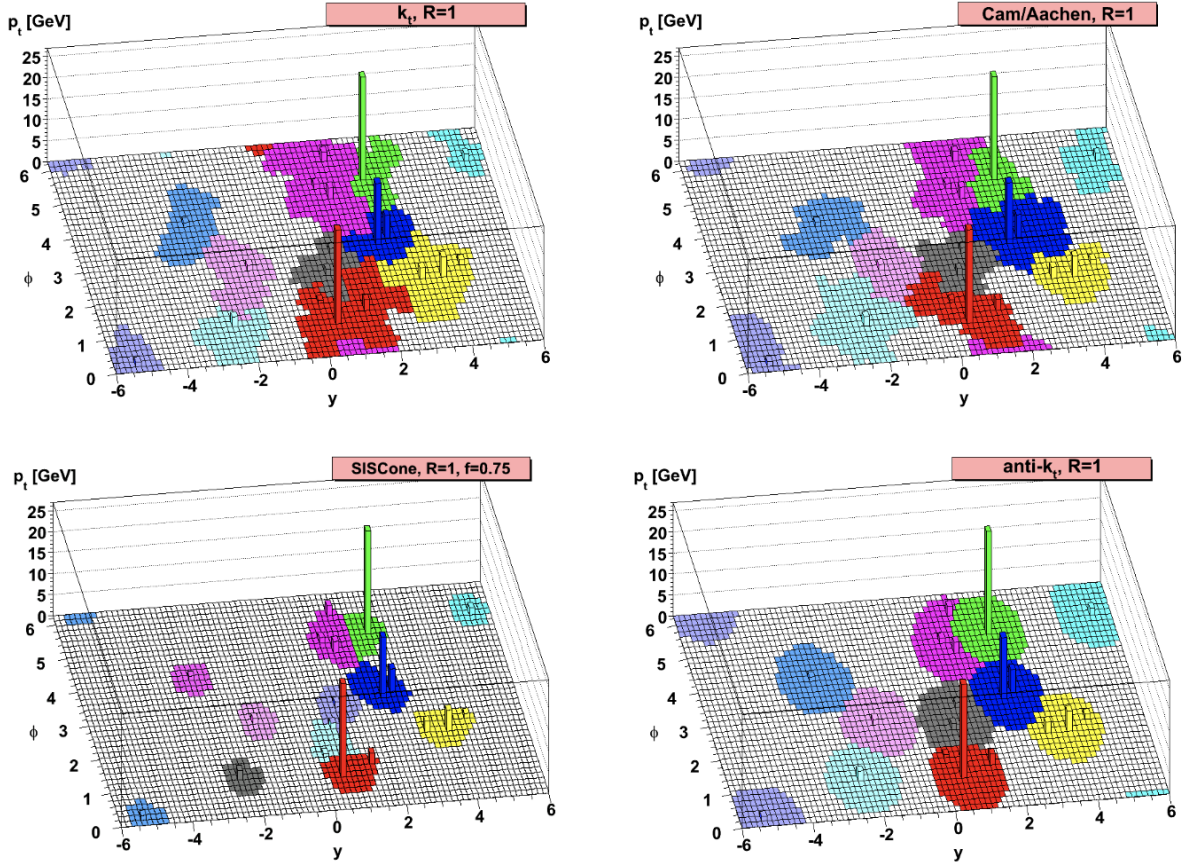
Figure 5.1: Representation of the different clustering algorithms [116].

other hadrons. The most notable feature that characterizes b-hadrons is their relatively long lifetimes. In earlier experiments this was used almost on its own to tag b quarks. In current analyses this is used in combination with other properties to fully exploit the capabilities of modern multivariate algorithms. The analysis presented here uses a boosted decision tree (BDT) algorithm called MV2 [119]. This algorithm was trained on a large sample of simulated b jets originated from $t\bar{t}$ production. The production of $t\bar{t}$ decaying to c (10% of events) and light jets (90% of events) is used as background. From the trained algorithm a per-jet classification is performed and several working points are defined based on their signal acceptance and background rejection. The calibrated working points are defined by the acceptance of b jets with $p_T > 20$ GeV and $|\eta| < 2.5$ at several efficiencies. This analysis uses the working point with the efficiency of 77%, corresponding to a c jet rejection of 6 and light jet rejection of 134 [3].

    It is common to have ambiguity when leptons and jets are reconstructed within a small radial distance. So any muon that deposits energy in the calorimeters and has a track that was previously identified (within the inner detector) as an electron is removed. After all the undesired muons are removed, electrons that

---

[3]It should be clarified that the signal efficiency is presented as the fraction of events correctly charaterized as signal, but the background rejection is presented with rejection factors, that are the inverse of of the efficiency. This means that a rejection factor of 100 accepts the associated jet 1 out of 100 times that it is seen.
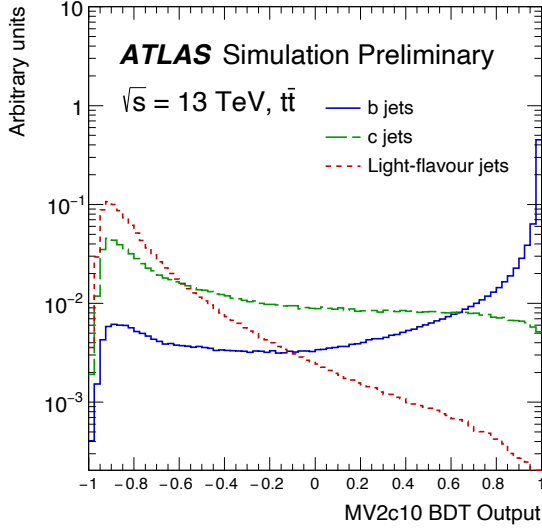
Figure 5.2: MV2 BDT output for b (blue), c (green) and light (red) flavour jets evaluated with $t\bar{t}$ events [119].

are identified in the same track as any other remaining muon is removed. Afterwards all jets that are within $\Delta R < 0.2$ of an electron are removed so that there is no reconstruction ambiguity in the calorimeter cell information. Next, any remaining electrons within $\Delta R < 0.4$ of a jet are removed, to reduce electron identification coming from c or b hadron decays. Jets that have not been b-tagged and that have at most two tracks with $p_T > 0.5$ within $\Delta R < 0.2$ of a remaining muon are removed. The last step is to remove any muons within $\Delta R < \min(0.4, 0.04 + 10 \text{ GeV}/p_T(\mu))$ of any remaining jet.

5.3 Event selection

The first stage of event selection happens at the trigger level: only events that pass the single lepton trigger are selected. This trigger requires an electron or a muon with a certain p_T threshold (that varies for different periods of data taking) in order to be satisfied. As this analysis looks for a leptonically decaying Z boson, at least 2 central leptons with $p_T > 28$ GeV are required. From the leptons that are selected, at least 2 must have the same flavor but opposite sign (OSSF), consistent with a Z boson decay. The OSSF pair with the mass $m_{\ell\ell}$ closest to the Z boson mass m_Z will then be selected as the Z boson candidate. Only events with $|m_{\ell\ell} - m_Z| < 10$ GeV are selected. Events must also have at least 2 central small-R jets with $p_T > 25$ GeV. The aforementioned cuts are referred to as preselection.

The requirement of a pair of OSSF leptons could, in principle, not be beneficial for high VLQ masses, given that lepton charge identification gets harder as the lepton p_T increases. Some analysis that exploit this high p_T regime choose to forgo this OSSF lepton requirement. It was, however, seen in the previous iteration of this analysis that this has a small effect on the sensitivity and so this cut was kept.

As can be seen in fig. 5.3a, which shows the lepton multiplicity in a histogram normalized to unity after
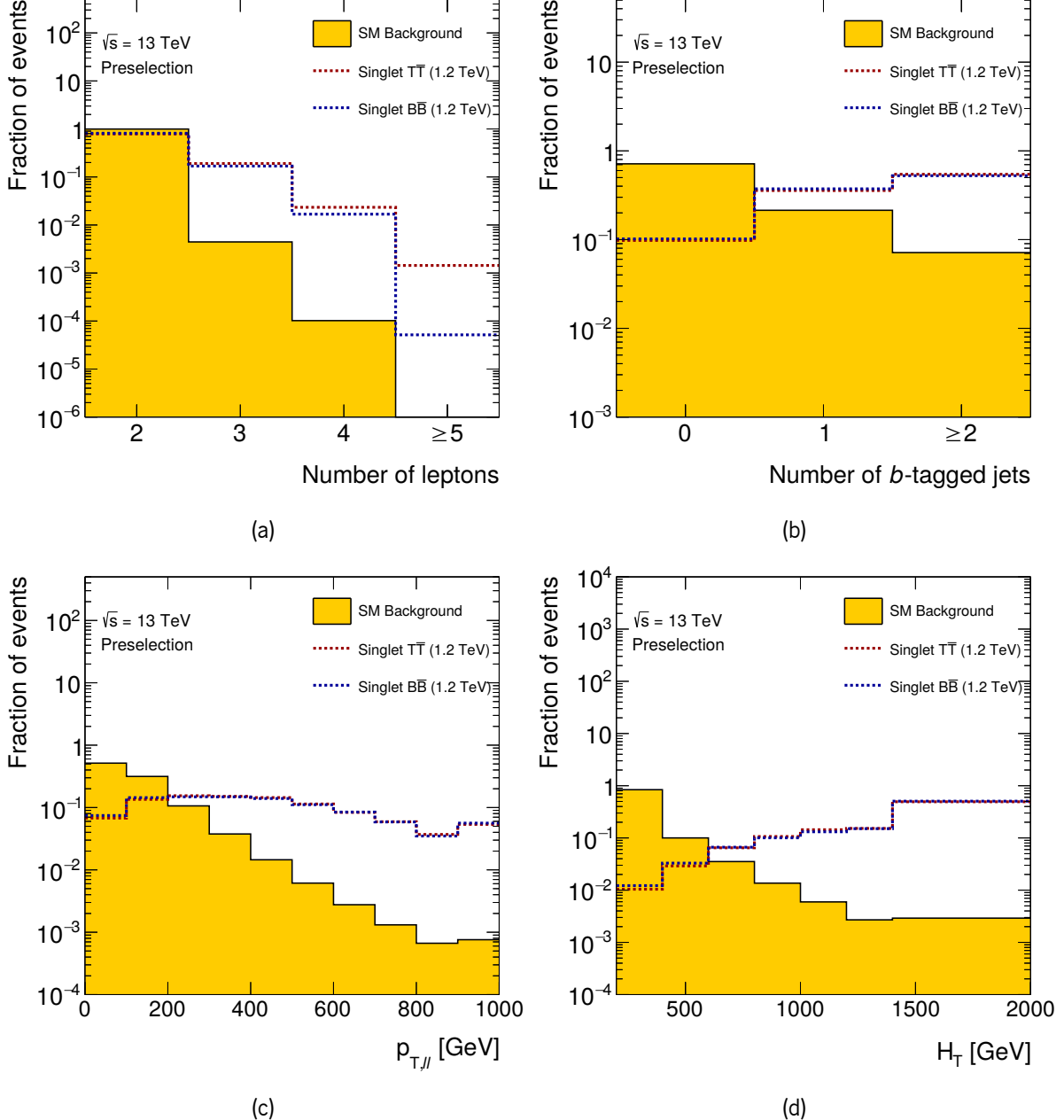
Figure 5.3: Distributions normalized to unit area obtained from MC simulation for the sum of all the background processes (solid area) and for benchmark signal processes (dashed lines): (a) lepton multiplicity, (b) b-tagged jet multiplicity, (c) $p_T(\ell\ell)$, and (d) $H_T(\text{jet})$.

preselection, most of the events have exactly 2 leptons. However, for events with higher lepton multiplicity the signal to background ratio is improved. With this in mind two channels are defined based on lepton multiplicity. Events with exactly two leptons belong to the dilepton channel (labeled in this thesis as 2ℓ) and events with at least 3 leptons belong to the trilepton channel (labeled as 3ℓ). The point of this separation is to exploit the different kinematic aspects of the two channels, optimize them individually and have a statistical combination afterwards.

The multiplicity of b-tagged jets also shows different signal to background ratios in each bin of fig. 5.3b. As the number of tags increases so does the signal purity. Therefore this quantity will be used in the construction of the regions.

From the previous round of VLQ searches we expect VLQs to have a mass of at least 800 GeV. This means that their decays products will be boosted and this will be exploited in the selection of events. Figure 5.3c shows the p_T distribution of the Z boson candidate. As expected, the signal events have a harder spectrum than background, so a cut on $p_T(\ell\ell)$ is applied, in order to reject background with little signal loss. The same thinking is applied to the final states objects so cuts on the scalar sum of the p_T (H_T) of jets, and jets plus leptons will be applied. The unit normalized distribution of $H_T(\text{jet})$ can seen to have a large shape difference in fig. 5.3d.

From the aforementioned selection a next step is taken in the definition of the regions. So that both channels have a richer fit, using multiple regions with different signal to background ratios and background compositions, the events after the selection are split into categories based on their topology. To that end, a multi-class boosted object tagger (MCBOT) is used. This an algorithm developed for a previous analysis [88] and was adapted to this search by the TU Dortmund group [120]. This tagger takes inputs from reclustered jets and outputs a 4 dimensional classification with the likelihood of the jet being originated from a top quark, a H boson or a Z/W boson, that from the difficulty of distinguishing among the two are merged as V, or a background jet. From this output cuts are set in order to establish a tagging working point for each category. In the case of jets having multiple tags the tag with the highest output is chosen.

The tagger was built from a deep neural network (DNN), trained on 18 input variables: reclustered jet mass, p_T and number of constituents; the 4-momentum of the 3 highest p_T small-R jets and their b-tagging information. For that Keras [121] and Tensorflow [122] were used. Reclustered jets from the simulation of $Z' \rightarrow t\bar{t}$, $W' \rightarrow WZ$ and $G^4 \rightarrow HH$, decaying exclusively to $b\bar{b}$ were used in the training of the neural network. The event generation ensured RC jets with $p_T > 40$ GeV with a uniform p_T distribution between 150 GeV and 3 TeV. The DNN consists of four hidden layers with Rectified linear units (ReLU) as the activation function, and an output layer using *softmax* as the activation function. To optimize the algorithm Adam [124] was the chosen method. Using MCBOT, a categorization of the final selection can be made, based on the multiplicity of each signal class. The data and Monte Carlo agreement can be assessed in the histograms presented in appendix A. It should be noted that in this analysis rcjets are only

---

[4]Kaluza-Klein graviton in the bulk Randal-Sundrum model [123].

used within MCBOT to build a signal region categorization and so there is no need to have any concerns with overlaps between rcjets and small-R jets.
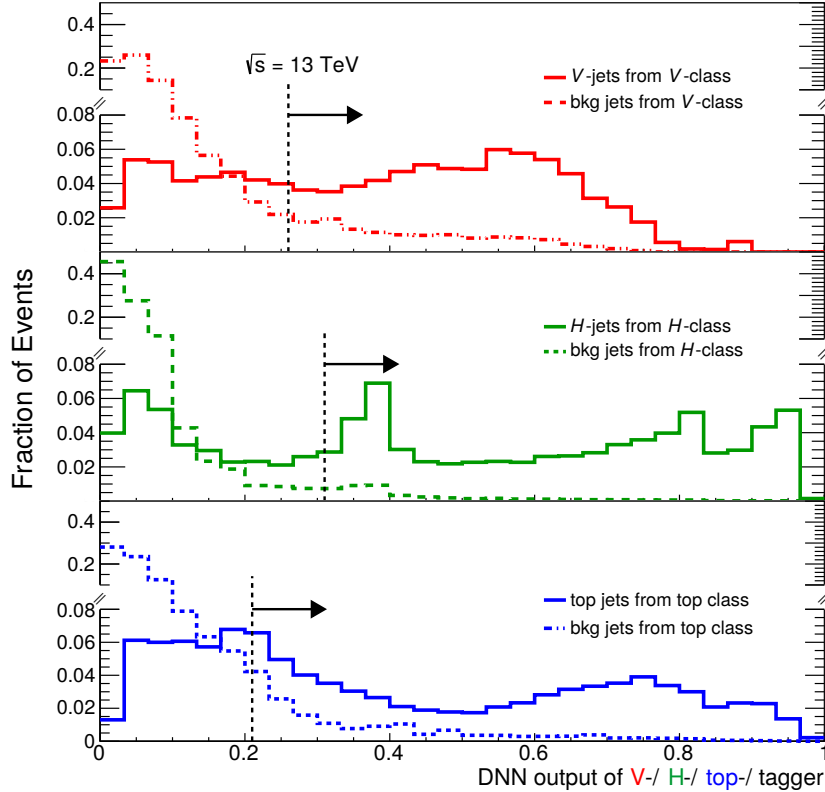

Figure 5.4: MCBOT outputs for each class. The vertical lines represent the thresholds chosen to be applied in the analysis.

In order to assess the modelling of some basic variables, distributions after pre-selection is applied will be shown. They will be compared before and after the application of a background only fit, that will be discussed in the next chapter. The signal represented in the histograms after fit is the pre-fit distribution.

The multiplicity of leptons after the 3ℓ pre-selection can be seen in fig. 5.5. All histograms shown in this thesis include under and overflow. The equivalent distribution for the 2ℓ channel is not shown as the multiplicity must be 2. In this distribution it can be seen that the agreement between data and MC is good, especially in the bin of 3 leptons. It can also be seen that the number of events with 4 leptons drops dramatically, along with the backgrounds that are present due to fake leptons: $t\bar{t}$ and Z+jets.

The multiplicity of jets for the 2ℓ channel can be found in fig. 5.6. The data and MC agreement is good for all multiplicities up to 9 jets.

The same distribution for the 3ℓ channel can be found in fig. 5.7. The data and MC agreement is good for all bins, as was the case in the 2ℓ channel. The contribution from $t\bar{t} + X$ increases for events with larger jet multiplicity, as expected. The same can be seen for the signal distribution.
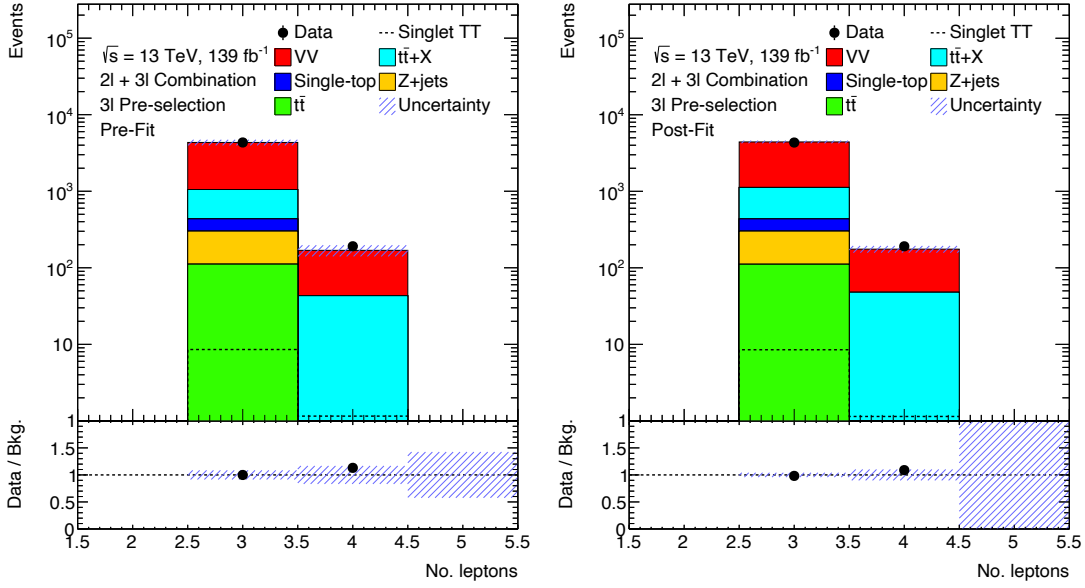
Figure 5.5: Distributions of the lepton multiplicity pre and post background only fit at the 3ℓ pre-selection.
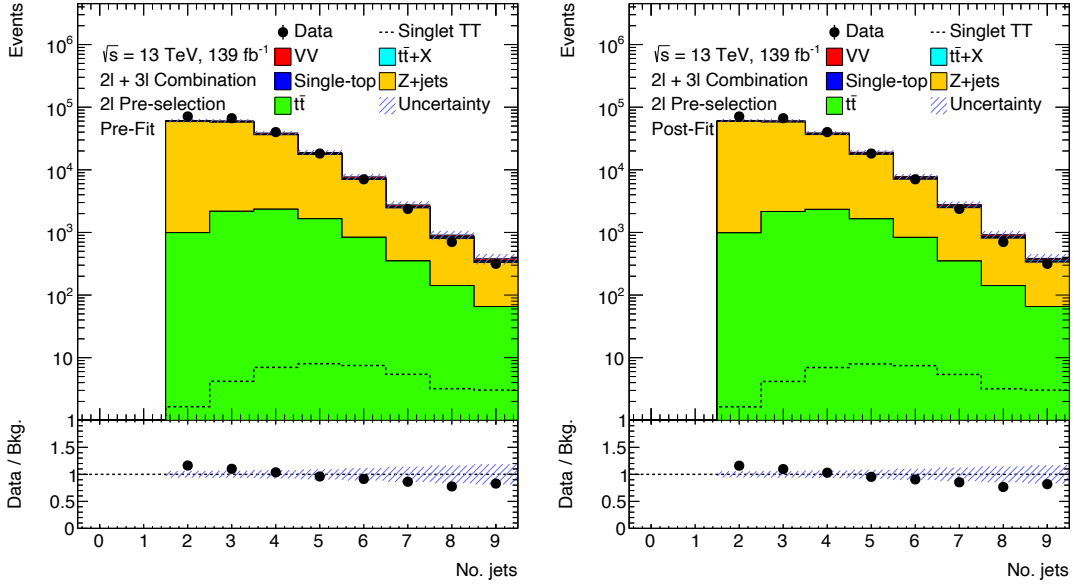
Figure 5.6: Distributions of the jet multiplicity pre and post background only fit at the 2ℓ pre-selection.

The number of b-tagged jets is shown, after the 2ℓ pre-selection, in fig. 5.8. This multiplicity is also well modeled, even for events with at least 4 b-tagged jets. As the number of b-jets increases so does the relative contribution from $t\bar{t}$.

The equivalent distribution after the 3ℓ pre-selection can be seen in fig. 5.9. The data and MC agreement is decent, especially for lower multiplicities, even though this effect is corrected by the fit. The signal distribution peaks at events with at least 2 b-tagged jets, which is expected. The 2ℓ distribution, which has a larger range, shows that signal peaks at events with 2 b-jets and softly drops for higher multiplicities.
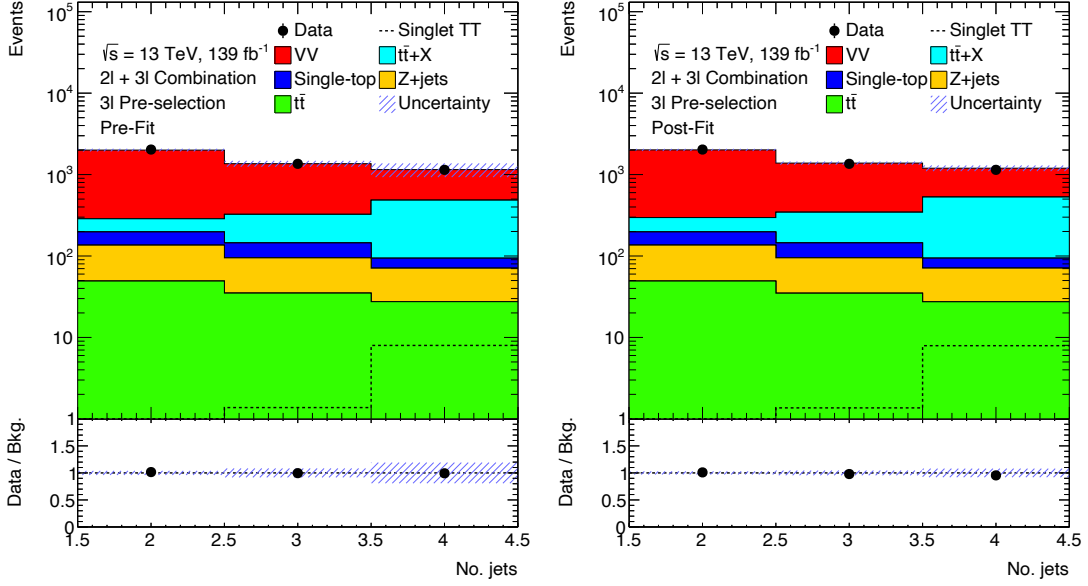
Figure 5.7: Distributions of the jet multiplicity pre and post background only fit at the 3ℓ pre-selection.
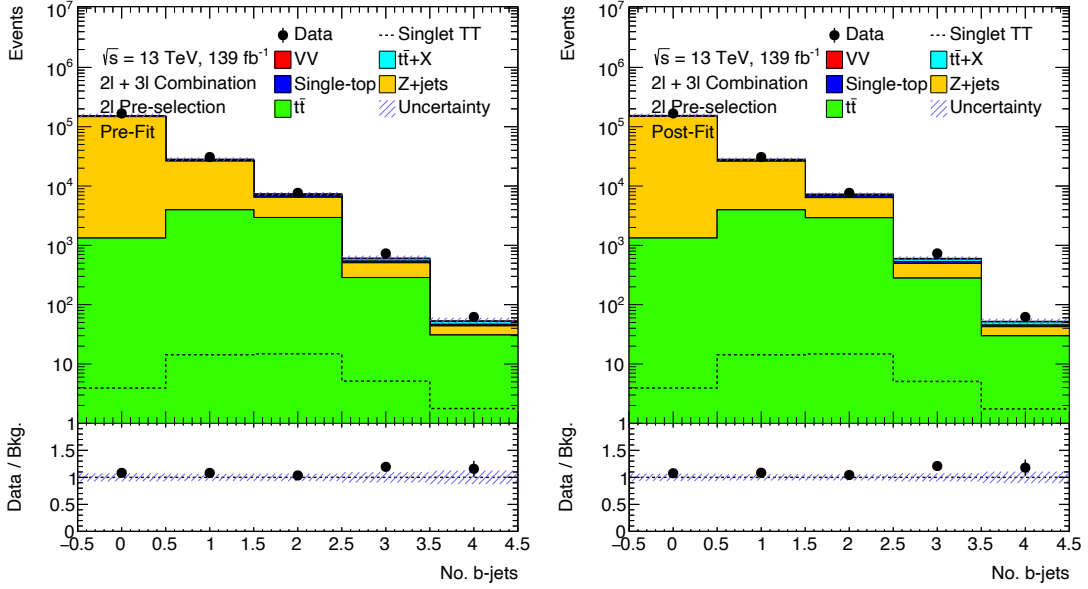
Figure 5.8: Distributions of the b-jet multiplicity pre and post background only fit at the 2ℓ pre-selection.

The signal represented is VLT, and pre-selection already restricts leptons inside the Z mass window, so one b-tagged jet is expected from that branch of the pair-production, from the top quark of the $T \to Zt$ decay. The other branch can be $T \to Ht$, $T \to Wb$ or $T \to Zt$, all of which should produce at least 1 b-jet, hence the peak at 2 b-tagged jets.

The p_T distribution of the leading lepton after the 2ℓ pre-selection can be seen in fig. 5.10. This variable is well modeled for the whole range up to 1 TeV.

The same distribution after the 3ℓ pre-selection can be seen in fig. 5.11. Data and Monte Carlo agree
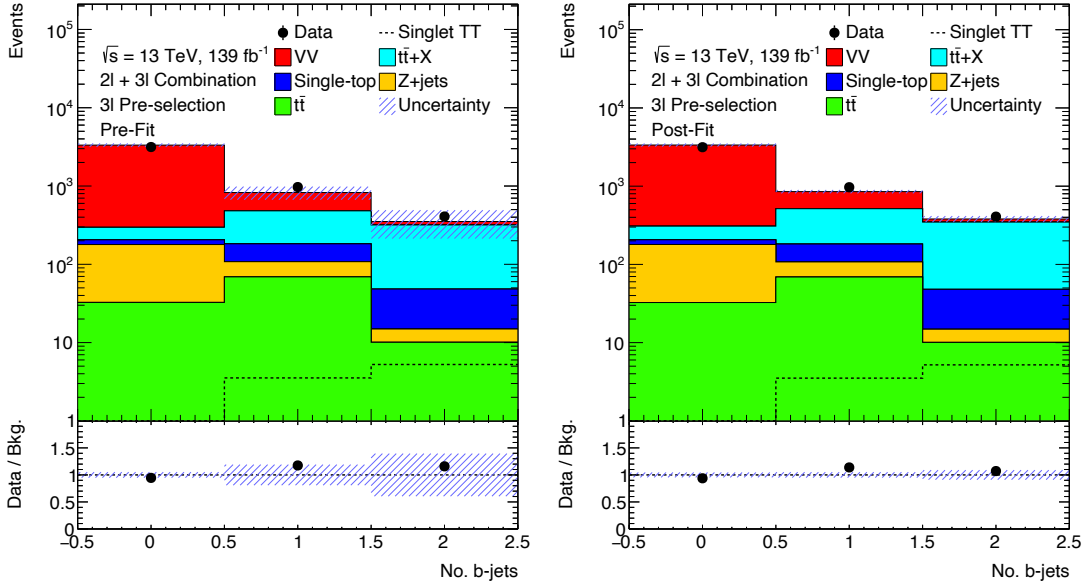
Figure 5.9: Distributions of the b-jet multiplicity pre and post background only fit at the 3ℓ pre-selection.
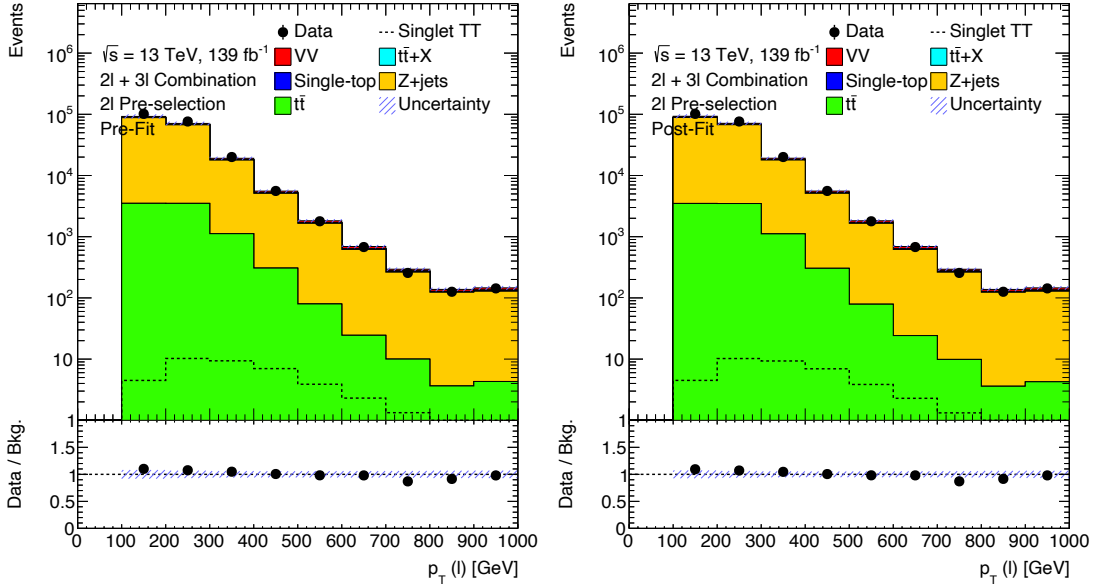

Figure 5.10: Distributions of the p_T of the leading lepton pre and post background only fit at the 2ℓ pre-selection.

well through the whole p_T range. It can be seen that the $t\bar{t}$ distribution falls steeply as the lepton p_T increases, as fake leptons are less likely to occur at higher energies.

The distribution of the leading jet p_T after the 2ℓ pre-selection is well modeled, and shows that signal jets are expected to be have a hard spectrum, as can be seen in fig. 5.12.

A very similar conclusion can be derived from fig. 5.13, for the 3ℓ channel.

The modelling of the leading b-tagged jet p_T can be seen, after the 2ℓ pre-selection, in fig. 5.14. Data
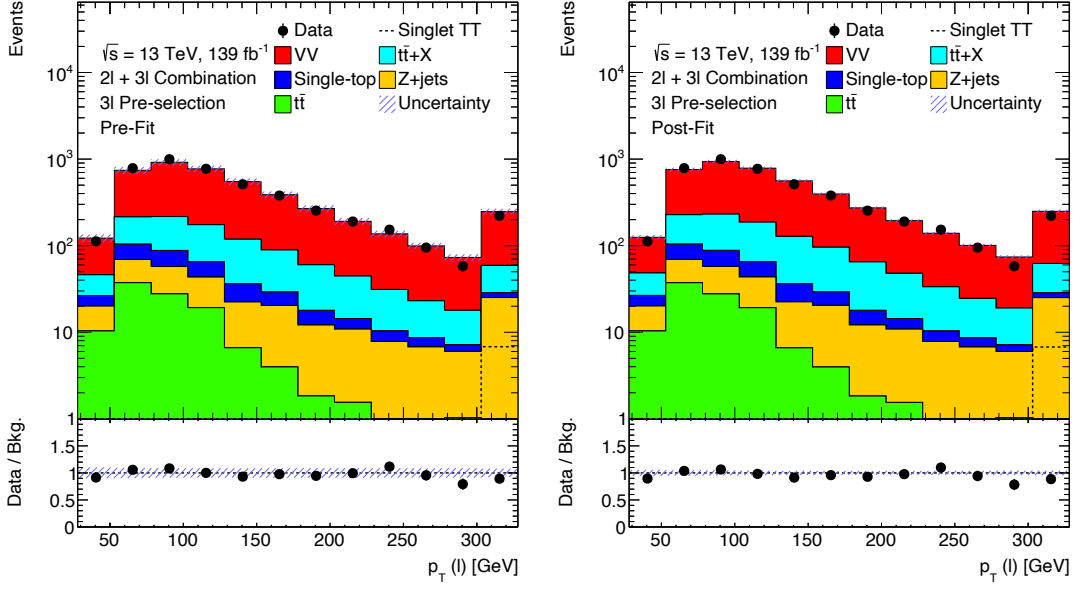
Figure 5.11: Distributions of the p_T of the leading lepton pre and post background only fit at the 3ℓ pre-selection.
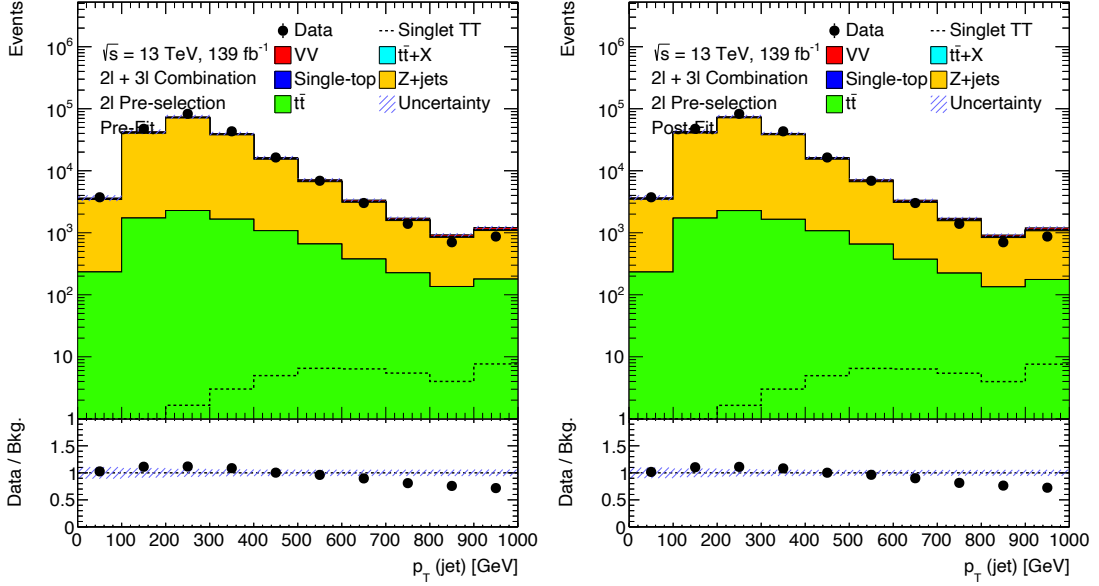
Figure 5.12: Distributions of the p_T of the leading jet pre and post background only fit at the 2ℓ pre-selection.

and MC show a good agreement. The signal distribution seems to be flat through most of the p_T range, as the decay products of a VLQ are expected to be boosted.

The same distribtions after 3ℓ pre-selection can be seen in fig. 5.15, which also shows good agreement between data and MC.

The bulk of the selected signal events, after preselection is applied, is expected to be a pair of VLQs where at least one of them decays to a pair of OSSF leptons consistent with a Z boson decay. It can,
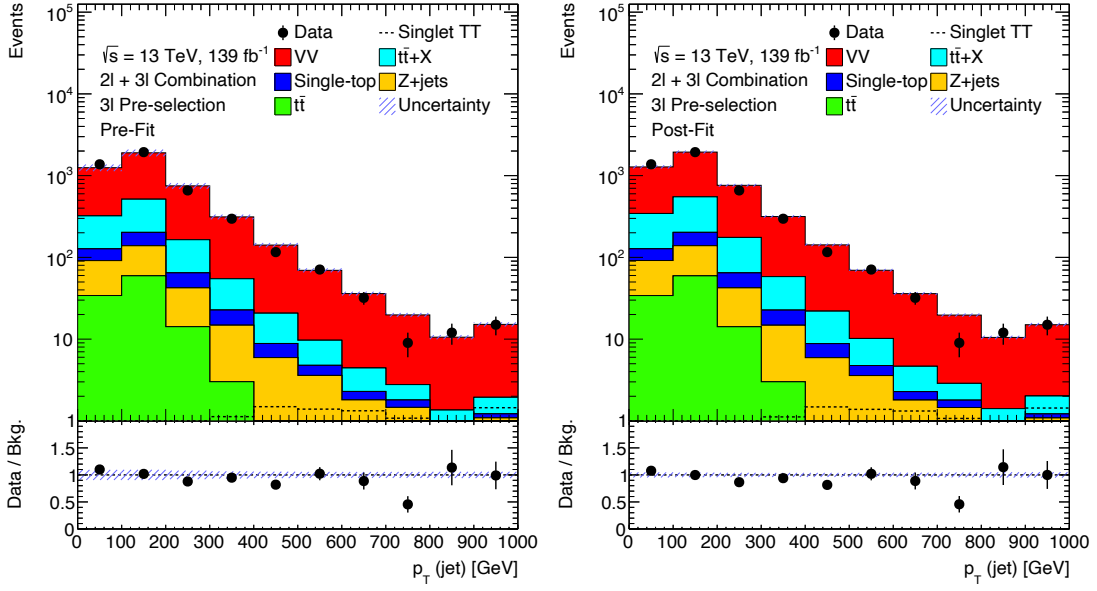
Figure 5.13: Distributions of the p_T of the leading jet pre and post background only fit at the 3ℓ pre-selection.
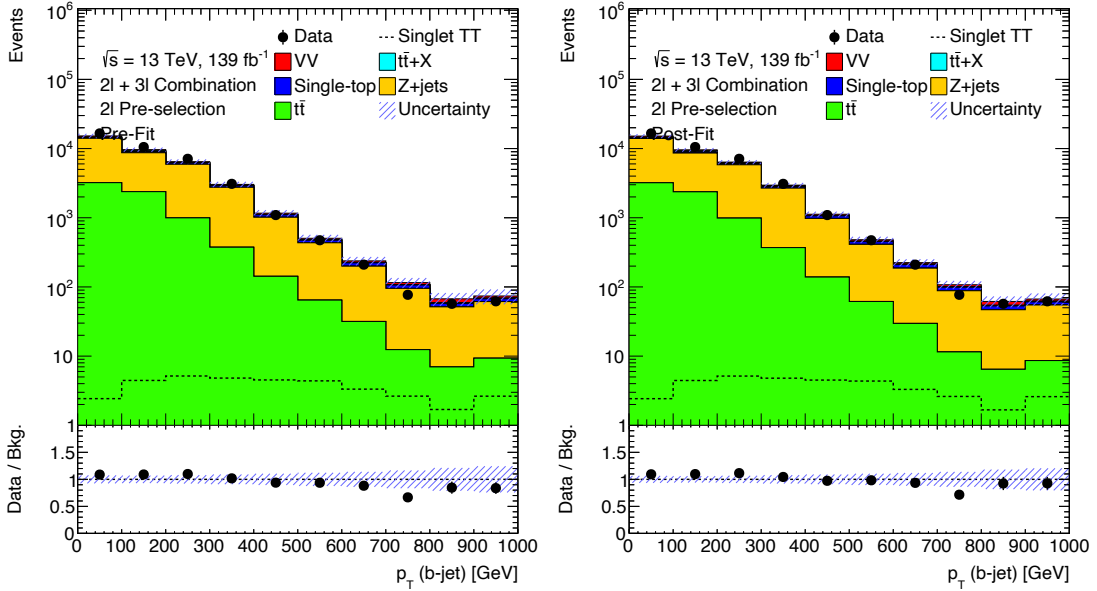
Figure 5.14: Distributions of the p_T of the leading b-jet pre and post background only fit at the 2ℓ pre-selection.

however, be the case that a pair of leptons from two semileptonically decaying top quarks is selected, if by chance their mass is within the selected mass window. In order to mitigate background selection as mentioned, a requirement on the $p_T(\ell\ell)$ is applied. The modelling of the Z boson candidate p_T can be seen in figs. 5.16 and 5.17, where in general it shows a decent data and Monte Carlo agreement.

For the case of the 2ℓ channel, an additional requirement on the $H_T(\text{jet})$ is made. In dilepton events there is also the possibility that the seconds VLQ decays invisibly, i.e. to two neutrinos, so it was found
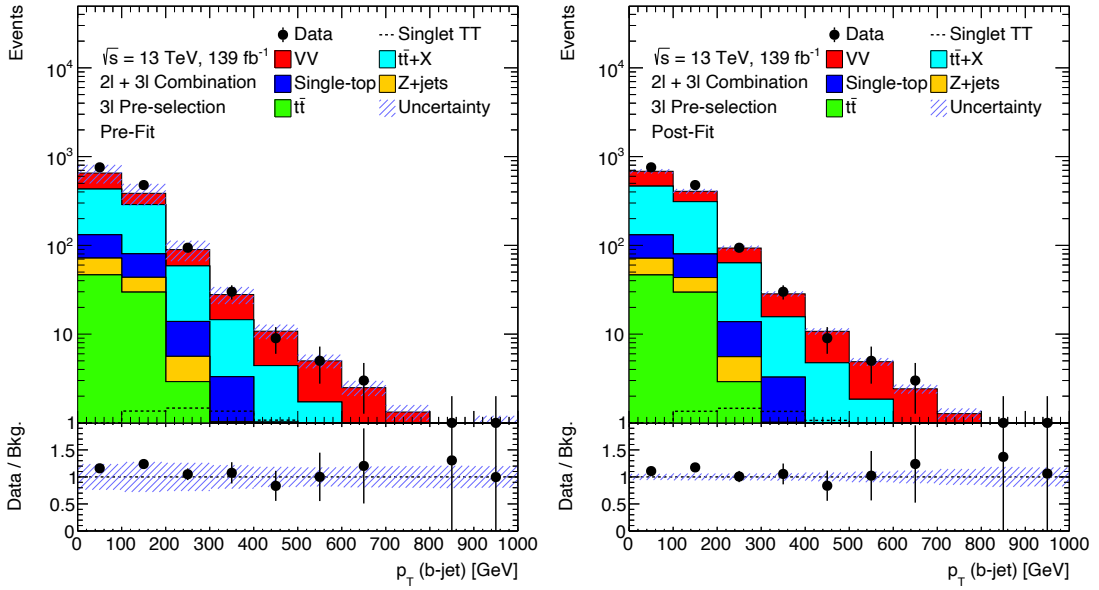
Figure 5.15: Distributions of the p_T of the leading b-jet pre and post background only fit at the 3ℓ pre-selection.

that using the combination of $H_T(\text{jet})$ and E_T^{miss} improves signal discrimination so a cut is applied. This variable suffers from some mismodeling in the 2ℓ regions, as can be seen in fig. 5.18. This is mostly mitigated after the inclusion of two control regions with this variable as the discriminant, split by b-tagged jet multiplicity. The fit is able to use its nuisance parameters to adjust this variable and improve its modelling, as can be seen in the post-fit figure in fig. 5.19. This is shown after the signal region selection, and it can be seen that the agreement is greatly improved. More details about the impact that the fit has on this correction will be given in section 5.6.1.3.

In the 3ℓ channel a cut on $H_T(\text{jet} + \text{lep})$ is applied, in order to benefit from the additional lepton multiplicity and the expected boost for signal events.

The value for all cuts was obtained via a optimization based on the expected mass limits[5] and are summarized in table 5.2. A set of 7 MCBOT categories in the 2ℓ channel were chosen based on a signal optimization procedure, used to split the 2 signal enriched regions. In the 3ℓ channel, 5 MCBOT categories are used: one with exactly no tags, three with at least one of each type and a final category with at least one tag from at least two types of signal tags. The categorization for both channels is summarized in table 5.3.

In order to aid the fit in the correction of the main backgrounds estimation signal-depleted control regions (CR) were created. In the 2ℓ channel these are constructed by inverting the $H_T(\text{jet}) + E_T^{\text{miss}}$ cut, whereas in the 3ℓ a region dedicated to VV is built by requiring exactly 0 b-tagged jets. The 2ℓ channel CRs also assist the fit in correcting the $H_T(\text{jet}) + E_T^{\text{miss}}$, as was discussed previously. For the benchmark model, the signal contribution is expected to be up to 1.2% in the 2ℓ 2b CR and between 0.03% and 0.2%

[5]More details about limits will be given in section 5.5.

61
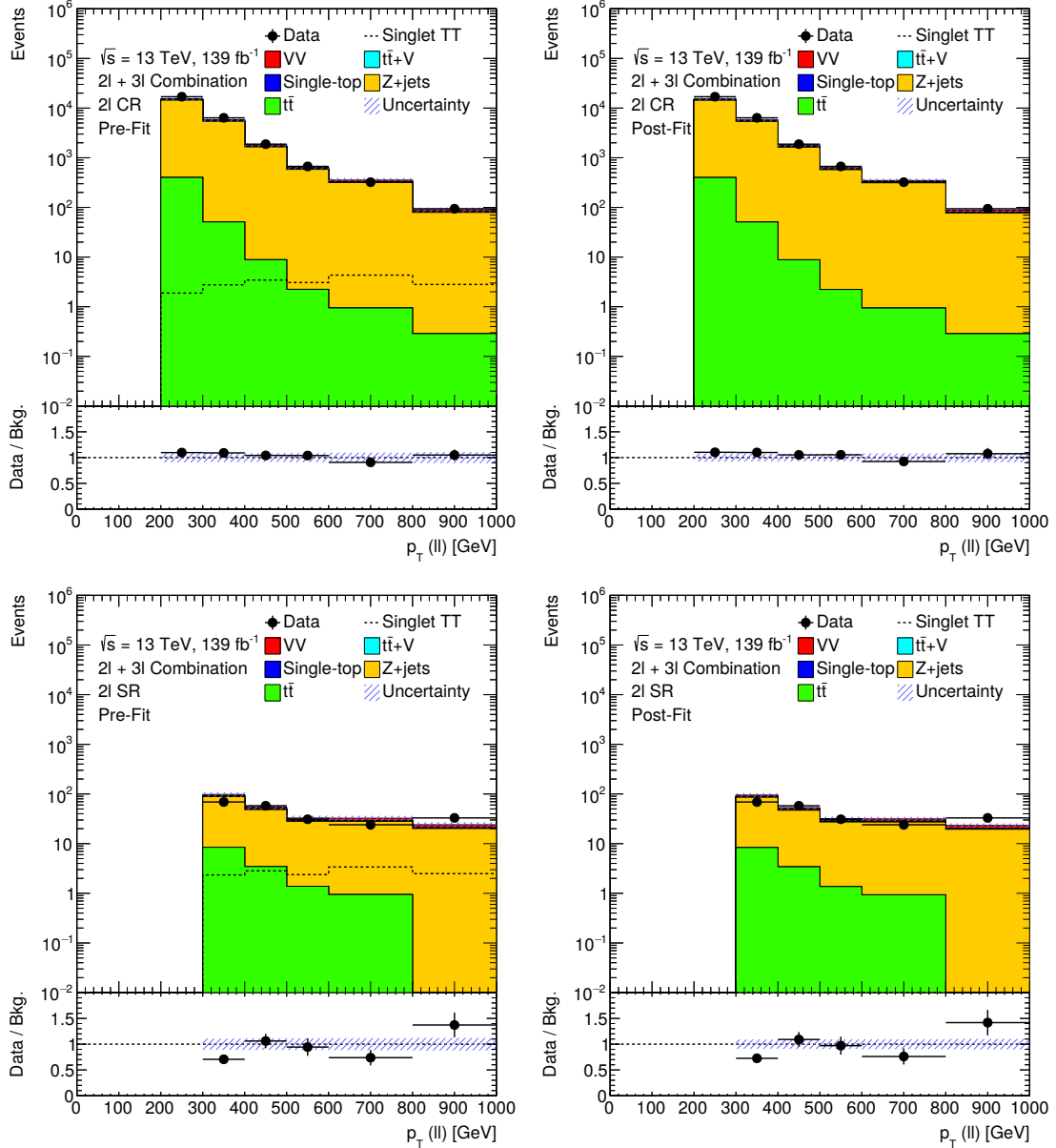
Figure 5.16: Distributions of the p_T of the leptonic Z boson candidate pre and post background only fit with the 2ℓ control and signal region selections.

in the other CRs.

The categorized regions are optimized in order to provide the best discrimination in a fit, and for that a binned final discriminant variable is used. In the 2ℓ channel the invariant mass of the Z candidate and a b-tagged jet is used. This is a useful variable as it possibly reconstructs the VLQ resonance, and a shape effect is expected around its mass value, as can be seen in figs. 5.21 to 5.24. The chosen b-tagged jet is the one with the highest p_T in the regions that require exclusively 1 b-tagged jet and the subleading b-tagged jet in the regions with at least 2. In the 3ℓ channel $H_T(\text{jet} + \text{lep})$ is used as the final discriminant. It uses the harder signal spectrum in order to provide a shape difference, as can be seen in fig. 5.25.
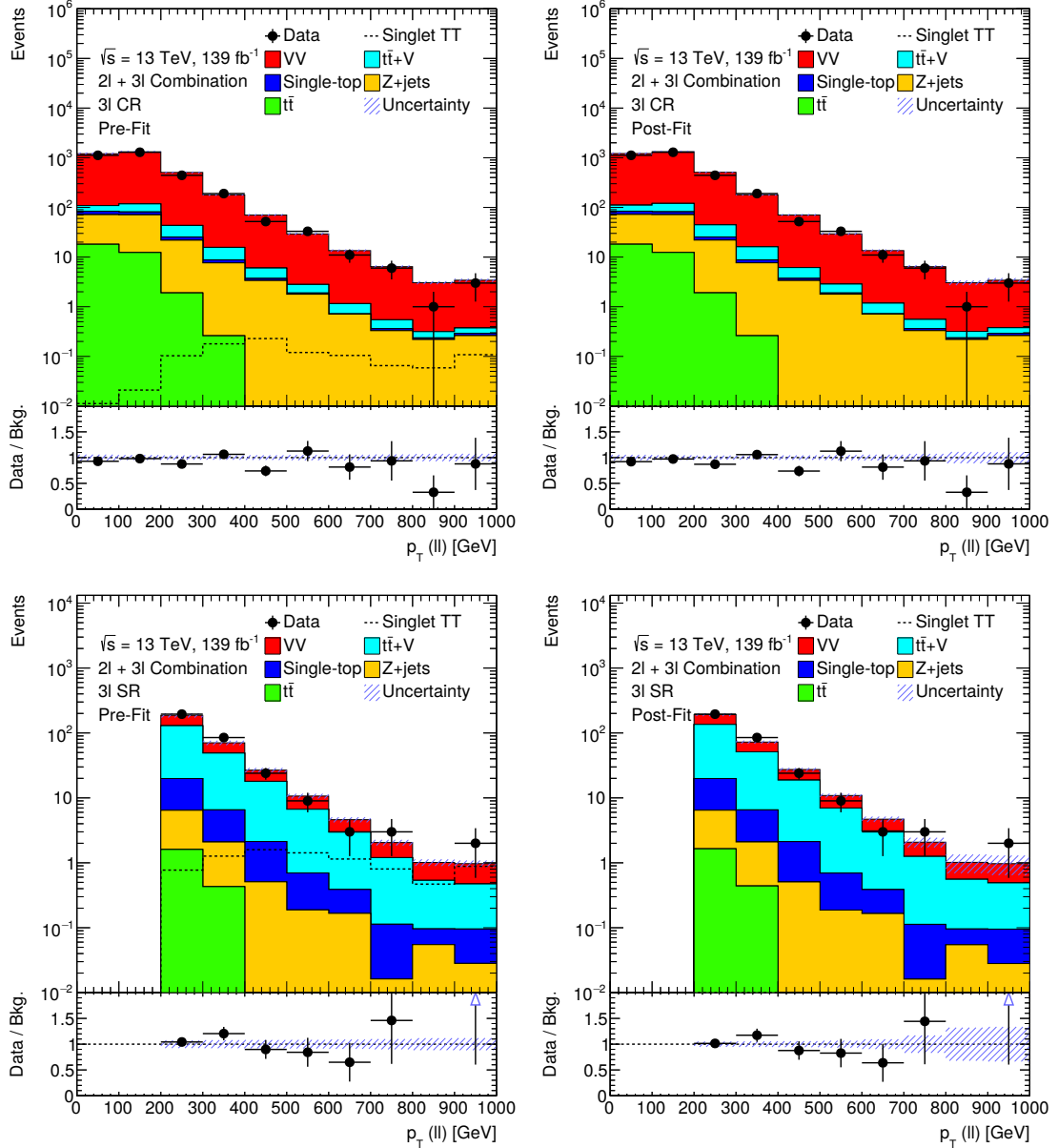
Figure 5.17: Distributions of the p_T of the leptonic Z boson candidate pre and post background only fit with the 3ℓ control and signal region selections.

Figure 5.20 shows the background composition of each region in both channels. It can be seen that it varies significantly across regions, justifying the intention of the categorization. A typical strategy, when building an analysis, in order to have control of the background estimations, is to build dedicated control regions for the major backgrounds of each channel. However, and especially given the high recorded luminosity that is available to analyse, a categorization allows for a richer fit, with multiple regions with different topologies contributing to the constraint of uncertainties and correction of the background estimation by the fit.
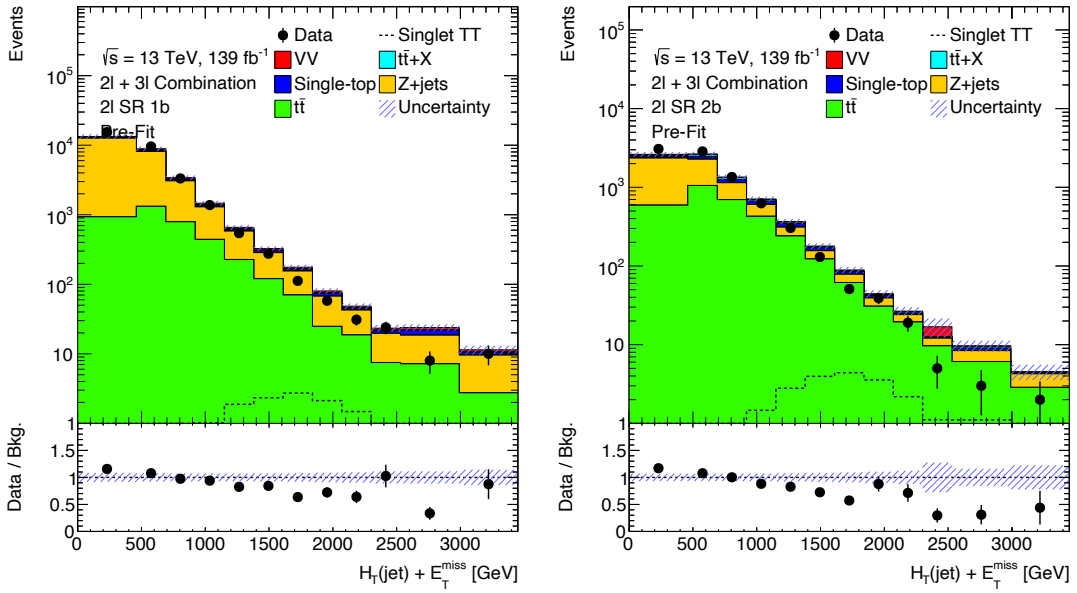
Figure 5.18: Distributions of the $H_T(\text{jet}) + E_T^{\text{miss}}$ before the background only fit at the 2ℓ pre-selection for regions with 1 b-tag and $\geq 2b$-tagged jets.
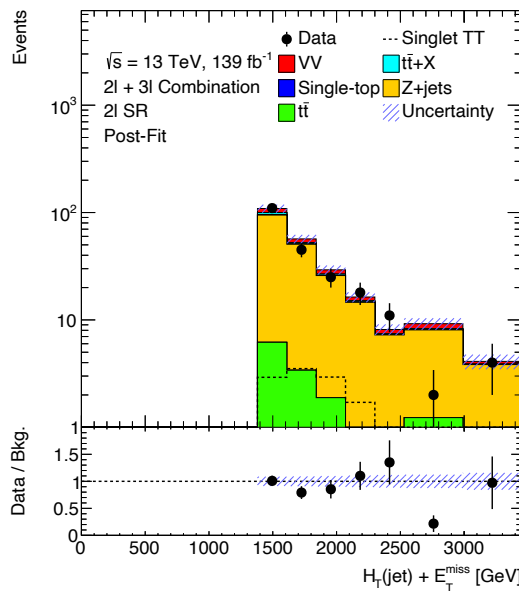
Figure 5.19: Distribution of $H_T(\text{jet}) + E_T^{\text{miss}}$ after the background only fit after the 2ℓ signal region selection inclusive in b-tagged multiplicity.

Preselection	≥ 2 central jets ≥ 2 leptons with $p_T > 28\,\text{GeV}$ $\|m(\ell\ell) - m(Z)\| < 10\,\text{GeV}$					
Channel selection	2ℓ $\equiv 2\ell$ $p_T(\ell\ell) > 300\,\text{GeV}$ $H_T(\text{jet}) + E_T^{\text{miss}} > 920\,\text{GeV}$				3ℓ $\geq 3\ell$ $p_T(\ell\ell) > 200\,\text{GeV}$ $H_T(\text{jet} + \text{lep}) > 300\,\text{GeV}$	
Region selection	1b **SR** $H_T(\text{jet}) + E_T^{\text{miss}} > 1380\,\text{GeV}$ $= 1$ b-jet	2b **SR** ≥ 2 b-jet	1b **CR** $H_T(\text{jet}) + E_T^{\text{miss}} < 1380\,\text{GeV}$ $= 1$ b-jet	2b **CR** ≥ 2 b-jet	**SR** - ≥ 1 b-jet	VV **CR** - $= 0$ b-jet
Discriminant variable	$m(Zb_1)$	$m(Zb_2)$	$H_T(\text{jet}) + E_T^{\text{miss}}$		$H_T(\text{jet} + \text{lep})$	

Table 5.2: Summary of the selection applied in the 2ℓ and 3ℓ channels.

Category	2ℓ channel						3ℓ channel		
	1b **SR**			2b **SR**			–		
	V-tags	H-tags	top-tags	V-tags	H-tags	top-tags	V-tags	H-tags	top-tags
No tag	0	0	0	0	0	0	0	0	0
V tag	1	0	0	1	0	0	≥ 1	0	0
H tag	0	1	0	0	1	0	0	≥ 1	0
top tag	0	0	1	0	0	1	0	0	≥ 1
Double tag 1	2 0 1	0 2 0 –	0 0 1	2 0 1 0	0 2 1 0	0 0 0 2	– – – –		
Double tag 2	0 0	1 0	1 2	0 –	1	1	– –		
Overflow (OF)	1 or > 2 tags – –	1	0	1 or > 2 tags –	0	1	0 ≥ 1 ≥ 1 ≥ 1	≥ 1 0 ≥ 1 ≥ 1	≥ 1 ≥ 1 0 ≥ 1

Table 5.3: Categorization summary for the 2ℓ and 3ℓ channels, based on the number of MCBOT tags.
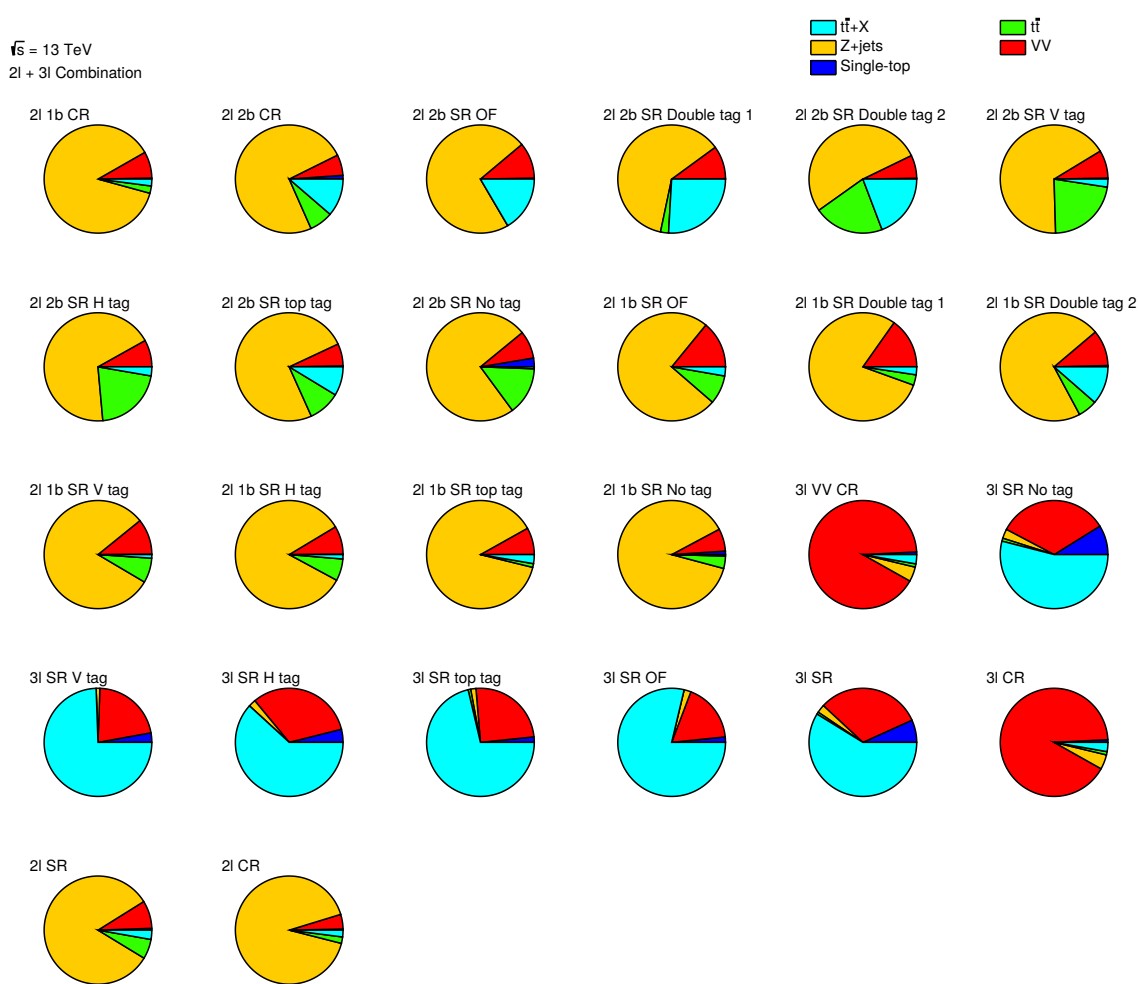
Figure 5.20: Background composition of the different regions.

Category	Data	Total background	VV	$t\bar{t} + X$	Single-top	Z+jets	$t\bar{t}$	Singlet $T\bar{T}$ $m_T = 1.2$ TeV	Singlet $B\bar{B}$ $m_B = 1.2$ TeV
2l 1b CR	610	630 ± 180	50 ± 18	13 ± 4	1.3 ± 0.6	550 ± 180	14 ± 4	1.06 ± 0.08	1.27 ± 0.09
2l 1b SR No tag	72	83 ± 26	5.6 ± 2.1	0.37 ± 0.14	0.8 ± 0.9	73 ± 25	3.1 ± 2.4	0.62 ± 0.13	1.52 ± 0.23
2l 1b SR V tag	18	21 ± 7	2.2 ± 0.9	0.22 ± 0.08	–	17 ± 6	1.5 ± 1.5	0.63 ± 0.07	1.31 ± 0.13
2l 1b SR H tag	34	28 ± 10	2.4 ± 1.0	0.37 ± 0.09	–	24 ± 9	1.8 ± 1.7	0.41 ± 0.05	0.66 ± 0.09
2l 1b SR top tag	32	45 ± 14	3.6 ± 1.4	1.20 ± 0.24	–	39 ± 13	0.5 ± 0.7	1.29 ± 0.14	1.40 ± 0.14
2l 1b SR Double tag 1	7	8.7 ± 2.8	1.3 ± 0.6	0.21 ± 0.10	–	6.9 ± 2.6	0.3 ± 0.4	1.14 ± 0.15	1.05 ± 0.17
2l 1b SR Double tag 2	2	3.6 ± 1.3	0.38 ± 0.21	0.41 ± 0.11	–	2.6 ± 1.2	0.21 ± 0.33	0.27 ± 0.06	0.19 ± 0.06
2l 1b SR OF	9	6.4 ± 2.7	0.9 ± 0.4	0.17 ± 0.05	–	4.8 ± 2.4	0.5 ± 0.8	0.62 ± 0.08	0.60 ± 0.11
2l 2b CR	150	150 ± 40	9 ± 4	17 ± 6	1.2 ± 0.6	110 ± 40	11 ± 4	1.58 ± 0.10	1.90 ± 0.13
2l 2b SR No tag	14	11.2 ± 3.3	0.9 ± 0.4	0.07 ± 0.08	0.2 ± 0.5	8.4 ± 3.1	1.6 ± 1.5	0.27 ± 0.07	1.11 ± 0.17
2l 2b SR V tag	1	2.7 ± 0.9	0.22 ± 0.13	0.06 ± 0.05	–	1.8 ± 0.9	0.6 ± 0.7	0.34 ± 0.04	0.81 ± 0.08
2l 2b SR H tag	10	9.6 ± 2.6	0.77 ± 0.35	0.26 ± 0.09	–	6.5 ± 2.3	2.0 ± 1.6	0.59 ± 0.09	1.90 ± 0.16
2l 2b SR top tag	10	12 ± 4	0.8 ± 0.4	1.07 ± 0.32	–	9 ± 4	1.2 ± 1.2	1.56 ± 0.18	1.97 ± 0.15
2l 2b SR Double tag 1	4	4.4 ± 1.6	0.43 ± 0.28	1.1 ± 0.6	–	2.7 ± 1.2	0.11 ± 0.27	1.71 ± 0.11	1.71 ± 0.18
2l 2b SR Double tag 2	0	3.9 ± 1.3	0.27 ± 0.16	0.75 ± 0.20	–	2.0 ± 1.0	0.8 ± 1.1	1.22 ± 0.10	1.12 ± 0.10
2l 2b SR OF	2	2.6 ± 1.0	0.28 ± 0.16	0.44 ± 0.21	–	1.9 ± 1.0	–	2.76 ± 0.25	2.02 ± 0.26
3l W CR	3149	3300 ± 600	3000 ± 600	92 ± 11	26.6 ± 1.6	150 ± 130	33 ± 15	1.00 ± 0.14	0.90 ± 0.14
3l SR No tag	198	196 ± 22	66 ± 14	106 ± 15	17.3 ± 0.6	5 ± 7	1.8 ± 1.7	1.37 ± 0.17	1.31 ± 0.17
3l SR V tag	20	14.9 ± 2.2	3.2 ± 0.9	11.1 ± 1.9	0.42 ± 0.07	0.17 ± 0.19	–	0.94 ± 0.07	0.71 ± 0.09
3l SR H tag	59	52 ± 6	17 ± 4	32 ± 4	2.04 ± 0.15	1.1 ± 0.5	–	1.44 ± 0.10	0.96 ± 0.08
3l SR top tag	40	36 ± 4	8.9 ± 2.0	25.7 ± 3.5	0.59 ± 0.07	0.6 ± 0.9	0.3 ± 0.9	2.54 ± 0.16	1.73 ± 0.12
3l SR OF	4	4.4 ± 1.2	0.77 ± 0.23	3.5 ± 1.1	0.07 ± 0.04	0.09 ± 0.07	–	2.07 ± 0.16	0.69 ± 0.13

Table 5.4: Table of yields in the control and signal regions, before the background only fit. The uncertainties include statistical and systematic uncertainties.
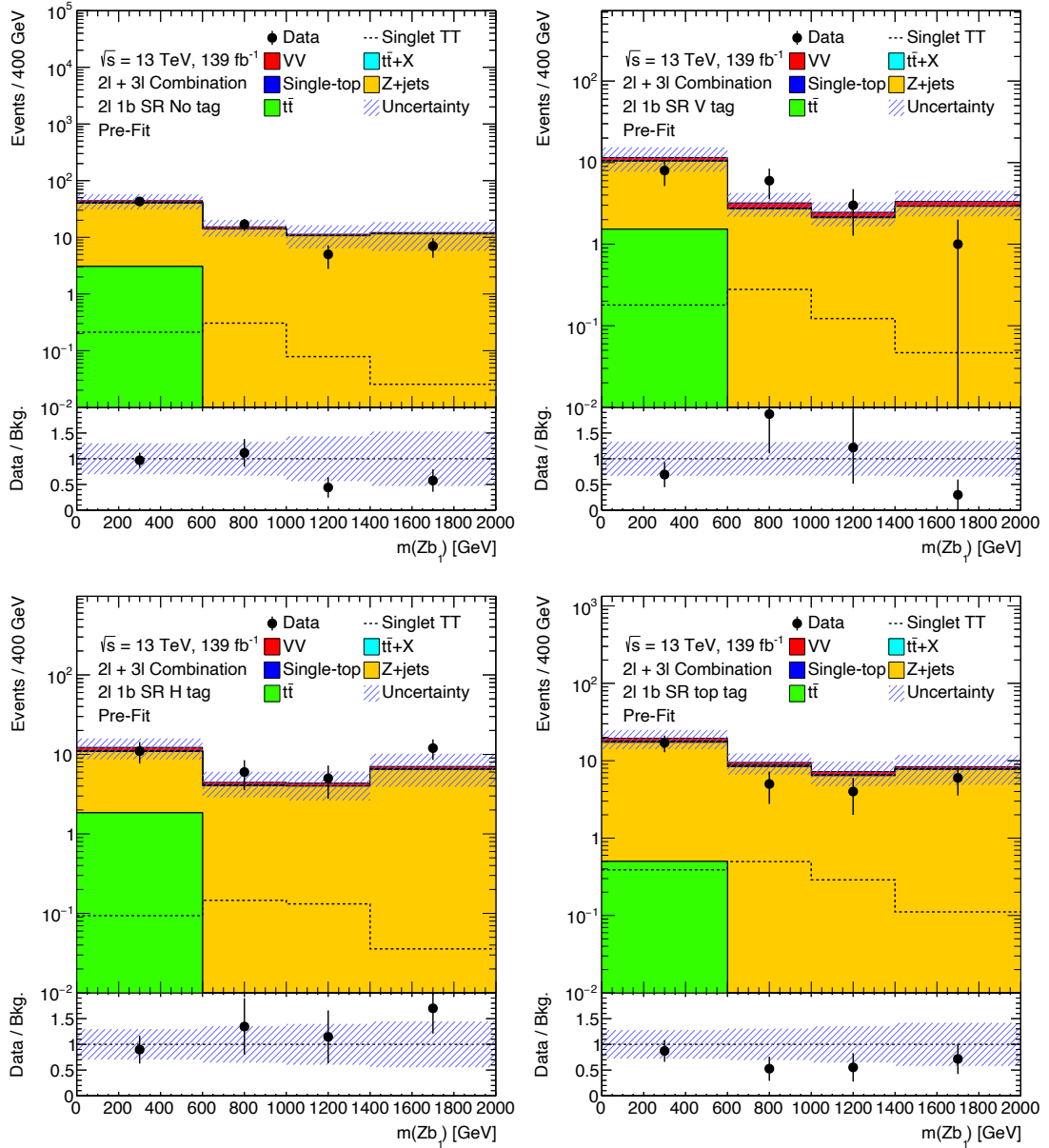
Figure 5.21: Pre-fit plots for 2ℓ regions with exactly 1 b-tagged jet with $m(Zb_1)$ as the discriminant variable.

5.3.1 Signal efficiency

The signal efficiency as a function of VLT mass is shown in fig. 5.26. Efficiency is here defined as the ratio of the number of events that are selected by the signal regions over the number of events generated in the signal sample at 139 fb^{-1}. It can be seen that, in general, it increases with VLT mass, which is to be expected as the signal regions are built to explore the boost VLQs provide. For our benchmark model of 1.2 TeV VLT, the efficiency in the 1b and 2b 2ℓ signal regions is 0.3% and 0.5%, respectively, whereas in the 3ℓ signal regions it is 0.5%.
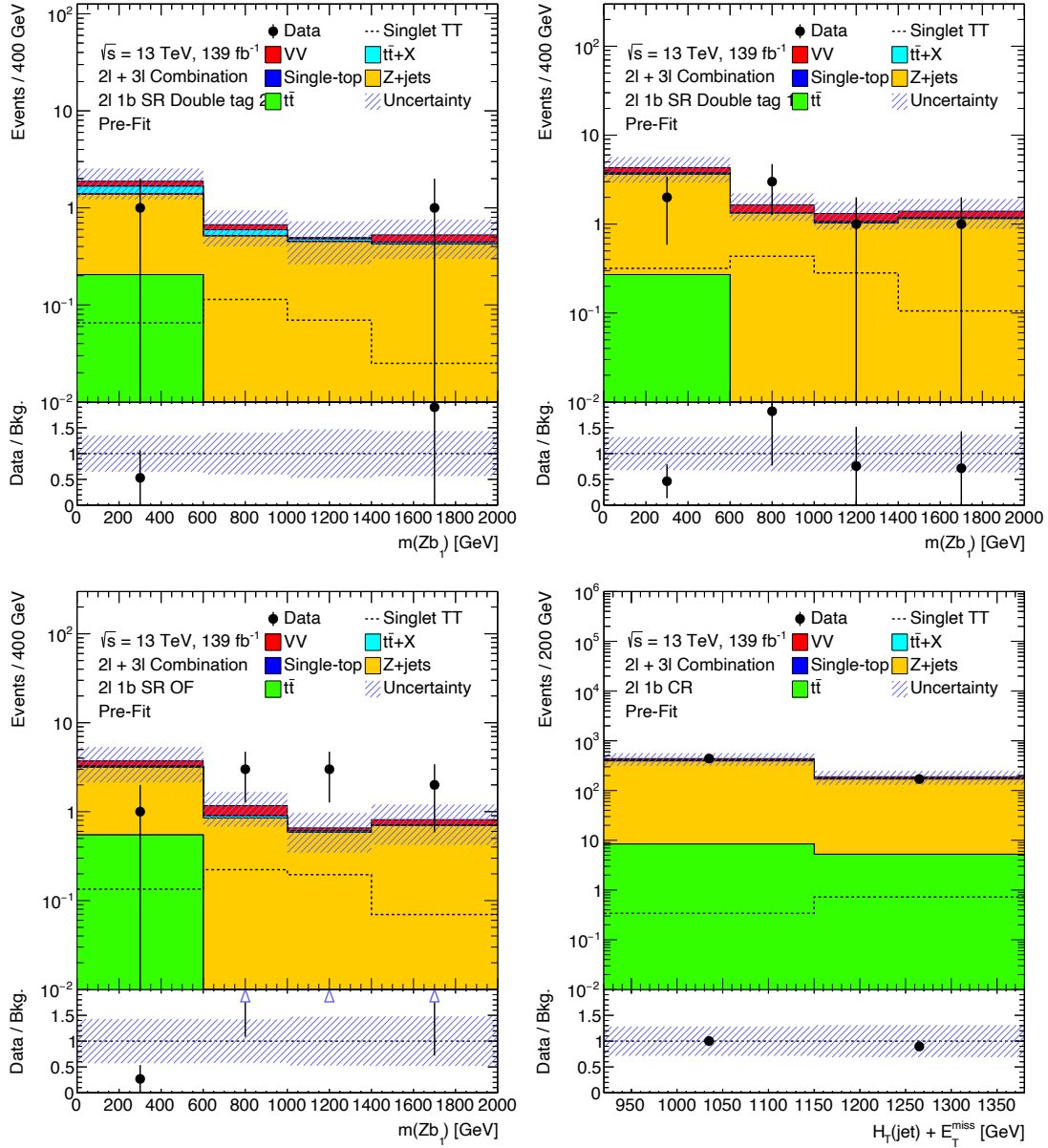
Figure 5.22: Pre-fit plots for 2ℓ regions with exactly 1 b-tagged jet with $m(Zb_1)$ as the discriminant variable, as well as the control region for exactly 1 b-tagged jet with $H_T(\text{jet}) + E_T^{\text{miss}}$ as the discriminant.

5.4 Systematic uncertainties

This analysis relies on detector measurements, which are compared to Monte Carlo simulations. Both of these are inevitably associated with uncertainties that must be taken into account when producing the discriminant variables and making statistical interpretations. Even though the results obtained in this analysis are mostly impacted by limitations in statistics[6], the systematic uncertainties must be well described and their fitting must be understood. Systematic uncertainties can be split into two sources that differ in nature:

---

[6]More details will be given in section 5.5.
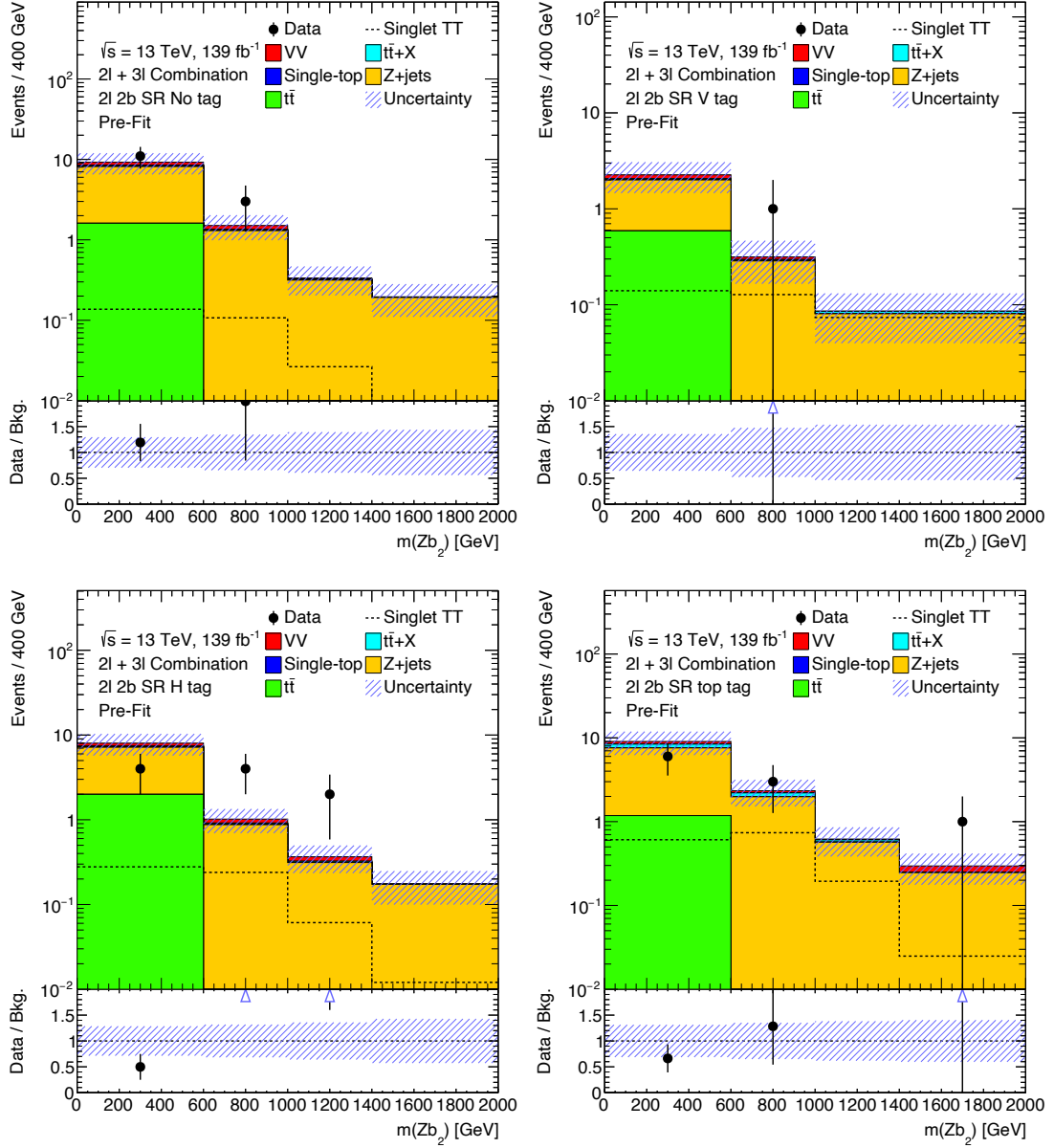
Figure 5.23: Pre-fit plots for 2ℓ regions with at least 2 b-tagged jets with $m(Zb_2)$ as the discriminant variable.

detector and theory systematics. Detector uncertainties are related to the object reconstruction and the limitations of the detector performance. These can be grouped into several categories, described below. Their description is followed by a name within parenthesis, indicating how it is identified in the fit plots.
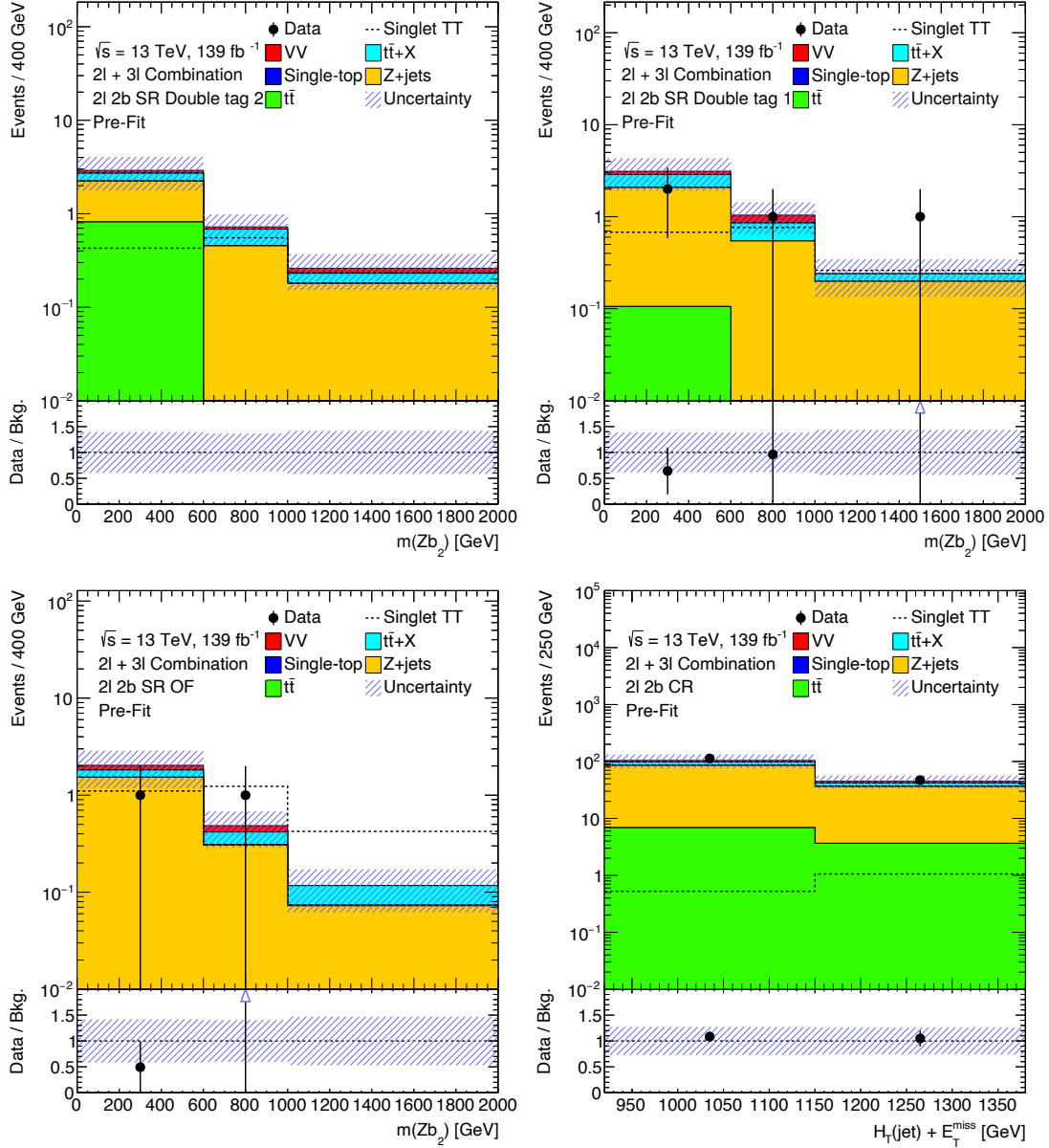
Figure 5.24: Pre-fit plots for 2ℓ regions with at least 2 b-tagged jets with $m(Zb_2)$ as the discriminant variable, as well as the control region for at least 2 b-tagged jets with $H_T(\text{jet}) + E_T^{\text{miss}}$ as the discriminant.

5.4.1 Detector systematics

5.4.1.1 Luminosity

Corresponds to the uncertainty associated with the measurement of the integrated luminosity, with the value of 1.7% [125] for the dataset used in this analysis, collected from 2015 to 2018.
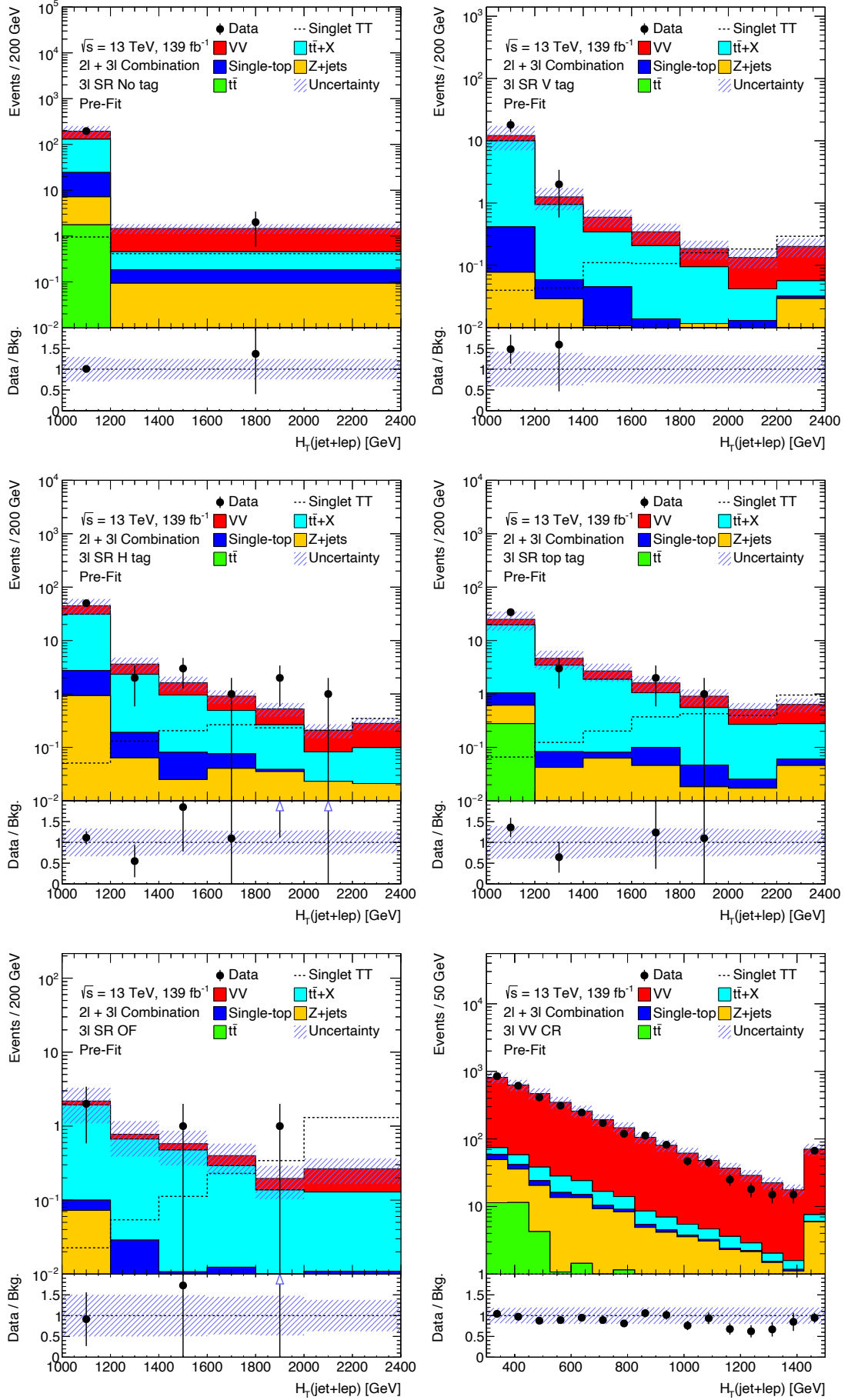
Figure 5.25: Pre-fit plots for all 3ℓ regions with $H_{\mathrm{T}}(\mathrm{jet} + \mathrm{lep})$ as the final discriminant.
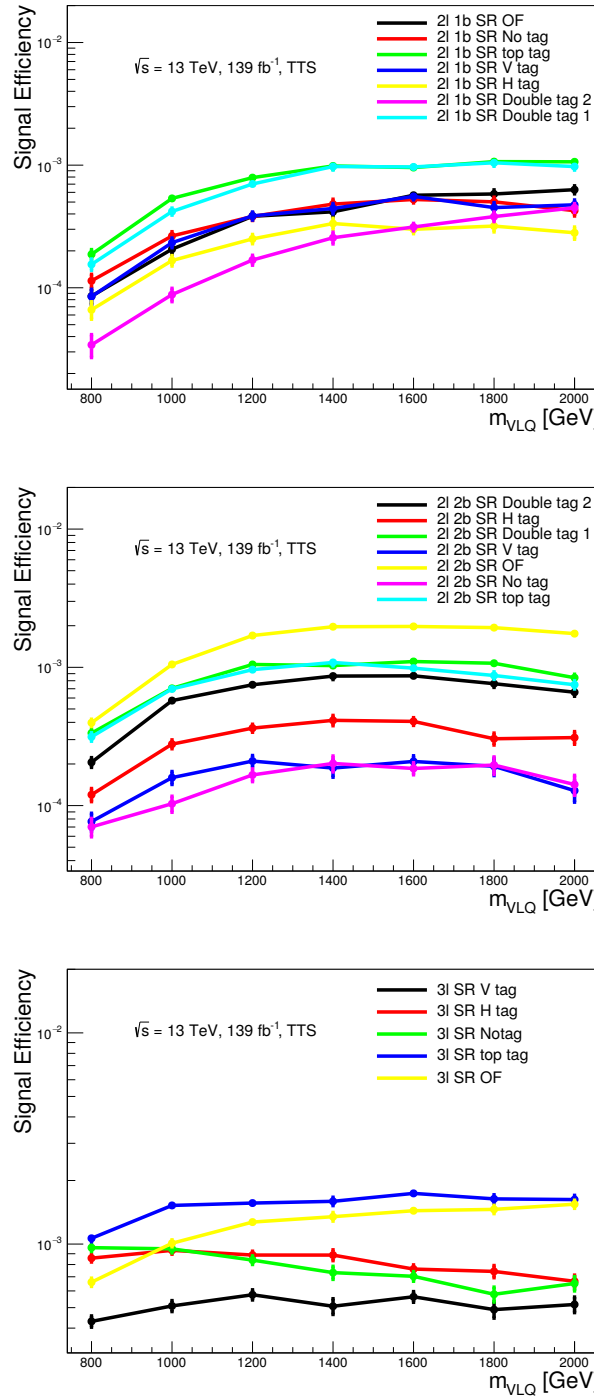
Figure 5.26: Signal efficiency as a function of VLQ mass for the 2ℓ 1b and 2b and 3ℓ signal regions.

5.4.1.2 Electrons

Uncertainties related to the electron energy resolution (EG_Res), their measurement and reconstruction, divided by the factors of trigger (El_trigger), identification (El_ID) and isolation (El_Isol). These are derived from tag-and-probe in $Z \rightarrow ee$ and $W \rightarrow e\nu$ events.

5.4.1.3   Muons

The set of uncertainties related to muons. It includes variations in the p_T smearing related to the inner detector (Mu_ID) and muon spectrometer (Mu_MS), and the p_T scale(Mu_Scale); scale factors related to trigger(Mu_Trigger_Syst and Mu_Trigger_Stat), identification (Mu_ID_Syst and Mu_ID_Stat, not to be confused with the uncertainty related with the inner detector smearing Mu_ID), isolation (Mu_Isol_Syst and Mu_Isol_Stat) and track-to-vertex association efficiencies (Mu_TTVA_Syst and Mu_TTVA_Stat). There are also uncertainties related to the identification at low p_T (Mu_Syst_LowpT, Mu_Stat_LowpT), muons momentum uncertainties related to the Z scale (Mu_rho) and momentum scale based on residual charge bias (Mu_resbias). These are derived from tag-and-probe in $Z \to \mu\mu$ events.

5.4.1.4   Jets

Uncertainties related to the jet energy scale(Jet_BJES), resolution, divided into 7 eigenvectors (Jet_JER_NPx) [117] and jet vertex tagging(JVT). There are also jet uncertainties related to pileup, such as the pileup offset to due the number of primary vertices (Jet_Pileup_OffsetNPV), the jets offset with changes in pileup (Jet_Pileup_OffsetMu), pileup dependence with jets p_T (Jet_Pileup_pT) and with the median p_T density (Jet_Pileup_rho). Other uncertainties related to flavor composition (Jet_Flavor_Comp) and response (Jet_Flavor_Resp) and resolution effects derived from comparing data and MC (Jet_JET_Data_VS_MC). There is also single-particle high-p_T response (Jet_Single_Particle) and uncertainties related to their punch through to MS (Jet_Punch_Through). Uncertainties related to jets pseudo-rapidity are included (Jet_Eta_Syst and Jet_Eta_Stat, Jet_Eta_Mod, Jet_EtaClosure_PosEta, Jet_EtaClosure_NegEta and Jet_Eta-Closure_HighE) The remaining uncertainties are related to in situ parameters, based on their source: 6 statistical eigenvectors (Jet_StatX), 2 detector eigenvectors (Jet_DetX), 4 modelling eigenvectors (Jet_ModX) and 3 mixed eigenvectors (Jet_MixX).

5.4.1.5 b-tagging

Uncertainties related to mistagging of jets are grouped by the jet class: b, c or light jets [126–129]. They are then decomposed into eigenvectors, of which there are 9 related to b (btag_Eigenv_b_x), 4 related to c (btag_Eigen_c_x) and 5 to light jets (btag_Eigen_light_x). The remaining b-tagging systematics are related to the extrapolation of the tagging to high-p_T regimes (btag_Extrapolation and btag_Extrapolation_c)

5.4.1.6   Missing transverse energy

E_T^{miss} uncertainties are related to the soft terms in the E_T^{miss} calculation [130]. They are divided by the term related to the scale (MET_Scale) and resolution, which in itself has a parallel (MET_Res_Para) and perpendicular (MET_Res_Perp) component.

5.4.1.7 Pileup

The instantaneous luminosity and the beam characteristics affect the pileup conditions, which are usually different in data and simulation. In order to correct those differences, an event by event reweighing is applied, to which there is an associated uncertainty (Pileup).

5.4.1.8 Fake leptons

Jets misidentified as leptons cause fake contributions of certain backgrounds in both channels. In the dilepton channel, single lepton $t\bar{t}$ events that are identified as dilepton events are the main contribution of fakes, but subleading sources include W+jets and singletop. In the trilepton channel $t\bar{t}$ and Z+jets contribute to fake events. The requirement in $p_{\mathrm{T}}(\ell\ell)$ and the high energy of the selected objects makes the importance of fakes very small, so no dedicated procedure is necessary. It is, in any case, included a global uncertainty of 25% to $t\bar{t}$ events ($2\ell\ t\bar{t}$ fakes) in the 2ℓ channel and $t\bar{t}$ ($3\ell\ t\bar{t}$ fakes) and Z+jets ($3\ell\ t\bar{t}$ fakes) in the 3ℓ channel.

5.4.1.9 MCBOT

The rcjet tagger uses small-R jet masses, which are not calibrated, so a 10% uncertainty is applied (MCBOT). Up and down factors are applied to the jet masses when doing the tagger inference. If the rcjet only has one constituent a 10% factor is also applied to its mass.

5.4.2 Theory systematics

Theory systematics are related to the uncertainties in the Monte Carlo simulations and in the calculation of the cross-sections. These can also be grouped into several categories, described below.

5.4.2.1 Cross section

Uncertainties related to the inherent errors in the cross section calculation. They are 5% for Z+jets [131] (Z + jets cross section), +5.6 and -6.1% for $t\bar{t}$ [102] ($t\bar{t}$ cross section), 6 % for Dibosons [132] (VV cross section), $\pm 50\%$ for $t\bar{t} + W$ ($t\bar{t} + W$ cross section), +10.4 and -11.9 for $t\bar{t} + Z$ ($t\bar{t} + Z$ cross section) and $t\bar{t} + \ell\ell$ [133] ($t\bar{t}$ + ll cross section).

5.4.2.2 Background modeling systematics

Uncertainty associated with the choice of modeling used to produce the simulations. Samples are produced with a different generator and used for comparison. The Z+jets generator systematic (Z + jets Generator) is derived with MadGraph5_aMC@NLO2.2.3, using the NNPDF3.0 NLO PDF set and Pythia 8 with the A14 tune. The $t\bar{t}$ generator systematic ($t\bar{t}$ Generator) is derived with MadGraph5_aMC@NLO2.2.3, using the

NNPDF3.0 NLO PDF set and Pythia 8 with the A14 tune. $t\bar{t} + X$ generator uncertainties ($t\bar{t}$ + X Generator) were generated with Sherpa 2.2.1.

5.4.2.3   Scale variations

Scale variations are divided into factorization and renormalization scales, each of which have 7 different scales that were changed during generation, from 0.5 to 2, with the nominal being 1, to assess the changes in their variations, by comparing to the nominal distribution. The comparison is made bin-by-bin with all the different variations and the largest difference is taken for each bin, usually referred to as the envelope. There are Z+jets scale variations (Z + jets scale), $t\bar{t}$ scale variations, Dibosons scale variations (VV scale) and $t\bar{t} + X$ scale variations ($t\bar{t}$ + X scale). In the case of $t\bar{t}$ these are divided between the factorization scales ($t\bar{t}$ Fact. scale) and renormalization scales ($t\bar{t}$ Ren. scale). An additional systematic is included for Z+jets in which the α_S factor is also varied (Z + jets α_S).

5.4.2.4   Shower systematics

Samples were generated with different hadron showering algorithms and used for comparison with the nominal samples. A $t\bar{t}$ shower systematic ($t\bar{t}$ Shower) was generated by changing the showering interface to Pythia 8.230 with the A14 tune. $t\bar{t} + X$ shower systematics was generated by interfacing with Pythia 8.210 using the NNPDF23LO PDF set and the A14 tune.

5.4.2.5   PDF variations

The impact of the choice of PDF set is assessed by generating samples with an alternative PDF set and the difference is taken as the systematic uncertainty. They are changed to MMHT2014 NLO [134] and CT14 NLO [135] PDF sets to derive the up and down variations. This effect is tested in $t\bar{t}$ ($t\bar{t}$ PDF), Z+jets (Z + jets PDF) and Dibosons (VV PDF).

5.4.2.6   ISR and FSR variations

The modelling of the initial and final state radiation can have impact on the modeling so samples are generated with different ISR and FSR scales, in a similar procedure to that done for the scale variations. This effect is tested for $t\bar{t}$ ($t\bar{t}$ ISR and $t\bar{t}$ FSR) in the 2ℓ channel.

5.4.2.7   Heavy flavor systematics

In addition to uncertainties related to flavor tagging, uncertainties associated with heavy flavor jets coming from Z+jets and VV events are applied. A 30% uncertainty is applied in the 2ℓ channel (Z + jets HF and VV HF) and a 50% uncertainty is applied in the 3ℓ channel. While in the 2ℓ channel a 30% factor was applied

to the Z+jets systematic, motivated by the cross section measurement of the production of a Z boson in association with b-jets [136], in which a disagreement of about 30% is observed in events with high p_T b-tagged jets, and was propagated to the VV systematic. In the 3ℓ, due to the presence of an extra lepton the situation is not as clear so a 50% factor is applied in order to be conservative, which was validated by studies based on truth information performed by the pair production 3ℓ channel in the previous iteration of the analysis. In order to derive the systematic, the truth information is used and the final discriminant histograms are split by the presence or lack of a heavy flavor jet (i.e. a b, c or τ jet). Then the histograms are added with the heavy component scaled by the uncertainty factor. As the 2ℓ channel splits its regions by b-tag multiplicities, this uncertainty is also split the same way.

5.5 Statistical framework

The analysis tries to select as much signal as possible while still rejecting background, in order to improve its sensitivity, but that must be quantified in order to derive a result, either a discovery or an exclusion limit. For this we use statistical methods that focus on hypothesis testing. We start with the formulation of a null hypothesis, H_0, often referred to as the background hypothesis. It is the scenario we are trying to reject, in the case of this analysis the SM only scenario. Then we build the alternative, or signal hypothesis, H_1. This is the scenario that is being sought out, in the case of this analysis, the hypothesis of the SM in addition to the presence of VLQs.

After the hypotheses are set, a test statistic, $q(x)$ needs to be defined. This is the metric to which there is the quantification of the agreement of data with either hypothesis, taking as a parameter the analysis' measurements, x. From the test statistic, the observed value of $q(x)$ will allow to set a decision on the agreement of a given hypothesis, set by a pre-determined threshold value on the test statistic.

We can define a multiplicative factor that allows the two hypotheses to be generalized. In this context it is called signal strength, μ, and acts as a multiplicative factor on the signal cross-section. So H_0 is set at $\mu = 0$ and H_1 at $\mu = 1$. With the definition of μ we can define the test statistic from this value, labeled here as q_μ.

With the definition of the test statistics and the collected measurements, a probability that the observed data originates from the considered hypothesis can be obtained. It is called the p-value, and is defined as:

$$p_\mu = \int_{q_{\mu,obs}}^{\infty} f(q_\mu|\mu)dq_\mu \tag{5.2}$$

With $q_{\mu,obs}$ being the observed value of the test statistic, and $f(q_\mu|\mu)$ being the probability density function of the test statistic under a given hypothesis μ. It is common to convert this probability value to a Gaussian significance, Z. This allows the probability to be quoted as a certain number of standard deviations.

We need to define thresholds for accepting or rejecting a given hypothesis. The exclusion threshold adopted in the ATLAS collaboration is at $p_\mu = 0.05$ (corresponding to $Z = 1.64$), which corresponds to a confidence level of 95%. The discovery threshold that is usually adopted by particle physics experiments in order to claim a discovery is $p_0 = 2.9 \times 10^{-7}$ (corresponding to 5σ).

By the construction we set in our exclusion procedure, that is given by the measured p_μ, the threshold for exclusion can be surpassed due to statistical fluctuations, that could set a premature exclusion of a given hypothesis given a particular downward fluctuation. In order to avoid such unphysical exclusions a new metric was constructed. It is still built around the measured probabilities but it tries to reduce its sensitivity to downward fluctuations. It is called the CL_S method [137] and is given by:

$$CL_S = \frac{p_\mu}{1 - p_0} \qquad (5.3)$$

With this fraction, if there is a downward fluctuation it will result in a larger value of p_0, which will result in a larger value of CL_S, thus avoiding the exclusion. This is the standard used in the LHC experiments when it comes to claim exclusions. For the discovery procedure, p_0 is still the used quantity.

In our search, in the case that the null hypothesis cannot be rejected we will want to set upper limits on the VLQ masses. This is done using the CL_S method, using the 95% CL, given by $CL_S < 0.05$.

The test statistic that will be used in our search is the profile likelihood ratio. It relies on the fact that the number of observed data in each bin obeys a Poisson statistic, so the likelihood is built as a product of Poisson probability terms:

$$L_0(\mu_{sig}, \mu_{bkg}, \theta) = \prod_{r \in regions} \frac{[N_r^{exp}(\mu_{sig}, \mu_{bkg}, \theta)]^{N_r^{obs}}}{N_r^{obs}!} \cdot \exp[N_r^{exp}(\mu_{sig}, \mu_{bkg}, \theta)] \qquad (5.4)$$

where θ is the set of nuisance parameters, defined by the systematic uncertainties of the analysis, μ_{bkg} are normalization factors associated with the backgrounds, and μ_{sig} is the signal strength. N_r^{exp} and N_r^{obs} are the expected and observed number of events in a given bin in region r, respectively.

The systematic uncertainties are parametrized with their central value set at $\theta = 0$, and shifting around this value. It is common for their $\pm 1\sigma$ values to be known, and interpolation and extrapolation to be done so that there is a smooth variation around these values. These values are used as constraint terms in the likelihood, in which they are usually implemented as Gaussians:

$$L(\mu_{sig}, \mu_{bkg}, \theta) = L_0(\mu_{sig}, \mu_{bkg}, \theta) \prod \frac{1}{2\pi} \exp(\frac{-\theta_i^2}{2}) \qquad (5.5)$$

The fitting procedure will try to estimate the parameters μ_{sig}, μ_{bkg} and θ by maximizing the likelihood given by eq. (5.5), in order to best describe the observed data.

At the end we arrive at the profile likelihood ratio by using the definition given on eq. (5.5):

$$\lambda(\mu_{sig}) = \frac{L(\mu_{sig}, \hat{\hat{\mu}}_{bkg}, \theta)}{L(\hat{\mu}_{sig}, \hat{\mu}_{bkg}, \theta)} \tag{5.6}$$

The numerator represents the Maximum Likelihood Estimator (MLE) of the μ_{bkg} and θ parameters for a given signal strength μ_{sig}. This is normalized by the likelihood using the MLE values of the μ_{sig}, μ_{bkg} and θ parameters.

While eq. (5.6) is the test statistic where we arrive when defining the search for the parameters that best fit the observed data, it is not what this analysis is actually using in the final estimation. For computational reasons it is better to minimize the log of the profile likelihood ratio, so the final test statistic used is given by:

$$q_{\mu_{sig}} = -2 \ln \lambda(\mu_{sig}) \tag{5.7}$$

5.6 Results

5.6.1 Fitting

The values of the systematic uncertainties are profiled, by pulling their central value and constraining their $1\,\sigma$ value. This allows for a more accurate description of the uncertainties, in the phase space that is being studied, which does not necessarily coincide with the phase space in which they were derived. This, therefore, should result in a set of more realistic systematic uncertainties, adjusted in a data driven way.

The search for the best parameters to describe the observed data is usually obtained by sampling the prediction within the systematic uncertainties, usually referred to as pseudo-experiments. This usually requires large samples, that are computationally expensive to obtain. However, if there are enough predicted events in each fitted bin, the toy experiment procedure approximates a chi-squared distribution, which removes the need for sampling. This is known as the asymptotic approximation [138] and it is used in this analysis. This approximation was tested in the analysis development to confirm its validity, as will be shown later in this section.

Given that there are over a 100 nuisance parameters to be fitted, and that not all of them will be relevant to the analysis, systematics with with normalization or shape differences smaller than 1% of the nominal distribution are pruned, i.e. disregarded from the fit. Figures 5.27 and 5.28 show the list of systematic uncertainties that are pruned from the fit. This value was chosen because it is the standard in VLQ searches. Analysis that are more sensitive to systematic effects usually study variations of this threshold, but as will be seen later in this text that is not the case of this search. The shape effects for the up and down variations (meaning the $\pm 1\sigma$) are symmetrized before the fit and a smoothing procedure is applied, in which noise bins are averaged with their neighbor bins.
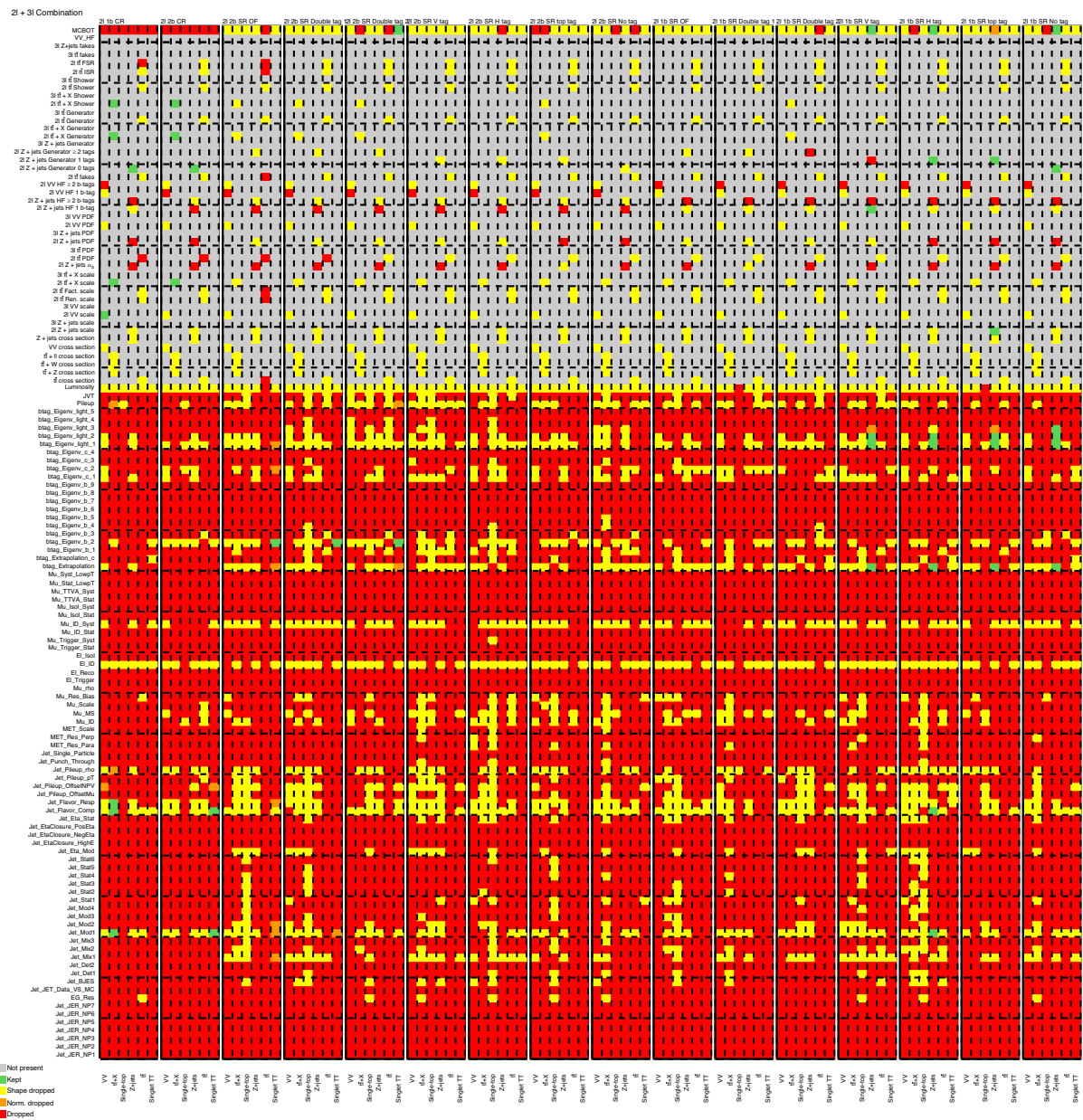
Figure 5.27: List of pruned systematics in the 2ℓ regions.

Most of the systematic uncertainties are common between the two channels, but not all of them should be correlated. It is particularly the case of modelling uncertainties, that are very specific to the kinematic region in which they are derived and therefore to be correlated across channels could possibly lead to undesired effects. To that end, all the theory systematics are decorrelated across channels, and will be identified with a 2l or 3l in the prefix. Different correlation schemes were tested, by grouping categories of systematics to decorrelate across channels: PDF variations, scale variations, generator systematics and shower systematics. Given that the changes to the fit were very small, the most conservative option was taken, i.e. to remove these correlations. The pull plots for the different correlation schemes can be seen in appendix C.

In the following discussion, when the background hypothesis is considered, the fit will be referred to as background only fit. In the case the signal hypothesis is considered it will be called signal plus background fit. For all shown figures, unless otherwise stated, the represented signal sample is the singlet VLT with a mass of 1.2 TeV.

Figures 5.29 to 5.34 show the discriminants after the background only fit. In general the data and Monte Carlo is fair, mostly within statistical uncertainties, besides a few bins with low background expectation where no data events are observed. The overall normalization agreement can be assessed in fig. 5.35, in which it can be seen that, besides a 2ℓ region that does not have data events, all regions have a good agreement. In all these post-fit figures the represented signal is taken for the pre-fit distributions, as in a background-only fit no signal contribution is expected after the fit. In the discriminant figures it can be seen that some background normalizations have changed, and so have the uncertainties.

5.6.1.1 Fit with Asimov data

In order to assess the stability of the fit the Asimov dataset [138] is used, i.e. pseudo-data that statistically compatible with the background expectation. This mimics a scenario where Monte Carlo models data to perfection, so no pulls are expected and therefore it works as a validation test. The effects of the background-only and signal plus background fits in the nuisance parameters can be seen in fig. 5.36. These show how each systematic entering the fit is pulled and constrained. The green and yellow bands represent the 1 and 2 σ values of the systematic before the fit. The markers show how each systematic is pulled by the fit, while the error band shows its constraints. No visible differences between the background only fit and the signal plus background fit can be found, which should be expected, given the use of the Asimov dataset. It can be seen that no pull is observed, which is the desired behavior. There are, however, a few constrained systematics. All of these are related to systematic uncertainties with large pre-fit values, and it will be seen that the same is observed in the fit with data. Another common feature of all the constrained systematics is that they are modelling uncertainties, which will be seen that are the systematics with the most impact on the results.

The correlations between systematic uncertainties can be seen in fig. 5.37. Only systematics with correlations higher than 20% are shown. They will be discussed in more detail in section 5.6.1.3, but their comparison can lead to important conclusions.

5.6.1.2 Fit with Asimov data and injected signal

Before performing the fit with data, another interesting test is to perform a fit with the Asimov dataset, but with signal injection. This means that the pseudo-data will be equal to the background plus signal expectation, and so, in a signal plus background fit, when deriving limits, should yield a signal strength corresponding to the value excluded by the Asimov dataset fit plus the injected value, which is of 1 in this

test, i.e. signal with the pre-fit normalization. The resulting pull plot for this test can be seen in fig. 5.38, where no deviations from the previous pull plot are visible. The signal strength obtained, without signal injection, is $0.66^{+0.30}_{-0.18}$, while it increases up to 1.79 when signal is injected. This corresponds within the range of what is expected, fulfilling the goal of the test.

5.6.1.3   Fit with data

The effects of the fit with real data on the systematic uncertainties can be better understood in fig. 5.39. While the constraints that are seen were already present in the fit with Asimov data, pulls are now present in the pull plot. The difference comes from the change in the data expectation, that is now not perfectly matching the background expectation, which allows the fit to correct background normalizations and shapes. There are a few NP that stand out and it is important that the fit behavior is understood. In appendix B the shapes of these and some other important (based on their impact on the fit) systematics are shown. In the set of 2ℓ systematics, two $t\bar{t}$ systematics are pulled. These are the fakes and FSR systematics and they are both correcting the slight excess in the $t\bar{t}$ normalization. $t\bar{t}$ is almost exclusively populating the first bin of the discriminant variables, in which a good number of them show some excess in the background expectation before the fit is applied. This is most notably seen in the regions with 1 b-tag, shown in fig. 5.22. The fit is pulling down on these $t\bar{t}$ systematics, reducing the background expectation in these mismodeled bins, therefore achieving a slightly better data and Monte Carlo agreement, as can be seen in the post-fit plots. The systematic corresponding to the 2ℓ Z+jets generator in the regions without MCBOT tags is pulled and constrained. The pull, in combination with the 2ℓ Z+jets HF ≥ 2 b-tags systematic, is fixing some normalization issues and modelling effects of the $H_T(\text{jet}) + E_T^{\text{miss}}$ in the 2ℓ regions that was observed pre-fit and discussed in section 5.3. As per the strategy, by building a control region with this variable as the discriminant, the fit is able to pull these two systematics and mitigate the disagreement, and it can be seen that the agreement is much improved after the fit. As will be seen in the correlations discussion, these two nuisance parameters are anti-correlated, hence the pulls in opposite directions. Both Z+jets HF systematics are constrained, just like the generator systematic. It can be seen in the pre-fit plots that the CRs have a excessive pre-fit estimation of the uncertainties, and with the high Z+jets presence in these the fit decreases their overestimated value.

In the set of 3ℓ systematics, it can be seen that the Z+jets generator systematic is constrained. The pre-fit values for this uncertainty goes from about 50% up to about 200%, so the fit is reducing their large values. The VV scale variations are also constrained, which is due to the large number of VV events in the CR, that allows for a better estimation of the uncertainty value. The CR data has a disagreement with the prediction in the last bins of the distribution, which causes the fit to pull this systematic, along with some corrections to the VV normalization in the other regions. The other systematic that is highly constrained is the $t\bar{t} + W$ cross-section systematic. The pre-fit value is 50%, and given the large number of $t\bar{t} + X$ events the fit is capable of reducing the value of this uncertainty. The large pre-fit uncertainties

are also visible in table 5.4.

Another important fit assessment involves the NP correlations. These can be seen in a matrix, for which only correlations higher than 20% are shown in fig. 5.40. Comparing them with the correlations seen in the fit with Asimov data shows that most of these were already present and had similar values, with the most notable exception of the correlations between the 3ℓ VV scale and the 3ℓ Z+jets fakes systematics, that was before seen with the 3ℓ Z+jets generator systematic. The changes should be explained by pulls in the fit with real data that are not present in the fit with Asimov data. Both the 3ℓ VV scales and the 3ℓ Z+jets fake systematics are pulled by the fit, and in opposite directions. This change should lead to an increase in the anti-correlation value with respect to that in the fit with Asimov data, even though the pull on the Z+jets systematic is rather small. Given that both the 3ℓ VV scales and 3ℓ Z+jets fake systematics act as normalization factors for each respective background in the 3ℓ Dibosons CR, and that these are two leading backgrounds in this region, this anti-correlation should be expected, The shapes of the 3ℓ VV scale systematic and the 3ℓ Z+jets generator systematic in the 3ℓ Dibosons CR increase in opposite directions: the Z+jets systematic decreases steadily, in relative terms to the nominal distribution, going to higher values of $H_{\mathrm{T}}(\mathrm{jet})$, while the VV systematic has the opposite behavior, even though not as dramatically. As they are pulled in opposite directions in the fit this anti-correlation effect should decrease, and the value of their correlation seen in the matrix of the Asimov fit is 24.6%, which is already close to the threshold. The shapes of both systematics in the 3ℓ Dibosons CR can be seen in fig. 5.41. The highest correlation is between the cross-sections of $t\bar{t} + W$ and $t\bar{t} + \ell\ell$, which are expected to be anti-correlated. Some VV systematics also show high correlations. This is the case of the scale variations and its respective heavy flavor systematic, as well as the jet systematic related to flavor composition. The later case can be understood as a large contribution to this background comes from its control region that is defined by the multiplicity of b-tagged jets. The correlation with the heavy flavor systematic is explained in a very similar way. The heavy flavor systematic increases in the presence of heavy flavor jets, which in the case of b-tagged jets takes the event out of the Dibosons CR, so an anti-correlation should be expected. Similar behavior can be seen between the two 2ℓ Z+jets HF uncertainties and between the Z+jets HF uncertainties and one of the b-tagging systematics.

The 10% value used to account for the lack of calibration of the small-R jet masses in the MCBOT inference was decided in consultation with the collaboration experts. The initial choice was an over conservative factor of 100%, in an attempt at being safe and cover any possible effects coming from the small-R jet masses. It was, however, observed that the pre-fit uncertainties were very large, resulting in very large error band in the pre-fit plots and a very large constraint by the fit. This caused the analysis team to revisit this value, and, in contact with the analysis sub group and jet related experts arrived at the 10% value. The effect of this change in the expected mass limits is of the order of 5 GeV, which can be considered very small.

In the 2ℓ channel, the $t\bar{t}$ shower and generator uncertainties were being largely pulled by the fit in

opposite directions, as can be seen in the pull plot of fig. 5.42. This is an unexpected behavior as the $t\bar{t}$ contribution is mainly located in a single bin, as was discussed before, and it was hard to have an explanation for this behavior. When consulting their distributions it was observed that they suffered from large statistical fluctuations, the likely cause of this effect in the fit. Given that this was not caused by a natural feature of the analysis, these uncertainties were changed by a flat systematic, choosing the largest variation as their magnitude. Therefore the $t\bar{t}$ generator and shower uncertainties in the 2ℓ channel are a factor of 50 and 20%, respectively.

As was discussed previously, the Z+jets generator systematic has a pull in the regions without MCBOT tags. In the original design of the systematic uncertainty it was inclusive in MCBOT tag multiplicities, and it was the pull observed that led to the decorrelation. In order to identify the origin of the pull, it was separated by MCBOT tags, as a means of categorizing by topological features. As was seen in the pull plot, the regions without MCBOT tags are almost exclusively driving this fit effect, so the systematic was kept separated. It was also verified that this separation has no effect in the expected mass limits.

In order to assess the impact of each systematic on the final result ranking plots were produced, and are show in fig. 5.43. This is determined by performing four fits fixing each NP to: pre-fit value $\pm$ pre-fit uncertainty and post-fit value $\pm$ post-fit uncertainty. With each value the impact on μ is obtained by comparing with the signal strength obtained in the nominal fit. The systematic that accounts for the uncalibrated small-R jet masses that are used in MCBOT has the most impact on the signal strength. Other important systematics include the modelling of the main backgrounds of each channel and b-tagging systematics, given that all channels have regions defined by multiplicity of b-jets. It is important, however, to note that the results are largely dominated by the statistical uncertainties. The obtained results are only affect by the systematic uncertainties up to 4%. The ratio of expected cross-sections limits with and without the inclusion of systematic uncertainties, as a function of the VLQ mass, can be seen in fig. 5.44. While the effect of systematic uncertainties is small for all the searched masses, it is noticeable that it steadily decreases as the VLQ masses increase. For the benchmark of 1.2 TeV VLT, the difference in expected mass limits with and without systematic uncertainties is about 25 GeV, which is considerably small. For reference, the $1\ \sigma$ band, with all systematic uncertainties, is +80/-60 GeV.

As a test of the analysis strategy, namely the signal region categorization and its contribution to the fit's ability to control backgrounds and improve the background modelling, a background only fit with only the control regions was performed. Signal regions are kept as validation regions, i.e. regions that do not contribute to the fit but to which the fit is applied, in order to appreciate its effect. By assessing the modelling agreement with the data after this control regions only fit one can get an appreciation for the role of signal regions in the nominal fit. The overall normalization of each region after this fit without signal regions can be seen in fig. 5.45. The left plot shows the control regions, which are the ones that enter the fit. It can be seen that the agreement is very good, as should be expected. The right plot shows the agreement in the signal regions, after the fit with the control regions only is applied to them. While the

agreement is mostly decent and the differences between data and MC are within uncertainties, it is slightly worse than what is obtained after the nominal fit, shown in fig. 5.35. The fit also does a worse job reducing uncertainties, and this effect is most visible in the 3ℓ regions.

The behavior of the fit does not change dramatically with respect to the systematic uncertainties. This can be assessed in fig. 5.46 While some small pulls seen in the nominal fit disappear, which is to be expected as all the signal regions are not present, and the control regions had decent modelling before the fit, the main pulls observed before remain, even though in larger magnitude in some cases. This serves as confirmation that the normalization effects that they should be correcting come from the control regions, as was discussed before. It is also noticeable that a lot of fit constraints also disappear. This should be further verification of the usefulness of the signal regions in the background modelling.

All the discriminant variables after a fit with no signal regions can be seen in appendix E, along with a yields table with the total background values shown for this fit and the nominal fit side by side.

The yields for each sample and region are summarized in table 5.7.

5.6.2 Limits

Once the fit is understood we set for a discovery but no significant deviations from the SM expectation were found. For the benchmark model of 1.2 TeV singlet VLT, the observed p-value is 0.52, corresponding to a significance of -0.057σ, which indicates compatibility with the background hypothesis. Given the absence of a discovery we derive upper mass limits. The expected and observed limits on the cross-section as a function of VLQ mass are shown in fig. 5.47, and the limit values are summarized in table 5.5. The expected limits represent the fit value for the expectation of perfect agreement of data with the background expectation, and are a good benchmark on the analysis sensitivity without the inherent randomness of the statistical fluctuations of data that can shift the limit values. The limits are, in general, more stringent for the doublet than singlet scenario, which is expected given that the BR to Z is higher in that case, going from about 25% to about 50%. The 3ℓ channel has better sensitivity for singlet than doublet in the case of VLB because the singlet scenario has more decays into Wt ($\sim 50\%$), which are forbidden in the doublet scenario, and that are likely to decay to a lepton. The presence of more W bosons in the VLT decays also explains the difference in sensitivity between the two VLQs for the 3ℓ channel. It can be seen that the observed and expected limits do not differ by more than 2σ in any of the benchmarks, for all mass points, which supports the compatibility of data with the background only hypothesis. These limits are interpolated linearly between the available mass points. Narrow signals (such as $H \rightarrow \gamma\gamma$, for example) need to account for the shape as a function of its mass when doing the interpolation. VLQ signals, however, are quite broad, so there is no missed signal between mass points, and so a linear interpolation is done.

Beyond the BR that are set by the VLQ isospin, upper mass limits were calculated for a scan of BR combinations, filling the whole plane of decays to SM bosons, shown in fig. 5.48. For illustration purposes

white lines are overlaid in the figure to show the contour of given VLQ masses. These results are interesting to understand where the sensitivity of the analysis lies, and how much of it is lost in different areas of the plane. As expected, most of the sensitivity of this search goes to the Z corner of the BR plane, even though strong results are obtained in the less sensitive set of BRs. This is the case even when there is no BR to Z. In this case there may be decays to a couple of W boson that may result in a lepton pair within the Z mass window. There is, however, the case of the decay to two H bosons, where one of these can still decay to $WW*$. In these BR scans it can be seen that the limits for the case of BR(H) = 1 can go up to 900 GeV. For our benchmark signal, 2.1 events are accepted at this reweighting point, but the number increases to 7.7 for the mass point of 800 GeV. So while the acceptance for this point in the BR plane may be small, the increase in cross-section for the smaller VLQ masses still provides some sensitivity to the analysis.

These results represent an improvement of about 0.2 TeV from those obtained in the previous iteration of this analysis, performed with a partial run-2 dataset, amounting to 36.1 fb^{-1} of integrated luminosity [30]. They are also comparable with the most stringent results to date, namely those from the previous ATLAS wide combination [85] and the CMS all-hadronic search [84], even extending by about 0.09 TeV the limits for the doublet VLT scenario.

The validity of the asymptotic approximation was tested by comparing the results with those obtained with pseudo-experiments for a few mass points. The results are summarized in table 5.6, obtained with 10^5 pseudo-experiments in all cases but the VLT 1.4 TeV case, that showed large fluctuations and was calculated with 5×10^5 pseudo-experiments. It can be seen that the differences are small, in most cases within a 5% difference. The 1.4 TeV mass point shows the largest deviations and the case may be for the number of pseudo-experiments. The factor 5 improvement in the sampling resulted in large differences (towards the asymptotic value) and it may be the case that is driving the differences from the asymptotic approximation. It is, however, impractical to test this explanation as the calculation with 5.10^5 pseudo-experiments already took a few weeks to run.

Model	Observed (Expected) Mass Limits [TeV]		
	2ℓ	3ℓ	Combination
$T\bar{T}$ Singlet	1.14 (1.16)	1.22 (1.21)	1.27 (1.29)
$T\bar{T}$ Doublet	1.34 (1.32)	1.38 (1.37)	1.46 (1.44)
100% $T \to Zt$	1.43 (1.43)	1.54 (1.50)	1.60 (1.57)
$B\bar{B}$ Singlet	1.14 (1.21)	1.11 (1.10)	1.20 (1.25)
$B\bar{B}$ Doublet	1.31 (1.37)	1.07 (1.04)	1.32 (1.38)
100% $B \to Zb$	1.40 (1.47)	1.16 (1.18)	1.42 (1.49)

Table 5.5: Observed (expected) mass limits for the singlet and doublet T and B and with 100% BR to Zt/b for the individual channels and their combination.

	Model [TeV]		Fit	-2σ	-1σ	Median	1σ	2σ	Ratio
2ℓ channel	VLB	1.2	Toys	0.570	0.649	0.841	1.222	3.818	0.99
			Asym.	0.452	0.607	0.842	1.225	1.776	
		1.6	Toys	0	5.370	7.295	9.727	15.514	1.00
			Asym.	3.905	5.242	7.275	10.698	15.805	
	VLT	1.2	Toys	0.717	0.801	1.020	1.345	1.511	1.00
			Asym.	0.546	0.733	1.017	1.480	2.142	
		1.6	Toys	4.489	6.022	8.178	10.056	19.437	1.03
			Asym.	4.256	5.714	7.930	11.657	17.284	
3ℓ channel	VLB	1.2	Toys	0.904	1.143	1.590	1.892	2.450	0.97
			Asym	0.881	1.183	1.641	2.460	3.696	
	VLT	1.2	Toys	0.587	0.745	1.003	1.436	1.757	1.04
			Asym	0.521	0.699	0.970	1.449	2.187	
		1.4	Toys	1.580	1.770	2.103	2.643	306.703	0.80
			Asym.	1.408	1.891	2.624	3.984	6.157	

Table 5.6: Expected limits on the signal strength using the asymptotic formula and pseudo-experiments including systematics, for the singlet VLT and VLB
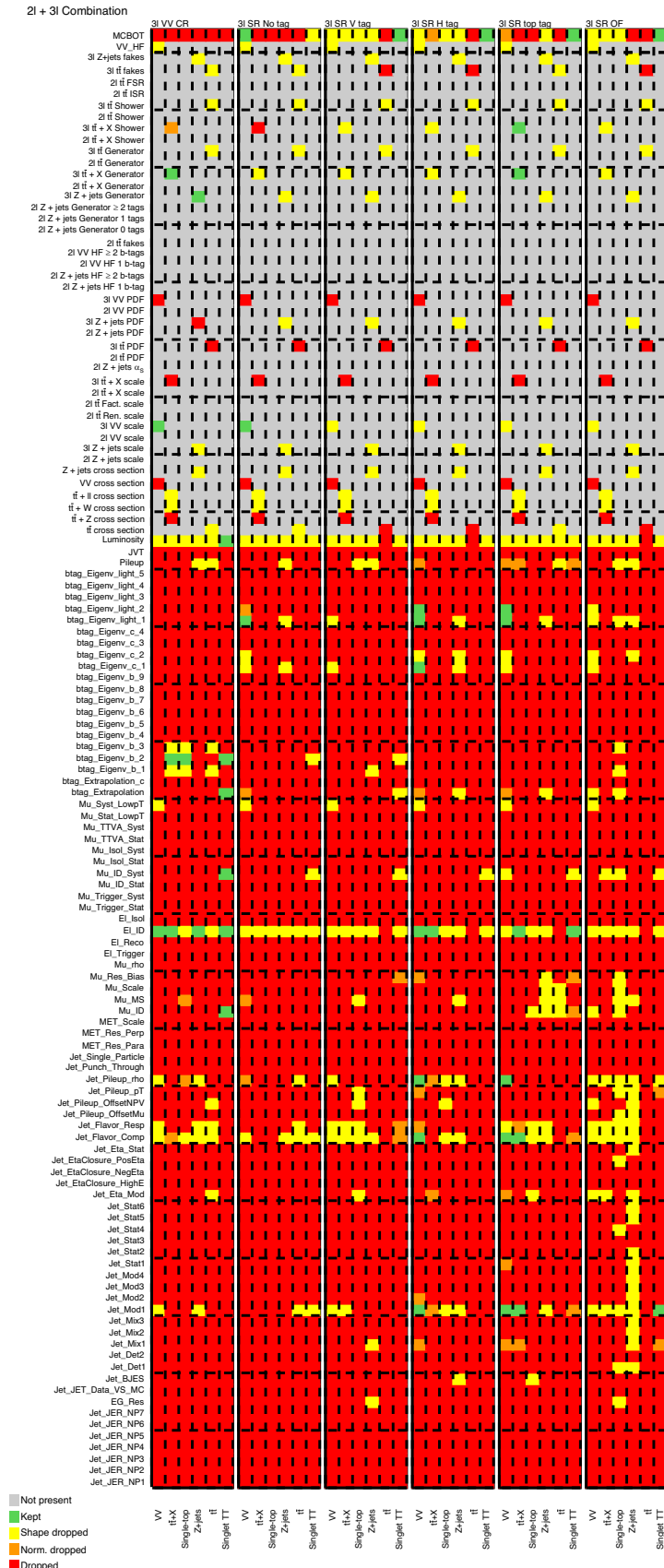
Figure 5.28: List of pruned systematics in the 3ℓ regions.
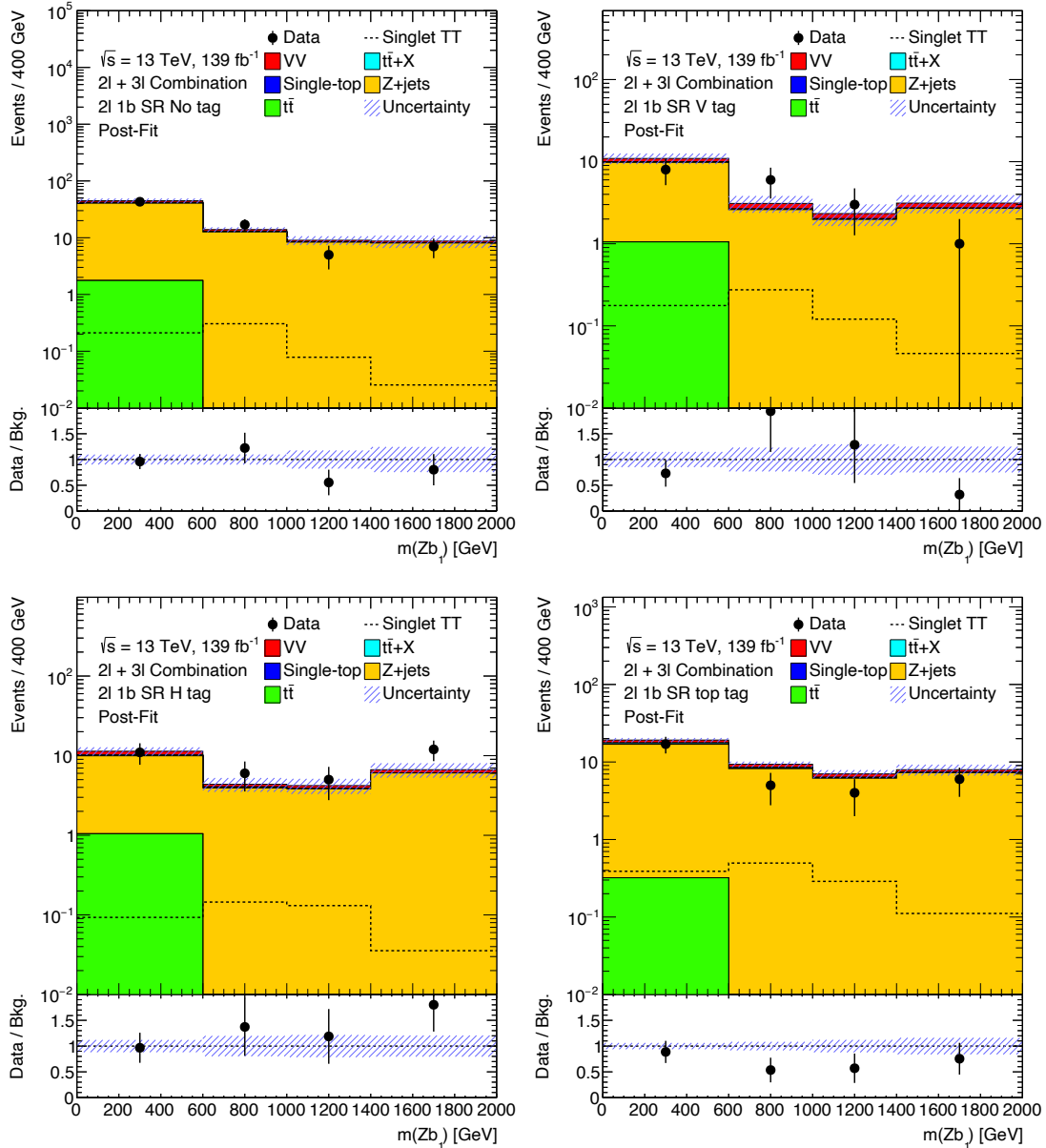
Figure 5.29: Post-fit plots for all 2ℓ regions with exactly 1 b-tagged jet with $m(Zb_1)$ as the discriminant variable.
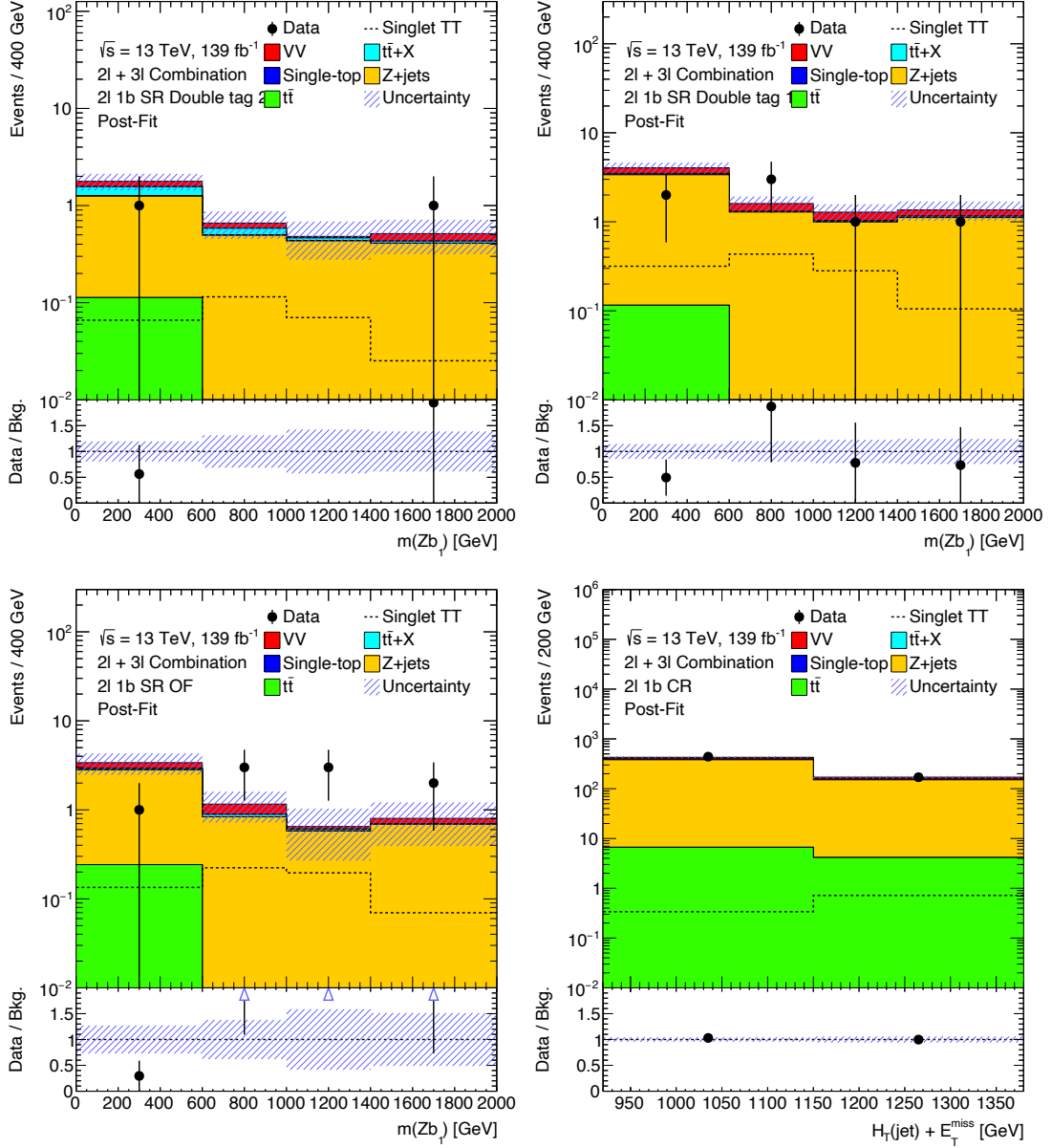
Figure 5.30: Post-fit plots for all 2ℓ regions with exactly 1 b-tagged jet with $m(Zb_1)$ as the discriminant variable, as well as the control region for exactly 1 b-tagged jet with $H_T(\text{jet}) + E_T^{\text{miss}}$ as the discriminant. The signal line corresponds to its pre-fit distribution.
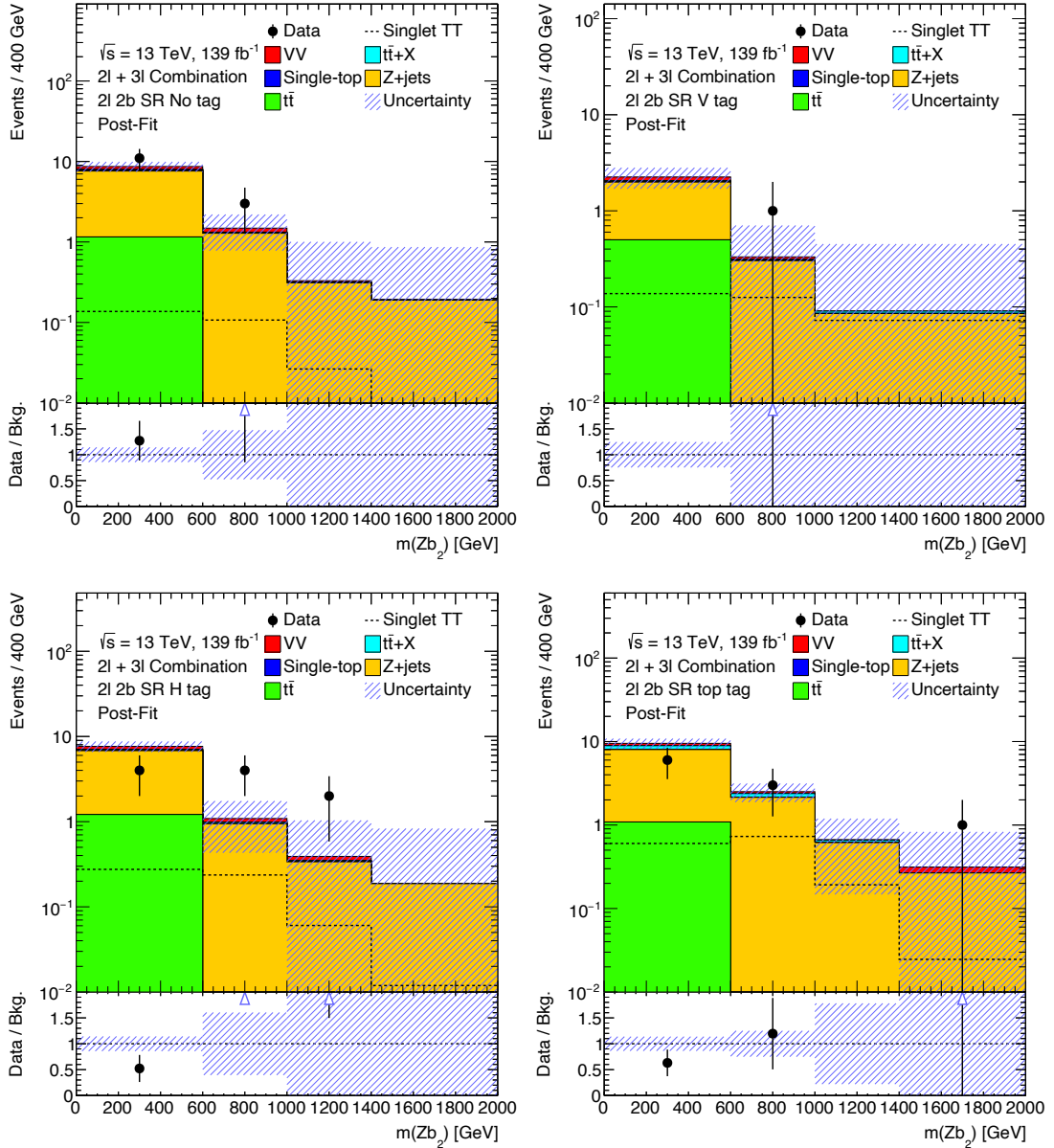
Figure 5.31: Post-fit plots for all 2ℓ regions with at least 2 b-tagged jets with $m(Zb_2)$ as the discriminant variable.
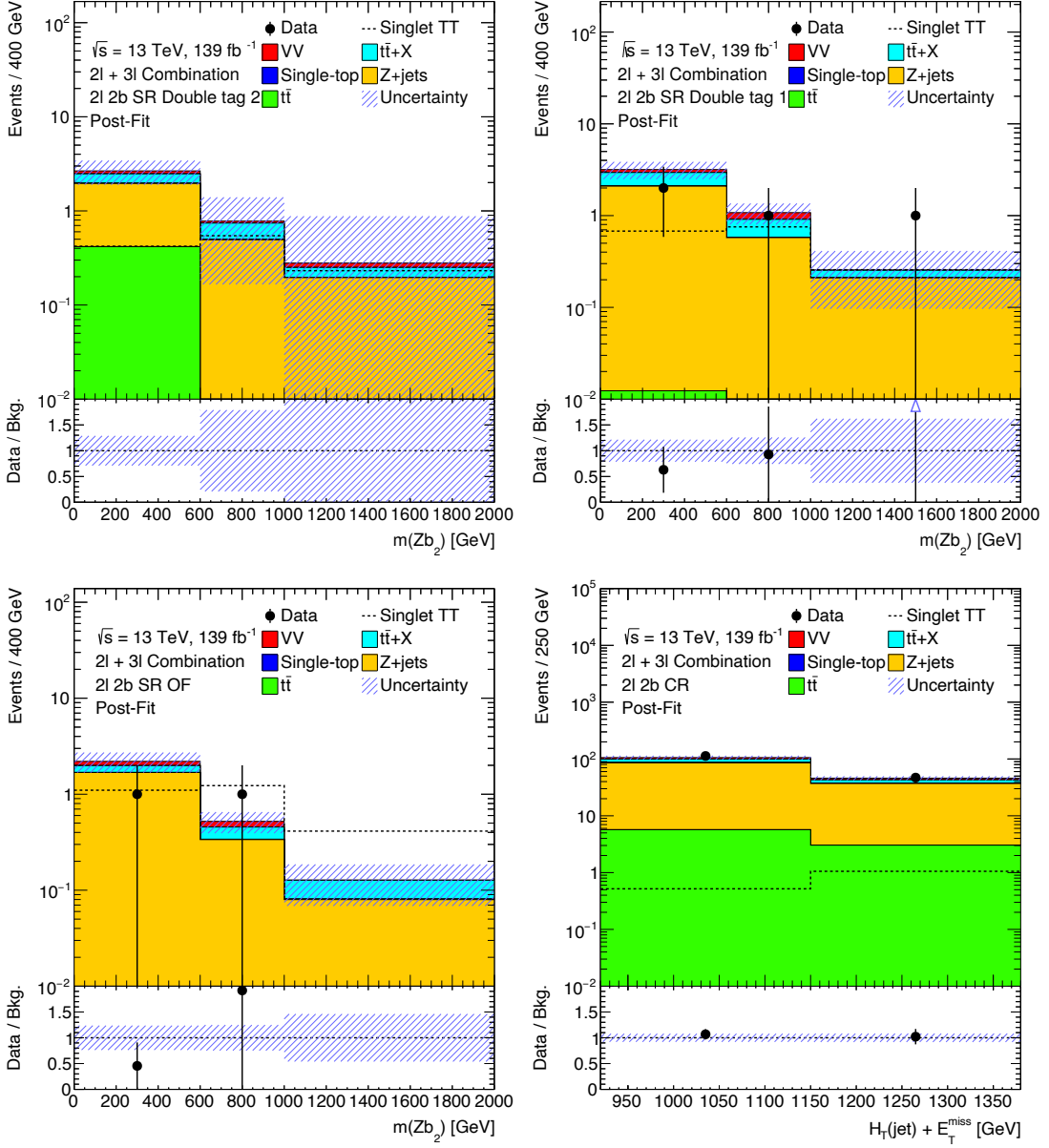
Figure 5.32: Post-fit plots for all 2ℓ regions with at least 2 b-tagged jets with $m(Zb_2)$ as the discriminant variable, as well as the control region for at least 2 b-tagged jets with $H_T(\text{jet}) + E_T^{\text{miss}}$ as the discriminant. The signal line corresponds to its pre-fit distribution.
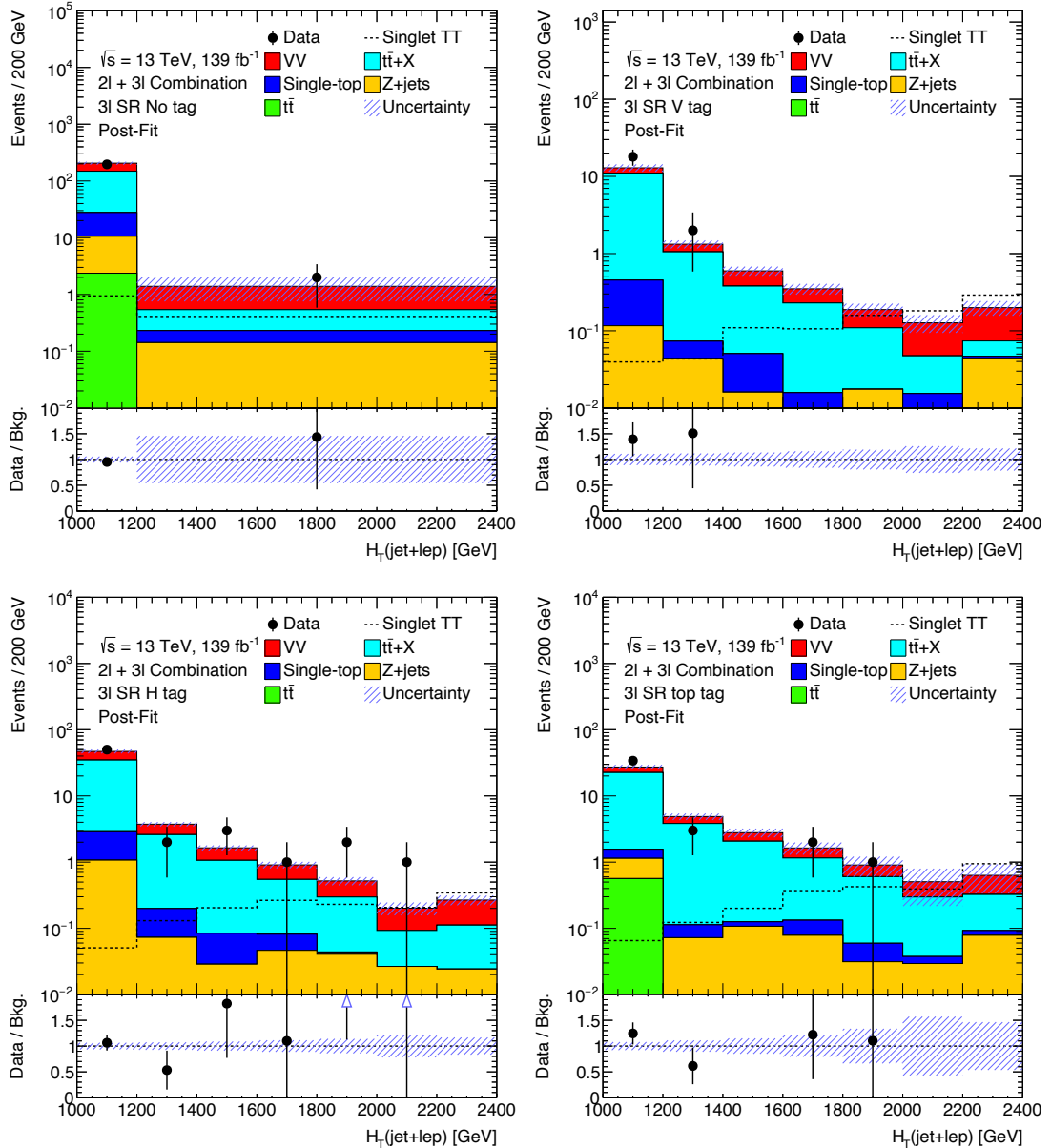
Figure 5.33: Post-fit plots in the 3ℓ channel with $H_T(\text{jet} + \text{lep})$ as the final discriminant. The signal line corresponds to its pre-fit distribution.
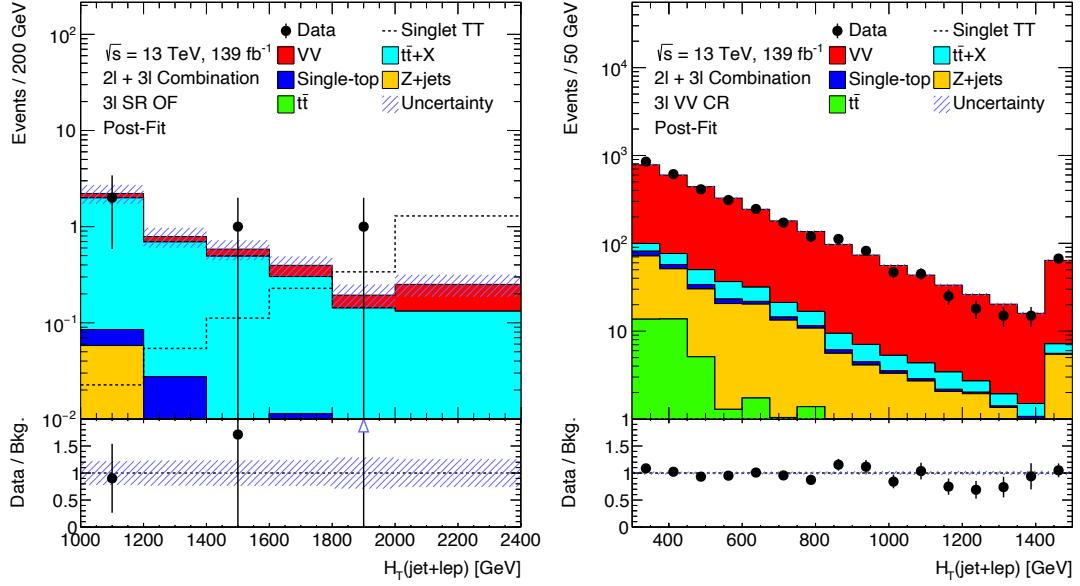
Figure 5.34: Post-fit plots in the 3ℓ channel with $H_{\mathrm{T}}(\mathrm{jet} + \mathrm{lep})$ as the final discriminant. The signal line corresponds to its pre-fit distribution.
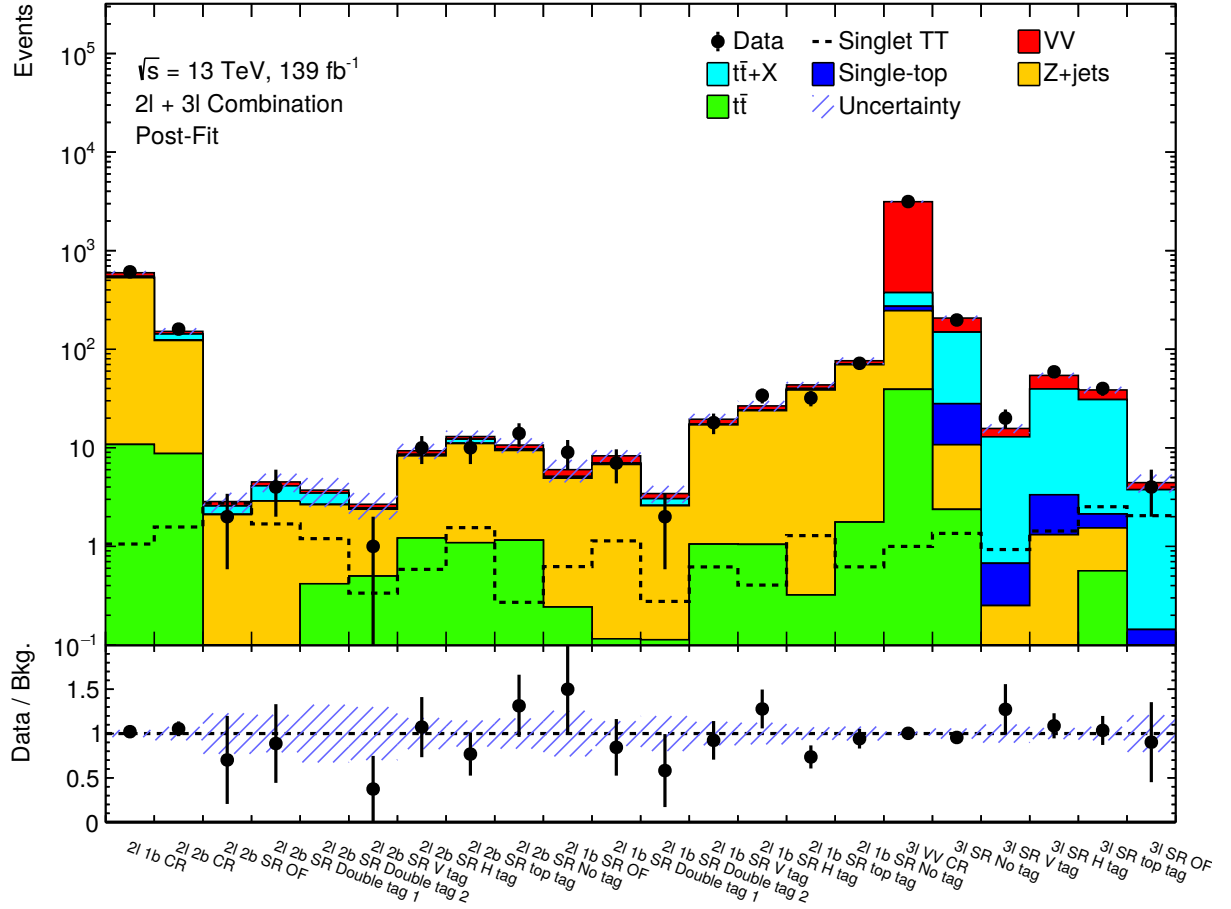
Figure 5.35: Summary of the yields in all regions after the background-only fit is performed.
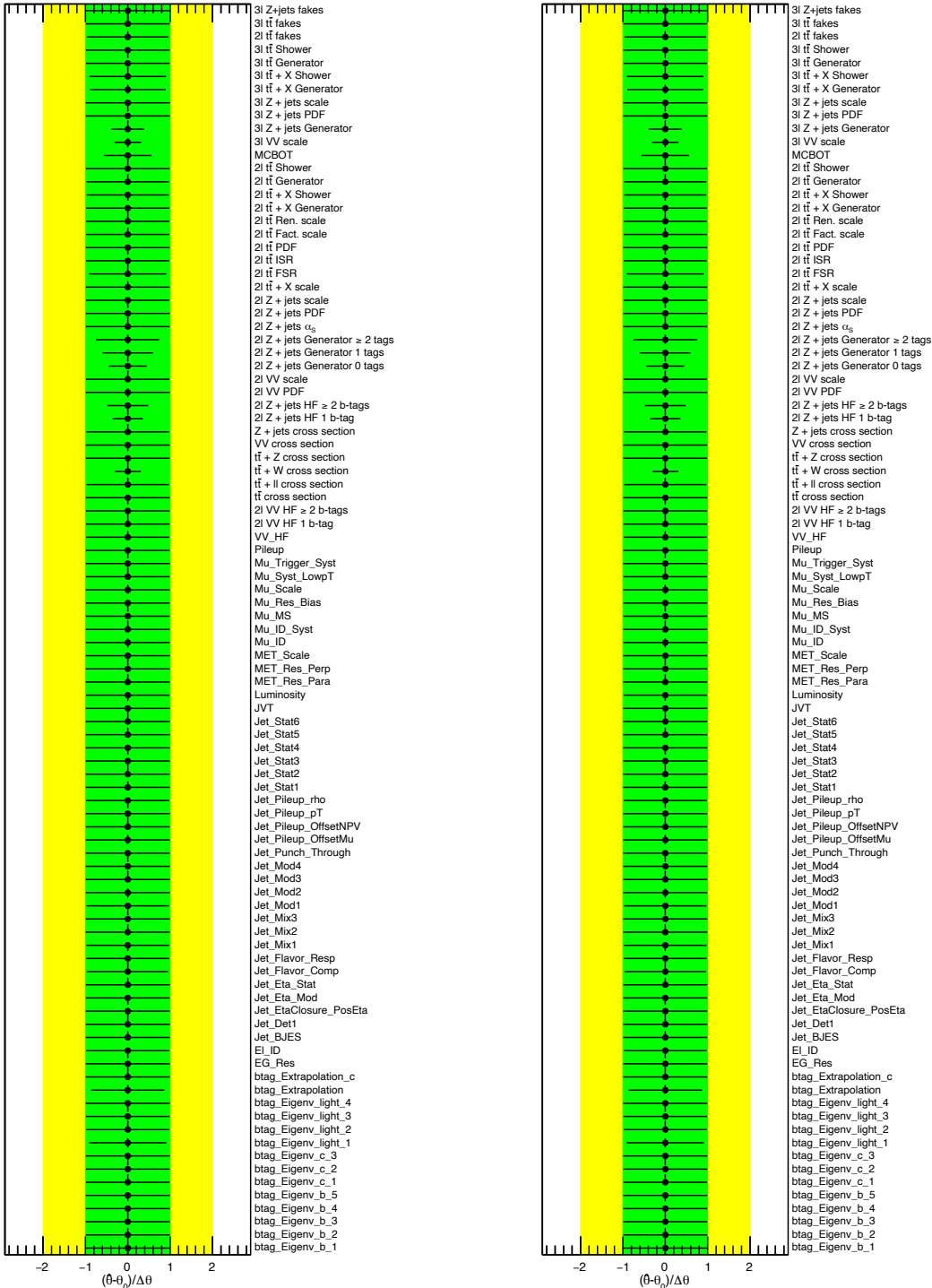
Figure 5.36: Pulls and constraints of the combined fit nuisance parameters for the background-only fit (left) and signal plus background fit (right) with the Asimov dataset. The green band represents the 1σ variation and the yellow band the 2σ variation.
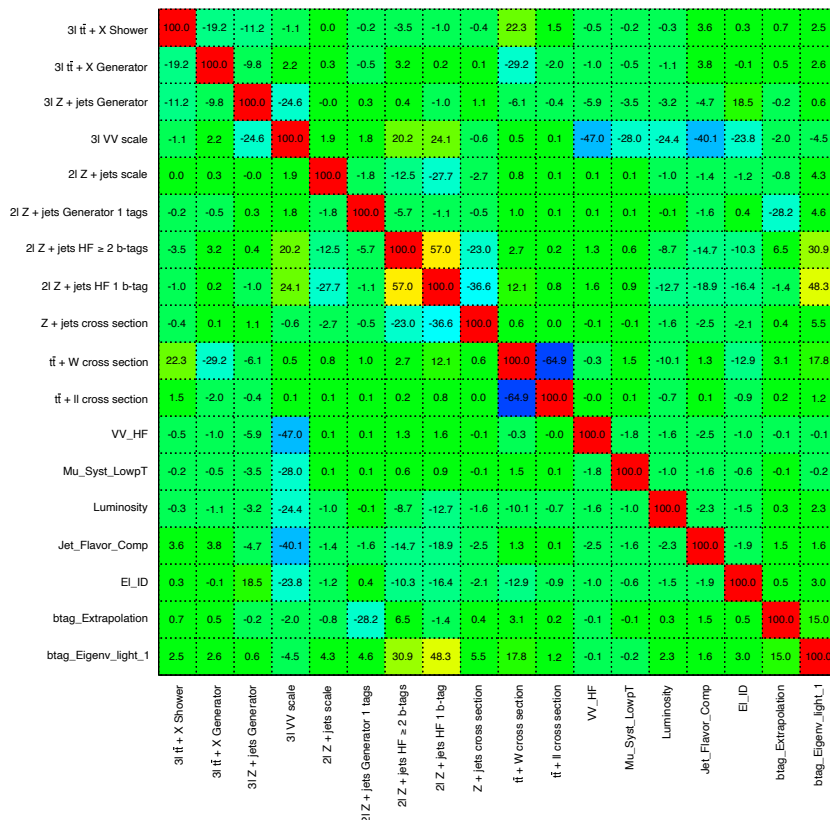
Figure 5.37: Correlation matrix of the combined fit nuisance parameters for the background-only fit with Asimov data. Only correlations above 20% are represented.
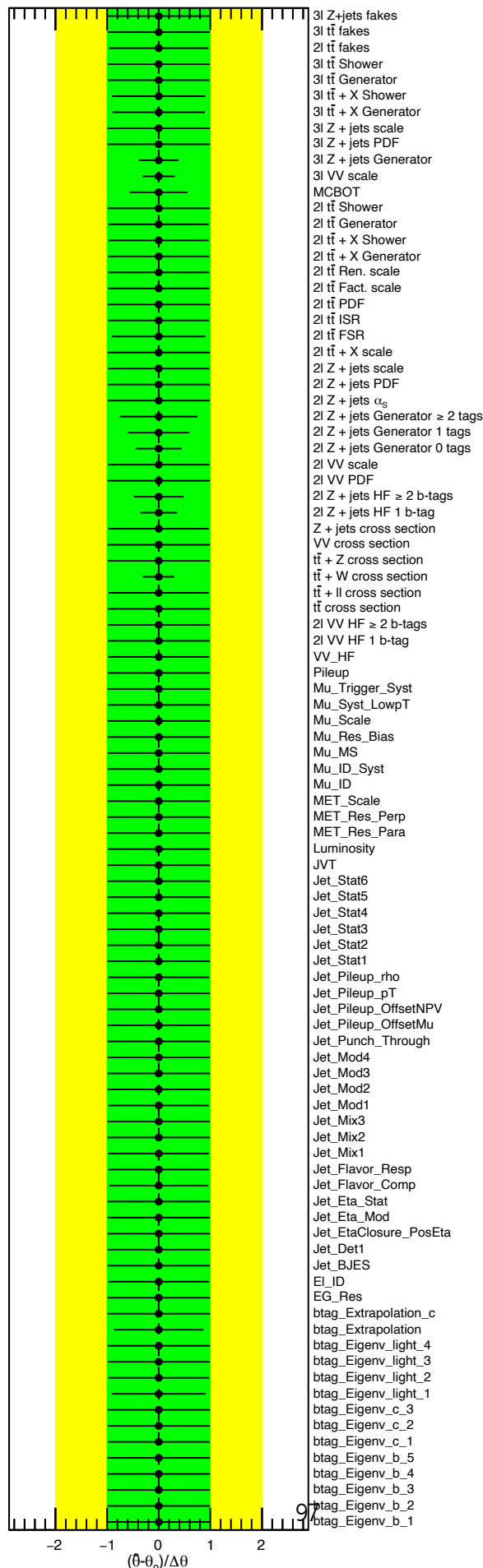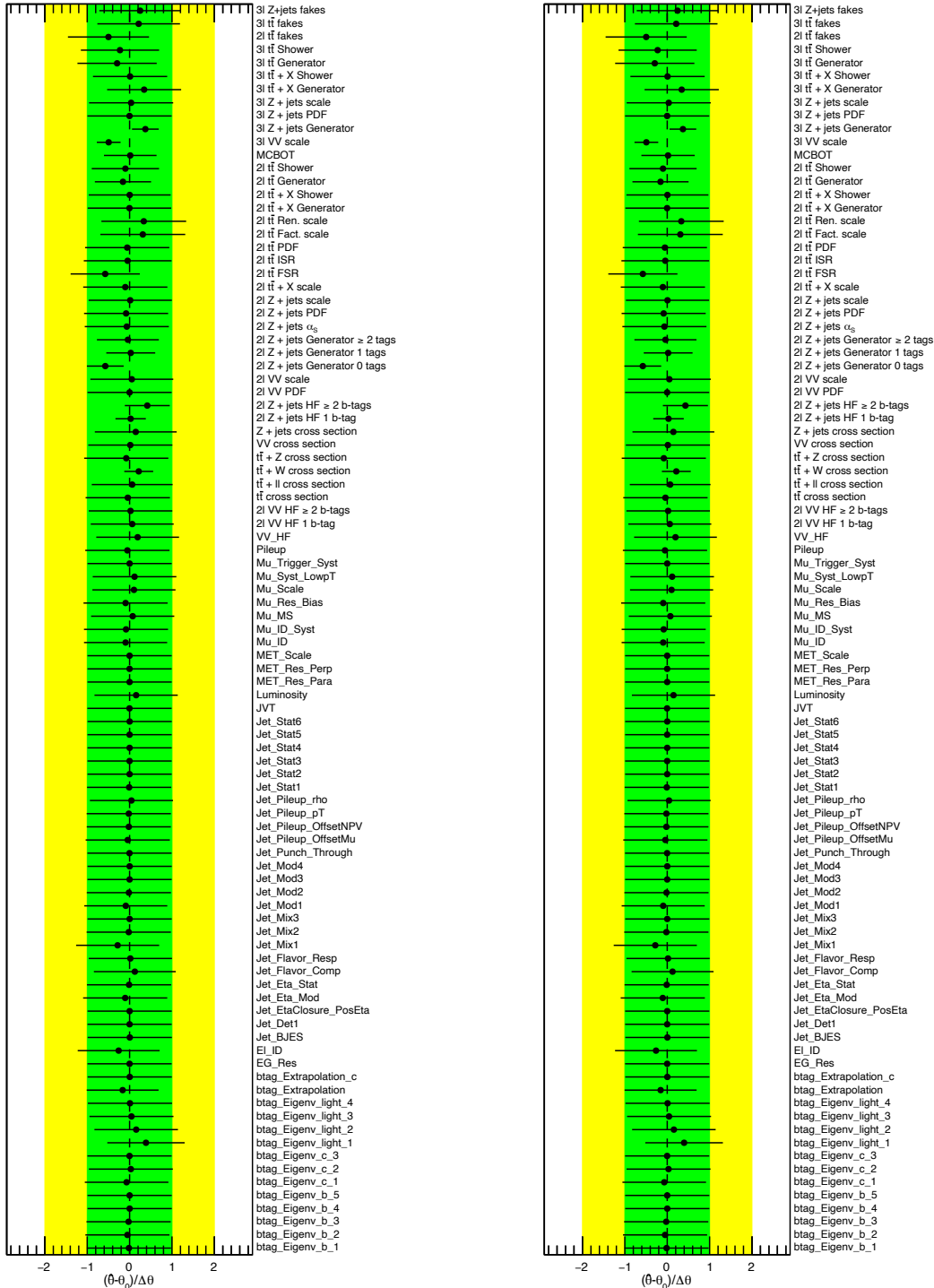
Figure 5.39: Pulls and constraints of the combined fit nuisance parameters for the background-only fit (left) and signal plus background fit (right). The green band represents the 1σ variation and the yellow band the 2σ variation.
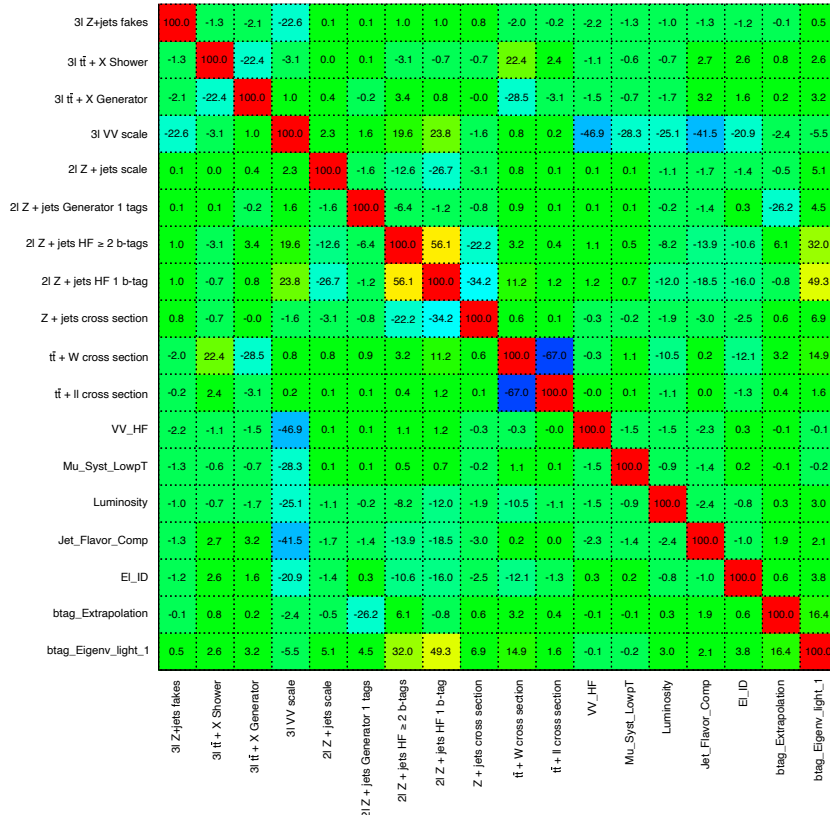
Figure 5.40: Correlation matrix of the combined fit nuisance parameters for the background-only fit. Only correlations above 20% are represented.
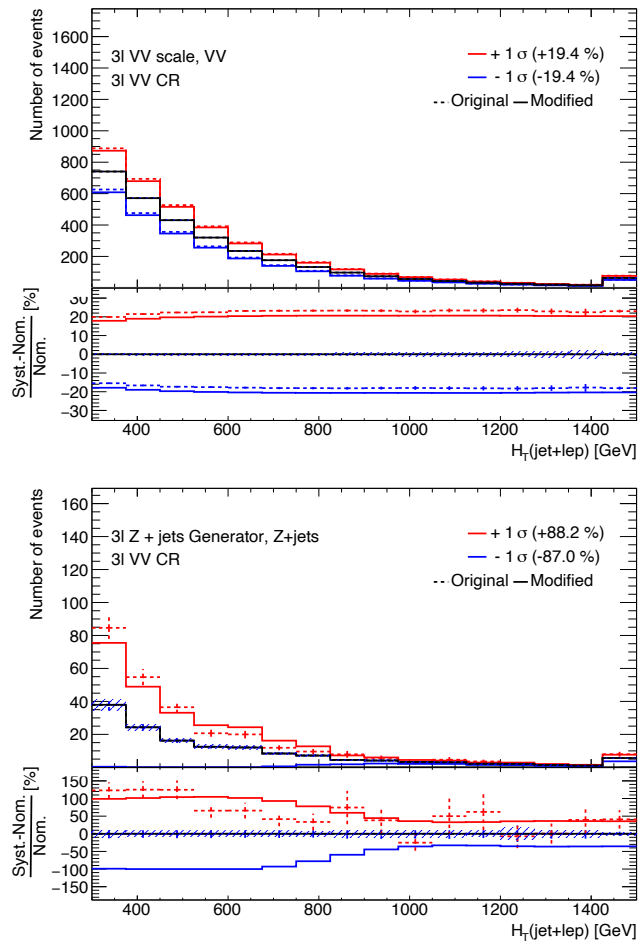
Figure 5.41: Shapes of the 3ℓ VV scale variations systematic (top) and the 3ℓ Z+jets generator systematic (bottom).
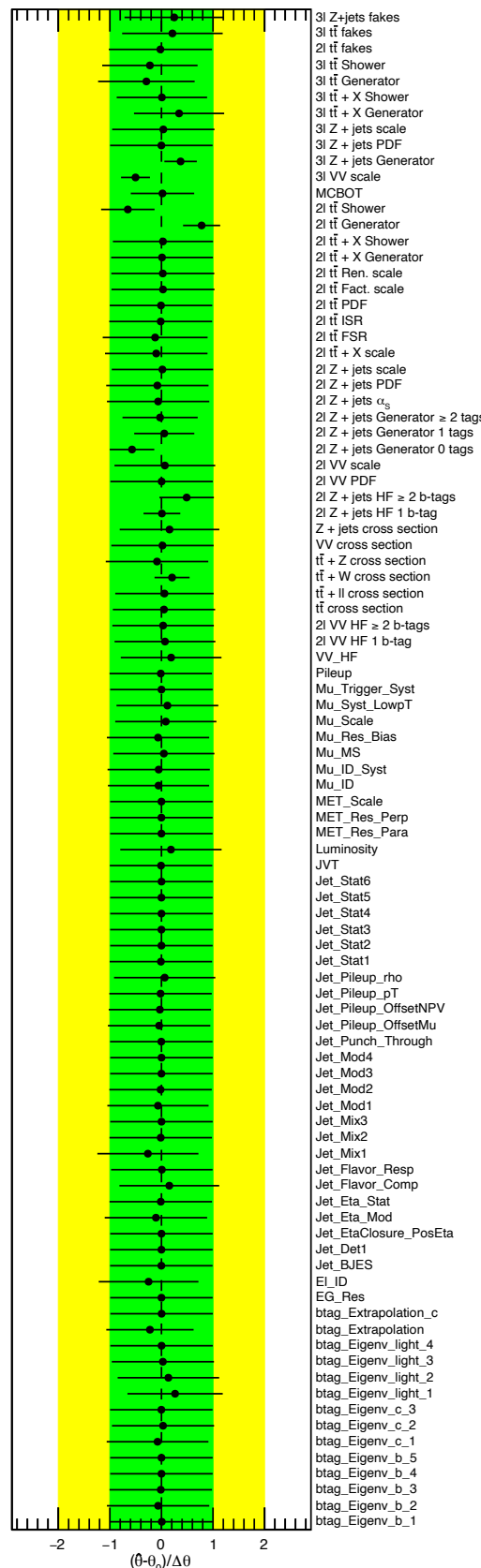
Figure 5.42: Pull plot with the 2ℓ $t\bar{t}$ Shower and Generator systematics before the changes to their definitions.
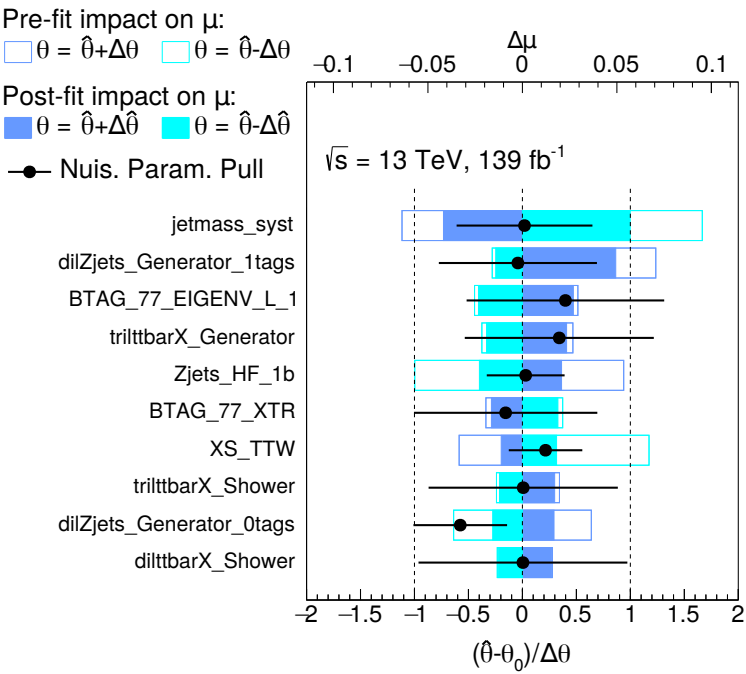
Figure 5.43: Ranking plot of the combined fit, with the signal benchmark of 1.2 TeV singlet VLT.
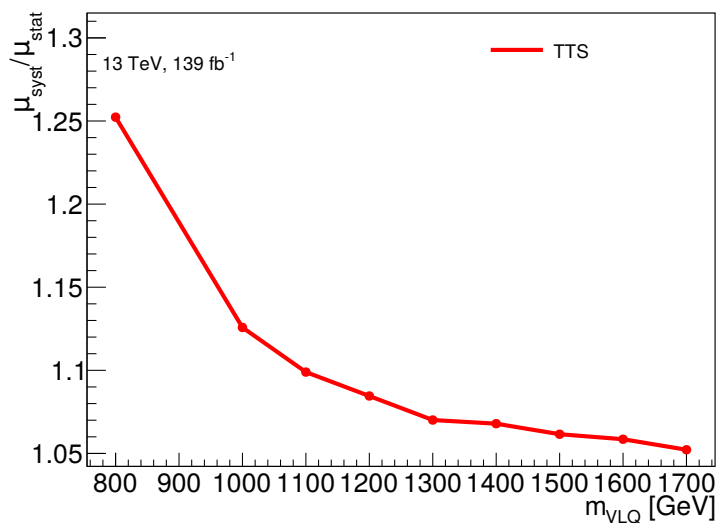
Figure 5.44: Ratio of the expected limit on cross-section in a fit with and without systematic uncertainties as a function of VLQ mass, for a singlet VLT.
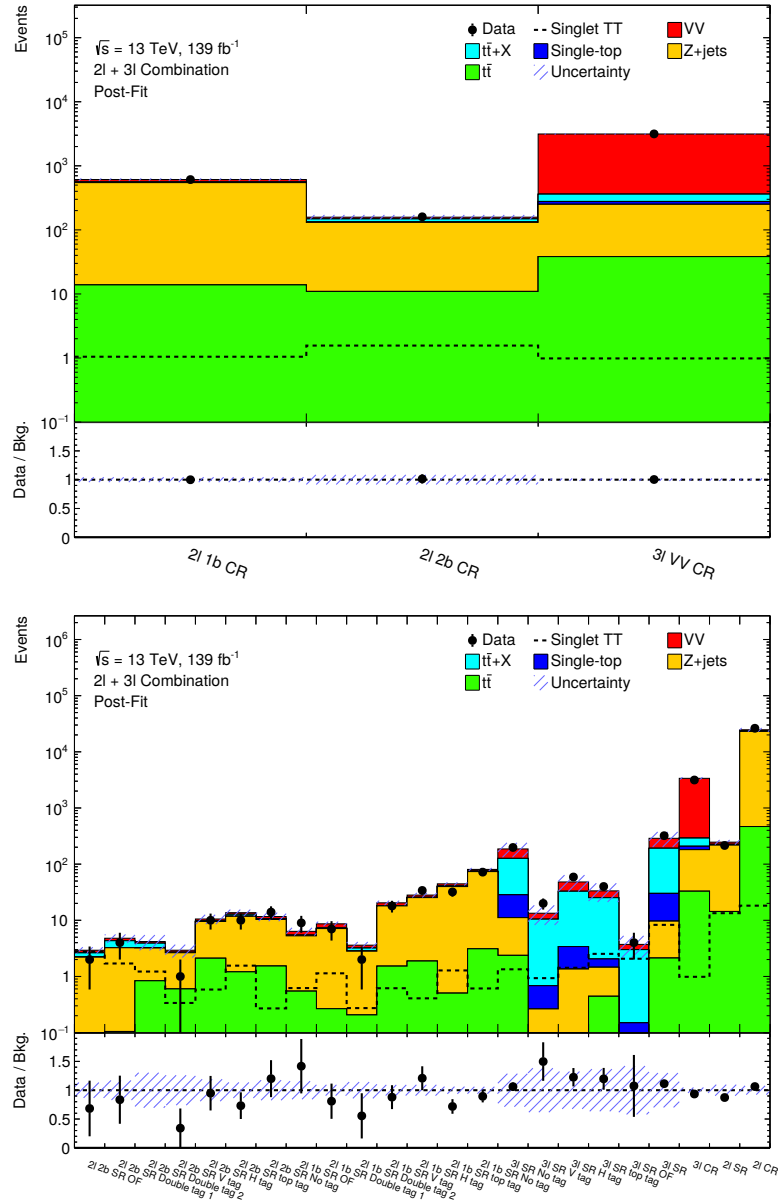
Figure 5.45: Summary of the data and Monte Carlo agreement in the control regions (top) and signal regions (bottom) in a background only fit without signal regions.
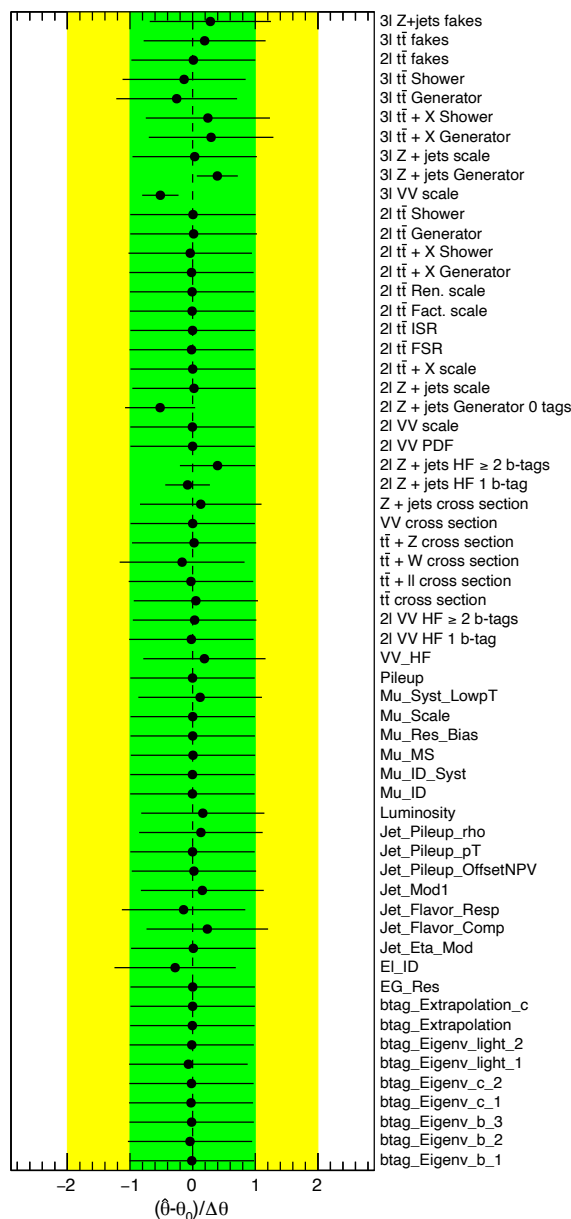
Figure 5.46: Pulls and constraints of the combined fit nuisance parameters for the background-only fit without signal regions. The green band represents the 1σ variation and the yellow band the 2σ variation.
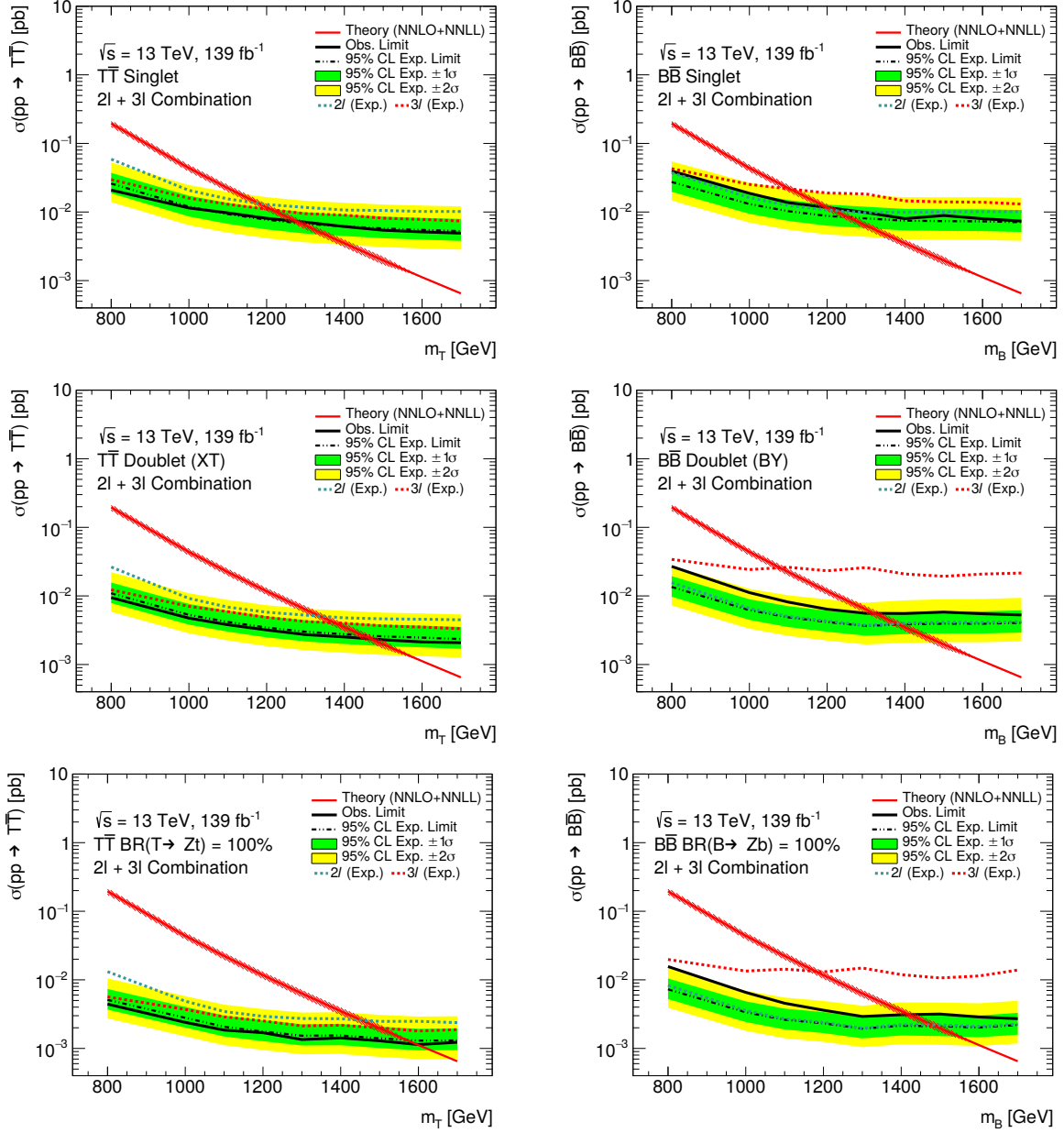
Figure 5.47: Expected and observed combined limits at 95% CL on the production cross-section for $T\bar{T}$ $B\bar{B}$ for the singlet and doublet benchmarks and for the case where BR(Z) = 1. The individual channel lines represent their expected limits.
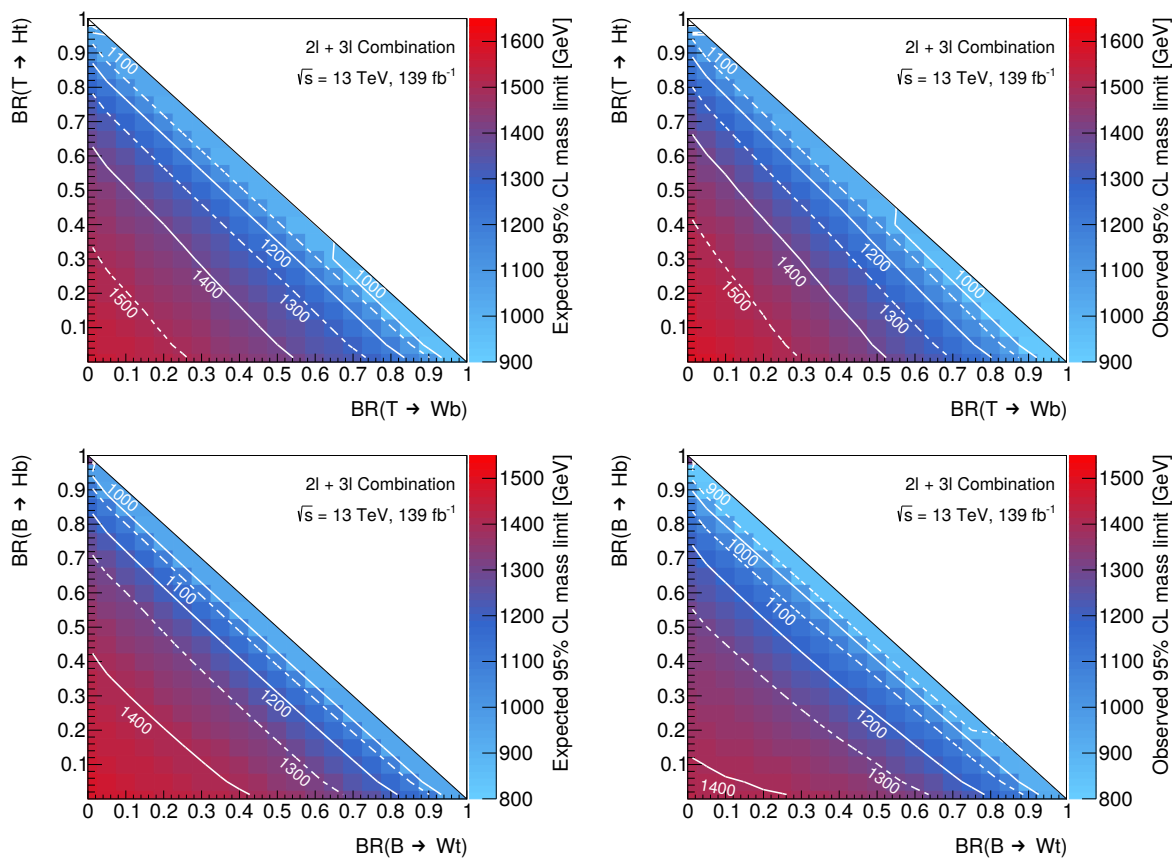
Figure 5.48: Expected and observed lower mass limits for the different BR possibilities. The white lines represent the contours of given VLQ masses.

Category	Data	Total background	VV	$t\bar{t} + X$	Single-top	Z+jets	$t\bar{t}$	Singlet $T\bar{T}$ $m_T = 1.2\,\text{TeV}$	Singlet $B\bar{B}$ $m_B = 1.2\,\text{TeV}$
2l 1b CR	610	598 ± 24	50 ± 18	13 ± 4	1.3 ± 0.6	522 ± 30	11 ± 4	1.06 ± 0.08	1.27 ± 0.09
2l 1b SR No tag	72	76 ± 6	5.5 ± 2.0	0.37 ± 0.13	0.8 ± 0.9	68 ± 6	1.8 ± 1.9	0.62 ± 0.13	1.52 ± 0.23
2l 1b SR V tag	18	19.6 ± 2.6	2.2 ± 0.8	0.22 ± 0.08	–	16.1 ± 2.1	1.1 ± 1.3	0.63 ± 0.07	1.31 ± 0.13
2l 1b SR H tag	34	26.6 ± 3.3	2.4 ± 0.9	0.38 ± 0.09	–	22.8 ± 3.0	1.1 ± 1.5	0.41 ± 0.05	0.66 ± 0.09
2l 1b SR top tag	32	43.5 ± 3.1	3.6 ± 1.3	1.25 ± 0.22	–	38.3 ± 3.3	0.3 ± 0.6	1.29 ± 0.14	1.40 ± 0.14
2l 1b SR Double tag 1	7	8.3 ± 1.2	1.3 ± 0.5	0.20 ± 0.09	–	6.7 ± 1.0	0.1 ± 0.4	1.14 ± 0.15	1.05 ± 0.17
2l 1b SR Double tag 2	2	3.4 ± 0.7	0.39 ± 0.19	0.42 ± 0.10	–	2.5 ± 0.5	0.11 ± 0.31	0.27 ± 0.06	0.19 ± 0.06
2l 1b SR OF	9	6.0 ± 1.6	0.9 ± 0.4	0.18 ± 0.05	–	4.7 ± 1.3	0.2 ± 0.7	0.62 ± 0.08	0.60 ± 0.11
2l 2b CR	160	152 ± 12	9 ± 4	18 ± 6	1.2 ± 0.6	115 ± 13	9.0 ± 3.5	1.58 ± 0.10	1.90 ± 0.13
2l 2b SR No tag	14	10.7 ± 1.9	0.9 ± 0.4	0.07 ± 0.08	0.3 ± 0.5	8.3 ± 1.1	1.2 ± 1.4	0.27 ± 0.07	1.11 ± 0.17
2l 2b SR V tag	1	2.7 ± 0.8	0.22 ± 0.13	0.06 ± 0.05	–	1.9 ± 0.5	0.5 ± 0.7	0.34 ± 0.04	0.81 ± 0.08
2l 2b SR H tag	10	9.4 ± 1.6	0.76 ± 0.34	0.26 ± 0.09	–	7.1 ± 1.0	1.2 ± 1.4	0.59 ± 0.09	1.90 ± 0.16
2l 2b SR top tag	10	13.0 ± 1.9	0.8 ± 0.4	1.10 ± 0.30	–	10.0 ± 1.6	1.1 ± 1.2	1.56 ± 0.18	1.97 ± 0.15
2l 2b SR Double tag 1	4	4.5 ± 1.0	0.40 ± 0.25	1.2 ± 0.6	–	2.9 ± 0.8	0.01 ± 0.19	1.71 ± 0.11	1.71 ± 0.18
2l 2b SR Double tag 2	0	3.7 ± 1.2	0.25 ± 0.14	0.78 ± 0.18	–	2.3 ± 0.6	0.4 ± 1.1	1.22 ± 0.10	1.12 ± 0.10
2l 2b SR OF	2	2.8 ± 0.7	0.28 ± 0.15	0.44 ± 0.20	–	2.1 ± 0.6	–	2.76 ± 0.25	2.02 ± 0.26
3l W CR	3149	3140 ± 70	2770 ± 90	98 ± 9	26.7 ± 1.6	210 ± 60	40 ± 18	1.00 ± 0.14	0.90 ± 0.14
3l SR No tag	198	203 ± 11	59 ± 5	117 ± 10	17.3 ± 0.6	8.5 ± 3.0	2.4 ± 2.0	1.37 ± 0.17	1.31 ± 0.17
3l SR V tag	20	15.3 ± 1.5	2.82 ± 0.34	11.8 ± 1.5	0.42 ± 0.06	0.25 ± 0.11	–	0.94 ± 0.07	0.71 ± 0.09
3l SR H tag	59	52.9 ± 2.8	14.9 ± 1.2	34.7 ± 2.7	2.03 ± 0.14	1.3 ± 0.4	–	1.44 ± 0.10	0.96 ± 0.08
3l SR top tag	40	37.7 ± 2.6	7.9 ± 0.6	27.6 ± 2.4	0.59 ± 0.07	1.0 ± 0.4	0.6 ± 1.2	2.54 ± 0.16	1.73 ± 0.12
3l SR OF	4	4.3 ± 0.9	0.68 ± 0.11	3.4 ± 0.8	0.071 ± 0.034	0.07 ± 0.05	–	2.07 ± 0.16	0.69 ± 0.13

Table 5.7: Table of yields in the control and signal regions, after the background only fit. The uncertainties include statistical and systematic uncertainties. Correlations may cause the total background uncertainty not to be exactly the sum in quadrature of the uncertainties of the individual background processes.

107

5.7   Going beyond this search

As discussed in section 4.1, combining all ATLAS VLQ pair production searches significantly improved the limits obtained. With the large increase in luminosity that was collected since then, it is already visible that the sensitivities that can still be achieved are much higher. The analysis presented in this text managed to reach by itself results compatible with the ATLAS combination. It is, therefore, natural to suggest that another ATLAS wide combination should be performed, which should allow to set very stringent limits on VLQ masses, if no deviation from the SM expectation is found.

Even though the results shown in this document are fairly general and prone to reinterpretation, some assumptions were made. It was assumed that VLQs decay exclusively to third generation quarks. This assumption is motivated by phenomenological considerations that lead to the prediction that the VLQ coupling to SM quarks is proportion to m/M, with m being the SM quark mass and M the VLQ mass [139–142]. This can, however, be revised by future analyses targeting lighter families. With the recent advances in charm and light jet flavor tagging [126, 143], this can be an interesting challenge for the next round of VLQ searches.

It was also assumed that VLQs decay only to SM bosons. Many of the models that predict the existence of VLQs can be extended and include exotic decays. A notable example is the case of Composite Higgs models. In section 2.3 the minimal scenario was considered, where the new sector led to the prediction of top partners that couple with the SM. Models that feature a larger group breaking result in the presence of extra scalars, from the new Goldstone bosons, that can be interpreted as dark matter candidates. They are predicted to mix naturally with VLQs, resulting in decays to invisible (by our detectors, at least) particles. This would mean that our considerations when interpreting the observed data result in the wrong measured cross-sections, as a part of the VLQ branching ratios go unconsidered, resulting in an overestimation of the excluded VLQ masses. With the published results there can be a phenomenological reinterpretation, by scaling the measured cross-sections to the missing BR, but, depending on the mass of the new scalar the observed kinematics can change enough that rescaling alone is not a realistic interpretation.

Another important assumption made in this analysis is that pair-production is mediated exclusively by SM QCD. Taking again into consideration the example of Composite Higgs models, which predict VLQs to mix with SM quarks, naturally predict a heavy gluon that can decay into pairs of VLQs, with a mass in the TeV range[7]. These decays would produce the same final states as those currently being considered in searches for VLQs, but the final state particles would take a large boost from the high mass of the heavy gluon. A similar scenario can show up in models with Z'.

A larger focus should also be put into single production analyses. As we start to exclude larger VLQ masses, single production starts to become the dominant production mechanism. The trickier interpretations that are necessary due to the coupling dependencies are starting to be generalized, as was discussed

---

[7]More details are given in section 2.2.

in chapter 4. This can pave the way for single production combinations similar to that done by the ATLAS experiment for pair production.

The generality of our search and the interpretation of the results should likely guide the next round of analyses, as well as the effort to combine the available results, towards fulfilling the potential of the recorded data.

6

Conclusions

The Standard Model is a successful theory, capable of predicting many phenomena in a large range of energies with a high precision, culminating with the discovery of the Higgs boson. Despite the many successes, the Standard Model still has open questions, such as the hierarchy problem. Trying to answer these questions leads to the creation of new models, most of which predict the existence of new particles. Vector like quarks are particles beyond the Standard Model that are predicted by some of the theories that try to solve these open questions. Finding vector like quarks would be a very important step towards understanding what lies in the realm of the unknown, so searches for these new particles were performed.

A first iteration, using a partial dataset of ATLAS data that amounts to 36.1 fb^{-1} at $\sqrt{s}$ = 13 TeV, was described. The author of this thesis was the main analyzer of the pair production dilepton channel with 0 or 1 large radius jets. The analysis was developed from the very start, by producing Monte Carlo simulation, defining the analysis strategy, performing and understanding the fit and developing the limit setting machinery to obtain the final results. Control and signal regions were designed in order to optimize these results, taking into account the expected features of VLQ production, and its main backgrounds. As no significant deviation from the Standard Model expectation was found, upper mass limits were derived. These limits reached the TeV range, going up to 1.34 in most favorable BR scenario. They represented the most stringent limits for this particular decay mode that were set at the time of their publication.

These results were largely improved by the combination of all ATLAS pair production searches. The author of this thesis was the analysis liaison, responsible for all the checks regarding overlaps with the other analyses, production of the combined limits from our analysis, following the conventions aiming at ensuring a compatible treatment of the background modeling and evaluation of the systematic sources of uncertainty. The improvement from the individual analyses was significant and the obtained results are still the most stringent results published so far, together with the all-hadronic results published by the CMS

collaboration.

These limits, however, are matched, and in some branching ratio scenarios even slightly surpassed by the latest iteration of the analysis presented in this thesis. This analysis, which was approved as a preliminary result [144] by the ATLAS Collaboration, and is expected to be published soon, was performed with the full run 2 dataset, amounting to an integrated luminosity of 139 fb^{-1}. It focuses on pair production of VLT and VLB in events with a Z boson decaying to leptons and a third generation quark. The author of this thesis is the analysis contact within the ATLAS collaboration, besides being the main analyzer of the 3ℓ channel and the responsible for the combination fit and limit setting. The inclusion of a deep neural network tagger that classifies jets as likely originated by top quarks, W or Z bosons, H bosons or light jets allowed to build better signal and control regions, improving in this way the fit quality and consequently the results. Instead of following the strategy of the previous analysis, in which control regions dedicated to the main backgrounds are built, the categorization of the signal regions creates many regions with different background compositions and signal to background ratios. It allows the fit to learn the different topologies created by VLQ pair production and use the signal regions to constrain uncertainties and adjust the modelling of the main background. The limits set by this analysis are a significant improvement over the previously existing ones. They represent an improvement of about 200 GeV in all branching ratio scenarios. The excluded lower mass limits range from 1.07 to 1.60 TeV, depending on the branching ratio. They represent the best results up to date in this decay mode. Following the lessons from the last iteration of the analysis, a new combination of ATLAS searches should significantly improve these results and therefore provide important experimental information which will allow to exclude significant regions of the parameter space of different beyond-SM models.

The published analysis should also be subject to reinterpretation by the phenomenology community. As was stated in the last of this thesis, even though the experiments try to make these results as general as possible, they still rely on assumptions that can be relaxed. The ATLAS experiment always made an effort to make the results reinterpretable, whether by publishing HEPData [145] results or with current increased efforts that go beyond that, taking advantage of current technologies that facilitate the storing and replication of results [146, 147]. The interpretation of the experimental results and the interplay between the two communities will lead to better results, with the correct focus, making the most profit of the available data.

The work done throughout the PhD was presented in different conferences and workshops, including posters at the Top 2018 and 2019 workshops, Jornadas Científicas do LIP in 2018 and UT Austin Portugal Program's 2019 Annual Conference; talks at IBERGRID 2019 and Epiphany 2020, besides several talks at schools and student workshops and several outreach activities. These analyses resulted in journal publications in Physical Review D and Physical Review Letters (Editors' Suggestion).

Besides the analyses presented in this thesis, some phenomenological works were also developed. They were not included in this document in order to maintain a theme of ATLAS searches but they are

nonetheless relevant to VLQs and BSM searches. One of these studies assessed the transferability of deep learning models with new physics signals [148]. As analyses become more reliant on machine learning, the question of how sensitive they are to physics not included in training becomes more relevant, i.e. would we miss new physics in our data because our models are trained on a specific signal? Trying to answer that question, different deep neural networks were trained on 3 signal models: tZ production via FCNC, VLT pair production via standard model QCD and VLT pair production via heavy gluon decay for masses of 1, 1.2 and 1.4 TeV. Limits were derived using inference of the neural networks on signals that were not included in the training, in order to assess the degradation of their discrimination power when classifying events from different class models. It was seen that the limits are compatible, within uncertainties for the VLT related signals. While the FCNC signal does not perform as well in neural networks trained with VLT signals, it was seen that they still perform better than deriving limits with a single discriminant variable.

The other phenomenological study [149] tested how performant the Earth Mover's Distance [150] is at discriminating rare processes in events from proton-proton colliders. In this study this quantity is generalized to quantify the similarity between two physics events using experimental information. It was seen that this observable, when applied to unsupervised methods that are tipically used for dimensionality reduction such as UMAP [151], is capable of grouping together different processes. Processes such as Dibosons are well separated from other processes that have top quarks, clustered continuously from Dibosons to $t\bar{t}$ + X. This could be a promising application for event classification in collider analyses. The use of these observables as inputs to a deep neural network were also tested. The overall performance of the DNN does not improve significantly with this addition, but still they are shown to be useful for the event-level information provided.

Bibliography

[1] E. Noether. "Invariante Variationsprobleme." ger. In: *Nachrichten von der Gesellschaft der Wissenschaften zu Göttingen, Mathematisch-Physikalische Klasse* 1918 (1918), pp. 235–257. url: http://eudml.org/doc/59024.

[2] E. Fischbach, H. Kloor, R. A. Langel, A. T. Y. Lui, and M. Peredo. "New geomagnetic limits on the photon mass and on long-range forces coexisting with electromagnetism." In: *Phys. Rev. Lett.* 73 (4 1994), pp. 514–517. doi: 10.1103/PhysRevLett.73.514. url: https://link.aps.org/doi/10.1103/PhysRevLett.73.514.

[3] D. J. Gross and F. Wilczek. "Ultraviolet Behavior of Non-Abelian Gauge Theories." In: *Phys. Rev. Lett.* 30 (26 1973), pp. 1343–1346. doi: 10.1103/PhysRevLett.30.1343. url: https://link.aps.org/doi/10.1103/PhysRevLett.30.1343.

[4] H. D. Politzer. "Reliable Perturbative Results for Strong Interactions?" In: *Phys. Rev. Lett.* 30 (26 1973), pp. 1346–1349. doi: 10.1103/PhysRevLett.30.1346. url: https://link.aps.org/doi/10.1103/PhysRevLett.30.1346.

[5] P. W. Higgs. "Broken symmetries, massless particles and gauge fields." In: *Phys. Lett.* 12 (1964), pp. 132–133. doi: 10.1016/0031-9163(64)91136-9.

[6] F. Englert and R. Brout. "Broken Symmetry and the Mass of Gauge Vector Mesons." In: *Phys. Rev. Lett.* 13 (9 1964), pp. 321–323. doi: 10.1103/PhysRevLett.13.321. url: https://link.aps.org/doi/10.1103/PhysRevLett.13.321.

[7] G. S. Guralnik, C. R. Hagen, and T. W. B. Kibble. "Global Conservation Laws and Massless Particles." In: *Phys. Rev. Lett.* 13 (20 1964), pp. 585–587. doi: 10.1103/PhysRevLett.13.585. url: https://link.aps.org/doi/10.1103/PhysRevLett.13.585.

[8] Super-Kamiokande Collaboration. "Evidence for Oscillation of Atmospheric Neutrinos." In: *Phys. Rev. Lett.* 81 (8 1998), pp. 1562–1567. doi: 10.1103/PhysRevLett.81.1562. url: https://link.aps.org/doi/10.1103/PhysRevLett.81.1562.

[9] ATLAS Collaboration. *Standard Model Summary Plots June 2021*. Tech. rep. Geneva: CERN, 2021. url: http://cds.cern.ch/record/2777014.

[10] Y. Fukuda et al. "Evidence for Oscillation of Atmospheric Neutrinos." In: *Phys. Rev. Lett.* 81 (8 1998), pp. 1562–1567. doi: `10.1103/PhysRevLett.81.1562`. url: `https://link.aps.org/doi/10.1103/PhysRevLett.81.1562`.

[11] V. Trimble. "Existence and Nature of Dark Matter in the Universe." In: *Annual Review of Astronomy and Astrophysics* 25.1 (1987), pp. 425–472. doi: `10.1146/annurev.aa.25.090187.002233`.

[12] J. L. Feng. "Dark Matter Candidates from Particle Physics and Methods of Detection." In: *Annual Review of Astronomy and Astrophysics* 48.1 (2010). issn: 1545-4282. doi: `10.1146/annurev-astro-082708-101659`. url: `http://dx.doi.org/10.1146/annurev-astro-082708-101659`.

[13] G. Bertone, D. Hooper, and J. Silk. "Particle dark matter: evidence, candidates and constraints." In: *Physics Reports* 405.5-6 (2005), pp. 279–390. issn: 0370-1573. doi: `10.1016/j.physrep.2004.08.031`. url: `http://dx.doi.org/10.1016/j.physrep.2004.08.031`.

[14] N. Aghanim, Y. Akrami, M. Ashdown, J. Aumont, C. Baccigalupi, M. Ballardini, A. J. Banday, R. B. Barreiro, N. Bartolo, and et al. "Planck 2018 results." In: *Astronomy & Astrophysics* 641 (2020), A6. issn: 1432-0746. doi: `10.1051/0004-6361/201833910`. url: `http://dx.doi.org/10.1051/0004-6361/201833910`.

[15] A. D. Sakharov. "Violation of CP invariance, C asymmetry, and baryon asymmetry of the universe." In: *Soviet Physics Uspekhi* 34.5 (1991), pp. 392–393. doi: `10.1070/pu1991v034n05abeh002497`. url: `https://doi.org/10.1070/pu1991v034n05abeh002497`.

[16] L. Susskind. "Dynamics of spontaneous symmetry breaking in the Weinberg-Salam theory." In: *Phys. Rev. D* 20 (10 1979), pp. 2619–2625. doi: `10.1103/PhysRevD.20.2619`. url: `https://link.aps.org/doi/10.1103/PhysRevD.20.2619`.

[17] Y. A. Golfand and E. P. Likhtman. "Extension of the Algebra of Poincare Group Generators and Violation of p Invariance." In: *JETP Lett.* 13 (1971), pp. 323–326.

[18] J. Wess and B. Zumino. "Supergauge transformations in four dimensions." In: *Nuclear Physics B* 70.1 (1974), pp. 39–50. issn: 0550-3213. doi: `https://doi.org/10.1016/0550-3213(74)90355-1`.

[19] J. Wess and B. Zumino. "Supergauge invariant extension of quantum electrodynamics." In: *Nuclear Physics B* 78.1 (1974), pp. 1–13. issn: 0550-3213. doi: `https://doi.org/10.1016/0550-3213(74)90112-6`.

[20] S. Ferrara and B. Zumino. "Supergauge invariant Yang-Mills theories." In: *Nuclear Physics B* 79.3 (1974), pp. 413–421. issn: 0550-3213. doi: `https://doi.org/10.1016/0550-3213(74)90559-8`.

[21] A. Salam and J. Strathdee. "Super-symmetry and non-Abelian gauges." In: *Physics Letters B* 51.4 (1974), pp. 353–355. issn: 0370-2693. doi: `https://doi.org/10.1016/0370-2693(74)90226-3`.

[22] D. Volkov and V. Akulov. "Is the neutrino a goldstone particle?" In: *Physics Letters B* 46.1 (1973), pp. 109–110. issn: 0370-2693. doi: `https://doi.org/10.1016/0370-2693(73)90490-5`.

[23] N. Arkani–Hamed, S. Dimopoulos, and G. Dvali. "The hierarchy problem and new dimensions at a millimeter." In: *Physics Letters B* 429.3 (1998), pp. 263–272. issn: 0370-2693. doi: `https://doi.org/10.1016/S0370-2693(98)00466-3`.

[24] N. Arkani-Hamed, S. Dimopoulos, and G. Dvali. "Phenomenology, astrophysics, and cosmology of theories with submillimeter dimensions and TeV scale quantum gravity." In: *Phys. Rev. D* 59 (8 1999), p. 086004. doi: `10.1103/PhysRevD.59.086004`.

[25] D. B. Kaplan, H. Georgi, and S. Dimopoulos. "Composite Higgs scalars." In: *Physics Letters B* 136.3 (1984), pp. 187–190. issn: 0370-2693. doi: `https://doi.org/10.1016/0370-2693(84)91178-X`. url: `https://www.sciencedirect.com/science/article/pii/037026938491178X`.

[26] K. Agashe, R. Contino, and A. Pomarol. "The minimal composite Higgs model." In: *Nuclear Physics B* 719.1 (2005), pp. 165–187. issn: 0550-3213. doi: `https://doi.org/10.1016/j.nuclphysb.2005.04.035`. url: `https://www.sciencedirect.com/science/article/pii/S0550321305003445`.

[27] K. Agashe, A. Delgado, M. J. May, and R. Sundrum. "RS1, custodial isospin and precision tests." In: *JHEP* 08 (2003), p. 050. doi: `10.1088/1126-6708/2003/08/050`. arXiv: `hep-ph/0308036`.

[28] M. Kobayashi and T. Maskawa. "CP-Violation in the Renormalizable Theory of Weak Interaction." In: *Progress of Theoretical Physics* 49.2 (Feb. 1973), pp. 652–657. issn: 0033-068X. doi: `10.1143/PTP.49.652`. eprint: `https://academic.oup.com/ptp/article-pdf/49/2/652/5257692/49-2-652.pdf`. url: `https://doi.org/10.1143/PTP.49.652`.

[29] N. Cabibbo. "Unitary Symmetry and Leptonic Decays." In: *Phys. Rev. Lett.* 10 (12 1963), pp. 531–533. doi: `10.1103/PhysRevLett.10.531`. url: `https://link.aps.org/doi/10.1103/PhysRevLett.10.531`.

[30] ATLAS Collaboration. "Search for pair and single production of new heavy quarks that decay to a Z boson and a third-generation quark in pp collisions at $\sqrt{s} = 8$ TeV with the ATLAS detector." In: *JHEP* 11.CERN-PH-EP-2014-188 (2014), p. 104. doi: `10.1007/JHEP11(2014)104`. arXiv: `1409.5500 [hep-ex]`.

[31] J. Aguilar-Saavedra, R. Benbrik, S. Heinemeyer, and M. Perez-Victoria. "Handbook of vectorlike quarks: mixing and single production." In: *Phys. Rev.* D88 (2013), p. 94010. doi: `10.1103/PhysRevD.88.094010`. arXiv: `1306.0572 [hep-ph]`.

[32] *CERN Annual Personnel Statistics 2018.* `https://cds.cern.ch/record/2677223`. 2018.

[33] *The CERN accelerator complex.* `http://cds.cern.ch/record/1621894`.

[34] L. R. Evans and P. Bryant. "LHC Machine." In: *JINST* 3 (2008), S08001. 164 p. doi: `10.1088/1748-0221/3/08/S08001`. url: `https://cds.cern.ch/record/1129806`.

[35] ATLAS Collaboration. "The ATLAS Experiment at the CERN Large Hadron Collider." In: *JINST* 3 (2008), S08003. 437 p. doi: `10.1088/1748-0221/3/08/S08003`. url: `https://cds.cern.ch/record/1129811`.

[36] CMS Collaboration. "The CMS experiment at the CERN LHC." In: *Journal of Instrumentation* 3.08 (2008), S08004–S08004. doi: `10.1088/1748-0221/3/08/s08004`. url: `https://doi.org/10.1088/1748-0221/3/08/s08004`.

[37] LHCb Collaboration. "The LHCb Detector at the LHC." In: *Journal of Instrumentation* 3.08 (2008), S08005–S08005. doi: `10.1088/1748-0221/3/08/s08005`. url: `https://doi.org/10.1088/1748-0221/3/08/s08005`.

[38] ALICE Collaboration. "The ALICE experiment at the CERN LHC." In: *Journal of Instrumentation* 3.08 (2008), S08002–S08002. doi: `10.1088/1748-0221/3/08/s08002`. url: `https://doi.org/10.1088/1748-0221/3/08/s08002`.

[39] *Luminosity Public Results Run 2.* `https://twiki.cern.ch/twiki/bin/view/AtlasPublic/LuminosityPublicResultsRun2`.

[40] S Haywood, L Rossi, R Nickerson, and A Romaniouk. *ATLAS inner detector: Technical Design Report, 2.* Technical design report. ATLAS. Geneva: CERN, 1997. url: `https://cds.cern.ch/record/331064`.

[41] ATLAS Collaboration. *ATLAS inner detector: Technical Design Report, 1.* Technical design report. ATLAS. Geneva: CERN, 1997. url: `https://cds.cern.ch/record/331063`.

[42] ATLAS Collaboration. *The ATLAS Inner Detector commissioning and calibration.* 2010. doi: `10.1140/EPJC/S10052-010-1366-7`.

[43] M Capeans, G Darbo, K Einsweiller, M Elsing, T Flick, M Garcia-Sciveres, C Gemme, H Pernegger, O Rohne, and R Vuillermet. *ATLAS Insertable B-Layer Technical Design Report.* Tech. rep. 2010. url: `https://cds.cern.ch/record/1291633`.

[44] ATLAS Collaboration. "ATLAS pixel detector electronics and sensors." In: *Journal of Instrumentation* 3.07 (2008), P07007–P07007. doi: `10.1088/1748-0221/3/07/p07007`. url: `https://doi.org/10.1088/1748-0221/3/07/p07007`.

[45] N. Wermes and G Hallewel. *ATLAS pixel detector: Technical Design Report*. Technical design report. ATLAS. Geneva: CERN, 1998. url: `https://cds.cern.ch/record/381263`.

[46] A. Ahmad et al. "The silicon microstrip sensors of the ATLAS semiconductor tracker." In: *Nuclear Instruments and Methods in Physics Research Section A: Accelerators, Spectrometers, Detectors and Associated Equipment* 578.1 (2007), pp. 98–118. issn: 0168-9002. doi: `https://doi.org/10.1016/j.nima.2007.04.157`. url: `https://www.sciencedirect.com/science/article/pii/S0168900207007644`.

[47] A. Abdesselam et al. "The barrel modules of the ATLAS semiconductor tracker." In: *Nuclear Instruments and Methods in Physics Research Section A: Accelerators, Spectrometers, Detectors and Associated Equipment* 568.2 (2006), pp. 642–671. issn: 0168-9002. doi: `https://doi.org/10.1016/j.nima.2006.08.036`. url: `https://www.sciencedirect.com/science/article/pii/S016890020601388X`.

[48] A. Abdesselam et al. "The ATLAS semiconductor tracker end-cap module." In: *Nuclear Instruments and Methods in Physics Research Section A: Accelerators, Spectrometers, Detectors and Associated Equipment* 575.3 (2007), pp. 353–389. issn: 0168-9002. doi: `https://doi.org/10.1016/j.nima.2007.02.019`. url: `https://www.sciencedirect.com/science/article/pii/S0168900207003270`.

[49] The ATLAS TRT Collaboration. "The ATLAS Transition Radiation Tracker (TRT) proportional drift tube: design and performance." In: *Journal of Instrumentation* 3.02 (2008), P02013–P02013. doi: `10.1088/1748-0221/3/02/p02013`. url: `https://doi.org/10.1088/1748-0221/3/02/p02013`.

[50] The ATLAS TRT Collaboration. "The ATLAS TRT Barrel Detector." In: *Journal of Instrumentation* 3.02 (2008), P02014–P02014. doi: `10.1088/1748-0221/3/02/p02014`. url: `https://doi.org/10.1088/1748-0221/3/02/p02014`.

[51] The ATLAS TRT Collaboration. "The ATLAS TRT end-cap detectors." In: *Journal of Instrumentation* 3.10 (2008), P10003–P10003. doi: `10.1088/1748-0221/3/10/p10003`. url: `https://doi.org/10.1088/1748-0221/3/10/p10003`.

[52] S Fratina and E Klinkby. *The Geometry of the ATLAS Transition Radiation Tracker*. Tech. rep. Geneva: CERN, 2010. url: `https://cds.cern.ch/record/1232064`.

[53] ATLAS Collaboration. *Particle Identification Performance of the ATLAS Transition Radiation Tracker*. Tech. rep. Geneva: CERN, 2011. url: `https://cds.cern.ch/record/1383793`.

[54] J. Pequenao. "Computer generated image of the ATLAS inner detector." 2008. url: `https://cds.cern.ch/record/1095926`.

[55] ATLAS Collaboration. *ATLAS liquid-argon calorimeter: Technical Design Report*. Technical design report. ATLAS. Geneva: CERN, 1996. url: `https://cds.cern.ch/record/331061`.

[56] ATLAS Collaboration. *ATLAS tile calorimeter: Technical Design Report*. Technical design report. ATLAS. Geneva: CERN, 1996. url: `https://cds.cern.ch/record/331062`.

[57] ATLAS Collaboration. *ATLAS muon spectrometer: Technical Design Report*. Technical design report. ATLAS. Geneva: CERN, 1997. url: `https://cds.cern.ch/record/331068`.

[58] F. Bauer, U. Bratzler, H. Dietl, H. Kroha, T. Lagouri, A. Manz, A. Ostapchuk, R. Richter, S. Schael, S. Chouridou, M. Deile, O. Kortner, A. Staude, R. Ströhmer, and T. Trefzger. "Construction and test of MDT chambers for the ATLAS muon spectrometer." In: *Nuclear Instruments and Methods in Physics Research Section A: Accelerators, Spectrometers, Detectors and Associated Equipment* 461.1 (2001). 8th Pisa Meeting on Advanced Detectors, pp. 17–20. issn: 0168-9002. doi: `https://doi.org/10.1016/S0168-9002(00)01156-6`. url: `https://www.sciencedirect.com/science/article/pii/S0168900200011566`.

[59] T. Argyropoulos, K. A. Assamagan, B. H. Benedict, V. Chernyatin, E. Cheu, J. Deng, A. Gordeev, I. G. Eschrich, V. Grachev, K. Johns, S. S. Junnarkar, A. Kandasamy, V. Kaushik, A. Khodinov, A. Lankford, X. Lei, R. M. Garcia, K. Nikolopoulos, P. O'Connor, C. L. Parnell-Lampen, W. Park, V. Polychronakos, R. Porter, M. Purohit, M. Schernau, B. K. Toggerson, and D. Tompkins. "Cathode Strip Chambers in ATLAS: Installation, Commissioning and in Situ Performance." In: *IEEE Transactions on Nuclear Science* 56.3 (2009), pp. 1568–1574. doi: `10.1109/TNS.2009.2020861`.

[60] S. Majewski, G. Charpak, A. Breskin, and G. Mikenberg. "A thin multiwire chamber operating in the high multiplication mode." In: *Nuclear Instruments and Methods in Physics Research* 217.1 (1983), pp. 265–271. issn: 0167-5087. doi: `https://doi.org/10.1016/0167-5087(83)90146-1`. url: `https://www.sciencedirect.com/science/article/pii/0167508783901461`.

[61] W. P. V. and. "The ATLAS Data Acquisition System in LHC Run 2." In: *Journal of Physics: Conference Series* 898 (2017), p. 032017. doi: `10.1088/1742-6596/898/3/032017`. url: `https://doi.org/10.1088/1742-6596/898/3/032017`.

[62] ATLAS Collaboration. *ATLAS Computing: technical design report*. Technical design report. ATLAS. Geneva: CERN, 2005. url: `https://cds.cern.ch/record/837738`.

[63] L Adamczyk, E Bana, A Brandt, M Bruschi, S Grinstein, J Lange, M Rijssenbeek, P Sicho, R Staszewski, T Sykora, M Trzebiski, J Chwastowski, and K Korcyl. *Technical Design Report for the ATLAS Forward Proton Detector*. Tech. rep. 2015. url: `https://cds.cern.ch/record/2017378`.

[64] L Adamczyk, E Bana, A Brandt, M Bruschi, S Grinstein, J Lange, M Rijssenbeek, P Sicho, R Staszewski, T Sykora, M Trzebiski, J Chwastowski, and K Korcyl. *Technical Design Report for the ATLAS Forward Proton Detector*. Tech. rep. 2015. url: https://cds.cern.ch/record/2017378.

[65] M. Trzebinski. *Prospects for Proton-Proton Measurements with Tagged Protons in ATLAS*. 2019. arXiv: 1909.10827 [physics.ins-det].

[66] ATLAS Collaboration. *Exclusive Jet Production with Forward Proton Tagging*. Tech. rep. Geneva: CERN, 2015. url: https://cds.cern.ch/record/1993686.

[67] M. Trzebiski, R. Staszewski, and J. Chwastowski. "On the possibility of measuring the single-tagged exclusive jets at the LHC." In: *The European Physical Journal C* 75.7 (2015). issn: 1434-6052. doi: 10.1140/epjc/s10052-015-3541-3. url: http://dx.doi.org/10.1140/epjc/s10052-015-3541-3.

[68] ATLAS Collaboration. "Search for pair- and single-production of vector-like quarks in final states with at least one Z boson decaying into a pair of electrons or muons in pp collision data collected with the ATLAS detector." In: *Phys. Rev. D* 98 (2018), p. 112010. doi: 10.1103/PhysRevD.98.112010. arXiv: 1806.10555 [hep-ex].

[69] T. Vale. *Search for vector-like quarks with the ATLAS experiment*. https://repositorium.sdum.uminho.pt/bitstream/1822/56014/1/Thesis_Tiago_.pdf.

[70] J. Thaler and K. Van Tilburg. "Identifying boosted objects with N-subjettiness." In: *Journal of High Energy Physics* 2011.3 (2011). issn: 1029-8479. doi: 10.1007/jhep03(2011)015. url: http://dx.doi.org/10.1007/JHEP03(2011)015.

[71] O. Matsedonskyi, G. Panico, and A. Wulzer. "On the interpretation of Top Partners searches." In: *Journal of High Energy Physics* 2014.12 (2014), p. 97. doi: 10.1007/JHEP12(2014)097. url: https://doi.org/10.1007/JHEP12(2014)097.

[72] CMS Collaboration. "Search for vector-like quarks in events with two oppositely charged leptons and jets in proton-proton collisions at $\sqrt{s} = 13$ TeV." In: *Eur. Phys. J.* C79.4 (2019), p. 364. doi: 10.1140/epjc/s10052-019-6855-8. arXiv: 1812.09768 [hep-ex].

[73] ATLAS Collaboration. "Search for large missing transverse momentum in association with one top-quark in proton–proton collisions at $\sqrt{s} = 13$ TeV with the ATLAS detector." In: *JHEP* 05 (2019), p. 041. doi: 10.1007/JHEP05(2019)041. arXiv: 1812.09743 [hep-ex].

[74] CMS Collaboration. "Search for single production of vector-like quarks decaying to a Z boson and a top or a bottom quark in proton-proton collisions at $\sqrt{s} = 13$ TeV." In: *JHEP* 05 (2017), p. 029. doi: 10.1007/JHEP05(2017)029. arXiv: 1701.07409 [hep-ex].

[75] CMS Collaboration. "Search for single production of a vector-like T quark decaying to a Z boson and a top quark in proton–proton collisions at $\sqrt{s}$=13TeV." In: *Physics Letters B* 781 (2018), pp. 574–600. issn: 0370-2693. doi: `10.1016/j.physletb.2018.04.036`. url: `http://dx.doi.org/10.1016/j.physletb.2018.04.036`.

[76] ATLAS Collaboration. "Search for single production of vector-like quarks decaying into Wb in pp collisions at $\sqrt{s} = 13$ TeV with the ATLAS detector." In: *JHEP* 05 (2019), p. 164. doi: `10.1007/JHEP05(2019)164`. arXiv: `1812.07343 [hep-ex]`.

[77] ATLAS Collaboration. "Search for new phenomena in events with same-charge leptons and b-jets in pp collisions at $\sqrt{s} = 13$ TeV with the ATLAS detector." In: *JHEP* 12 (2018), p. 039. doi: `10.1007/JHEP12(2018)039`. arXiv: `1807.11883 [hep-ex]`.

[78] CMS Collaboration. "Search for electroweak production of a vector-like T quark using fully hadronic final states." In: (2019). arXiv: `1909.04721 [hep-ex]`.

[79] CMS Collaboration. "Search for single production of vector-like quarks decaying to a top quark and a W boson in proton-proton collisions at $\sqrt{s} = 13$ TeV." In: *Eur. Phys. J.* C79 (2019), p. 90. doi: `10.1140/epjc/s10052-019-6556-3`. arXiv: `1809.08597 [hep-ex]`.

[80] CMS Collaboration. "Search for single production of vector-like quarks decaying to a b quark and a Higgs boson." In: *JHEP* 06 (2018), p. 031. doi: `10.1007/JHEP06(2018)031`. arXiv: `1802.01486 [hep-ex]`.

[81] A. Roy, N. Nikiforou, N. Castro, and T. Andeen. "Novel interpretation strategy for searches of singly produced vectorlike quarks at the LHC." In: *Phys. Rev. D* 101.11 (2020), p. 115027. doi: `10.1103/PhysRevD.101.115027`. arXiv: `2003.00640 [hep-ph]`.

[82] A. Buckley, J. Butterworth, L. Corpe, D. Huang, and P. Sun. "New sensitivity of current LHC measurements to vector-like quarks." In: *SciPost Physics* 9.5 (2020). issn: 2542-4653. doi: `10.21468/scipostphys.9.5.069`. url: `http://dx.doi.org/10.21468/SciPostPhys.9.5.069`.

[83] J. M. Butterworth, D. Grellscheid, M. Krämer, B. Sarrazin, and D. Yallup. "Constraining new physics with collider measurements of Standard Model signatures." In: *Journal of High Energy Physics* 2017.3 (2017). issn: 1029-8479. doi: `10.1007/jhep03(2017)078`. url: `http://dx.doi.org/10.1007/JHEP03(2017)078`.

[84] CMS Collaboration. "Search for pair production of vector-like quarks in the fully hadronic final state." In: (2019). arXiv: `1906.11903 [hep-ex]`.

[85] ATLAS Collaboration. "Combination of the searches for pair-produced vector-like partners of the third-generation quarks at $\sqrt{s} = 13$ TeV with the ATLAS detector." In: *Phys. Rev. Lett.* 121 (2018), p. 211801. doi: `10.1103/PhysRevLett.121.211801`. arXiv: `1808.02343 [hep-ex]`.

[86] ATLAS Collaboration. "Search for pair production of vector-like top quarks in events with one lepton, jets, and missing transverse momentum in $\sqrt{s} = 13$ TeV pp collisions with the ATLAS detector." In: *Journal of High Energy Physics* 2017.8 (2017). issn: 1029-8479. doi: 10.1007/jhep08(2017) 052. url: http://dx.doi.org/10.1007/JHEP08(2017)052.

[87] ATLAS Collaboration. "Search for pair production of up-type vector-like quarks and for four-top-quark events in final states with multiple b-jets with the ATLAS detector." In: *Journal of High Energy Physics* 2018.7 (2018). issn: 1029-8479. doi: 10.1007/jhep07(2018)089. url: http://dx.doi.org/10.1007/JHEP07(2018)089.

[88] ATLAS Collaboration. "Search for pair production of heavy vectorlike quarks decaying into hadronic final states in pp collisions at $\sqrt{s} = 13$ TeV with the ATLAS detector." In: *Phys. Rev. D* 98 (9 2018), p. 092005. doi: 10.1103/PhysRevD.98.092005. url: https://link.aps.org/doi/10.1103/PhysRevD.98.092005.

[89] ATLAS Collaboration. "Search for pair production of heavy vector-like quarks decaying to high-pT W bosons and b quarks in the lepton-plus-jets final state in pp collisions at $\sqrt{s} = 13$ TeV with the ATLAS detector." In: *Journal of High Energy Physics* 2017.10 (2017). issn: 1029-8479. doi: 10.1007/jhep10(2017)141. url: http://dx.doi.org/10.1007/JHEP10(2017)141.

[90] ATLAS Collaboration. "Search for pair production of heavy vector-like quarks decaying into high-pT W bosons and top quarks in the lepton-plus-jets final state in pp collisions at $\sqrt{s} = 13$TeV with the ATLAS detector." In: *Journal of High Energy Physics* 2018.8 (2018). issn: 1029-8479. doi: 10.1007/jhep08(2018)048. url: http://dx.doi.org/10.1007/JHEP08(2018)048.

[91] S. Agostinelli et al. "GEANT4 – a simulation toolkit." In: *Nucl. Instrum. Meth. A* 506 (2003), p. 250. doi: 10.1016/S0168-9002(03)01368-8.

[92] T. Gleisberg, S. Höche, F. Krauss, M. Schönherr, S. Schumann, F. Siegert, and W. J. "Event generation with SHERPA 1.1." In: *JHEP* 02 (2009), p. 007. doi: 10.1088/1126-6708/2009/02/007. arXiv: 0811.4622 [hep-ph].

[93] S. Höche, F. Krauss, S. Schumann, and F. Siegert. "QCD matrix elements and truncated showers." In: *JHEP* 05 (2009), p. 053. doi: 10.1088/1126-6708/2009/05/053. arXiv: 0903.1219 [hep-ph].

[94] T. Gleisberg and S. Höche. "Comix, a new matrix element generator." In: *JHEP* 12 (2008), p. 039. doi: 10.1088/1126-6708/2008/12/039. arXiv: 0808.3674 [hep-ph].

[95] S. Schumann and F. Krauss. "A parton shower algorithm based on Catani–Seymour dipole factorisation." In: *JHEP* 03 (2008), p. 038. doi: 10.1088/1126-6708/2008/03/038. arXiv: 0709.1027 [hep-ph].

[96] C. Anastasiou, L. J. Dixon, K. Melnikov, and F. Petriello. "High precision QCD at hadron colliders: Electroweak gauge boson rapidity distributions at next-to-next-to leading order." In: *Phys. Rev. D* 69 (2004), p. 094008. doi: `10.1103/PhysRevD.69.094008`. arXiv: `hep-ph/0312266`.

[97] R. D. Ball et al. "Parton distributions for the LHC run II." In: *JHEP* 04 (2015), p. 040. doi: `10.1007/JHEP04(2015)040`. arXiv: `1410.8849 [hep-ph]`.

[98] S. Höche, F. Krauss, M. Schönherr, and F. Siegert. "QCD matrix elements + parton showers. The NLO case." In: *Journal of High Energy Physics* 2013.4 (2013), p. 27. doi: `10.1007/JHEP04(2013)027`. url: `https://doi.org/10.1007/JHEP04(2013)027`.

[99] S. Alioli, P. Nason, C. Oleari, and E. Re. "A general framework for implementing NLO calculations in shower Monte Carlo programs: the POWHEG BOX." In: *JHEP* 06 (2010), p. 043. doi: `10.1007/JHEP06(2010)043`. arXiv: `1002.2581 [hep-ph]`.

[100] J. M. Campbell, R. K. Ellis, P. Nason, and E. Re. "Top-Pair Production and Decay at NLO Matched with Parton Showers." In: *JHEP* 04 (2015), p. 114. doi: `10.1007/JHEP04(2015)114`. arXiv: `1412.1828 [hep-ph]`.

[101] ATLAS Collaboration. *ATLAS Pythia 8 tunes to 7 TeV data*. ATL-PHYS-PUB-2014-021. 2014. url: `https://cds.cern.ch/record/1966419`.

[102] M. Czakon and A. Mitov. "Top++: A program for the calculation of the top-pair cross-section at hadron colliders." In: *Comput. Phys. Commun.* 185 (2014), p. 2930. doi: `10.1016/j.cpc.2014.06.021`. arXiv: `1112.5675 [hep-ph]`.

[103] M. Czakon, P. Fiedler, and A. Mitov. "Total Top-Quark Pair-Production Cross Section at Hadron Colliders Through $O(\alpha_S^4)$." In: *Phys. Rev. Lett.* 110 (2013), p. 252004. doi: `10.1103/PhysRevLett.110.252004`. arXiv: `1303.6254 [hep-ph]`.

[104] M. Beneke, P. Falgari, S. Klein, and C. Schwinn. "Hadronic top-quark pair production with NNLL threshold resummation." In: *Nucl. Phys. B* 855 (2012), pp. 695–741. doi: `10.1016/j.nuclphysb.2011.10.021`. arXiv: `1109.1536 [hep-ph]`.

[105] M. Cacciari, M. Czakon, M. Mangano, A. Mitov, and P. Nason. "Top-pair production at hadron colliders with next-to-next-to-leading logarithmic soft-gluon resummation." In: *Phys. Lett. B* 710 (2012), pp. 612–622. doi: `10.1016/j.physletb.2012.03.013`. arXiv: `1111.5869 [hep-ph]`.

[106] M. Czakon and A. Mitov. "NNLO corrections to top pair production at hadron colliders: the quark-gluon reaction." In: *JHEP* 01 (2013), p. 080. doi: `10.1007/JHEP01(2013)080`. arXiv: `1210.6832 [hep-ph]`.

[107] M. Czakon and A. Mitov. "NNLO corrections to top-pair production at hadron colliders: the all-fermionic scattering channels." In: *JHEP* 12 (2012), p. 054. doi: `10.1007/JHEP12(2012)054`. arXiv: `1207.0236 [hep-ph]`.

[108]   P. Bärnreuther, M. Czakon, and A. Mitov. "Percent-Level-Precision Physics at the Tevatron: Next-to-Next-to-Leading Order QCD Corrections to $q\bar{q} \rightarrow t\bar{t} + X$." In: *Phys. Rev. Lett.* 109 (2012), p. 132001. doi: 10.1103/PhysRevLett.109.132001. arXiv: 1204.5201 [hep-ph].

[109]   J. Aguilar-Saavedra. *Protos - PROgram for TOp Simulations.*

[110]   T. Sjöstrand, S. Ask, J. R. Christiansen, R. Corke, N. Desai, P. Ilten, S. Mrenna, S. Prestel, C. O. Rasmussen, and P. Z. Skands. "An introduction to PYTHIA 8.2." In: *Comput. Phys. Commun.* 191 (2015), p. 159. doi: 10.1016/j.cpc.2015.01.024. arXiv: 1410.3012 [hep-ph].

[111]   A. D. Martin, W. J. Stirling, R. S. Thorne, and G. Watt. "Parton distributions for the LHC." In: *Eur. Phys. J. C* 63 (2009), p. 189. doi: 10.1140/epjc/s10052-009-1072-5. arXiv: 0901.0002 [hep-ph].

[112]   A. D. Martin, W. J. Stirling, R. S. Thorne, and G. Watt. "Uncertainties on α_S in global PDF analyses and implications for predicted hadronic cross sections." In: *Eur. Phys. J. C* 64 (2009), pp. 653–680. doi: 10.1140/epjc/s10052-009-1164-2. arXiv: 0905.3531 [hep-ph].

[113]   A. D. Martin, W. J. Stirling, R. S. Thorne, and G. Watt. "Heavy-quark mass dependence in global PDF analyses and 3- and 4-flavour parton distributions." In: *Eur. Phys. J. C* 70 (2010), pp. 51–72. doi: 10.1140/epjc/s10052-010-1462-8. arXiv: 1007.2624 [hep-ph].

[114]   ATLAS Collaboration. *Electron efficiency measurements with the ATLAS detector using the 2015 LHC proton-proton collision data*. Tech. rep. Geneva: CERN, 2016. url: https://cds.cern.ch/record/2157687.

[115]   ATLAS Collaboration. "Muon reconstruction performance of the ATLAS detector in proton–proton collision data at $\sqrt{s}$=13 TeV." In: *The European Physical Journal C* 76.5 (2016), p. 292. doi: 10.1140/epjc/s10052-016-4120-y. url: https://doi.org/10.1140/epjc/s10052-016-4120-y.

[116]   M. Cacciari, G. P. Salam, and G. Soyez. "The anti-k_t jet clustering algorithm." In: *JHEP* 04 (2008), p. 063. doi: 10.1088/1126-6708/2008/04/063. arXiv: 0802.1189 [hep-ph].

[117]   ATLAS Collaboration. "Jet energy scale measurements and their systematic uncertainties in proton-proton collisions at $\sqrt{s}$=13TeV with the ATLAS detector." In: *Phys. Rev. D* 96 (7 2017), p. 072002. doi: 10.1103/PhysRevD.96.072002. url: https://link.aps.org/doi/10.1103/PhysRevD.96.072002.

[118]   ATLAS Collaboration. "Performance of pile-up mitigation techniques for jets in ppcollisions at $\sqrt{s} = 8$ TeV using the ATLAS detector." In: *The European Physical Journal C* 76.11 (2016), p. 581. doi: 10.1140/epjc/s10052-016-4395-z. url: https://doi.org/10.1140/epjc/s10052-016-4395-z.

[119] ATLAS Collaboration. *Optimisation of the ATLAS b-tagging performance for the 2016 LHC Run*. Tech. rep. Geneva: CERN, 2016. url: https://cds.cern.ch/record/2160731.

[120] https://www.tu-dortmund.de/.

[121] F. Chollet et al. *Keras*. 2015. url: https://keras.io.

[122] Martín Abadi et al. *TensorFlow: Large-Scale Machine Learning on Heterogeneous Systems*. 2015. url: https://www.tensorflow.org/.

[123] K. Agashe, H. Davoudiasl, G. Perez, and A. Soni. "Warped gravitons at the CERN LHC and beyond." In: *Phys. Rev. D* 76 (3 2007), p. 036006. doi: 10.1103/PhysRevD.76.036006. url: https://link.aps.org/doi/10.1103/PhysRevD.76.036006.

[124] D. P. Kingma and J. Ba. *Adam: A Method for Stochastic Optimization*. 2014. eprint: 1412.6980.

[125] ATLAS Collaboration. *Luminosity determination in pp collisions at $\sqrt{s}$ = 13 TeV using the ATLAS detector at the LHC*. ATLAS-CONF-2019-021. 2019. url: https://cds.cern.ch/record/2677054.

[126] ATLAS Collaboration. "ATLAS b-jet identification performance and efficiency measurement with $t\bar{t}$ events in pp collisions at $\sqrt{s}$ = 13 TeV." In: *The European Physical Journal C* 79.11 (2019). issn: 1434-6052. doi: 10.1140/epjc/s10052-019-7450-8. url: http://dx.doi.org/10.1140/epjc/s10052-019-7450-8.

[127] A. Collaboration. *Optimisation and performance studies of the ATLAS b-tagging algorithms for the 2017-18 LHC run*. Tech. rep. Geneva: CERN, 2017. url: https://cds.cern.ch/record/2273281.

[128] ATLAS Collaboration. *Measurement of b-tagging Efficiency of c-jets in $t\bar{t}$ Events Using a Likelihood Approach with the ATLAS Detector*. Tech. rep. Geneva: CERN, 2018. url: https://cds.cern.ch/record/2306649.

[129] ATLAS Collaboration. *Calibration of light-flavour b-jet mistagging rates using ATLAS proton-proton collision data at $\sqrt{s}$ = 13 TeV*. Tech. rep. Geneva: CERN, 2018. url: https://cds.cern.ch/record/2314418.

[130] ATLAS Collaboration. "Performance of missing transverse momentum reconstruction with the ATLAS detector using proton–proton collisions at $\sqrt{s}$=13 TeV." In: *The European Physical Journal C* 78.11 (2018). issn: 1434-6052. doi: 10.1140/epjc/s10052-018-6288-9. url: http://dx.doi.org/10.1140/epjc/s10052-018-6288-9.

[131] *Measurement of W and Z Boson Production Cross Sections in pp Collisions at root s = 13 TeV in the ATLAS Detector*. Tech. rep. Geneva: CERN, 2015. doi: oai:cds.cern.ch:2045487. url: https://cds.cern.ch/record/2045487.

[132] J Butterworth, E Dobson, U Klein, B Mellado Garcia, T Nunnemann, J Qian, D Rebuzzi, and R Tanaka. *Single Boson and Diboson Production Cross Sections in pp Collisions at $\sqrt{s}$=7 TeV*. Tech. rep. Geneva: CERN, 2010. url: https://cds.cern.ch/record/1287902.

[133] *Modelling of the $t\bar{t}H$ and $t\bar{t}V$ ($V = W, Z$) processes for $\sqrt{s} = 13$ TeV ATLAS analyses*. Tech. rep. Geneva: CERN, 2016. url: http://cds.cern.ch/record/2120826.

[134] L. A. Harland-Lang, A. D. Martin, P. Motylinski, and R. S. Thorne. "Parton distributions in the LHC era: MMHT 2014 PDFs." In: *The European Physical Journal C* 75.5 (2015). issn: 1434-6052. doi: 10.1140/epjc/s10052-015-3397-6. url: http://dx.doi.org/10.1140/epjc/s10052-015-3397-6.

[135] S. Dulat, T.-J. Hou, J. Gao, M. Guzzi, J. Huston, P. Nadolsky, J. Pumplin, C. Schmidt, D. Stump, and C.-P. Yuan. "New parton distribution functions from a global analysis of quantum chromodynamics." In: *Physical Review D* 93.3 (2016). issn: 2470-0029. doi: 10.1103/physrevd.93.033006. url: http://dx.doi.org/10.1103/PhysRevD.93.033006.

[136] ATLAS Collaboration. "Measurements of the production cross-section for a Z boson in association with b-jets in proton-proton collisions at $\sqrt{s}$ = 13 TeV with the ATLAS detector." In: *Journal of High Energy Physics* 2020.7 (2020). issn: 1029-8479. doi: 10.1007/jhep07(2020)044. url: http://dx.doi.org/10.1007/JHEP07(2020)044.

[137] A. L. Read. "Presentation of search results: the CL_S technique." In: *J. Phys. G* 28 (2002), p. 2693. doi: 10.1088/0954-3899/28/10/313.

[138] G. Cowan, K. Cranmer, E. Gross, and O. Vitells. "Asymptotic formulae for likelihood-based tests of new physics." In: *Eur. Phys. J. C* 71 (2011), p. 1554. doi: 10.1140/epjc/s10052-011-1554-0. arXiv: 1007.1727 [physics.data-an].

[139] F. Del Aguila and M. Bowick. "The possibility of new fermions with ΔI = 0 mass." In: *Nuclear Physics B* 224.1 (1983), pp. 107–136. issn: 0550-3213. doi: https://doi.org/10.1016/0550-3213(83)90316-4. url: https://www.sciencedirect.com/science/article/pii/0550321383903164.

[140] F. del Aguila, M. Pérez-Victoria, and J. Santiago. "Effective description of quark mixing." In: *Physics Letters B* 492.1-2 (2000), pp. 98–106. issn: 0370-2693. doi: 10.1016/s0370-2693(00)01071-6. url: http://dx.doi.org/10.1016/S0370-2693(00)01071-6.

[141] F. d. Aguila, J. Santiago, and M. Pérez-Victoria. "Observable contributions of new exotic quarks to quark mixing." In: *Journal of High Energy Physics* 2000.09 (2000), pp. 011–011. issn: 1029-8479. doi: 10.1088/1126-6708/2000/09/011. url: http://dx.doi.org/10.1088/1126-6708/2000/09/011.

[142]   J. A Aguilar–Saavedra. "Identifying top partners at LHC." In: *Journal of High Energy Physics* 2009.11 (2009), pp. 030–030. issn: 1029-8479. doi: 10.1088/1126-6708/2009/11/030. url: http://dx.doi.org/10.1088/1126-6708/2009/11/030.

[143]   ATLAS Collaboration. *Direct constraint on the Higgs-charm coupling from a search for Higgs boson decays to charm quarks with the ATLAS detector*. Tech. rep. Geneva: CERN, 2021. url: https://cds.cern.ch/record/2771724.

[144]   ATLAS Collaboration. *Search for pair-production of vector-like quarks in pp collision events at $\sqrt{s} = 13$ TeV with at least one leptonically-decaying Z boson and a third-generation quark with the ATLAS detector*. Tech. rep. Geneva: CERN, 2021. url: http://cds.cern.ch/record/2773300.

[145]   https://www.hepdata.net.

[146]   K. Cranmer and I. Yavin. "RECAST — extending the impact of existing analyses." In: *Journal of High Energy Physics* 2011.4 (2011). issn: 1029-8479. doi: 10.1007/jhep04(2011)038. url: http://dx.doi.org/10.1007/JHEP04(2011)038.

[147]   L. Heinrich, M. Feickert, and G. Stark. *scikit-hep/pyhf: v0.6.2*. Version v0.6.2. June 2021. doi: 10.5281/zenodo.5009162. url: https://doi.org/10.5281/zenodo.5009162.

[148]   M. C. Romão, N. F. Castro, R. Pedro, and T. Vale. "Transferability of deep learning models in searches for new physics at colliders." In: *Phys. Rev. D* 101 (3 2020), p. 035042. doi: 10.1103/PhysRevD.101.035042. url: https://link.aps.org/doi/10.1103/PhysRevD.101.035042.

[149]   M. Crispim Romão, N. F. Castro, J. G. Milhano, R. Pedro, and T. Vale. "Use of a generalized energy Mover's distance in the search for rare phenomena at colliders." In: *The European Physical Journal C* 81.2 (2021). issn: 1434-6052. doi: 10.1140/epjc/s10052-021-08891-6. url: http://dx.doi.org/10.1140/epjc/s10052-021-08891-6.

[150]   P. T. Komiske, E. M. Metodiev, and J. Thaler. "Metric Space of Collider Events." In: *Phys. Rev. Lett.* 123 (4 2019), p. 041801. doi: 10.1103/PhysRevLett.123.041801. url: https://link.aps.org/doi/10.1103/PhysRevLett.123.041801.

[151]   L. McInnes, J. Healy, and J. Melville. *UMAP: Uniform Manifold Approximation and Projection for Dimension Reduction*. 2020. arXiv: 1802.03426 [stat.ML].

MCBOT outputs

The MCBOT outputs for the control and signal region selections are shown in this appendix.
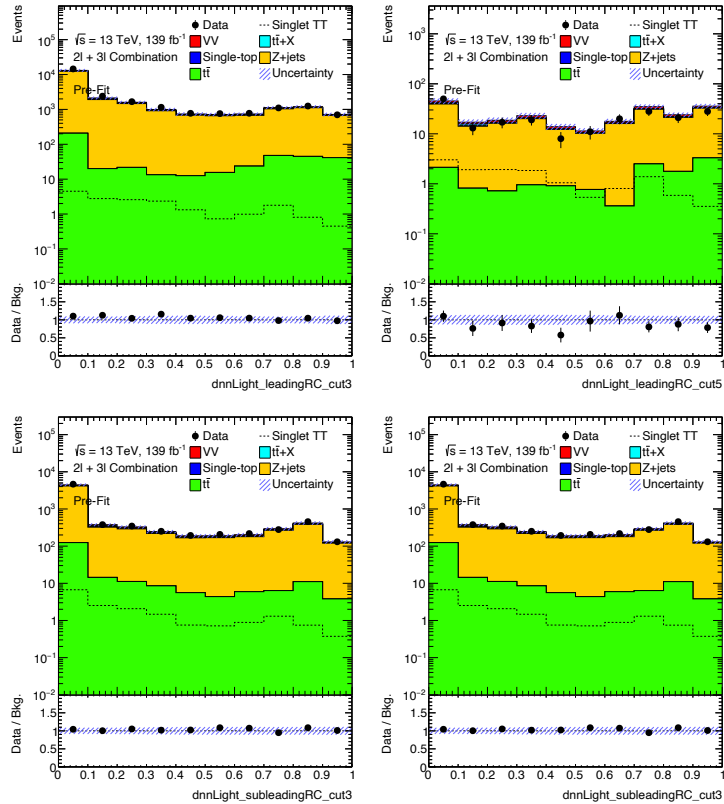
Figure A.1: MCBOT light class outputs for the 2ℓ channel SR (right) and CR (left) cuts, for the leading (top) and sub-leading (bottom) rcjets.
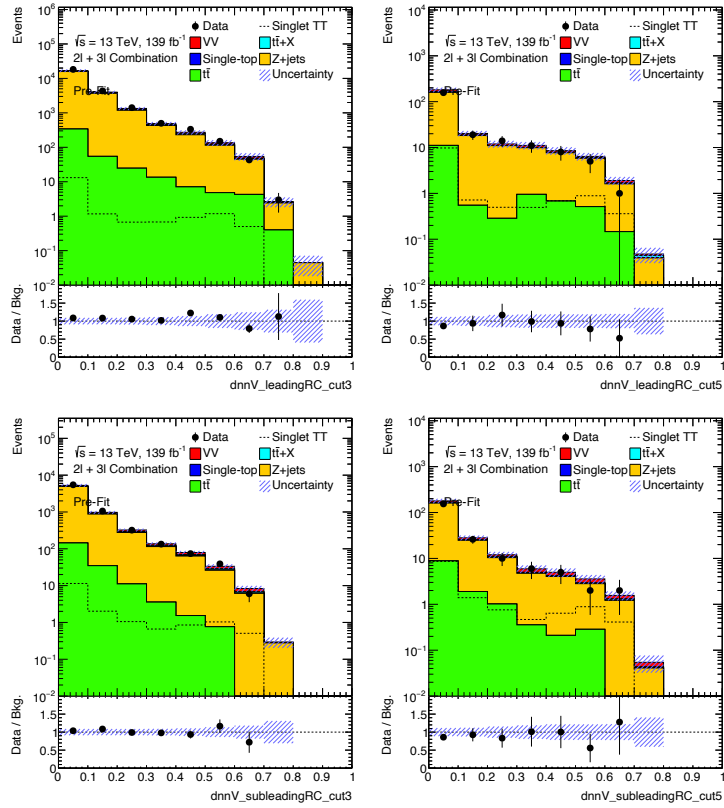
Figure A.2: MCBOT V class outputs for the 2ℓ channel SR (right) and CR (left) cuts, for the leading (top) and sub-leading (bottom) rcjets.
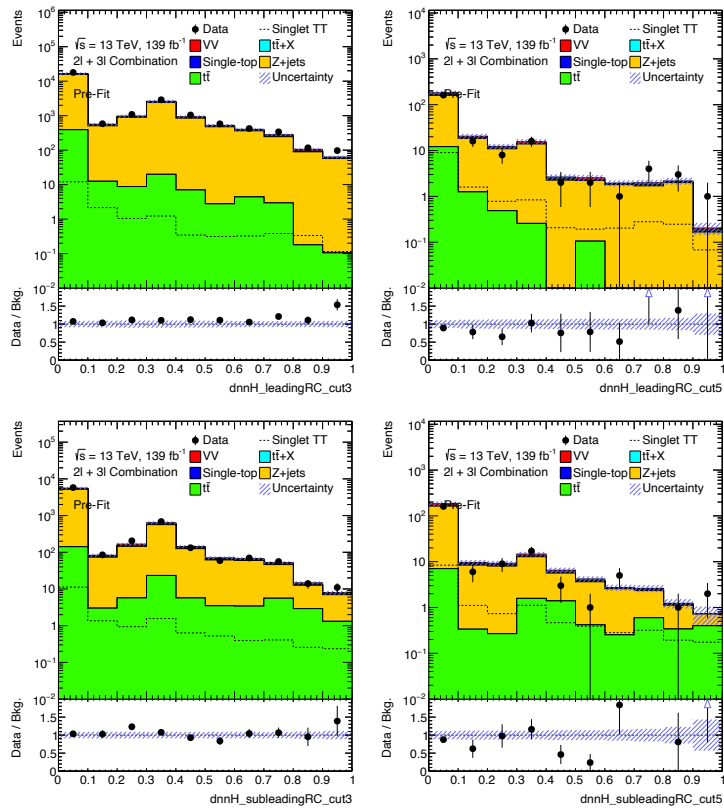
Figure A.3: MCBOT H class outputs for the 2ℓ channel SR (right) and CR (left) cuts, for the leading (top) and sub-leading (bottom) rcjets.
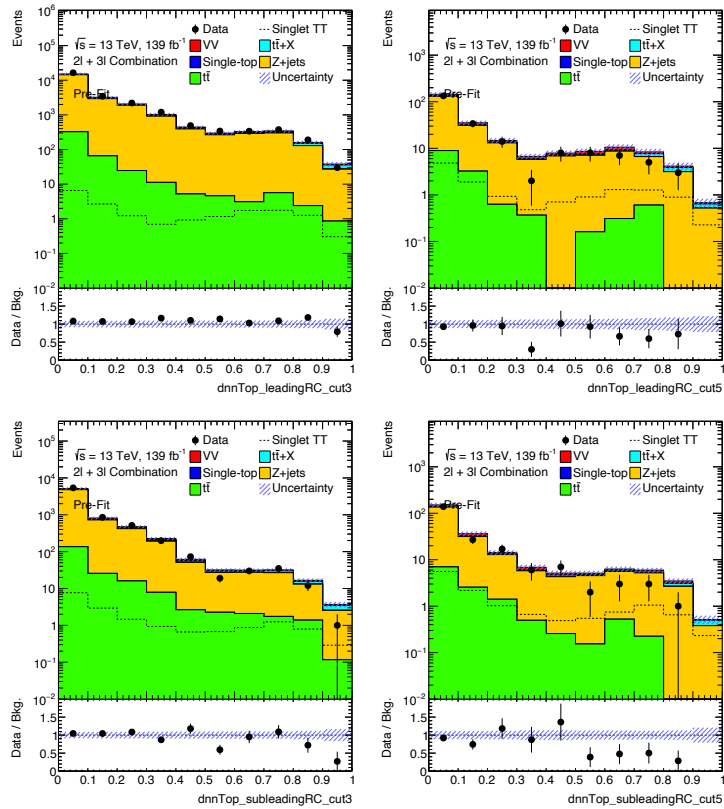
Figure A.4: MCBOT top class outputs for the 2ℓ channel SR (right) and CR (left) cuts, for the leading (top) and sub-leading (bottom) rcjets.
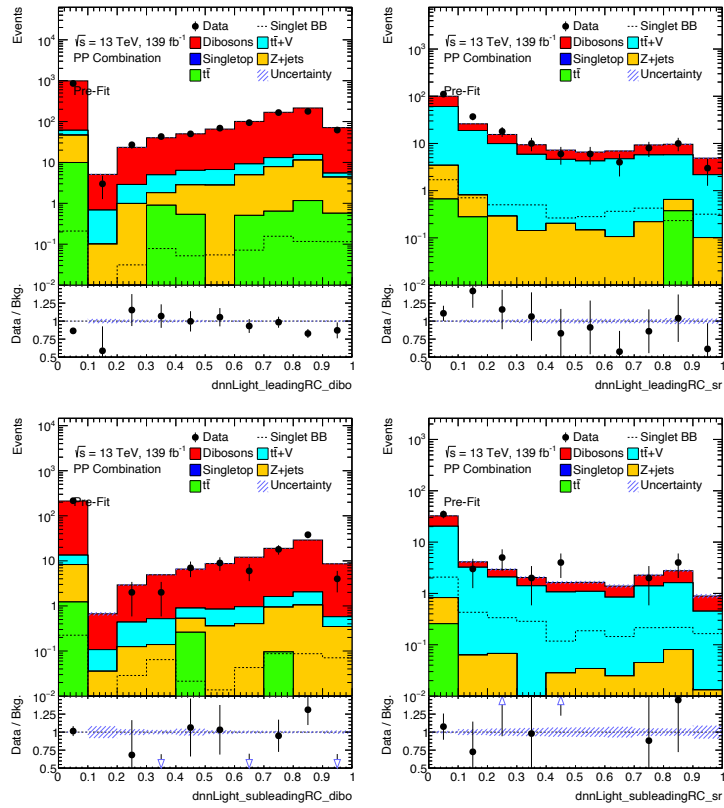
Figure A.5: MCBOT light class outputs for the 3ℓ channel SR (right) and CR (left) cuts, for the leading (top) and sub-leading (bottom) rcjets.
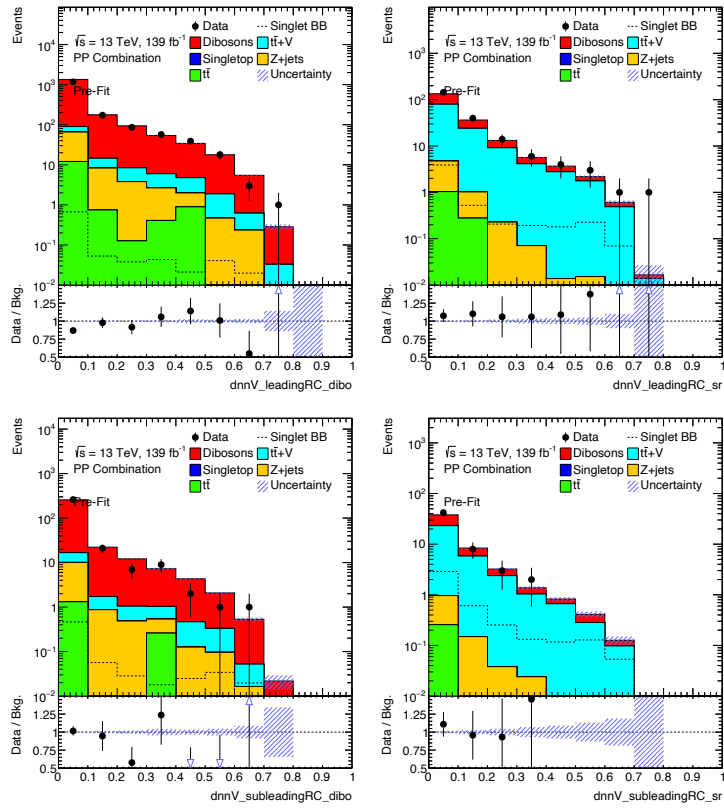
Figure A.6: MCBOT V class outputs for the 3ℓ channel SR (right) and CR (left) cuts, for the leading (top) and sub-leading (bottom) rcjets.
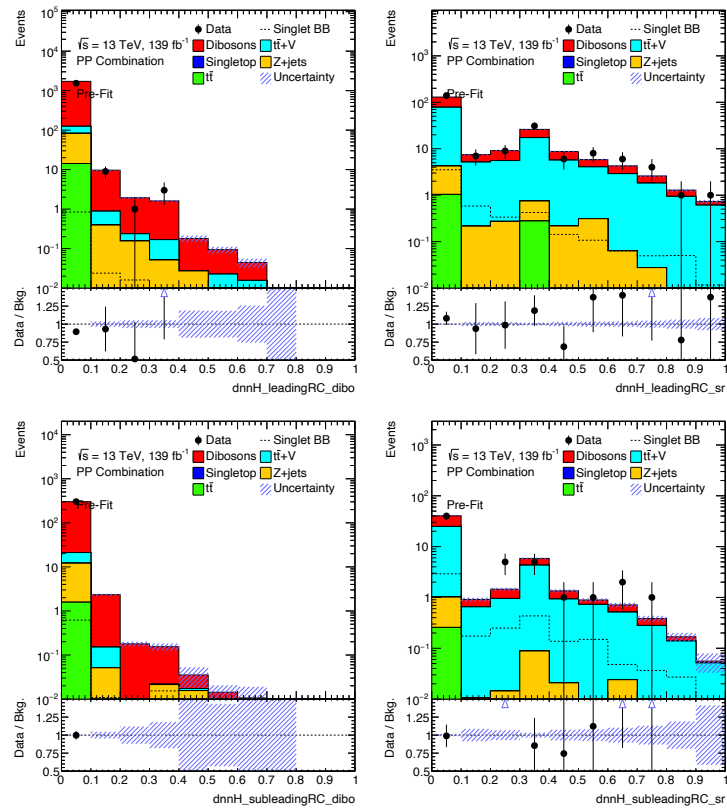
Figure A.7: MCBOT H class outputs for the 3ℓ channel SR (right) and CR (left) cuts, for the leading (top) and sub-leading (bottom) rcjets.
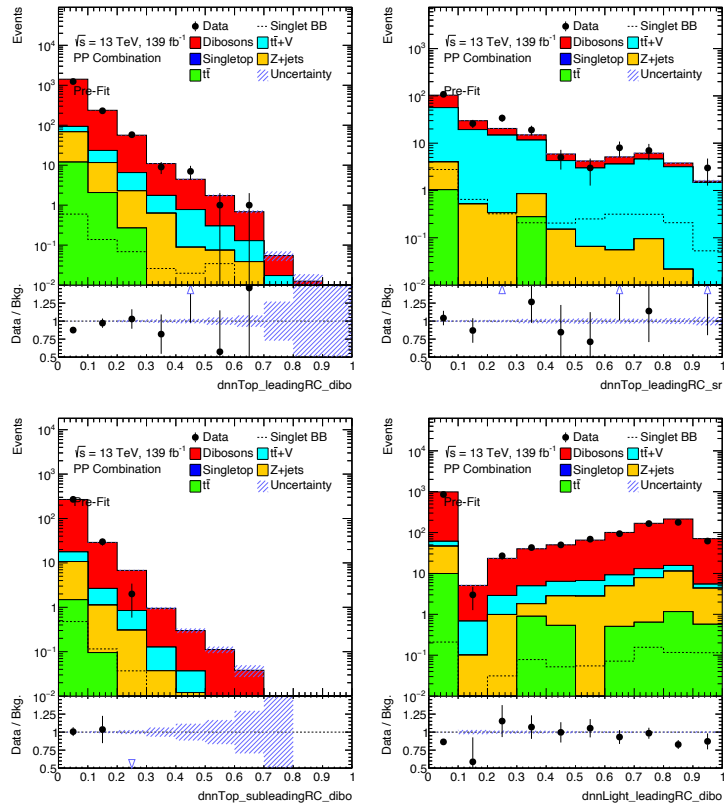
Figure A.8: MCBOT top class outputs for the 3ℓ channel SR (right) and CR (left) cuts, for the leading (top) and sub-leading (bottom) rcjets.

Systematic shape plots

The shapes of systematics can be a very useful resource in order to understand the fit. This appendix shows the shapes of the systematics mentioned during the discussion about the fit.
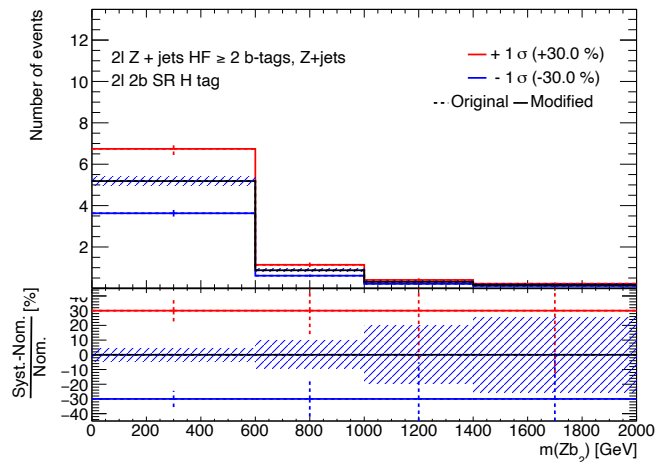
Figure B.1: Shape of Z+jets HF 2b systematic
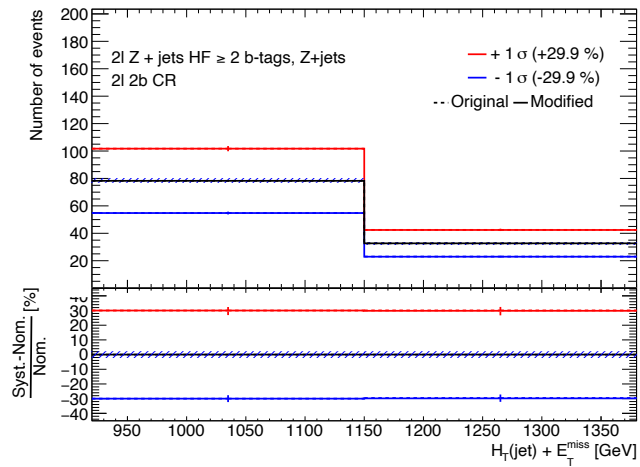
Figure B.2: Shape of Z+jets HF 2b systematic
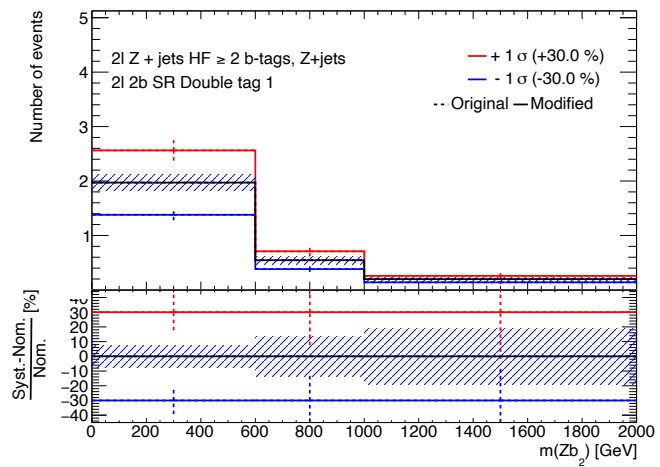
Figure B.3: Shape of Z+jets HF 2b systematic
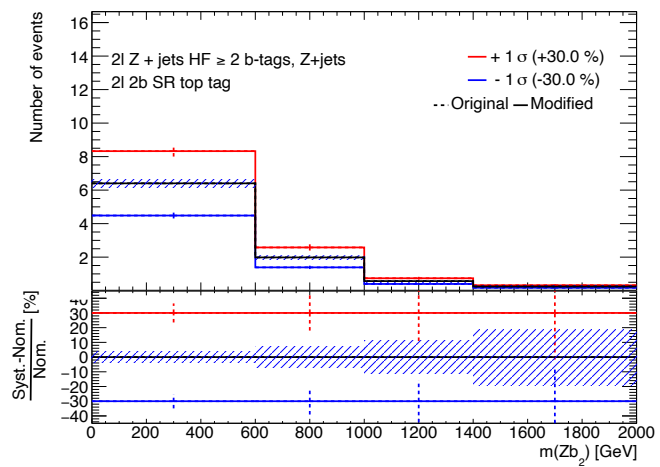
Figure B.4: Shape of Z+jets HF 2b systematic
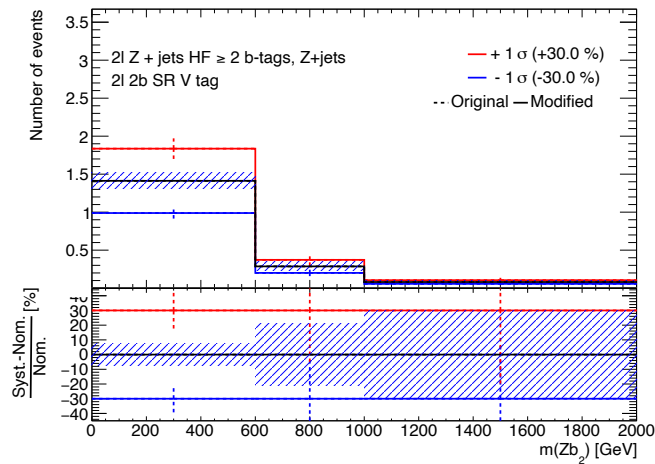
Figure B.5: Shape of Z+jets HF 2b systematic
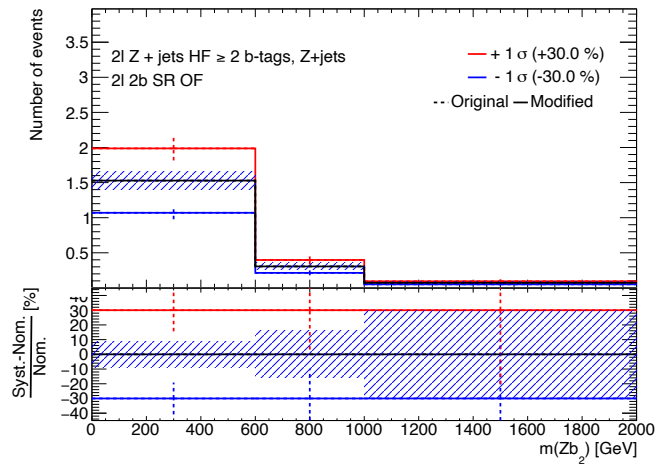
Figure B.6: Shape of Z+jets HF 2b systematic
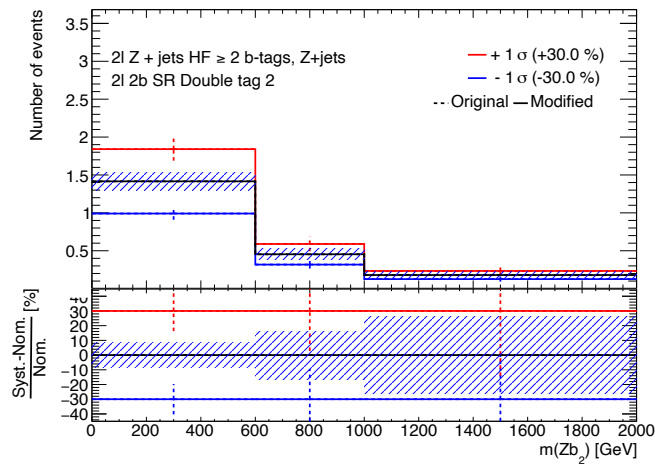
Figure B.7: Shape of Z+jets HF 2b systematic
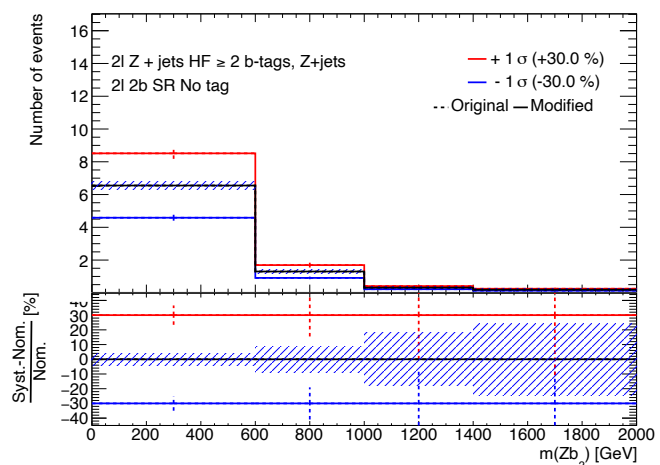
Figure B.8: Shape of Z+jets HF 2b systematic
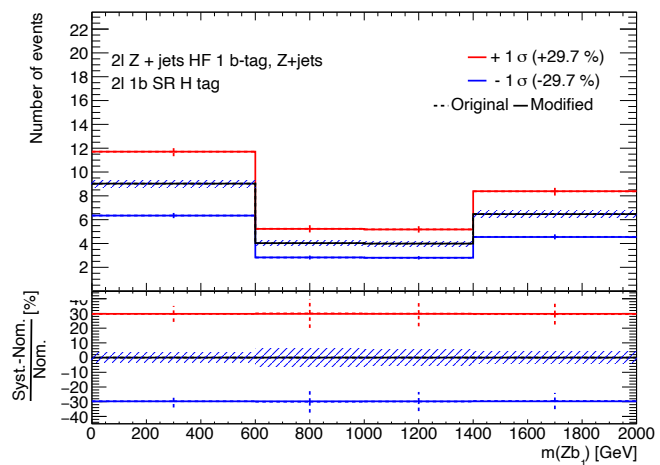
Figure B.9: Shape of Z+jets HF 1b systematic
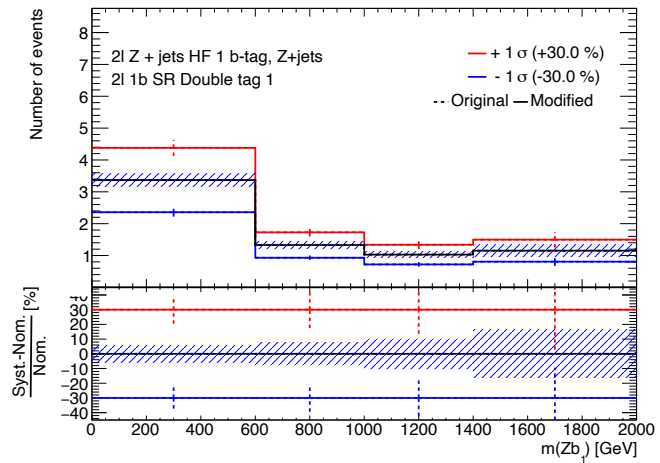
Figure B.10: Shape of Z+jets HF 1b systematic
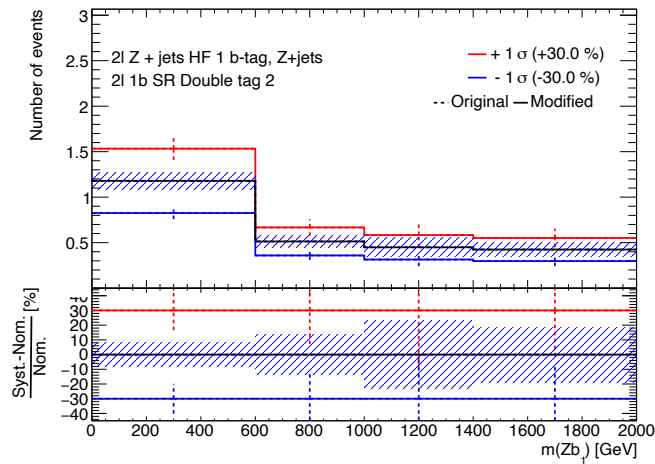
Figure B.11: Shape of Z+jets HF 1b systematic
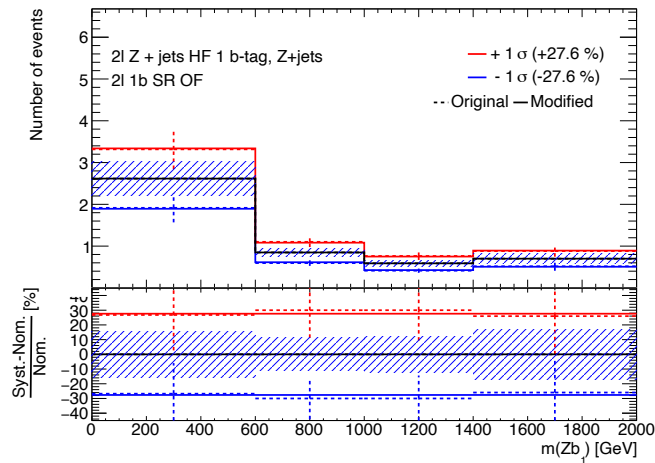
Figure B.12: Shape of Z+jets HF 1b systematic
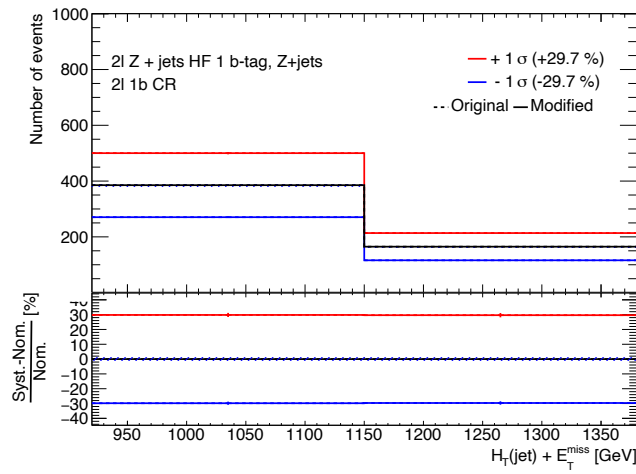
Figure B.13: Shape of Z+jets HF 1b systematic
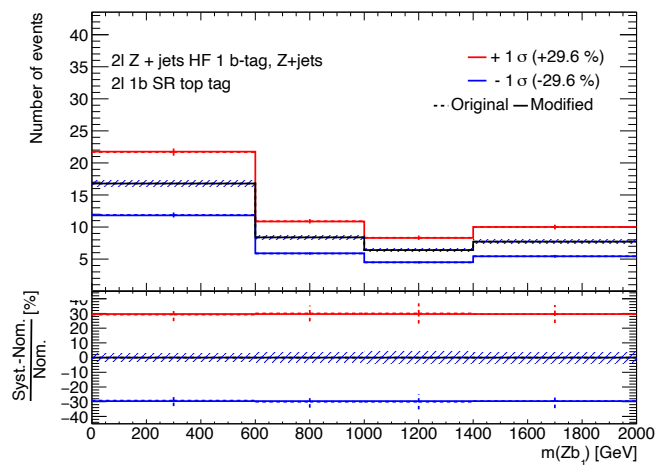
Figure B.14: Shape of Z+jets HF 1b systematic
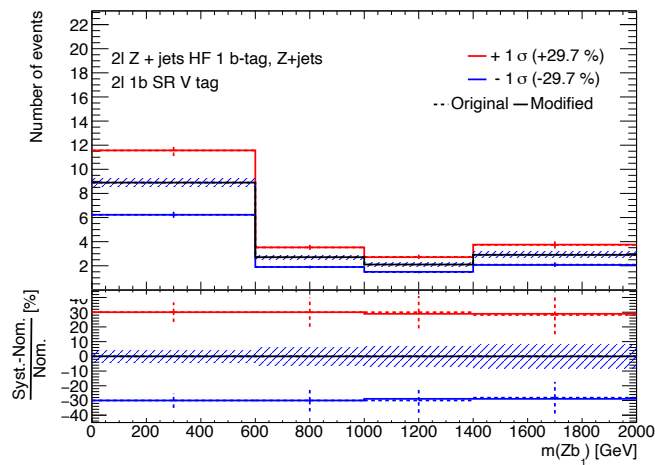
Figure B.15: Shape of Z+jets HF 1b systematic
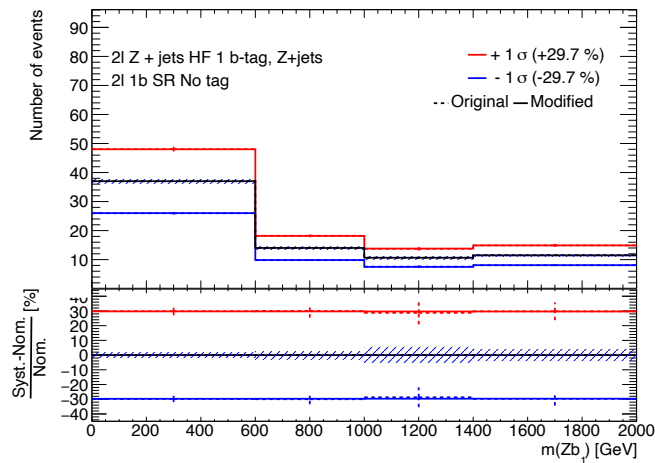
Figure B.16: Shape of Z+jets HF 1b systematic
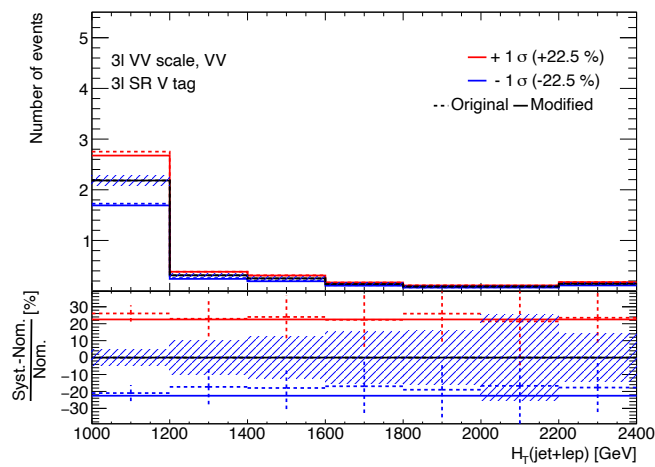
Figure B.17: Shape of 3l VV scale systematic
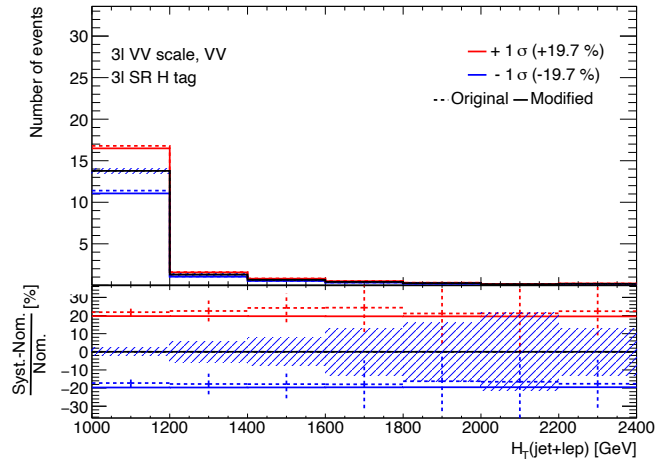
Figure B.18: Shape of 3l VV scale systematic

142
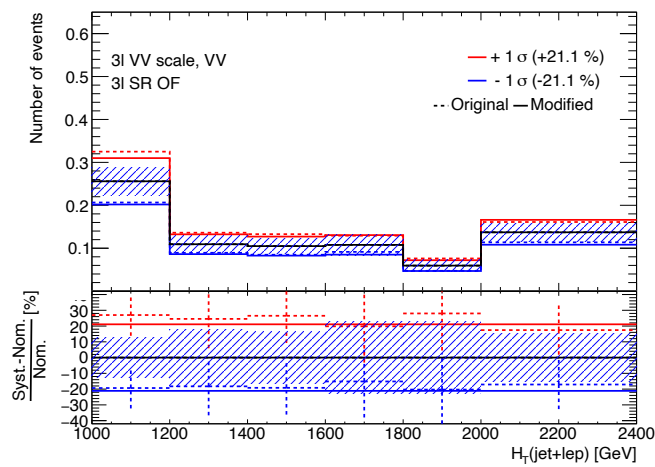
Figure B.19: Shape of 3l VV scale systematic
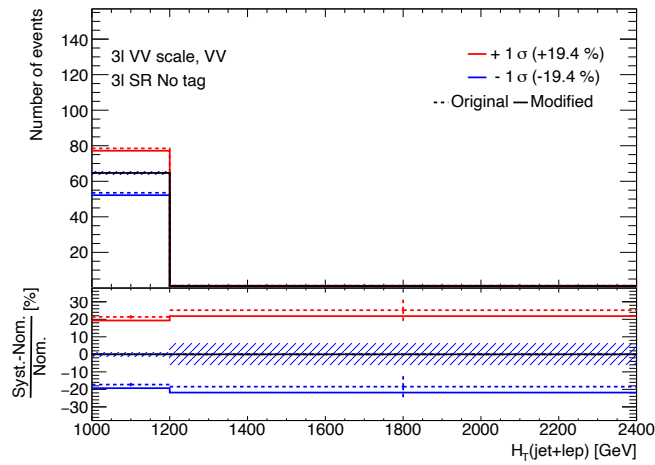
Figure B.20: Shape of 3l VV scale systematic
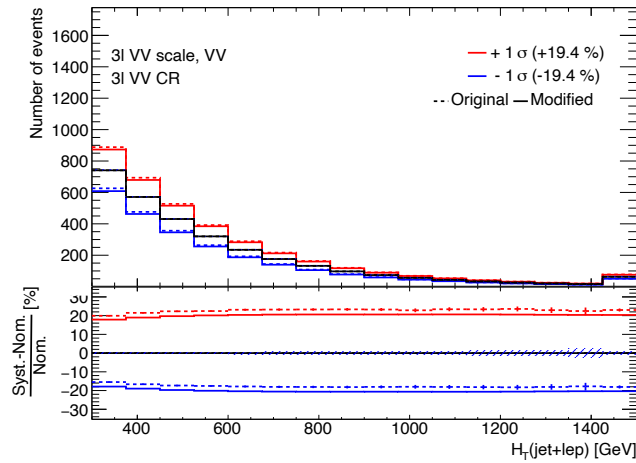
Figure B.21: Shape of 3l VV scale systematic
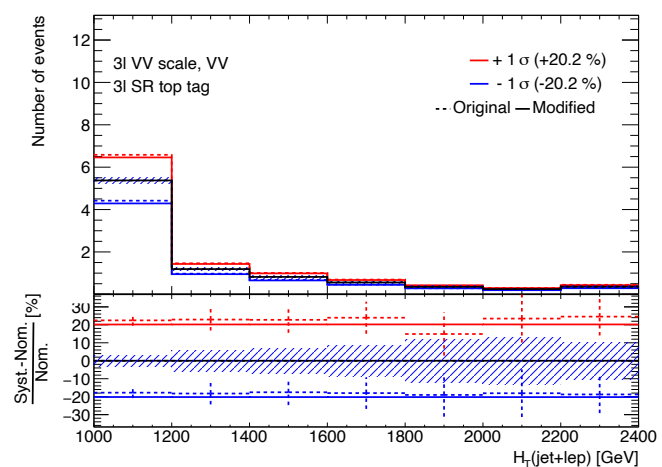
Figure B.22: Shape of 3l VV scale systematic
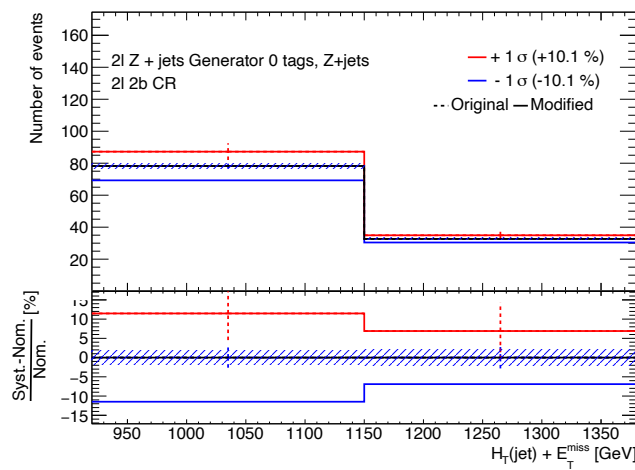
Figure B.23: Shape of 2l Z+jets Generator 0 tags systematic
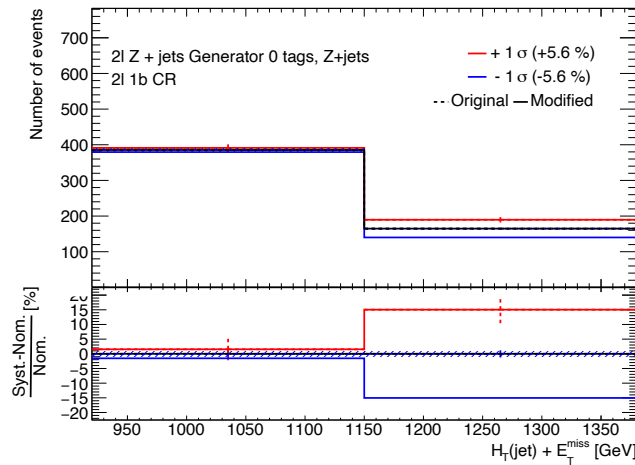
Figure B.24: Shape of 2l Z+jets Generator 0 tags systematic
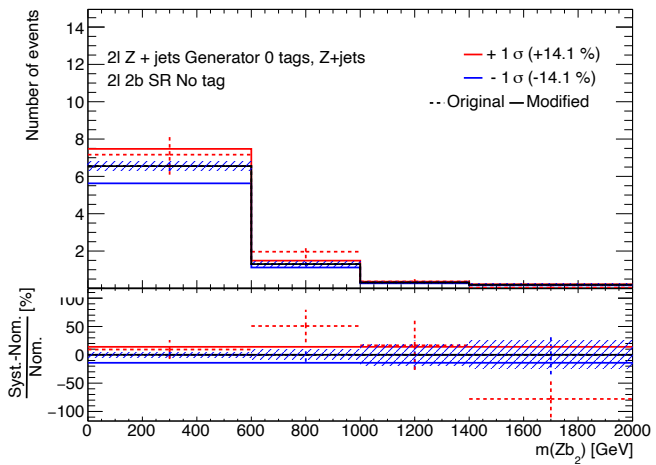
Figure B.25: Shape of 2l Z+jets Generator 0 tags systematic
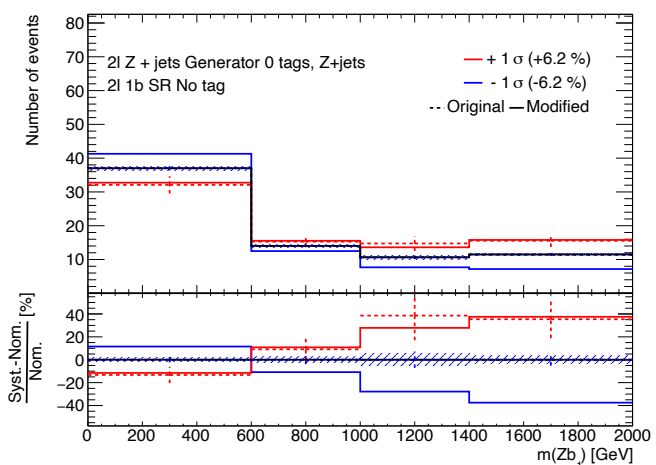
Figure B.26: Shape of 2l Z+jets Generator 0 tags systematic
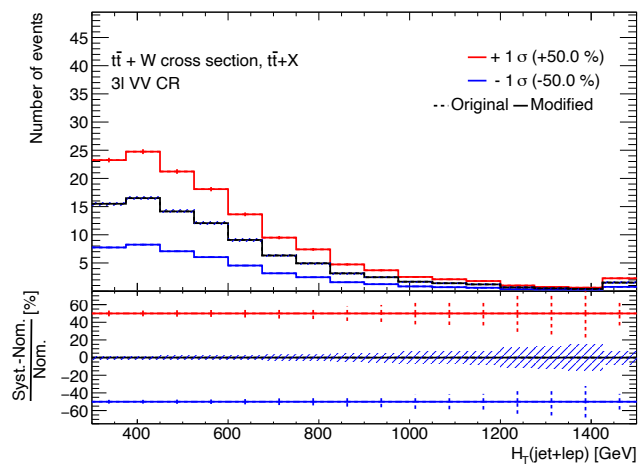
Figure B.27: Shape of $t\bar{t} + W$ cross section systematic
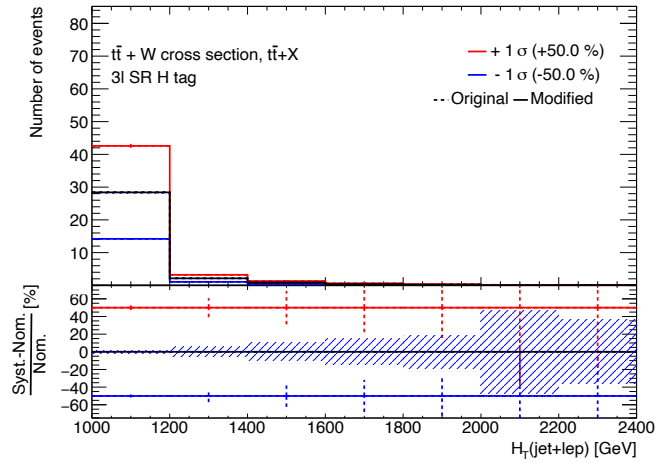
Figure B.28: Shape of $t\bar{t} + W$ cross section systematic

147
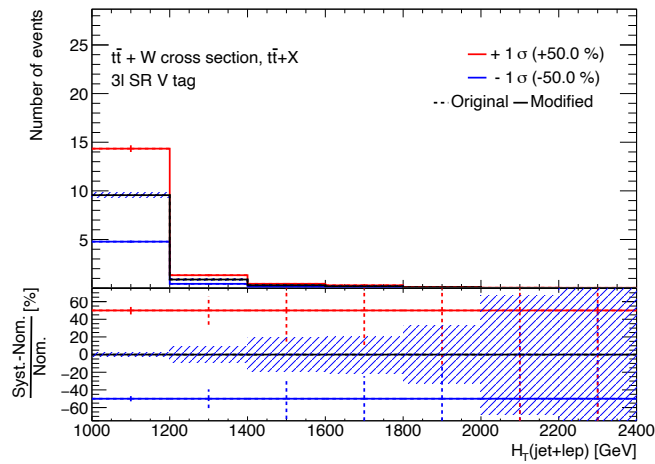
Figure B.29: Shape of $t\bar{t} + W$ cross section systematic
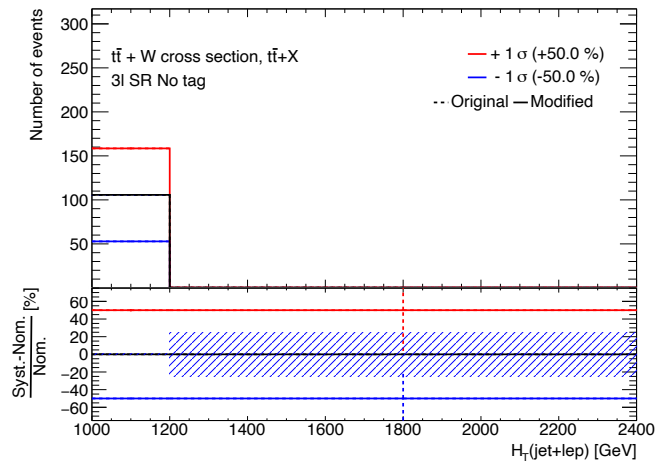
Figure B.30: Shape of $t\bar{t} + W$ cross section systematic
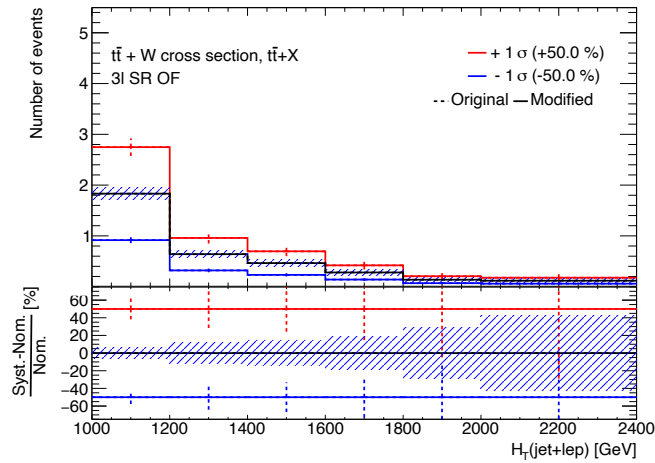
Figure B.31: Shape of $t\bar{t} + W$ cross section systematic
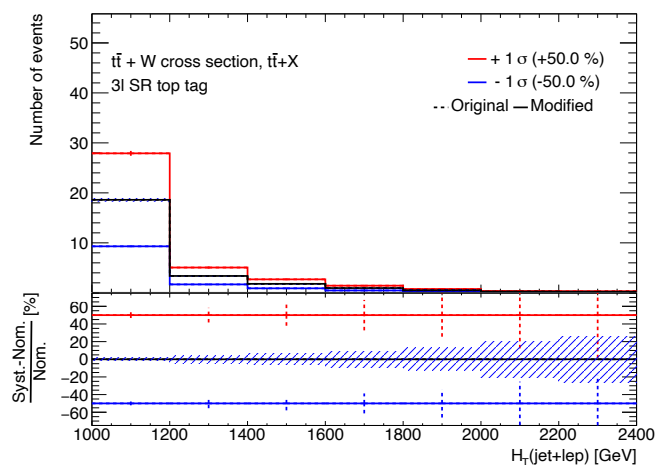
Figure B.32: Shape of $t\bar{t} + W$ cross section systematic
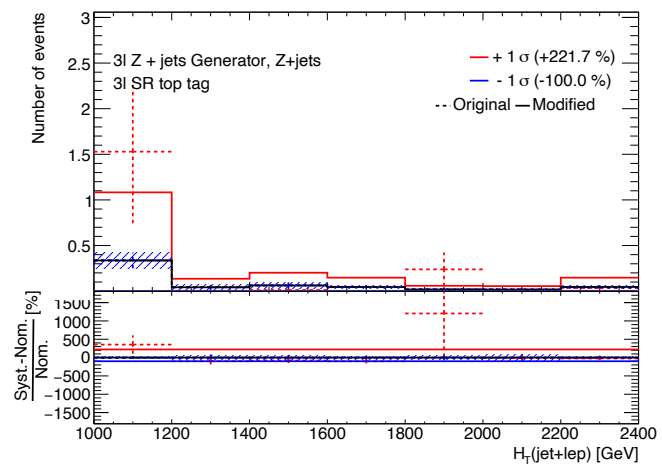
Figure B.33: Shape of 3l Z+jets Generator systematic
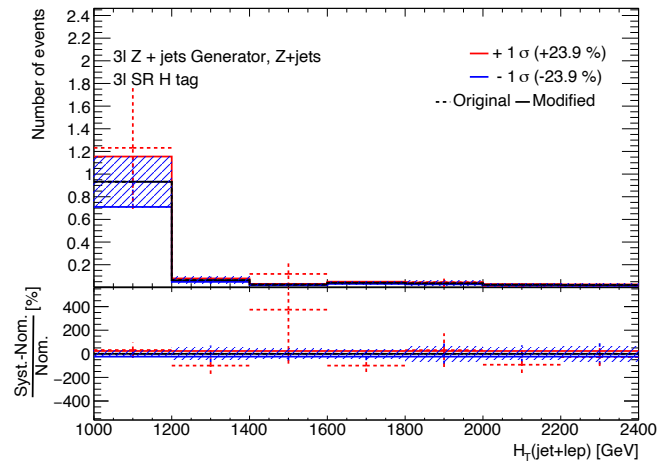
Figure B.34: Shape of 3l Z+jets Generator systematic
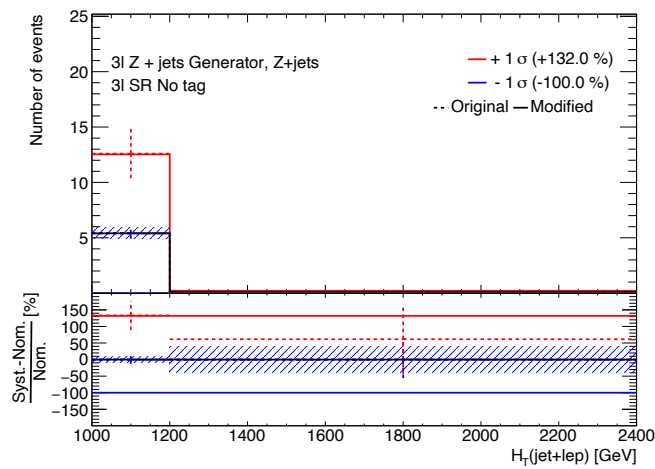
Figure B.35: Shape of 3l Z+jets Generator systematic
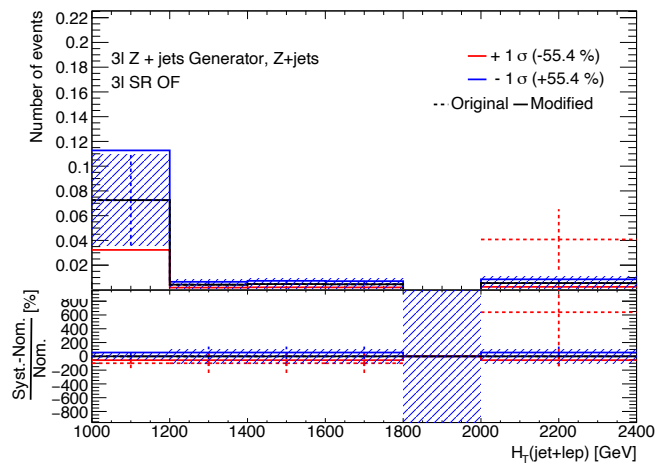
Figure B.36: Shape of 3l Z+jets Generator systematic
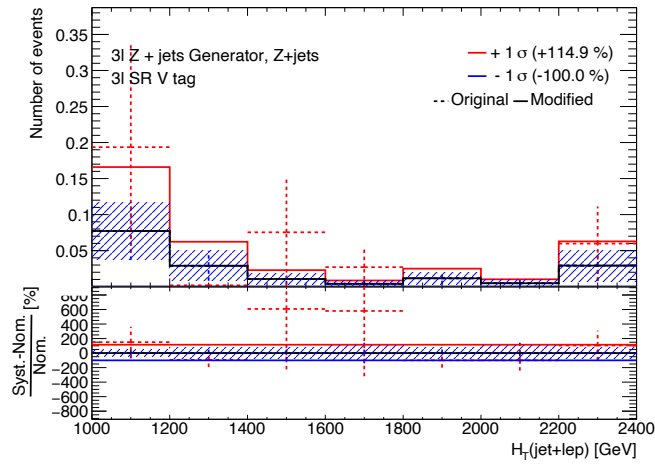
Figure B.37: Shape of 3l Z+jets Generator systematic

151
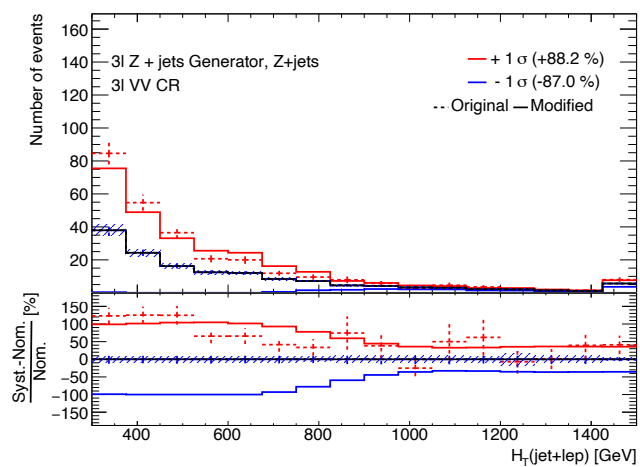
Figure B.38: Shape of 3l Z+jets Generator systematic
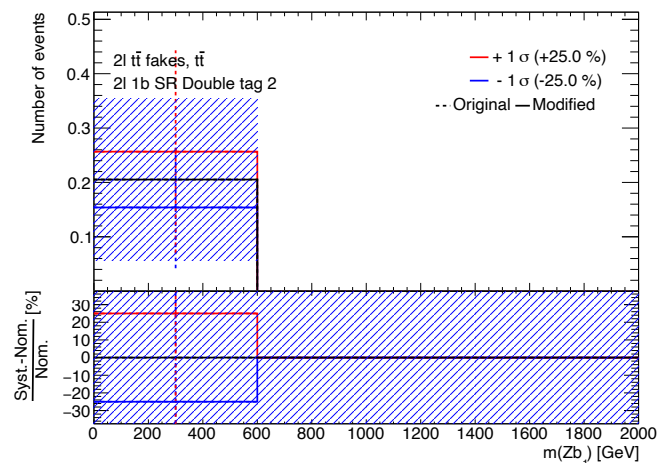
Figure B.39: Shape of 2l $t\bar{t}$ fakes systematic
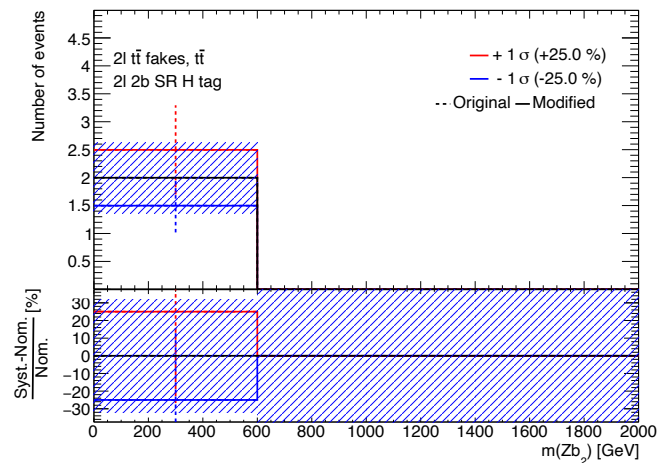
Figure B.40: Shape of 2l $t\bar{t}$ fakes systematic
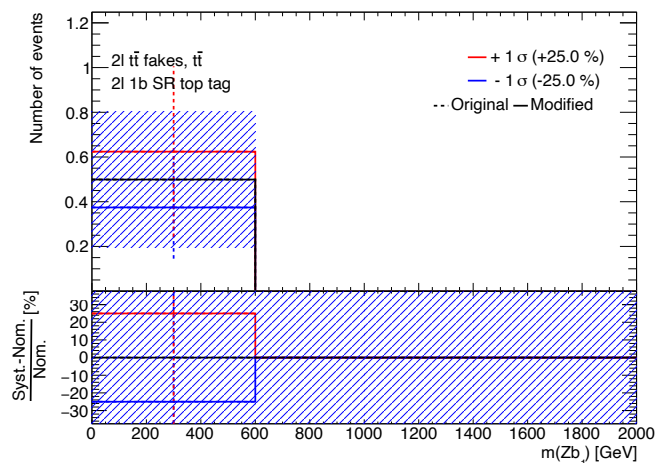
Figure B.41: Shape of 2l $t\bar{t}$ fakes systematic
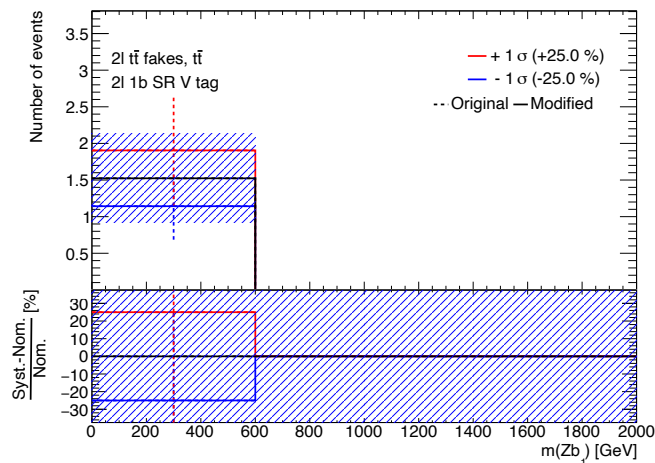
Figure B.42: Shape of 2l $t\bar{t}$ fakes systematic
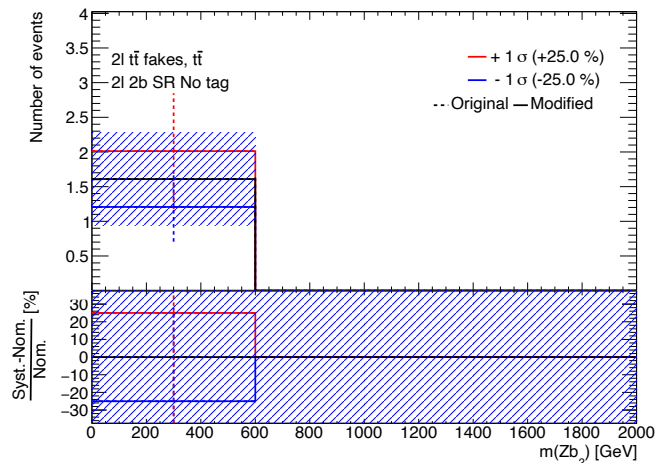
Figure B.43: Shape of 2l $t\bar{t}$ fakes systematic
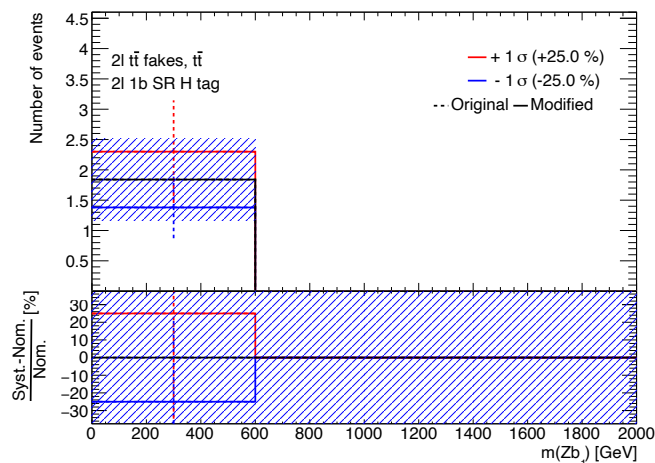
Figure B.44: Shape of 2l $t\bar{t}$ fakes systematic
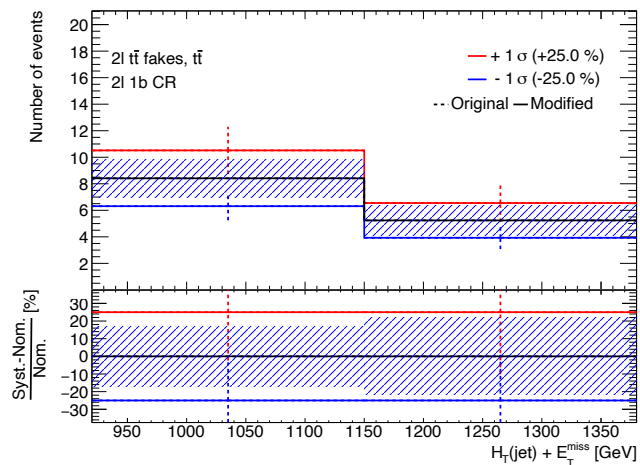

Figure B.45: Shape of 2l $t\bar{t}$ fakes systematic
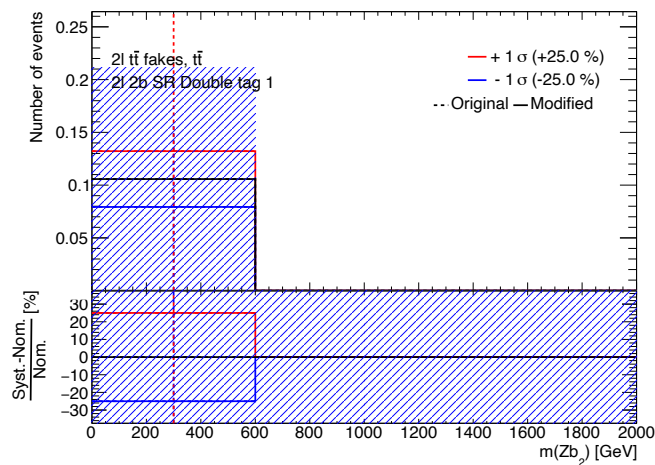
Figure B.46: Shape of 2l $t\bar{t}$ fakes systematic
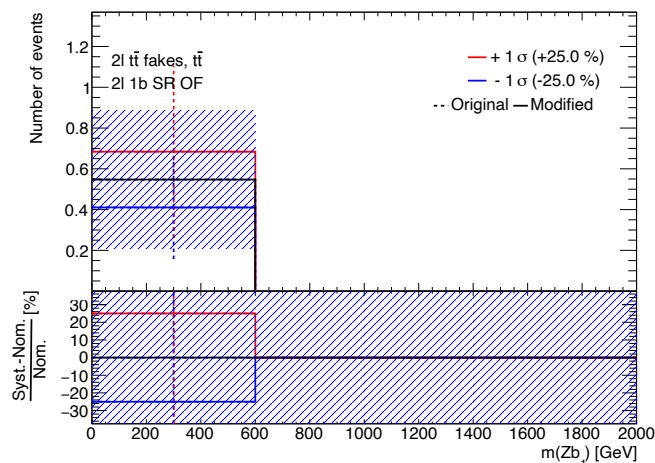
Figure B.47: Shape of 2l $t\bar{t}$ fakes systematic
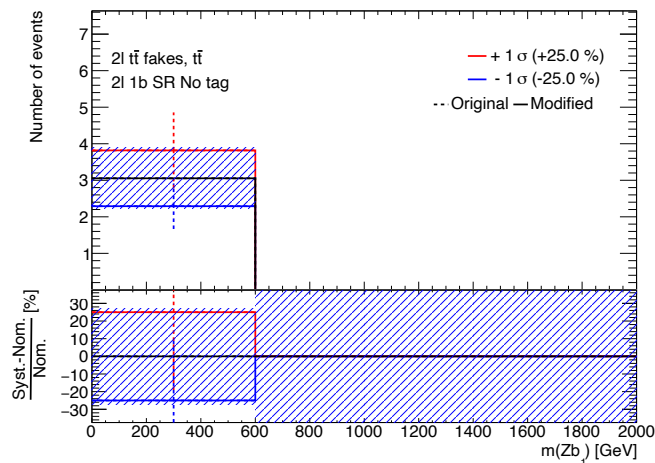
Figure B.48: Shape of 2l $t\bar{t}$ fakes systematic
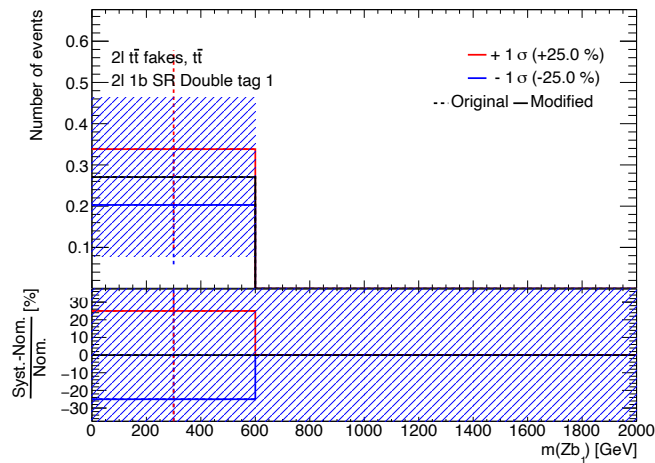
Figure B.49: Shape of 2l $t\bar{t}$ fakes systematic
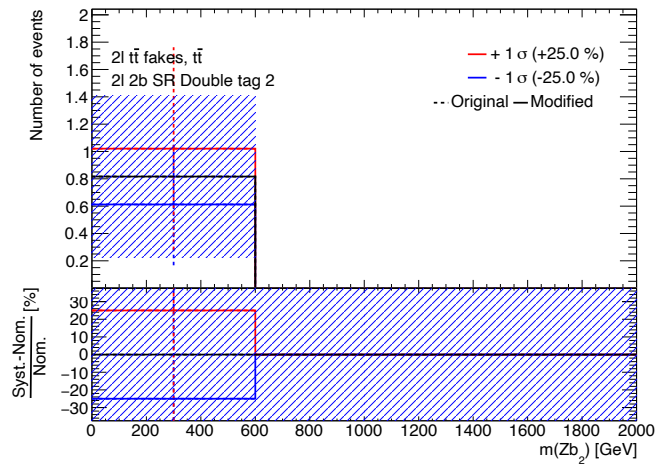
Figure B.50: Shape of 2l $t\bar{t}$ fakes systematic
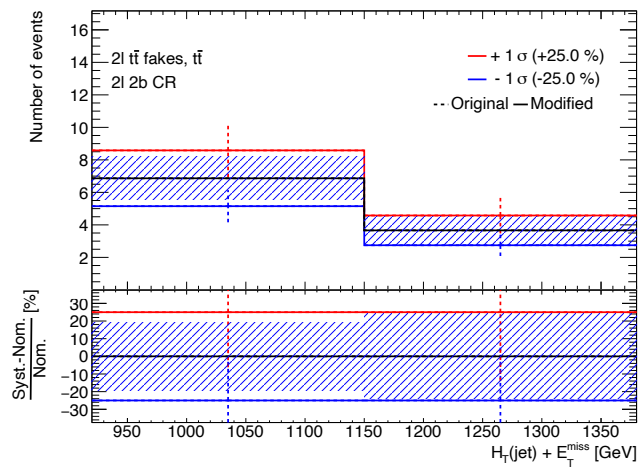
Figure B.51: Shape of 2l $t\bar{t}$ fakes systematic
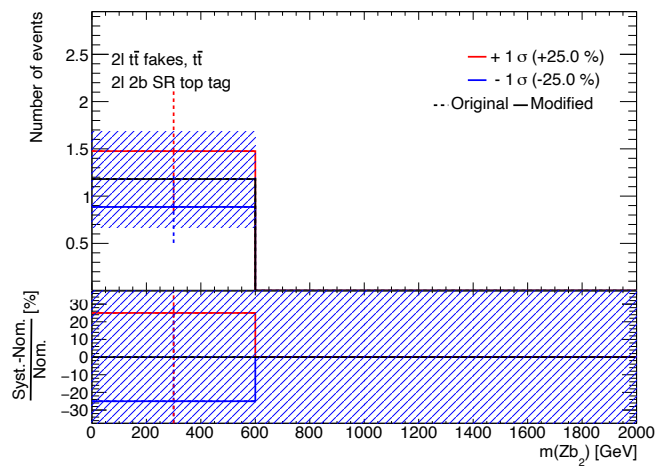
Figure B.52: Shape of 2l $t\bar{t}$ fakes systematic
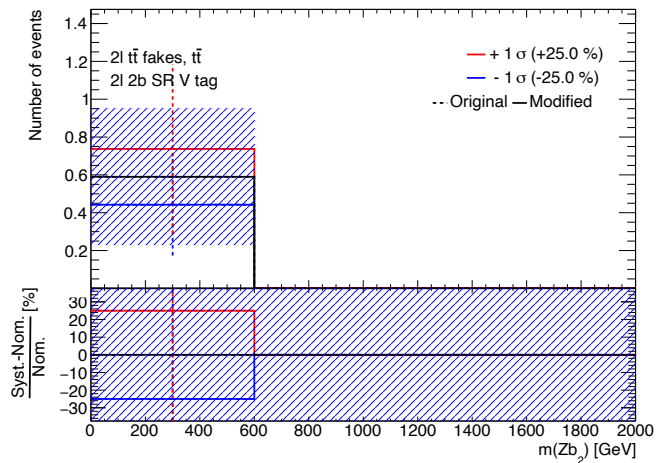
Figure B.53: Shape of 2l $t\bar{t}$ fakes systematic
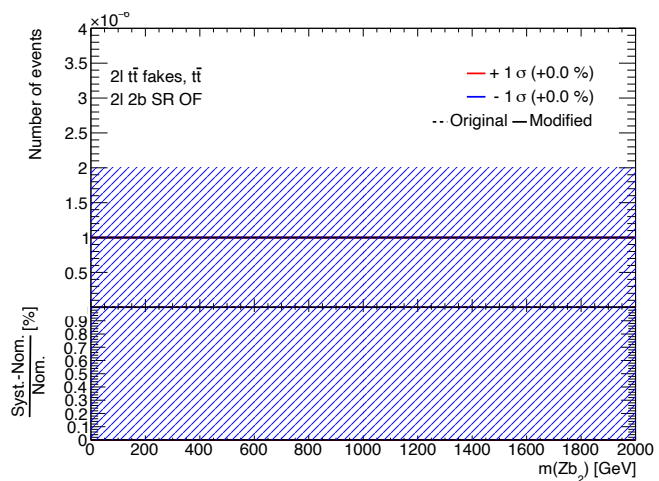

Figure B.54: Shape of 2l $t\bar{t}$ fakes systematic
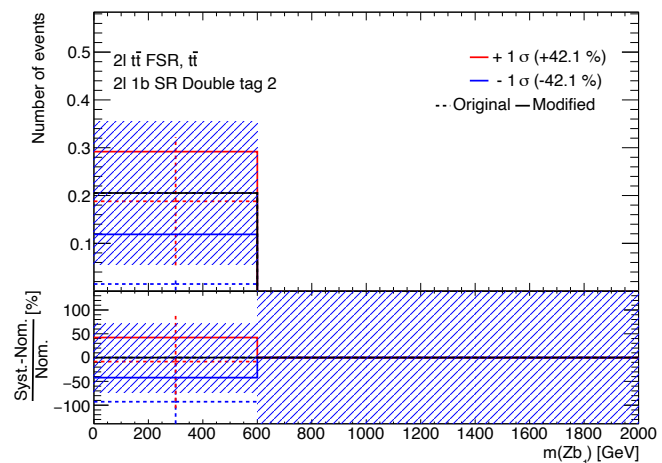
Figure B.55: Shape of 2l $t\bar{t}$ FSR systematic
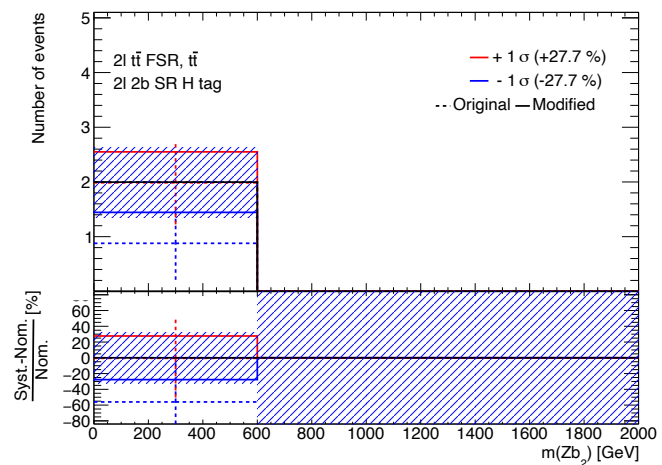
Figure B.56: Shape of 2l $t\bar{t}$ FSR systematic
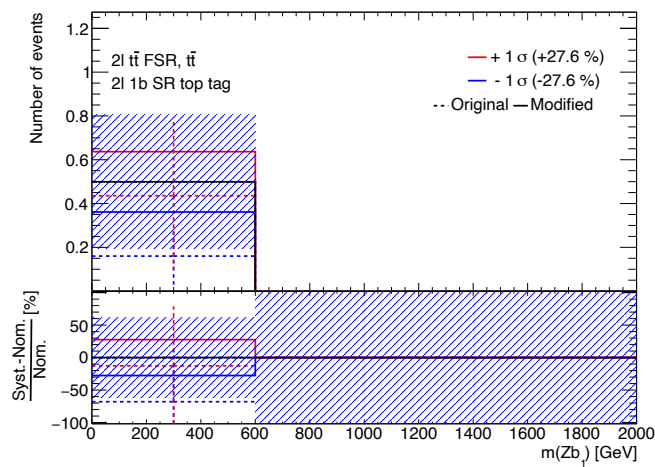
Figure B.57: Shape of 2l $t\bar{t}$ FSR systematic
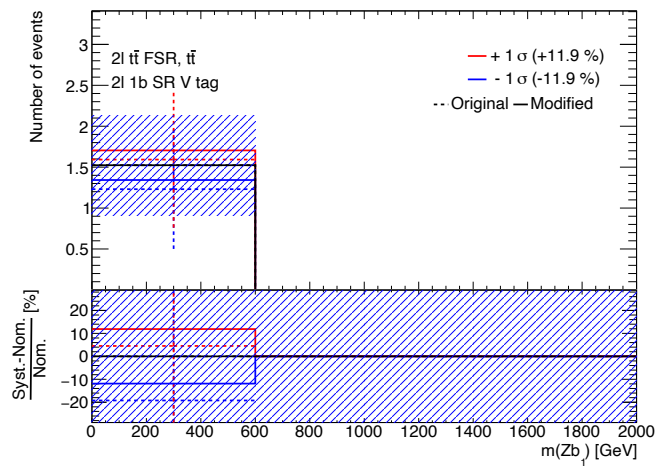
Figure B.58: Shape of 2l $t\bar{t}$ FSR systematic
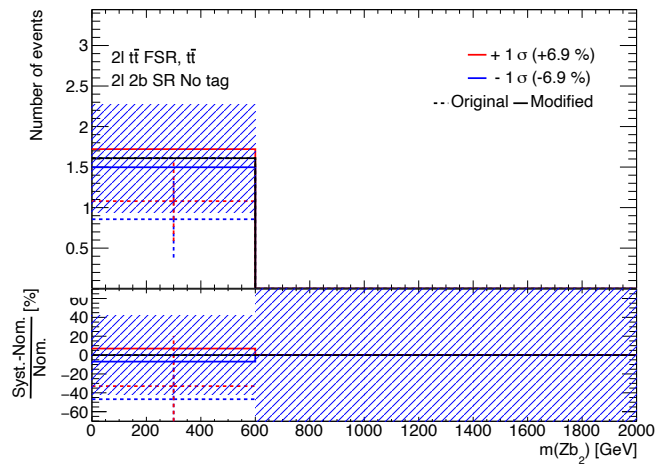
Figure B.59: Shape of 2l $t\bar{t}$ FSR systematic

Figure B.60: Shape of 2l $t\bar{t}$ FSR systematic

Figure B.61: Shape of 2l $t\bar{t}$ FSR systematic

Figure B.62: Shape of 2l $t\bar{t}$ FSR systematic

161
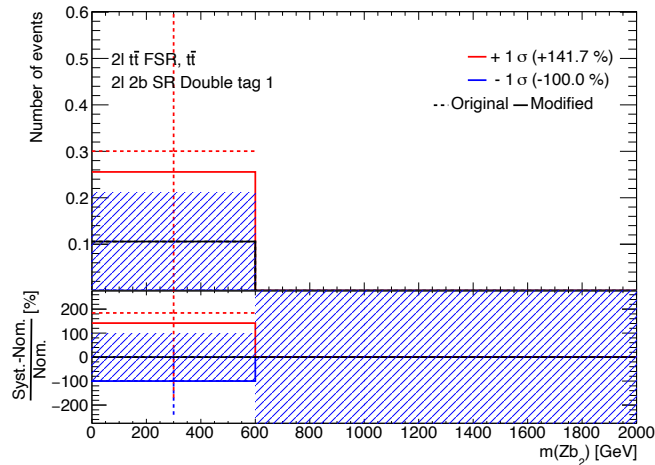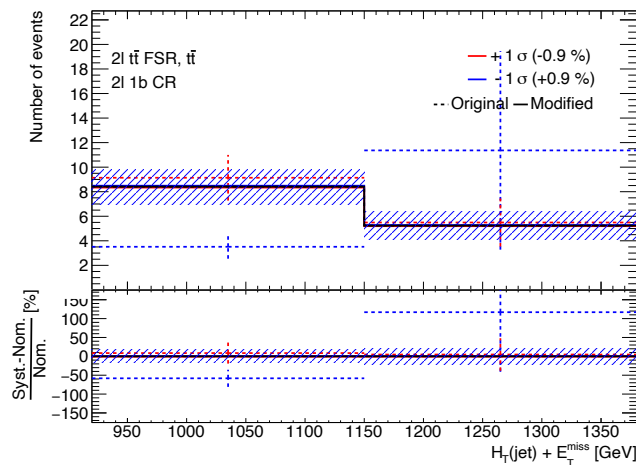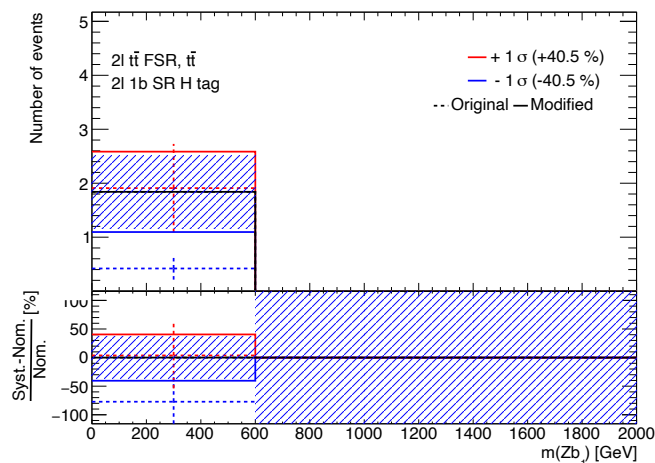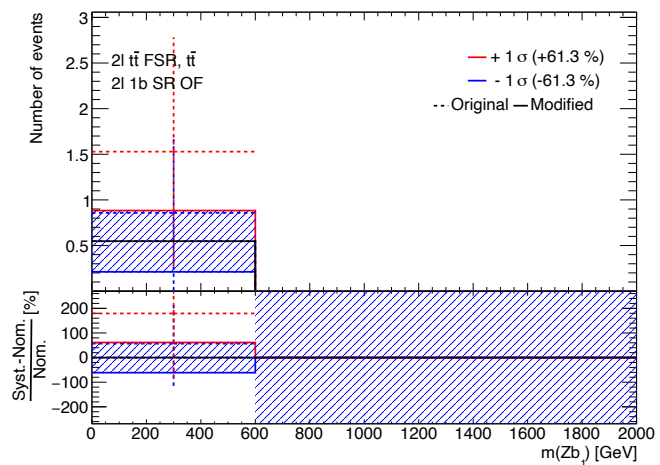
Figure B.63: Shape of 2l $t\bar{t}$ FSR systematic
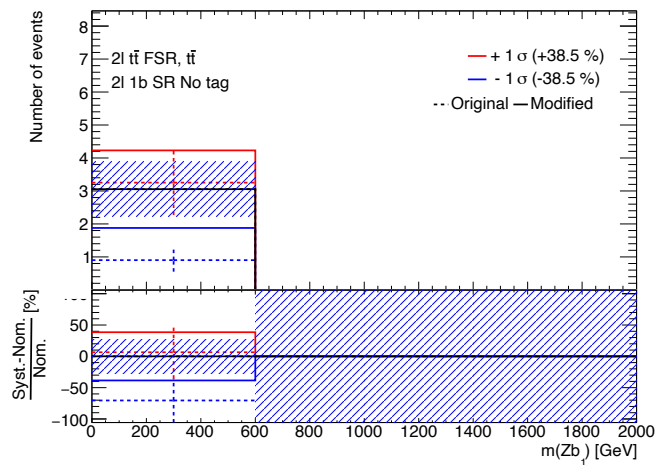

Figure B.64: Shape of 2l $t\bar{t}$ FSR systematic
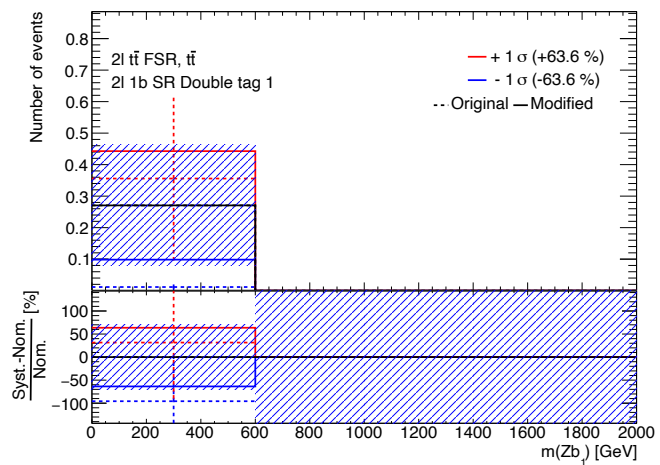
Figure B.65: Shape of 2l $t\bar{t}$ FSR systematic
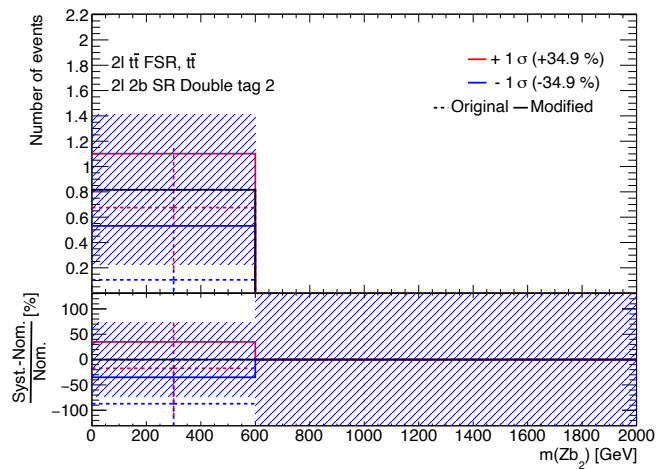
Figure B.66: Shape of 2l $t\bar{t}$ FSR systematic
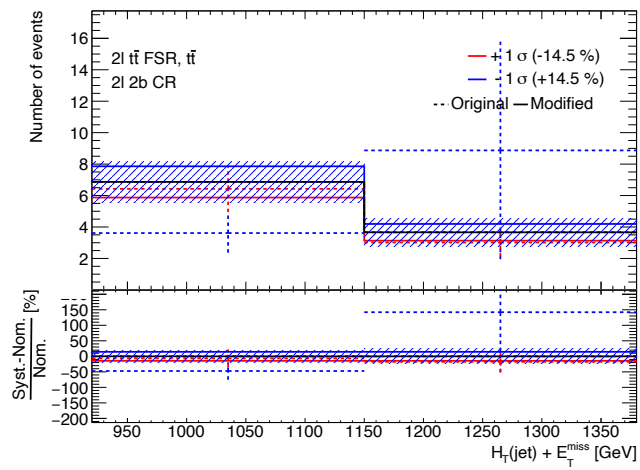

Figure B.67: Shape of 2l $t\bar{t}$ FSR systematic
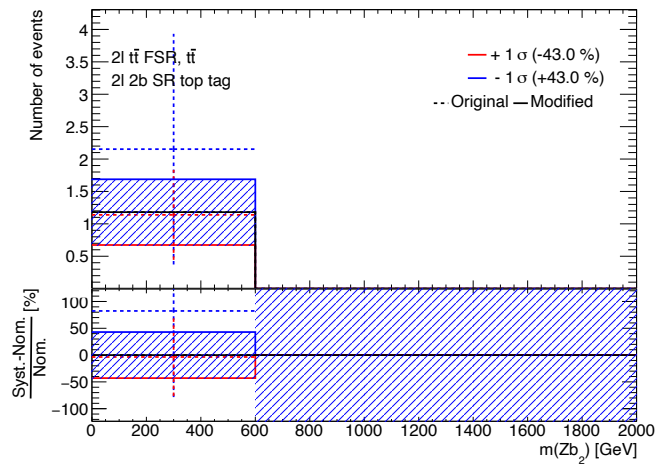
Figure B.68: Shape of 2l $t\bar{t}$ FSR systematic
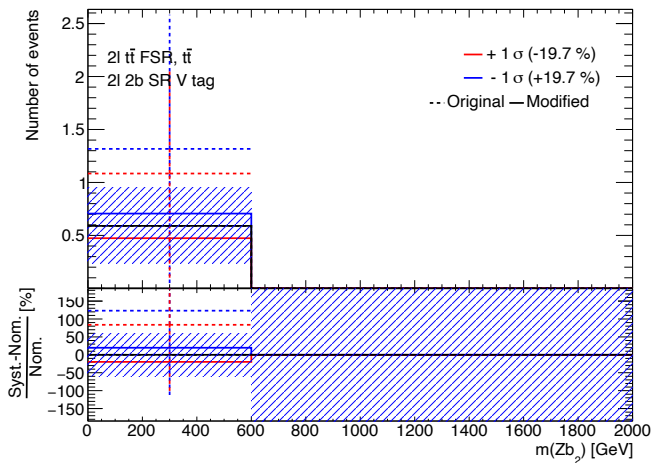
Figure B.69: Shape of 2l $t\bar{t}$ FSR systematic
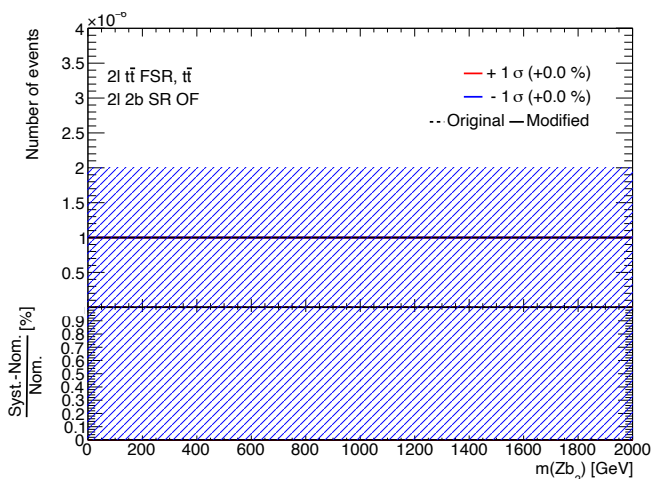
Figure B.70: Shape of 2l $t\bar{t}$ FSR systematic

Combination correlation schemes

In order to determine the best scheme of correlations among the two channels a few different combinations were tried. The set of nuisance parameters considered were the modelling systematics. This means all PDF systematics, scale variations, shower and generator systematics. Below are the pull plots for the different setups.

Given that the choice of combination schemes does not seem to affect the fit too much the most conservative setup was chosen and all modelling systematics will be uncorrelated across channels.
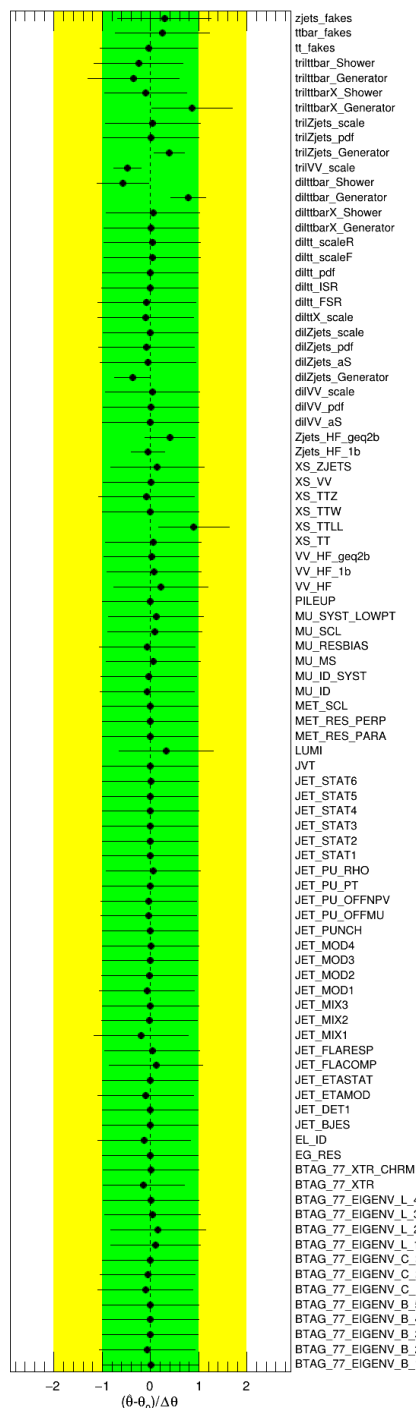
Figure C.1: Combination pull plot with all systematics correlated.
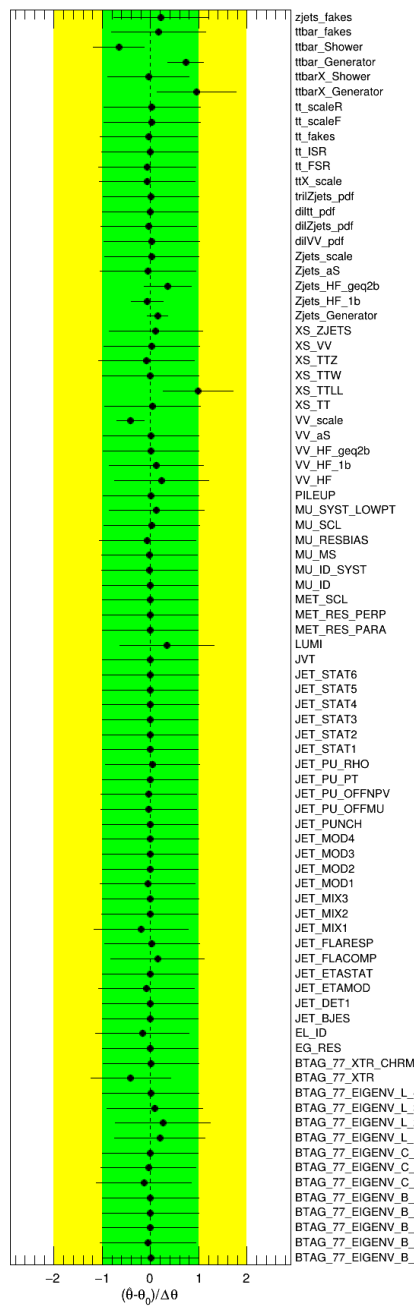
Figure C.2: Combination pull plot with all PDF systematics uncorrelated across channels.
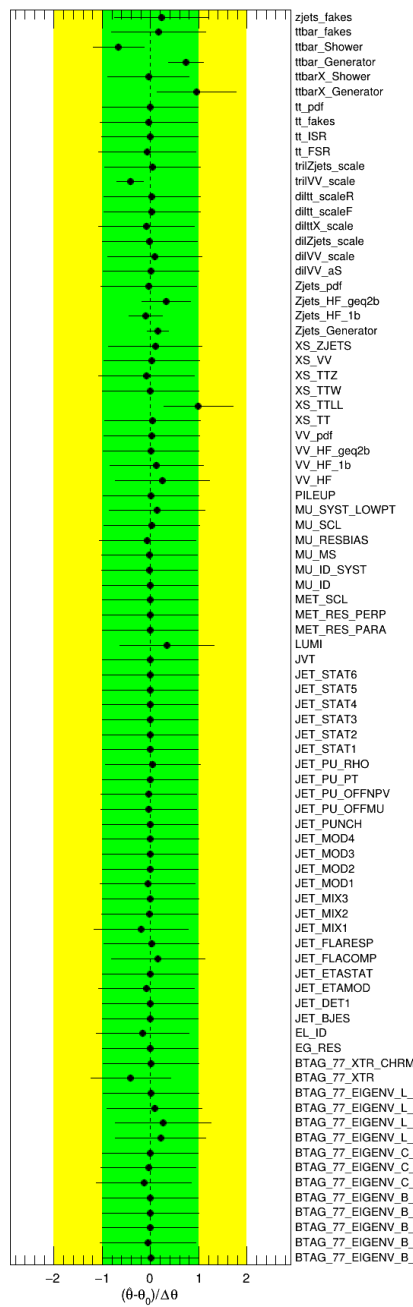
Figure C.3: Combination pull plot with all scale variations uncorrelated across channels.
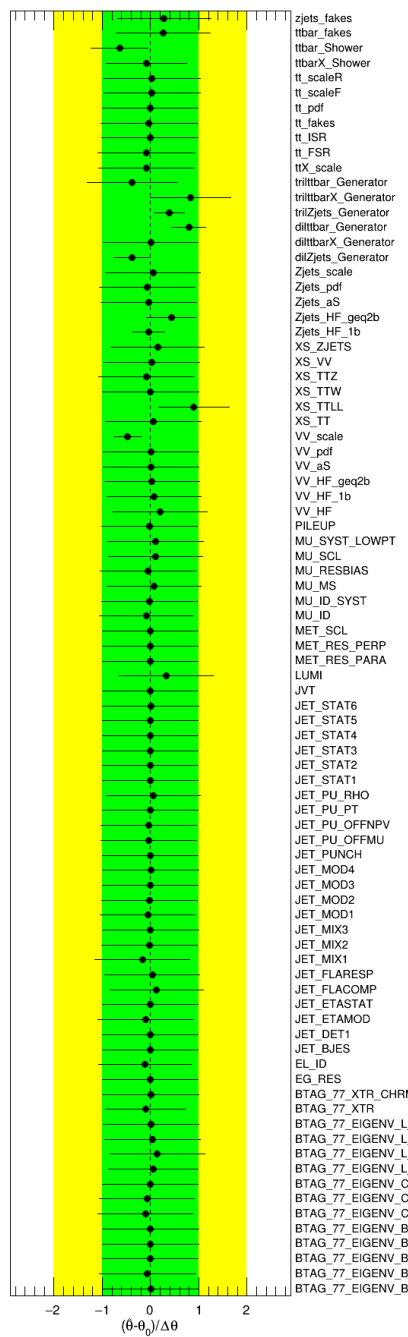
Figure C.4: Combination pull plot with all generator systematics uncorrelated across channels.
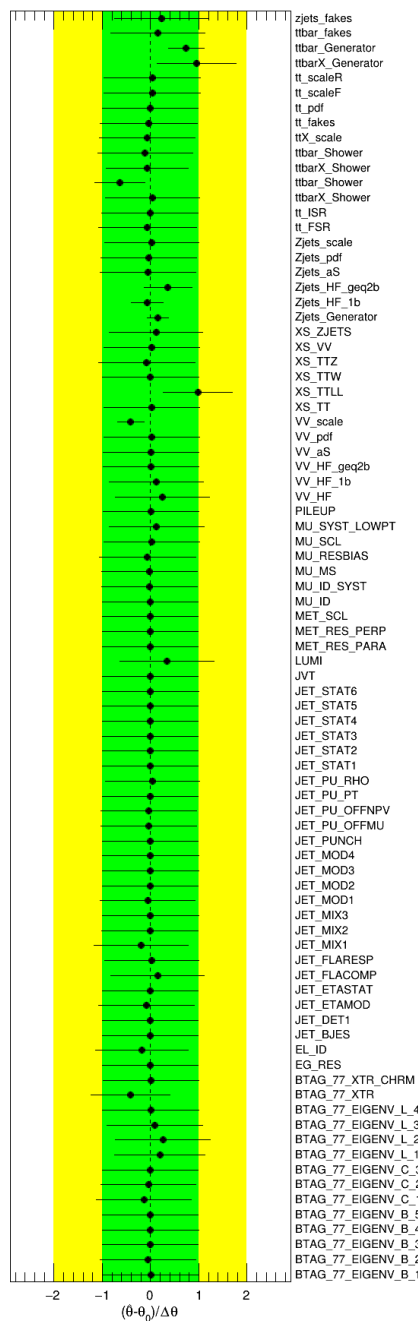
Figure C.5: Combination pull plot with all shower systematics uncorrelated across channels.
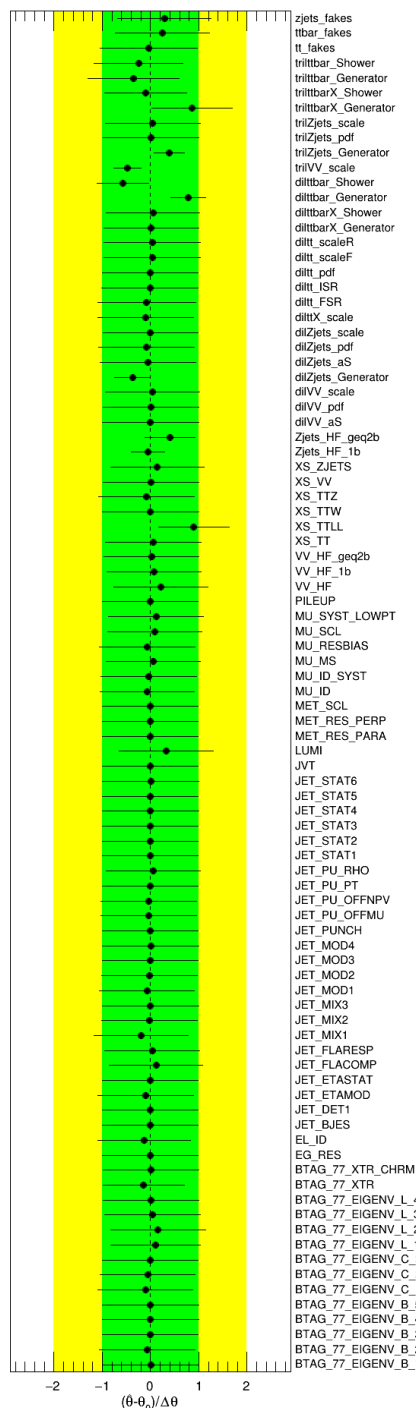
Figure C.6: Combination pull plot with all modelling systematics uncorrelated across channels.

Singlet and doublet comparison

The assumption made in this analysis is that the kinematic differences arising from the choice of a given model don't have a sizable effect on the analysis and that the only difference is the different contributions of each channel through the branching-ratios that are taken into account in the BR reweighting procedure. In order to show that this is the case, the main distributions used in both the 2ℓ and 3ℓ channel are compared in the singlet and doublet models. The samples used in these figures are the samples simulated with the singlet model with a VLQ mass of 1200 GeV and are compared with the samples generated with the doublet model for the same mass. Both, T and B quarks are shown. The discriminant variables for each channel are shown. The distributions compare singlet and doublet model and show the ratio between the corresponding singlet and doublet model case with the same color in the ratio pane.

For a VLT with 1.2 TeV, the expected limits on the signal strength using a doublet sample or the reweighting procedure change by about 2%.
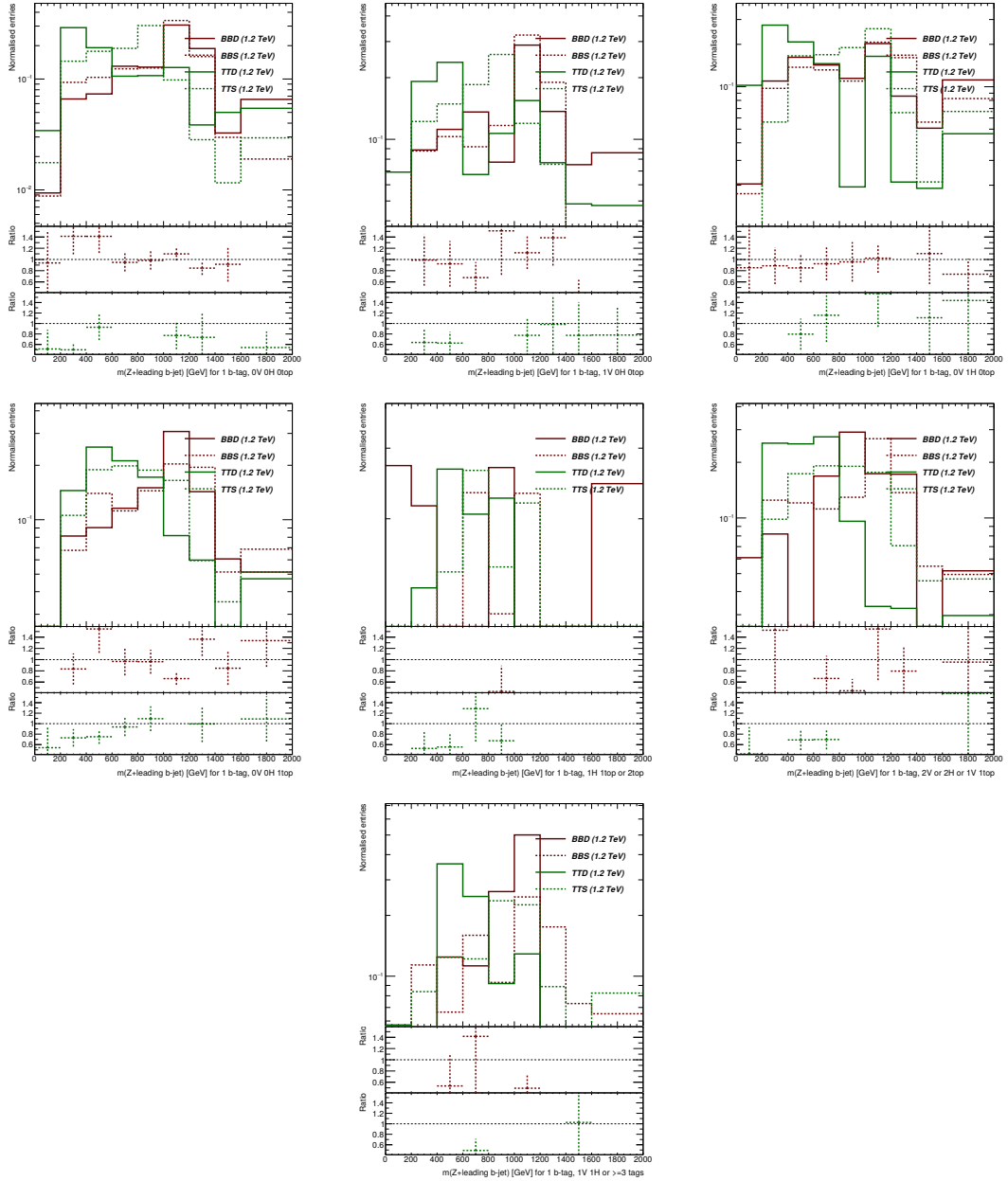
Figure D.1: Comparison between singlet and doublet model for BB and TT pair production using the final discriminants in the dilepton channel 1 btag regions.
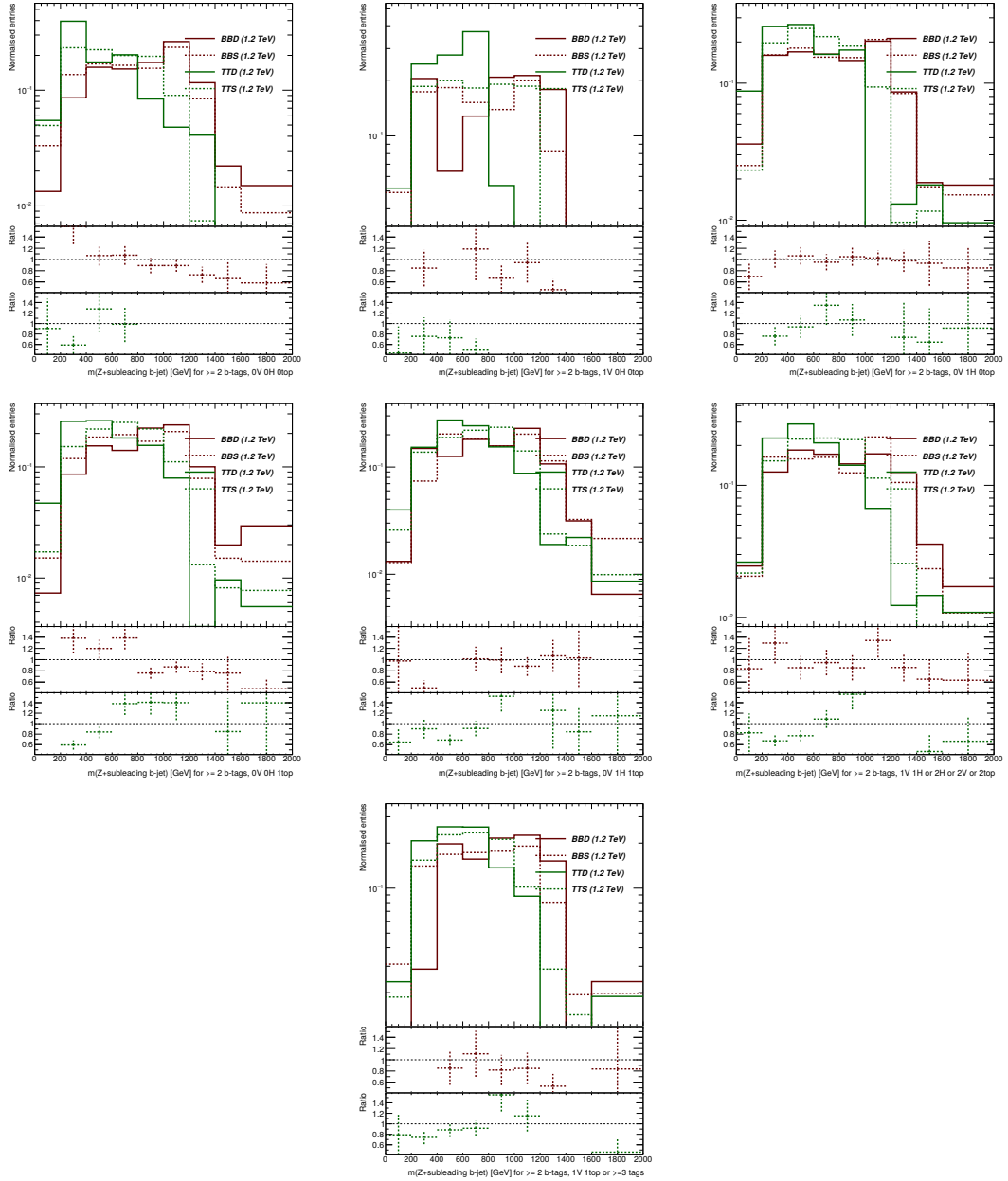
Figure D.2: Comparison between singlet and doublet model for BB and TT pair production using the final discriminants in the dilepton channel 2 btag regions.
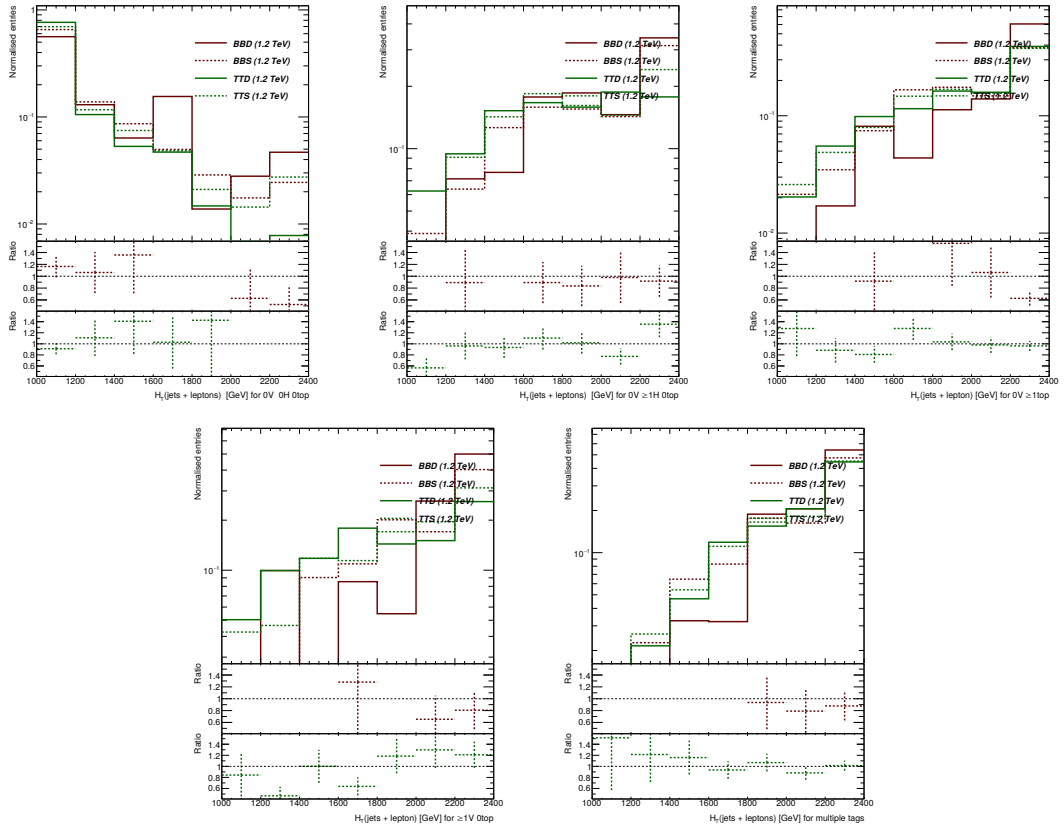
Figure D.3: Comparison between singlet and doublet model for BB and TT pair production using the final discriminants in the trilepton channel.
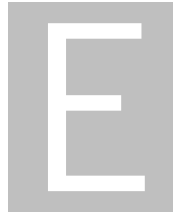
Signal regions contribution to the fit

As was stated in chapter 5, MCBOT is used in order to have a richer fit, and have many signal regions with different background composition that contribute to the fit. In this appendix the contribution of the signal regions to the fit is assessed, by doing the background only fit with the signal regions as validations regions, i.e., regions that do not contribute to the fit but to which the fit is applied, in order to appreciate its effect. Below the yields table and post-fit plots are shown. It can be seen that while the effect is not very large, in general the data/MC agreement is improved by the presence of the SRs. This is more easily seen in table E.1 where the total backgrounds for this fit setup and the nominal fit with all regions are shown next to each other and next to the data yields.

	2l 1b CR	2l 2b CR	2l 2b SR OF	2l 2b SR Double tag 1	2l 2b SR Double tag 2	2l 2b SR V tag	2l 2b SR H tag	2l 2b SR top tag	2l 2b SR No tag	2l 1b SR OF	2l 1b SR Double tag 1	2l 1b SR Double tag 2	2l 1b SR V tag	2l 1b SR H tag	2l 1b SR top tag	2l 1b SR No tag	3l W CR	3l SR No tag	3l SR V tag	3l SR H tag	3l SR top tag	3l SR OF
W	50(18)	9(4)	0.30(16)	0.46(26)	0.28(16)	0.22(13)	0.79(35)	0.9(4)	0.9(4)	0.9(4)	1.3(5)	0.40(19)	2.2(9)	2.4(9)	3.6(13)	5.6(20)	2780(100)	60(5)	2.89(27)	15.3(13)	8.1(6)	0.72(9)
$t\bar{t}+X$	12(7)	16(10)	0.42(29)	1.1(8)	0.7(4)	0.06(5)	0.23(15)	1.0(6)	0.07(8)	0.16(10)	0.19(13)	0.37(22)	0.20(12)	0.34(20)	1.1(6)	0.36(22)	80(50)	100(50)	10(5)	29(16)	2.3(12)	2.9(16)
Single-top	1.9(6)	1.7(6)	0.08(6)	3.1(5)	2.4(4)	0.007(8)	0.002(14)	0.036(13)	0.30(25)	0.04(6)	0.002(7)	0.04(5)	0.019(13)	0.034(17)	0.008(18)	0.9(5)	26.8(16)	17.3(5)	0.42(6)	2.05(13)	0.59(7)	0.079(35)
Z+jets	5.3(3.3)	120(17)	2.2(4)	0.10(23)	0.8(12)	2.04(35)	7.4(12)	10.6(16)	8.8(14)	4.7(6)	6.9(6)	2.6(32)	16.5(13)	23.5(21)	39.4(29)	71(5)	210(70)	8.8(32)	0.26(11)	1.4(4)	1.0(5)	0.07(5)
$t\bar{t}$	14(6)	11(5)	-	-	-	0.6(7)	2.1(17)	1.2(13)	1.5(15)	0.5(8)	0.3(4)	0.21(33)	1.5(14)	1.9(18)	0.5(7)	3.1(25)	38(7)	2.4(20)	-	-	0.4(10)	-
Total bkg. (CRs)	611(26)	158(13)	2.9(4)	4.8(8)	4.2(13)	2.9(8)	10.5(20)	13.7(18)	11.7(20)	6.4(10)	8.7(8)	3.6(5)	20.5(19)	28.1(26)	44.6(28)	81(5)	3140(70)	190(50)	13(5)	48(16)	33(12)	3.7(16)
Total bkg. (All regions)	598(24)	152(12)	2.8(7)	4.5(10)	3.7(12)	2.7(8)	9.4(16)	13.0(19)	10.7(19)	6.0(16)	8.3(12)	3.4(7)	19.6(26)	26.6(33)	43.5(31)	76(6)	3140(70)	203(12)	15.3(15)	52.9(28)	37.7(26)	4.3(9)
Data	610	160	2	4	0	1	10	10	14	9	7	2	18	34	32	72	3149	198	20	59	40	4

Table E.1: Yields after the background only fit using only the control regions.
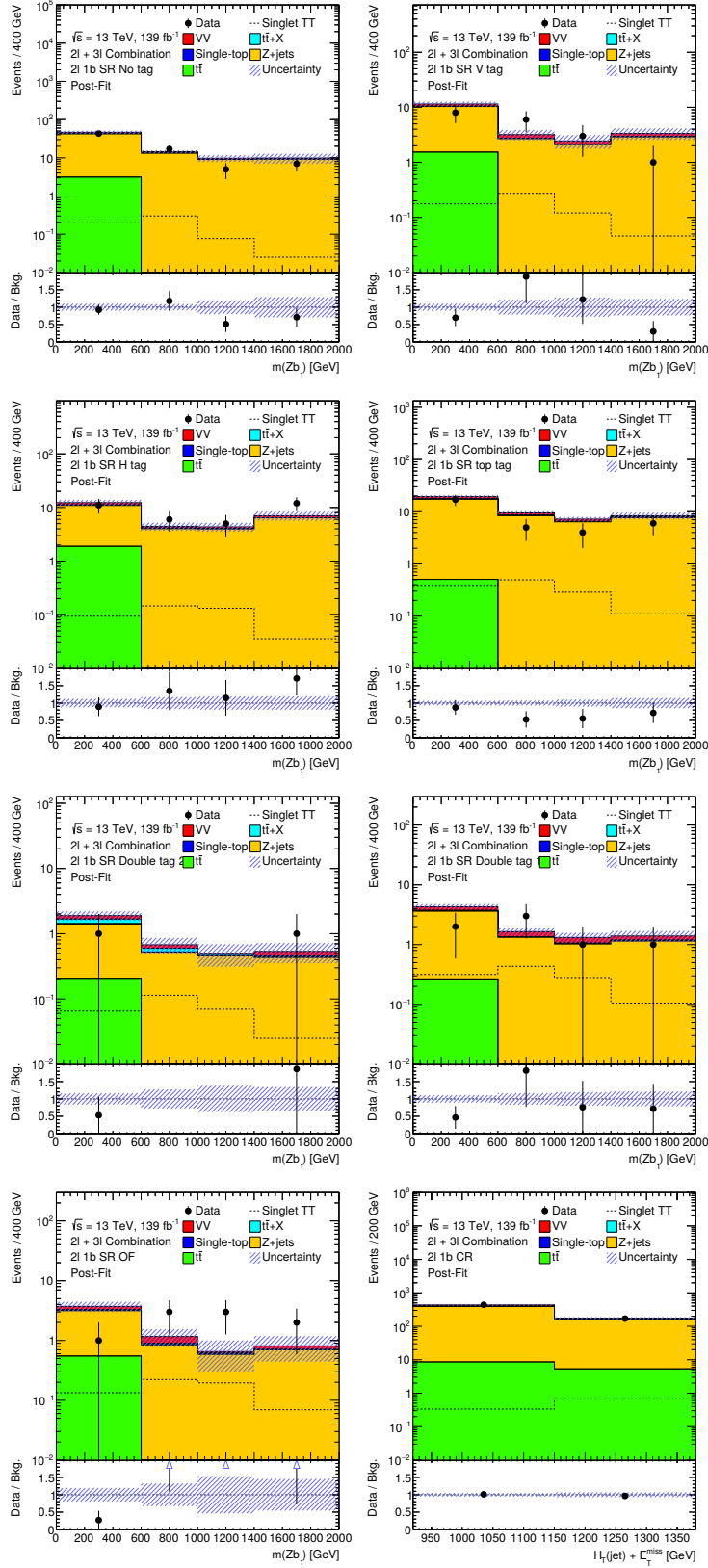
Figure E.1: Discriminant after a background only fit without signal regions in the 2ℓ regions with 1 b-tagged jet
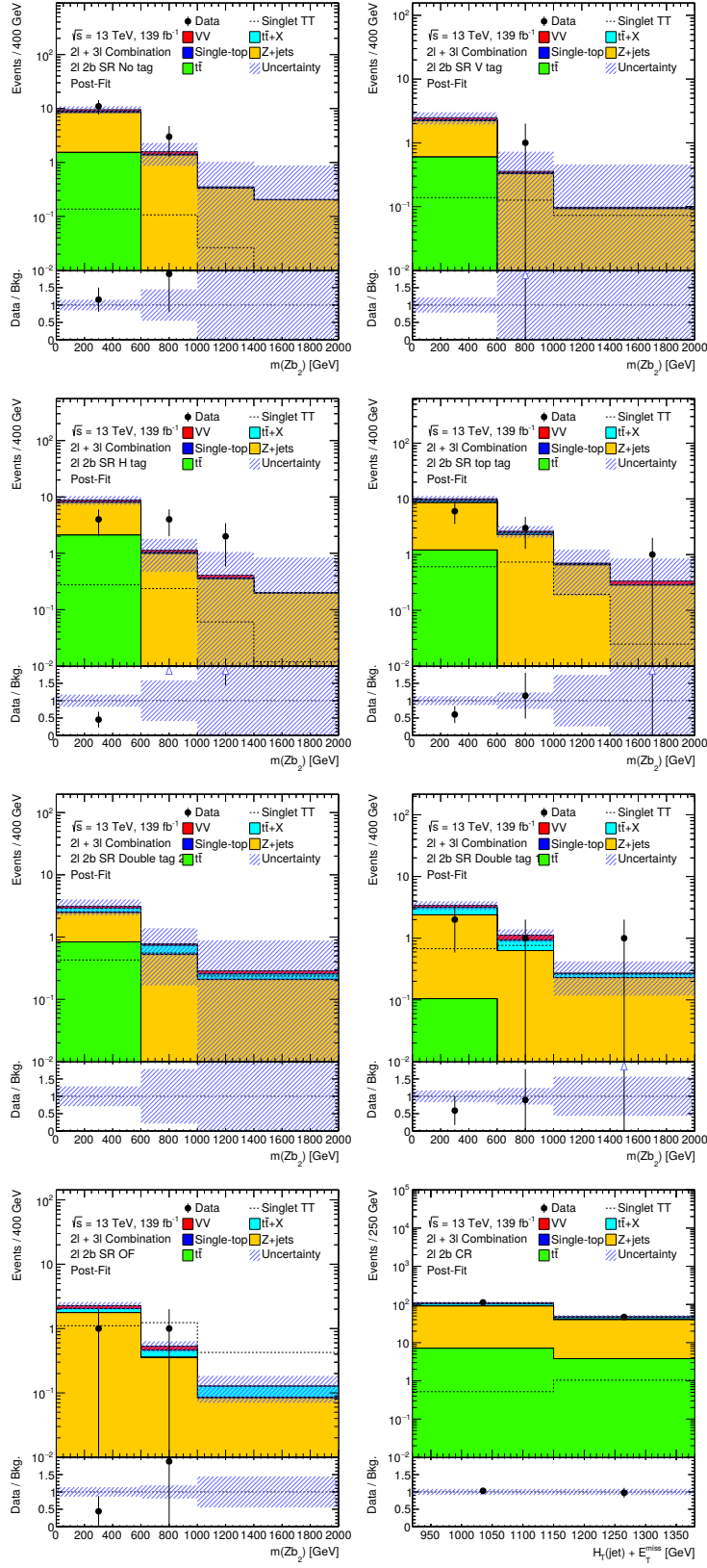
Figure E.2: Discriminant after a background only fit without signal regions in the 2ℓ regions with $\geq 2b$-tagged jets
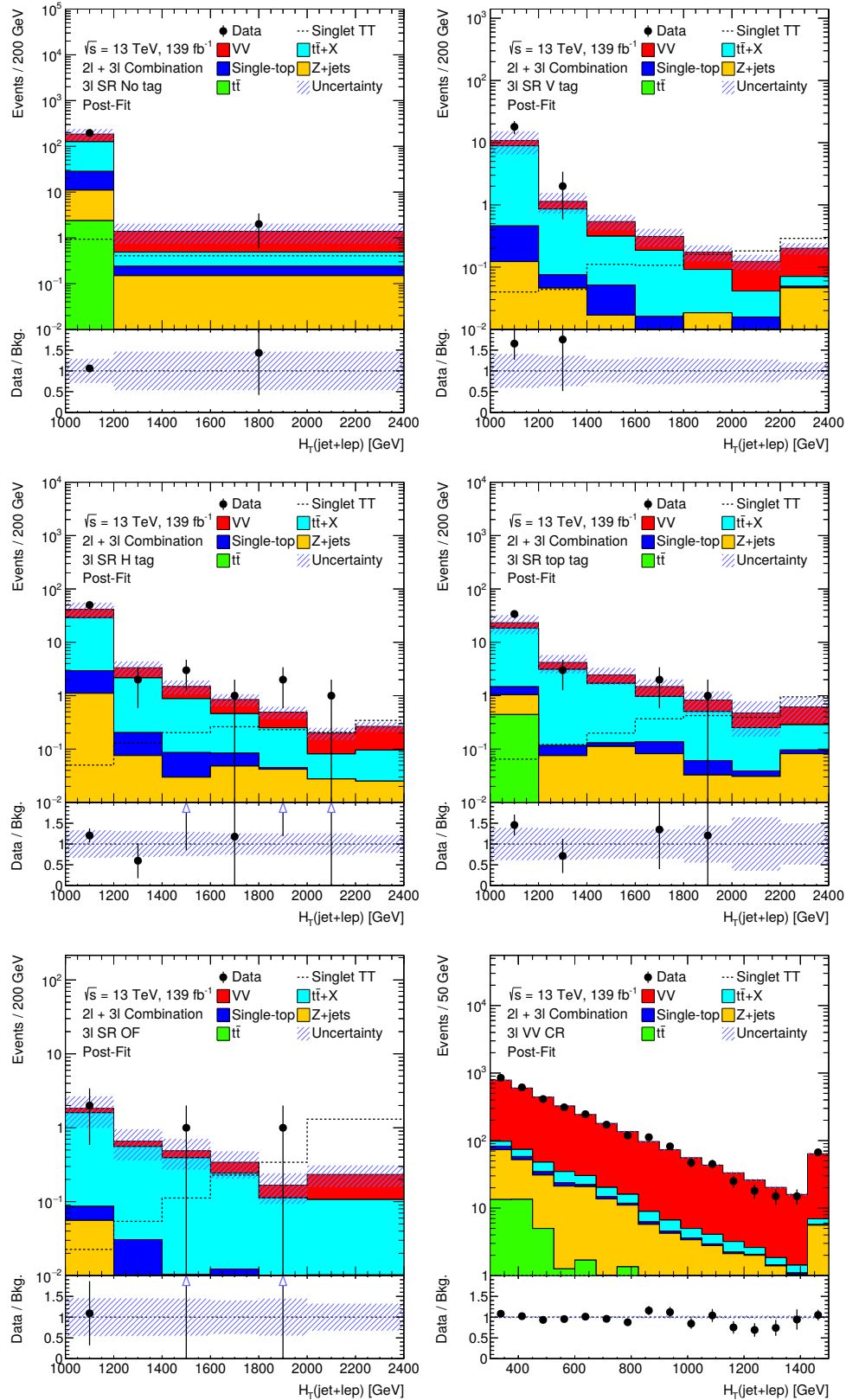
Figure E.3: Discriminant in the 3ℓ channel after a background only fit without signal regions